${}^{3}_{\Lambda}$H studies in relativistic ion-ion collisions: matter radius and production mechanisms

Studien zu ${}^{3}_{\Lambda}$H in relativistischen Ion-Ion-Kollisionen: Materieradius und Produktionsmechanismen

Zur Erlangung des Grades eines Doktors der Naturwissenschaften (Dr. rer. nat.)
Genehmigte Dissertation von Simone Velardita aus Caltagirone (Italien)
Tag der Einreichung: 13 November 2023, Tag der Prüfung: 11 Dezember 2023

1. Gutachten: Prof. Dr. Alexandre Obertelli
2. Gutachten: Prof. Dr. Tetyana Galatyuk
Darmstadt, Technische Universität Darmstadt

TECHNISCHE UNIVERSITÄT DARMSTADT

Physics Department
Institut für Kernphysik
AG-Obertelli

$^{3}_{\Lambda}$H studies in relativistic ion-ion collisions: matter radius and production mechanisms
Studien zu $^{3}_{\Lambda}$H in relativistischen Ion-Ion-Kollisionen: Materieradius und Produktionsmechanismen

Accepted doctoral thesis by Simone Velardita

Date of submission: 13 November 2023
Date of thesis defense: 11 Dezember 2023

Darmstadt, Technische Universität Darmstadt

Bitte zitieren Sie dieses Dokument als:
URN: urn:nbn:de:tuda-tuprints-264619
URL: http://tuprints.ulb.tu-darmstadt.de/26461
Jahr der Veröffentlichung auf TUprints: 2024

Dieses Dokument wird bereitgestellt von tuprints,
E-Publishing-Service der TU Darmstadt
http://tuprints.ulb.tu-darmstadt.de
tuprints@ulb.tu-darmstadt.de

Erklärungen laut Promotionsordnung

§ 8 Abs. 1 lit. c PromO

Ich versichere hiermit, dass die elektronische Version meiner Dissertation mit der schriftlichen Version übereinstimmt.

§ 8 Abs. 1 lit. d PromO

Ich versichere hiermit, dass zu einem vorherigen Zeitpunkt noch keine Promotion versucht wurde. In diesem Fall sind nähere Angaben über Zeitpunkt, Hochschule, Dissertationsthema und Ergebnis dieses Versuchs mitzuteilen.

§ 9 Abs. 1 PromO

Ich versichere hiermit, dass die vorliegende Dissertation selbstständig und nur unter Verwendung der angegebenen Quellen verfasst wurde.

§ 9 Abs. 2 PromO

Die Arbeit hat bisher noch nicht zu Prüfungszwecken gedient.

Darmstadt, 13 November 2023

S. Velardita

Zusammenfassung

Bei der Erforschung der Kernphysik stellen Hypernuklei einzigartige Einheiten dar, die Ungewöhnliches in die nukleare Landschaft einbringen und sie erweitern, um neue strukturelle Phänomene zu enthüllen. Die Untersuchung ihrer inneren Zusammensetzung ermöglicht den Zugang zu den Hyperon-Nukleon- und Hyperon-Hyperon-Wechselwirkungen, deren direkte Untersuchung (z. B. durch elastische Streuung) aufgrund der kurzen Lebensdauer von Hyperonen schwierig ist. Ein besseres Verständnis der Baryonen-Wechselwirkungen, einschließlich der Hyperonen, verbessert die Kenntnisse über die Zustandsgleichungen der Kerne und damit auch über die innere Kernstruktur von Neutronensternen. Unter den Hyperkernen wurde das Hypertritium ($^{3}_{\Lambda}$H), insbesondere seine bisher nicht gemessene Größe, als Schlüsselsonde für das Verständnis der Nukleosynthesemechanismen in relativistischen Schwerionenkollisionen bezeichnet. Diese Arbeit konzentriert sich auf $^{3}_{\Lambda}$H, das in relativistischen Ionen-Ionen-Kollisionen bei GSI/SIS18-Energien (bis zu 2 AGeV) erzeugt wird, um seinen Materieradius und mögliche Produktionsmechanismen zu untersuchen.

Im ersten Teil der Arbeit wird das Konzept eines neuen akzeptierten Experiments vorgestellt, das im Jahr 2025 an der R^{3}B-Anlage der GSI unter Verwendung von ^{12}C+^{12}C-Kollisionen bei 1,9 AGeV durchgeführt werden soll. Das Experiment zielt auf die erste Bestimmung der $^{3}_{\Lambda}$H-Größe, welches als Halo-Hypernukleus vorhergesagt wird, durch Messungen des Wechselwirkungsquerschnitts. Um dies zu erreichen, wurde eine neue experimentelle Methode zur Extraktion des Wechselwirkungsquerschnitts von Hypernuklei mit einem Targetkern entwickelt, die empfindlich auf deren Materieradien reagiert. Der Wechselwirkungsquerschnitt kann mit einer Genauigkeit von 15% oder besser bestimmt werden, was die Extraktion des unbekannten $^{3}_{\Lambda}$H-Materieradius und die Bewertung seines Halo- oder Nicht-Halo-Charakters ermöglicht. Darüber hinaus wurden realistische GEANT4-Simulationen durchgeführt, um den Aufbau des Experiments zu optimieren, einschließlich des Hauptdetektors und der Mini-HYDRA-time projection chamber (HYpernuclei Decay at R^{3}B Apparatus), und um die Durchführbarkeit des Experiments zu bewerten. Schließlich wird der Entwurf und die Validierung eines neuen Detektors, der HYDRA-plastic-wall, vorgestellt, der als Trigger für die Messung verwendet werden soll.

Der zweite Teil der Arbeit befasst sich mit den Produktionsmechanismen von $^{3}_{\Lambda}$H in Schwerionenkollisionen an der HADES-Anlage der GSI. Hier wird die Produktion durch die Analyse bestehender Datensätze aus den Jahren 2019 und 2012 mit unterschiedlichen Kollisionsenergien untersucht, d.h. Ag+Ag bei 1,58 AGeV und 1,23 AGeV, sowie Au+Au bei 1,23 AGeV. Während der erste Satz genau an der Schwelle der Strangeness-Produktion aus elementaren Nukleon-Nukleon-Kollisionen liegt (1,58 GeV), liegen die anderen darunter. Die Datenanalyse identifizierte eindeutig das $^{3}_{\Lambda}$H-Signal aus der invarianten Masse seiner Zerfallsprodukte, $\pi^- + {}^3$He, sowohl für die Hoch- als auch für die Niedrigenergiedaten-

sätze: Das Signifikanzniveau für die Peaks beträgt 18,27, 5,16 und 4,00 für Ag+Ag bei 1,58 AGeV, 1,23 AGeV bzw. Au+Au bei 1,23 AGeV. Anschließend werden die zugehörigen Produktionsquerschnitte an und unterhalb der Strangeness-Produktionsschwelle extrahiert und das Verhältnis der Produktionsquerschnitte von niedriger zu hoher Energie aus dem Ag+Ag-Datensatz beträgt 0,30 $\pm$0,08(stat.)$\pm$0,03(sys.). Diese Ergebnisse deuten auf Beiträge zusätzlicher Produktionsmechanismen für Hypernuklei hin, die durch den Vergleich der experimentellen Ergebnisse mit Vorhersagen aus Transportmodellen weiter untersucht werden müssen.

Abstract

In the exploration of nuclear physics, hypernuclei stand as unique entities, introducing strangeness into the nuclear landscape and extending it to reveal new structural phenomena. Investigating their internal composition gives access to the hyperon-nucleon and hyperon-hyperon interactions, which are challenging to study directly (e.g., by elastic scattering) due to the short lifetime of hyperons. A better understanding of baryon interactions, including hyperons, improves the knowledge on the nuclear equation of state and, consequently, the inner core structure of neutron stars. Among hypernuclei, the hypertriton ($^{3}_{\Lambda}$H), and specifically its size, not measured so far, has been indicated as a key probe to understand the nucleosynthesis mechanisms in relativistic heavy-ion collisions. This thesis focuses on $^{3}_{\Lambda}$H produced in relativistic ion-ion collision at GSI/SIS18 energies (up to 2 AGeV), in order to access its matter radius and possible production mechanisms.

In the first part of the thesis, the concept of a new accepted experiment that will be performed in 2025 at the R^{3}B setup in GSI using ^{12}C+^{12}C collisions at 1.9 AGeV is detailed. The experiment aims at the first determination of the $^{3}_{\Lambda}$H size, predicted to be a halo hypernucleus, through interaction cross section measurements. To achieve that, a new experimental method to extract the interaction cross section of hypernuclei with a target nucleus, sensitive to their matter radii, was developed. A precision of 15% or better in the interaction cross section can be achieved, allowing extraction of the unknown $^{3}_{\Lambda}$H matter radius and assessing its halo or non-halo character. In addition, realistic GEANT4 simulations have been performed in order to optimize the design of the experimental setup, including the main detector, the mini-HYDRA (HYpernuclei Decay at R^{3}B Apparatus) time-projection chamber, and to assess the feasibility of the experiment. Finally, the design and validation of a new detector, the HYDRA plastic wall, is presented, which is intended to be used as a trigger in the measurement.

The second part of the thesis focuses on the production mechanisms of $^{3}_{\Lambda}$H in heavy-ion collisions at the HADES setup in GSI. Here, the production is explored by analyzing existing datasets, taken in 2019 and 2012, with different collision energies, *i.e.*, Ag+Ag at 1.58 AGeV and 1.23 AGeV, and Au+Au at 1.23 AGeV. While the first set is exactly at the strangeness production threshold from elementary nucleon-nucleon collisions (1.58 GeV) the others are below it. The data analysis identified clearly the $^{3}_{\Lambda}$H signal from the invariant mass of its decay products, $\pi^- + {}^3$He, for both the high and low energy datasets: the significance level for the peaks are 18.27, 5.16, and 4.00 for the Ag+Ag at 1.58 AGeV, 1.23 AGeV, and Au+Au at 1.23 AGeV, respectively. Following that, the associated production cross-sections at and below the strangeness production threshold are extracted and the production cross section ratio of low-to-high energy from the Ag+Ag dataset amounts to $0.30\pm0.08(\text{stat.})\pm0.03(\text{sys.})$. These findings indicate contributions from additional production mechanisms for hypernuclei that

need to be further investigated by comparing the experimental results with predictions from transport models.

Acknowledgment

It has been an amazing journey, and it all began because Prof. Dr. Alexandre Obertelli gave me the opportunity to join the project, believing that I was a good fit for it. I appreciate your continuous support and guidance over the years. All the words that you will read in this thesis have been read and meticulously checked by Meytal, to whom goes my sincere thanks. The thesis would not be the same without the countless hours of discussion we had. I am grateful to my colleagues for *Indian Thursday* and for creating a relaxed working environment where mutual help is a priority: mini-boss(FW), CX, MS, AE, JF and AS. In particular, I'd like to thank Alex and Jonas for all the time we spent outside work. I haven't forgotten about you, Sabrina, my former office-mate, who made the days we spent in the office and outside so much better, giving me one of my best German memories (haunting the Autumn), and whom I blame for my addiction to mate.

Of course, none of this would have been possible without the support of my family and friends, who, with one call, can make me feel at home. To my mother and father, who never doubted my choices and believed I could succeed in this difficult adventure: *Grazie!*. I would like to thank my "Famiglia allargata", who are proud of me and don't miss a chance to brag about my achievements, making me feel special. Finally, to all my friends with whom I'm in contact, even if we are scattered all around Europe, you are too many to list. If we spoke in the last 6 months at least once, I'm talking about you. Special mention to Santo and Carolina, whose arrival in Darmstadt significantly improved my social life and introduced me to my new passion for bouldering.

It's all very nice, but my best cheerleader has undoubtedly been Miriam, who, over the past years, supported me and tried to be as present as she could despite us living in two different countries. I could not have asked for a better person to be in my life.

Finally, I would like to warmly thank Prof. Dr. Tetyana Galatyuk, Prof. Dr. Robert Roth and Prof. Dr. Regine von Klitzing for agreeing to be the examiners of this defense.

Contents

List of Figures

List of Tables

1. Introduction

1.1. The Standard model of particle physics

The Standard Model (SM) of particle physics describes the fundamental particles and their interactions. It provides a framework for understanding the building blocks of matter and the forces that govern its properties. A schematic description is given in Fig. 1.1.

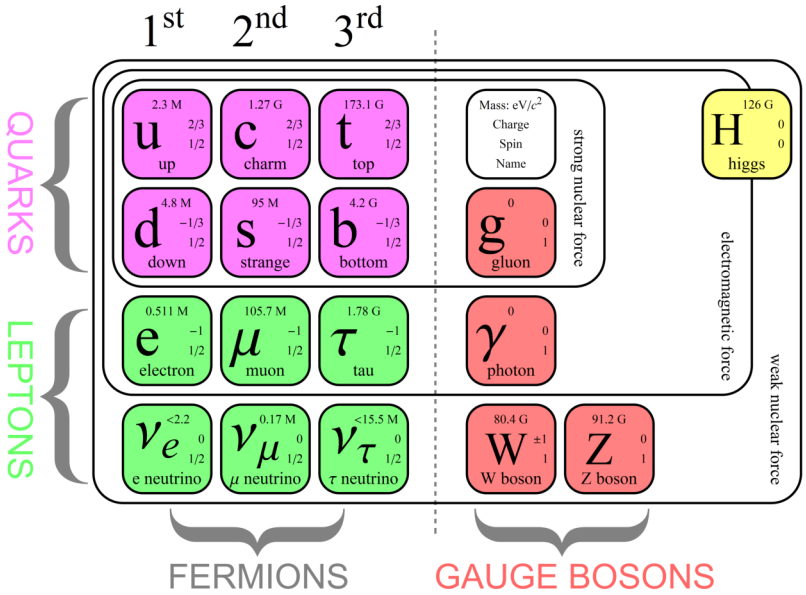

Figure 1.1.: The Standard Model of particle physics, with quarks (purple), leptons (green), gauge bosons (red), and the Higgs boson (yellow). The first, second, and third columns show the three generations of fermions, the fourth, fifth columns show the vector bosons, and the sixth column shows the scalar boson. Details are given in the text. Figure is taken from [1].

According to the SM, matter is composed from two types of spin 1/2 fermions (particles with half-odd integer spin): quarks and leptons. Quarks are elementary particles that combine to form hadrons and, depending on the number of quarks constituents, are called mesons (even) or baryons (odd). The quarks can be grouped in three generations: *u, c, t* (up, charm, top) have fractional electric charge $+\frac{2}{3}$ of the proton charge and *d, s, b* (down, strange, bottom) $-\frac{1}{3}$. Meanwhile, leptons include particles like *e, μ, τ* (electron, muon, tau) that have electric charge -1 and their neutrinos ν_e, ν_μ and ν_τ have null electric charge. An antiparticle is associated to each particle, for a total of 24 elementary fermions.

The SM also describes three of the four fundamental forces in nature: the electromagnetic, the weak and the strong force. The different interactions are described in terms of the exchange of characteristic *gauge bosons* (particles of integral spin) between the *fermion* constituents. The electromagnetic force is responsible for interactions involving electrically charged particles mediated by the massless photon (γ) exchange, while the weak force is involved in processes like radioactive decay and the mediators are the $W^{\pm}$ and Z^0 bosons, with masses of order 100 times the proton mass. The unified electroweak interaction is described by the Glashow-Weinberg-Salam model [2], which combines Quantum Electrodynamics (QED) and the theory for weak interactions. The strong force holds atomic nuclei together and is mediated by the gluon (*g*), a massless particle. The fundamental theory that describes this force is the Quantum Chromodynamics (QCD), see Sec. 1.1.3.

In addition to the particles and forces, the SM incorporates the Higgs mechanism, which explains the origin of particles' masses. The Higgs boson (spinless), a particle discovered at the Large Hadron Collider (LHC) in 2012 [3, 4], is associated with this mechanism.

The discovery of strangeness cleared the path to the formulation of the SM as we know it nowadays, described in the following subsection.

1.1.1. Strangeness

Strangeness was postulated in 1953, by M. Gell-Mann [5], T. Nakano and K. Nishijima [6], each working independently. They were trying to explain why certain unstable heavy particles V_1 (later on they will be called Λ) were produced abundantly (typical time of 10^{-23} s) suggesting that they were produced by the strong interaction and decaying relatively slowly (typical time of $10^{-13} - 10^{-6}$ s) in accordance with a weak decay. The name "*strange*" particle is related to this unprecedented behaviour. The first interpretation came from A. Pais [7], suggesting that their production and disintegration are two different mechanisms. Following this idea, Gell-Mann assigned to each particle a new quantum property "*strangeness*" that is conserved in any strong interaction but not conserved in a weak one. By convention, the value assigned to the strangeness number is -1 for the particles.

In 1961 Gell-Mann introduced the so called Eightfold way [8] in order to classify baryons and mesons according to their charge and strangeness. This successful scheme, also predicted the existence of the $\Omega^-(sss)$, which was later confirmed. He proposed in 1964 that all hadrons are composed of the elementary constituents, quarks, where at that time only 3 were known (*u,d,s*). Every baryon is composed of three quarks while anti-baryon is composed of three anti-quark, and every meson of a quark and anti-quark. The ensembles of baryons composed of quarks (*u,d,s*) can be characterized by the electric charge *Q*, the baryon number *B* (defined as $\frac{1}{3}(n_q - n_{\bar{q}})$, where n_q is the number of quarks and $n_{\bar{q}}$ is the number of anti-quarks), the strangeness $S(-(n_s - n_{\bar{s}}))$, the projection of the isospin I_3 ($\frac{1}{2}(n_u - n_d)$) and spin projection S_z. The Gell-Mann-Nishijima formula relates the four conserved quantum numbers *B, S, Q,* I_3:

$$Q = I_3 + \frac{B+S}{2} = I_3 + \frac{Y}{2}\,, \tag{1.1}$$

where $Y = (B + S)$ is the hypercharge. Figure 1.2 shows the ground state of baryonic

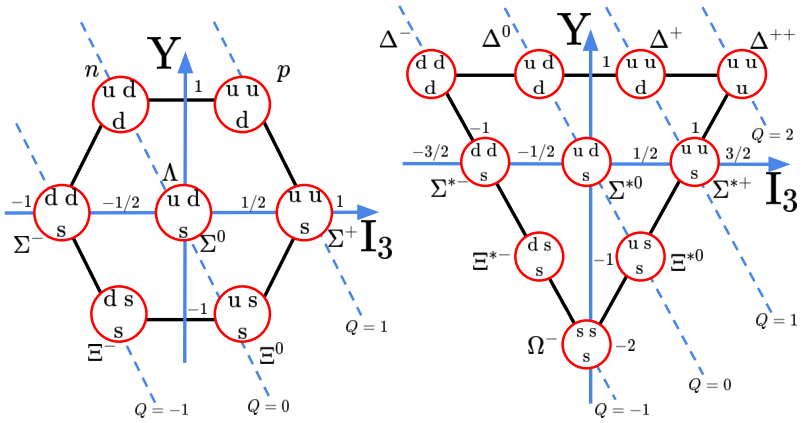

Figure 1.2.: Baryonic octet of spin 1/2 (left) and baryonic decuplet of spin 3/2 (right) particles as a function of the hypercharge Y and their projection of isospin I_3. Details are given in the text.

octet of spin 1/2 (left panel) and baryonic decuplet of spin 3/2 (right panel) particles as a function of Y and I_3. It is possible to observe that the particles are arranged along oblique lines according to their charge, Q. When a baryon has $S \neq 0$, *i.e.*, contains one or more strange quarks, is called *hyperon*.

This model encountered two main obstacles: no individual quark has ever been observed and since a hadron can be formed by multiple quarks of the same type it violates the Pauli exclusion principle. These obstacles were overcome thanks to O. W. Greenberg [9] which suggested that each quark exists in three colors: red, green, and blue. To make a baryon each quark has to carry a different color, in this way, the Pauli principle is not violated, and considering that all naturally occurring particles are colorless it explains why no single quark can be found. The colorless combinations are $q\bar{q}$ (mesons), qqq (baryons) and $\bar{q}\bar{q}\bar{q}$ (anti-baryons). This gave the starting kick to the QCD theory.

1.1.2. Nuclear equation of state

The SM directly provides the framework necessary for studying nuclear matter and its associated equation of state. The nuclear equation of state (EoS) is a fundamental concept in nuclear physics that describes the relationship between the energy (E), temperature (T), density (ρ) and the individual neutron and proton densities (ρ_n, ρ_p) related to the *isospin* asymmetry. At zero temperature, the binding energy per nucleon of nuclear matter can be approximated by considering the second order expansion in the isospin asymmetry parameter $\delta = (\rho_n - \rho_p)/\rho$:

$$E(\rho, \delta) = E_0(\rho, 0) + S(\rho)\delta^2 + \mathcal{O}(\delta^4) + \dots , \tag{1.2}$$

where ρ is the total density ($\rho_n + \rho_p$), $E_0(\rho, 0)$ is the binding energy of symmetric nuclear matter ($\rho_n = \rho_p$), and

$$S(\rho) = \frac{1}{2} \cdot \frac{\partial^2 E(\rho, \delta)}{\partial \delta^2}\bigg|_{\delta=0} \tag{1.3}$$

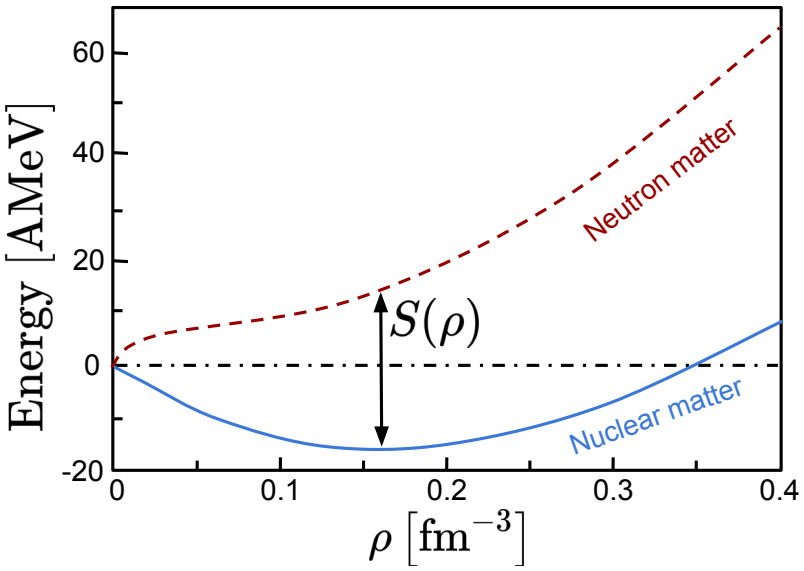

Figure 1.3.: Nuclear (blue line) and neutron (red dashed line) matter equation of states (EoS) as a function of the nuclear density ρ. $S(\rho)$ is the symmetry energy in asymmetric nuclear matter.

is the nuclear symmetry energy. It describes the difference between the EoS of pure neutron matter and symmetric nuclear matter, and, therefore, the energy required to separate protons and neutrons in nuclear matter, see Fig. 1.3. The absence of odd-order terms in Eq. 1.2 is due to neutron-proton exchange symmetry in nuclear matter when the Coulomb interaction is neglected and the charge symmetry of nuclear force is assumed.

To go further and study the effects of density variations, it is useful to expand the symmetry energy term in a Taylor series around the saturation density $\rho_0 (\sim 0.16$ fm$^{-3})$, where the binding energy of symmetric matter reaches its maximum value of $\sim$16 MeV:

$$S(\rho) = S_0 + \frac{L}{3}\left(\frac{\rho-\rho_0}{\rho_0}\right) + \frac{K_{sym}}{18}\left(\frac{\rho-\rho_0}{\rho_0}\right)^2 + \mathcal{O}\left(\frac{\rho-\rho_0}{\rho_0}\right)^3 + \dots , \tag{1.4}$$

where S_0 is the symmetry energy at the saturation density, and

$$L = 3\rho_0 \left.\frac{\partial S(\rho)}{\partial \rho}\right|_{\rho=\rho_0} = \frac{3}{\rho_0} P_0 , \tag{1.5}$$

$$K_{sym} = 9\rho_0^2 \left.\frac{\partial^2 S(\rho)}{\partial^2 \rho}\right|_{\rho=\rho_0} \tag{1.6}$$

are respectively the *slope* and the *incompressibility parameter* of the symmetry energy. The slope parameter L governs P_0, the pressure from the symmetry energy in pure neutron matter at ρ_0. It provides the link between the dominant baryonic contribution to the pressure in the neutron star at ρ_0 and influences the inner crust and radius of neutron stars [10].

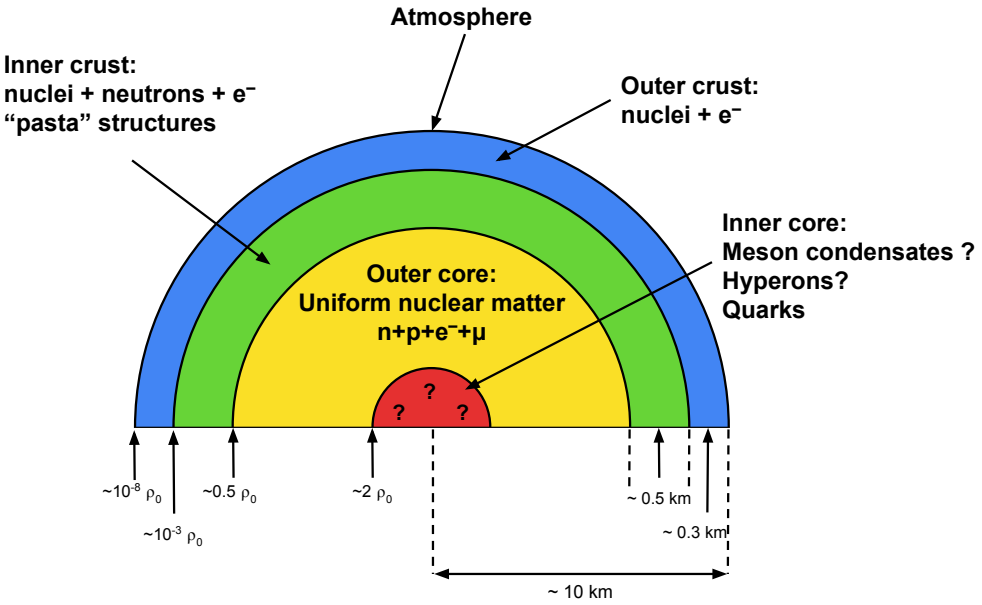

Figure 1.4.: Schematic view of the inner structure of a neutron star. Reproduced with permission from Springer Nature [11].

The Hyperon puzzle

Neutron stars (NS) are dense and compact astrophysical objects formed from the remnants of a massive star after a supernova explosion, and are made primarily of neutrons. The neutron degeneracy pressure supports the NSs against the gravitational collapse. The main characteristics of the NSs are small radii (10-12 km) and large masses (1-2 solar masses $M_\odot$) that correspond to an averaged density of the order $\sim 10^{14}$ g/cm^3. Figure 1.4 illustrates the internal structure of a NS: i) the most external region, the atmosphere, is a very thin plasma layer (few cm) made of low mass number elements, such as H, He, C. ii) Then, the outer crust begins ($\sim 10^{-8}\,\rho_0$) and extends for few hundred meters. It is a solid region where heavy nuclei, mainly around the iron mass number, are present. iii) Below it is the inner crust ($\sim 10^{-3}\,\rho_0$) with a thickness of around half kilometer. Here the increase of density induces electron capture on nuclei and the matter become more neutron-rich. In particular, this region is a mixture of very neutron-rich nuclei, electrons and free neutrons. iv) Finally, the core of the NS is reached, it is divided in two parts: the outer core, where the density is in the range of $0.5\rho_0 \leq \rho \leq 2\rho_0$ and extends for several kilometers. Matter is mainly composed of protons, neutrons, electrons and muons. The inner core reaches very high density ($\rho > 2\rho_0$) and its composition is still not known. Only hypotheses can be made, that include the formation of hyperonic matter, pion or kaon condensates, or deconfined quarks [11]. Among these hypotheses, the hyperonic matter will be discussed in the following. At those densities, the nucleon chemical potential is strong enough to make energetically favourable the conversion of nucleons into hyperons. This conversion relieves the Fermi pressure of the system, making the EoS softer when hyperons are present [12].

The structure of NSs can be established through the use of Einstein's general theory of relativity. Einstein's field equations for a spherical static star are expressed in form of

the Tolman-Oppenheimer-Volkoff (TOV) structure equations [13]. These equations are formulated employing the gravitational constant G and the speed of light in natural units ($c = 1$):

$$\frac{dP(r)}{dr} = -\frac{G}{r^2}[\varepsilon(r) + P(r)]\left[M(r) + 4\pi r^3 P(r)\right]\left[1 - \frac{2GM(r)}{r}\right]^{-1}, \tag{1.7}$$

$$\frac{dM(r)}{dr} = 4\pi r^2 \varepsilon(r)\,, \tag{1.8}$$

where P is the pressure, r the radius of a shell of matter with thickness dr, ε the energy density, and M the mass. The left-hand side of Eq. 1.7 shows the combined force pushing outwards on the surface of the shell because of the pressure difference $dP(r)$ between the inside and the outside, whereas the right-hand side represents the gravitational force acting on the shell by the mass in the interior. As a result, the matter and the internal composition of a NS are defined by the relation between the pressure P and the energy density ε, *i.e.*, the nuclear EoS. Consequently, a method to test the accuracy of an EoS is to predict the NS mass and radius and then compare with the astrophysical observations [12].

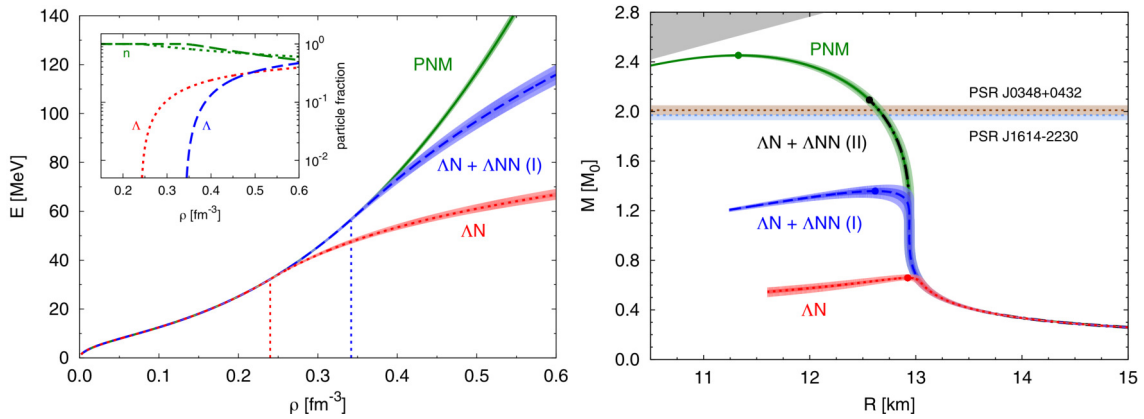

Figure 1.5.: Left. Three different EoS with and without the inclusion of the hyperon-nucleons interactions, details are given in the text. In the inset, neutron and Λ fractions corresponding to the two HNM EoSs. Right. Mass-radius relation using the EoSs from the left panel. The dots represent the predicted maximum masses. Horizontal bands at $\sim 2M_\odot$ are the observed masses of heavy pulsars [14, 15]. These figures are reprinted with permission from [16] ©2023 by the American Physical Society.

As an example, the left panel of Fig. 1.5, shows the trends of three different EoSs: pure neutron matter (PNM) in green, hyperneutron matter (HNM) including an attractive two-body hyperon-nucleon (ΛN) interaction in red and with the inclusion of a repulsive three-body hyperon-nucleon (ΛNN) force in blue. The presence of hyperons in the medium reduces the nucleonic Fermi energy and consequently the nuclear EoS is softened, limiting the maximum mass that a NS can reach. However, the predicted masses with these interactions are lower than recent astrophysical observations of NSs with $\sim 2M_\odot$, see right panel Fig. 1.5, leading to the so-called "*hyperon-puzzle*". For the HNM including the two-body ΛN interaction only,

hyperons appear from density of 0.24(1) fm^{-3}. It should be noted that when including the three-body ΛNN interaction two parametrizations are used: (I) results in threshold density for hyperons formation of 0.34(1) fm^{-3} [17], while, (II) provides an additional repulsion [18] (included in order to satisfactorily reproduce some measured hypernuclear data) that pushes the threshold towards a density region ($\gtrsim$ 0.56(1) fm^{-3}) where the contribution coming from the hyperon-nucleon potential cannot be compensated by the gain in kinetic energy [16], predicting maximum mass (dot-dashed black line) which is consistent with the observations. This demonstrates that a strong repulsive ΛNN interaction, barely known experimentally, can potentially solve this hyperon-puzzle. Therefore, constraints on the ΛN and ΛNN interactions and in particular the hyperon-neutron force are necessary in order to properly assess the role of hyperons in neutron stars. A powerful tool to achieve this goal is the study of hypernuclei, see Sec. 1.4.

1.1.3. QCD phase diagram

Exploring the properties of hadronic matter at different conditions of temperature and density gives the unique opportunity to investigate the nuclear EoS and to search for phase transitions. This research helps to test the current understanding of QCD and different effective theories based on hadronic/quark degrees of freedom. The QCD Lagrangian [19] density is used to describe the quark and gluon interaction

$$\mathcal{L} = \sum_f \bar{\psi}_k \left(i\gamma_\mu \partial^\mu - \alpha_s \gamma_\mu A_a^\mu G_a - m_f \right) \psi_k - \frac{1}{4} F_a^{\mu\nu} F_{\mu\nu}^a \,, \tag{1.9}$$

where ψ_k are quark-field spinors, γ_μ the Dirac matrices, α_s the QCD coupling constant, A_a^μ the gluon field, G_a matrices that are generators of the SU(3) color group, m_f the mass of quark flavor f, $F_{\mu\nu}^a$ the color field tensor, and $a = 1, ..., N_c^2 - 1$ where $N_c^2 - 1 = 8$ is the number of gluons color charges. A unique property of QCD is the non constant α_s, which determines two main characteristics of the strong interaction. The first one is the confinement of the strong charge [20]: the required color neutrality forbids the appearance of a single quark. This results in an increasing force strength for larger interaction distances. The second property appears for short distances with a weaker interaction, therefore, the particle moves freely, the so-called asymptotic freedom [21].

In Fig. 1.6 is shown a schematic view of the QCD phase diagram. It aims to describe the behaviour of matter at different conditions, with the baryochemical potential (μ_b) on the x-axis and the temperature on the y-axis. The baryochemical potential (μ_b) is the energy necessary to bring one additional nucleon into the system, that can be replaced by the net-baryon density since they are strongly correlated. Starting from the bottom right of the figure: $T = 0$ and μ_b=900 MeV ($\rho/\rho_0 = 1$), corresponds to the state of ordinary matter, *i.e.*, the nuclei. If matter is heated up such that molecular, atomic and nuclear binding effects can be neglected, it can be described as a gas of hadrons in which the quarks are confined. If the temperature or quark density is increased much further, the confinement of the quarks ceases due to the effect of asymptotic freedom, meaning that at high temperatures and/or high densities the strong interaction gets weaker and weaker, causing hadrons to break up.

In this state, which is called Quark Gluon Plasma (QGP), the quarks are still strongly coupled but can move freely in the entire medium. The QGP state is assumed to have existed shortly after the big bang (up to 10^{-6} s) before the universe cooled down to energy densities where quarks and gluons formed bound states of hadronic matter. It's expected to be found in the inner core of NSs, with conditions of low temperature but very high density. The transition from the hadron gas into the QGP state can be described as a thermodynamic phase transition.

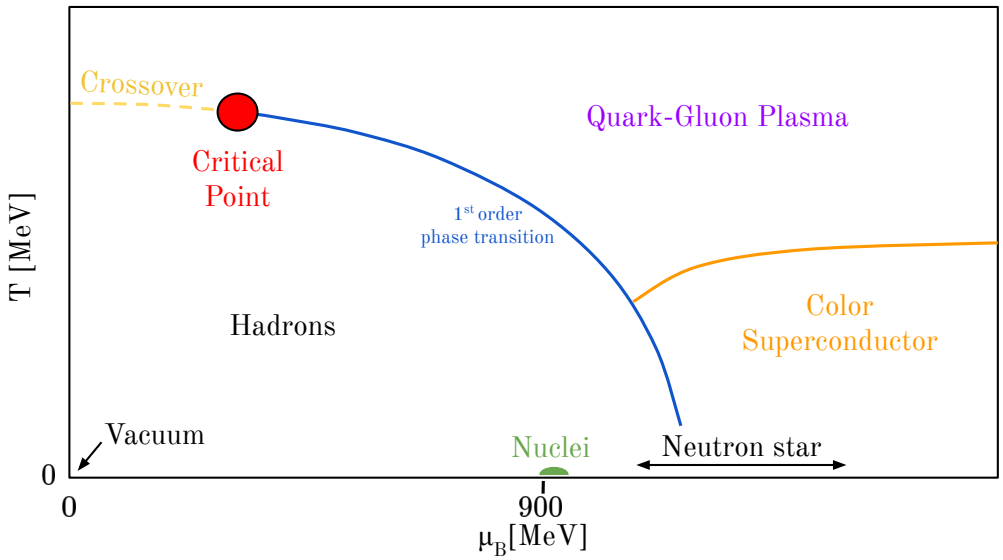

Figure 1.6.: Phase diagram (temperature, baryon chemical potential) of QCD matter.

The nature of the transition is still under debate theoretically and experimentally. Experimentally, the study of the phase diagram can be done systematically only by terrestrial experiments that allow to explore different nuclear matter conditions, *i.e.*, Heavy Ion Collisions (HIC), see next section. Theoretically, the parameters of the transition are studied by computer simulations of lattice QCD starting from first principles (Eq. 1.9), without any physical assumptions. Lattice QCD calculations predict a rapid but smooth crossover phase transition around the critical temperature $T_c \simeq 155$ MeV at small $\mu_B \to 0$. While for high density and low temperature matter is expected to be a color superconductor, which is a degenerate Fermi gas of quarks with a condensate of Cooper pairs[1]. In the presence of such a condensate of Cooper pairs, the ground state of quark matter becomes a color superconductor [22].

1.2. Heavy Ion collisions

Heavy Ion Collisions (HIC) experiments are a powerful tool to study systematically nuclear matter in different conditions of temperature and density and, in this way, being able to

[1]Cooper pairs are made of quarks from around the highly degenerate Fermi surface, *i.e.*, quarks with the absolute value of momenta $p \simeq p_F$. Cooper pairs are bosons, and they occupy the same lowest energy quantum state at zero temperature, producing a Bose condensate [22].

constrain the nuclear EoS. In the course of the collision matter is compressed and heated up, and the QGP phase can be formed. Nevertheless, due to the extremely short time scale of the strong interaction processes (10^{-23} s), it is impossible to observe it directly. As a result, the properties of matter can only be inferred from the measurements of particles emerging from the system. Depending on initial conditions, various densities and temperatures can be reached, thus enabling a large-scale exploration of the nuclear matter phase diagram. In particular, the kinetic energy of the incident ion beam governs both. In terms of beam energy it can be divided into three regions [19]: *intermediate* (10-100 AMeV), *relativistic* (100 AMeV-10 AGeV), and *ultra-relativistic* (>10 AGeV).

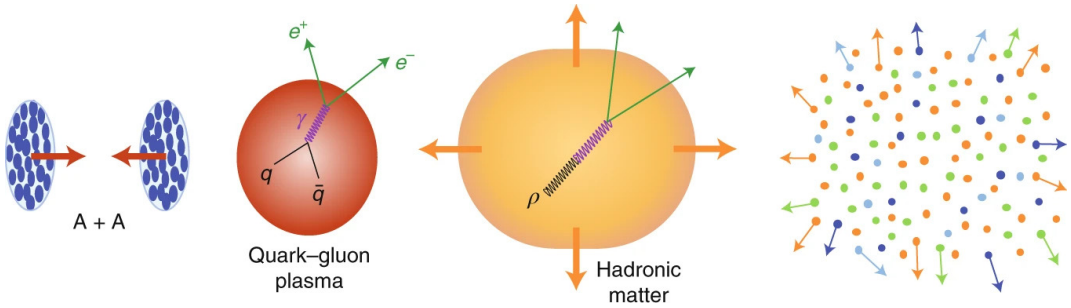

Figure 1.7.: Schematic view of a Heavy Ion Collision in the center-of-mass frame. Figure is taken from [23].

Figure 1.7 shows schematically the time evolution of relativistic HIC at few AGeV energies: i) pre-collision phase, in the center-of-mass (CM) frame two ions (A+A) approach each other with a certain impact parameter b (see Fig. 2.1), ii) the overlapping volumes create a high density region, called fireball. Inside this region, one of the hypotheses is that it experiences a phase transition to the QGP that also emits real and virtual photons, which penetrate the QCD medium and thus carry information on the interior of the fireball. iii) Due to the high density, in the collision zone, a strong pressure will be generated that will expand the system resulting in a fast reduction of temperature and density. iv) Once the mean nucleon distances are large enough the inelastic collisions stop and hence the particle production stops, this temperature is called *chemical freeze-out temperature*. The expansion will continue and at a certain point also the elastic collisions will stop and therefore the momentum and angular distribution of the particles will remain unchanged until they are measured in the detectors. This temperature is called *kinetic freeze-out temperature* [24].

Figure 1.8 shows the measured chemical freeze-out point in the temperature baryochemical potential plane for different experiments, where from the lowest to the highest energies the points align on a common trajectory. It also shows the regions of the QCD phase diagram that the different facilities can access, in particular at the LHC, where ultra-relativistic collisions (ATeV) reach very high temperatures and extremely low densities. On the other side the HADES (High Acceptance DiElectron Spectrometer) experiment, at GSI (Gesellschaft für Schwer-Ionenforschung[2]) performed with relativistic collisions (few AGeV) using the SIS18 synchrotron, reaches moderate temperature and the highest μ_b (densities) currently

[2]It translates in English as: Facility for Heavy Ion Research

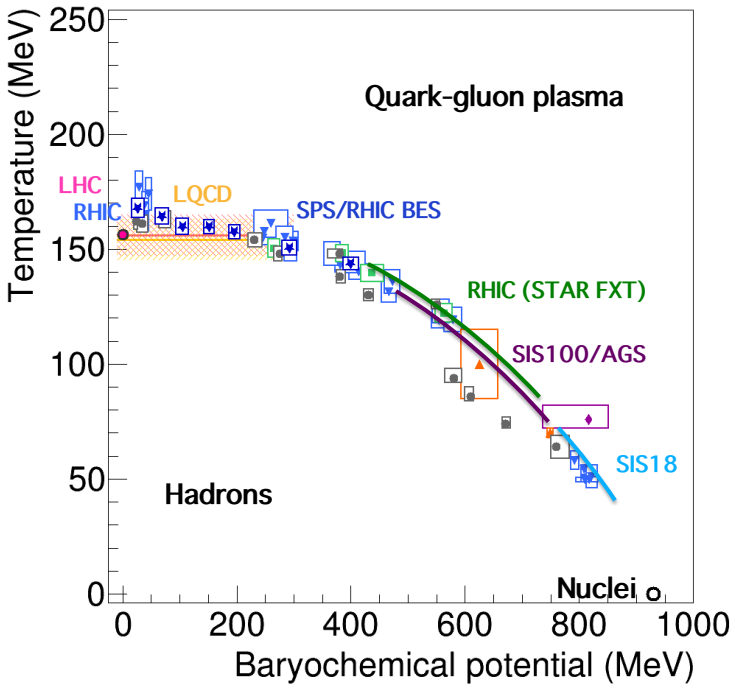

Figure 1.8.: Chemical freeze-out temperatures accessible in various facilities and experiments. Figure is taken from [25].

accessible. In the future HADES will move into the new CBM (Compressed Baryonic Matter) cave at the SIS100 synchrotron at FAIR, which allows the use of higher energy beams, e.g. Au with energy up to 11 AGeV that can compress nuclear matter to densities up to $8\rho_0$ [26].

1.3. Mechanisms to produce clusters

The complete understanding of the formation mechanism of light (anti-)nuclei in high-energy ion collisions remains an ongoing challenge. These processes cannot be calculated using lattice QCD since they involve QCD interactions at non-perturbative scales. Consequently, phenomenological models are used to estimate the resulting light-nuclei yields. Typically, these models fall into one out of the two categories: statistical hadronization models or models based on the coalescence approach.

1.3.1. Statistical hadronization model

The statistical hadronization model (SHM) relies on the assumption that the QCD interactions lead to the formation of an extended massive object called cluster or fireball. This entity disintegrate into hadrons through a statistical process when the system reaches a critical energy density. Statistical models require few parameters to successfully describe hadron multiplicities at chemical freeze-out. Using experimental data on measured particle yields and fitting the relevant parameters of the model (T, μ_B, V) provides insight on the nature of the medium they originate from. The description of a system with volume V in the statistical

approach is carried on within the ensemble theory introduced by Gibbs [27]. In this approach the equilibrium behavior of thermodynamical observables can be evaluated as an average over statistical ensembles (rather than as a time average for a particular state). Among the different types of ensembles, the grand-canonical ensemble (GCE) has been proven to give an adequate description of hadron abundances in the limit of high temperature and/or large system size. In the GCE the system can have any number of particles but the average number is determined by μ_B. For the SHM, the yields (dN/dy) of light nuclei can be approximated as follows [28]:

$$\frac{dN}{dy} \propto (2J_A + 1)e^{-\frac{m}{T_{chem}}}, \tag{1.10}$$

where J_A is the spin of the nucleus, m is its mass, T_{chem} is the chemical freeze-out temperature, and y is the *rapidity*, a dimensionless variable describing the velocity at which a particle is moving with respect to a chosen reference point situated on the line of motion (z):

$$y = \frac{1}{2}\ln\left(\frac{1+\beta_z}{1-\beta_z}\right) = \frac{1}{2}\ln\left(\frac{E+p_z}{E-p_z}\right), \tag{1.11}$$

where E is the energy, and β_z and p_z are the velocity and momentum of the particle along z direction, respectively. An important feature of the rapidity is that it is an additive quantity and therefore differences in rapidity are invariant. In fact, to transform between the laboratory frame and the CM system of the collision it only requires a shift between the two frames. The rapidity in the CM system is called *mid-rapidity* (y_{cm}) and for a fixed-target collision with a projectile of energy E_p, it is:

$$y_{cm} = \frac{1}{4}\ln\left(\frac{E_p + p_z}{E_p - p_z}\right). \tag{1.12}$$

The SHM model has been extensively used to describe the yields of particles from HIC, one exemplar case is the result obtained by the ALICE (A Large Ion Collider Experiment) collaboration in Ref. [29]: using the SHM they were able to describe well the yields of light particles produced in Pb-Pb collisions at 2.76 TeV, which span over 9 order of magnitude, with a single chemical freeze-out temperature, $T_{chem} \sim 156$ MeV.

1.3.2. Coalescence model

The coalescence model assumes that the formation of nuclei in HIC occurs when nucleons which are close to each other in space and have similar velocity form a bound state at the chemical freeze-out temperature. For a nucleus with mass number $A = N + Z$, the coalescence parameter B_A is defined to quantify the coalescence probability to produce a nucleus of mass number A:

$$E_A\frac{\mathrm{d}^3N_A}{\mathrm{d}p_A^3} = B_A\left(E_\mathrm{n}\frac{\mathrm{d}^3N_\mathrm{n}}{\mathrm{d}p_\mathrm{n}^3}\right)^{(A-Z)}\Bigg|_{\vec{p}_\mathrm{n}=\frac{(A-Z)}{A}\vec{p}_A}\left(E_\mathrm{p}\frac{\mathrm{d}^3N_\mathrm{p}}{\mathrm{d}p_\mathrm{p}^3}\right)^{Z}\Bigg|_{\vec{p}_\mathrm{p}=\frac{Z}{A}\vec{p}_A}, \tag{1.13}$$

where $p_{A,p,n}$ and $E_{A,p,n}$ are the momenta and energies of nucleus, protons and neutrons, respectively. In this simple approach, the coalescence is expected to be independent of the

momentum and the size of the object relative to the volume of particle emission (source size). In a more advanced approach, the size of the source (R) is taken into account, as the coalescence probability decreases for nucleons with similar velocity which are produced far away. In this case the coalescence parameter can be written as

$$B_A = \frac{2J_A+1}{2^A}\frac{1}{\sqrt{A}}\frac{1}{m_T^{A-1}}\left(\frac{2\pi}{R^2+\left(\frac{r_A}{2}\right)^2}\right)^{\frac{3}{2}(A-1)}, \tag{1.14}$$

where J_A and r_A are the spin and size of the nucleus, respectively and m_T the transverse mass of the coalescing nucleons [28].

1.3.3. Models comparison

In the left panel of Fig. 1.9, it is shown the comparison of the coalescence parameter of different nuclei as a function of the source size. As can be seen, for the deuteron and ^{3}He the ALICE data, from p-p and Pb-Pb collisions, show a good agreement with both models within two confidence level 2σ (where σ is the total uncertainty in the data). For the hypertriton $^3_\Lambda$H, see bottom panel, the only available data point (Pb-Pb) agrees with the SHM prediction. For the coalescence model, on the other side, it shows a large discrepancy, with both predictions, more than 6σ caused by the significantly larger size predicted for the $^3_\Lambda$H with respect to ^{3}He. The black solid line represents a size parameter of the wave function of the harmonic oscillator potential r($^3_\Lambda$H)=6.8 fm and the black dashed line r($^3_\Lambda$H)=14.1 fm, corresponding to a nucleus size (r_A) of 4.9 fm and 10 fm, respectively. However, if one looks at the most recent ALICE results from 2022 [31] (see right panel of Fig. 1.9), where also p-Pb collisions were analyzed, it can be seen that for a smaller colliding system the $^3_\Lambda$H/Λ yield ratio[3] from the p-Pb data favours the coalescence model predictions.

In conclusion, the cluster production mechanism is still an open question and the $^3_\Lambda$H is suggested to be a key-probe to understand the nature of nucleosynthesis in relativistic HIC. In particular, the determination of the size of the $^3_\Lambda$H to be used as an input, and not a free parameter, in coalescence models will greatly improve our understanding.

The first part of the thesis focuses on the development of a method to extract the size of hypernuclei, with a dedicated experiment to infer the size of the $^3_\Lambda$H using HIC.

1.4. Λ-Hypernuclei

A hypernucleus is a bound system of nucleons with one or more hyperons ($\Lambda, \Sigma, \Xi, \Omega$). Single-$\Lambda$ hypernuclei are indicated as $^A_\Lambda$X with X the symbol of the isotope according to its nuclear charge, A the total number of baryons, and the Λ indicates that the hypernucleus contains one Λ-hyperon, such that it has $N = A-Z-1$ neutrons. $^3_\Lambda$H means a nuclear system composed of three baryons: one proton, one neutron and one Λ(uds) particle, comparing to

[3]While the SHM can compute directly the absolute yields of particles, in the coalescence model the yield of bound states can be computed only relative to the yields of other particles.

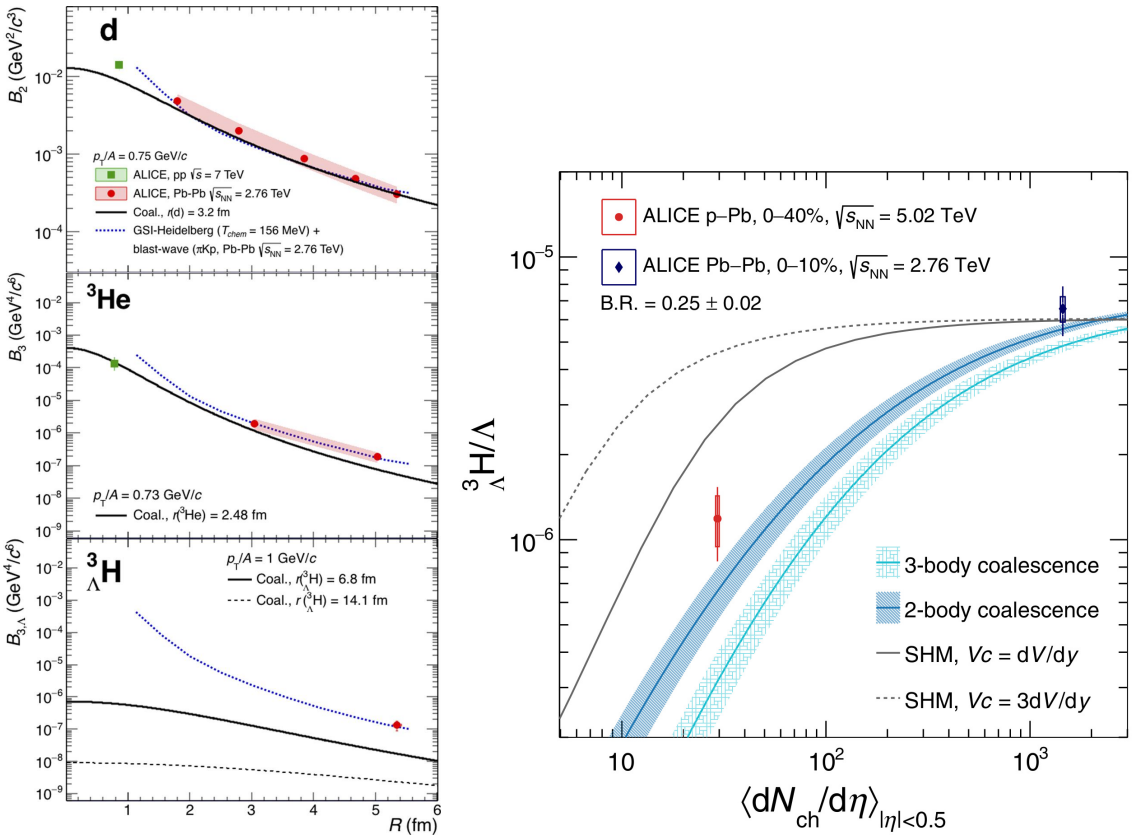

Figure 1.9.: Left. Coalescence parameters measured by ALICE (filled symbols) for deuteron, ^{3}He, and $^3_\Lambda$H in p-p and Pb-Pb collisions, together with predictions from the thermal + blast-wave (blue dotted line) and the coalescence (black solid line) models. The black dashed line in the lower panel corresponds to the coalescence prediction for the $^3_\Lambda$H with a larger radius. This figure is reprinted from [28] under CC BY 4.0. Right. $^3_\Lambda$H/Λ yield ratio measured in p-Pb (red symbol) and Pb-Pb collisions (blue symbol) as a function of the mean-charged-particle multiplicity. The predictions for the SHM and coalescence model are shown. This figure is reprinted from [30] under CC BY 4.0.

^{2}H with one proton and one neutron.

In a simple single-particle model, the nucleons and hyperons are distinguishable particles, each of them placed in a different effective potential well. In this way, the hyperons inside the nucleus will not experience the Pauli blocking with the nucleons, and, therefore, they can occupy any orbital. This feature makes the hyperon, embedded in a hypernucleus, a unique means to explore the inner nuclear density that is not accessible for unstable nuclei. The glue-like role of a hyperon could facilitate the existence of neutron-rich hypernuclei allowing to study the neutron drip line region, forming bound nuclear systems, such as the ground state of ^{5}H [32], ^{7}He [33] and ^{10}Li [34], *i*.e., by forming the hypernuclei $^6_\Lambda$H [35], $^8_\Lambda$He [36, 37] and $^{11}_\Lambda$Li [36], respectively. Another advantage to study hypernuclei is the opportunity to explore baryon-baryon interactions such as hyperon-nucleon (YN) and hyperon-hyperon

(YY). To be noted, these interactions cannot be studied by performing scattering or capture experiments with hyperon beams since their lifetime is in the sub-nanosecond regime. In fact, only few scattering data $p\Lambda$ [38] exists, and other information is obtained through femtoscopy measurements [39, 40].

The discovery of hypernuclei dates back to 1953 with the observation of a hyperfragment produced by interaction of a high energy cosmic ray in a stack of photographic emulsion [41]. Since then, thanks to the development of intense high-energy accelerator facilities worldwide, more hypernuclei have been synthesized (∼40). In Fig. 1.10 the current status of the hypernuclear chart is shown. The mechanisms to produce them are detailed in the next section.

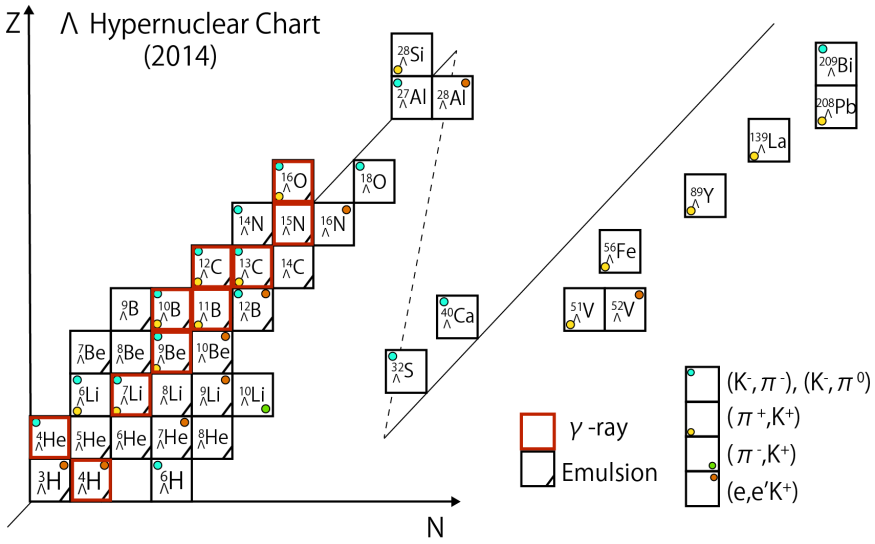

Figure 1.10.: Single-Λ hypernuclear chart. The experimentally identified hypernuclei and the experimental methods used to study them are indicated. The only hypernucleus missing is the ${}^{19}_{\Lambda}$F discovered at JLab in 2018 using γ-ray measurement [42]. Figure is taken from [43].

1.4.1. Hypernuclei production and decay mechanisms

There are several mechanisms that can be used to produce Λ-hypernuclei [44]: i) strangeness exchange, ii) associated production using pion or electron beams, and iii) heavy ion collisions. i) replaces a d quark with an s quark, by using a K^- beam impinging on a neutron of the target nucleus changing it into a Λ and emitting a π^-:

$$K^- + {}^{A}Z \rightarrow {}^{A}_{\Lambda}Z + \pi^- \,, \tag{1.15}$$

an exothermic process with a Q-value of $\sim$ 178 MeV. ii) Produces an $s\bar{s}$ pair. A π^+ beam impinging on a neutron creates a K^+ and a Λ:

$$\pi^+ + {}^{A}Z \rightarrow {}^{A}_{\Lambda}Z + K^+ \,, \tag{1.16}$$

an endothermic reaction with a Q-value $\sim$ -530 MeV. The production cross section for this reaction is lower with respect to i), but the loss in statistics is compensated by the higher intensity that can be reached with the π^+ beam. A second possibility is to use e^- beam, when the electron exchanges a virtual photon with a proton of the nuclear target, that produces a Λ and a K^+:

$$e^- + {}^{A}Z \rightarrow e^- + K^+ + {}^{A}_{\Lambda}(Z-1)\,, \tag{1.17}$$

an endothermic reaction with a Q-value $\sim$ -328 MeV. The cross section for this reaction is the lowest, but the intensity of the electron beam is higher.

These two mechanisms are limited to production of hypernuclei close to the valley of stability since they convert one nucleon into a Λ from stable nuclear targets. HIC iii) can potentially extend the hypernuclear chart far from stability as it can be performed in inverse kinematics using exotic beams. The main production mechanism in HIC is elementary nucleon-nucleon collisions

$$N + N \rightarrow N + \Lambda + K\,, \tag{1.18}$$

an endothermic reaction with an energy threshold of 1.58 GeV. The participant-spectator model well describes the collision process between two ions: first the hyperon Λ is produced in the participant (overlapping) region at mid-rapidity (y_{cm}), then the hypernucleus can be formed if there is an overlap between the rapidity of the pre-formed fragment and the Λ (see Fig. 1.11), that then has a certain probability to be captured. Since many fragments are produced in a collision, various hypernuclei can be created, unlike the methods presented above where only one specific hypernucleus can be formed in a reaction. The technique of using relativistic heavy-ion collisions to produce hypernuclei was first introduced in 1973 [45]. Since then, it has been exploited with light ions at several facilities [46, 47], in particular, at GSI this method was pioneered by the HypHI (Hypernuclei with Stable Heavy Ion Beam and RI-beam Induced Reactions at GSI) collaboration [48].

Equation 1.18 describes an isolated NN collision, however, a HIC is a process involving many nucleons and, therefore, multiple NN collisions. Consequently, all measurements of hadrons carrying strangeness cannot merely be explained by primary elementary reactions inside the reaction zone. Instead, their production occurs through secondary or multi-step processes facilitated in the high-density environment formed during the collision enabling sub-threshold production mechanisms. The first consideration comes from the fact that nucleons inside the nucleus, due to the Pauli exclusion principle, are not at rest but have an intrinsic momentum that can contribute to an additional momenta for the collision up to Fermi momentum p_F $\sim$270 MeV/c. Then, there can be a production through a two-step mechanism, where a fast pion is produced in a first NN interaction, and the Λ is produced in a second step by associated production (Eq. 1.16) that has an energy threshold of 0.76 GeV. Finally, there is the possibility of accumulation of energy through multi-step processes, that means elastic scattering processes with other hadrons in medium as well as inelastic collisions that result in resonant intermediate states like Δ or N^* resonance that decay producing strange particles [50].

A different two-step mechanism to produce hypernuclei is using antiproton ($\bar{p}$) beam. The annihilation at the surface of a nucleus, which is about 4% of all $p\bar{p}$ annihilations, produces

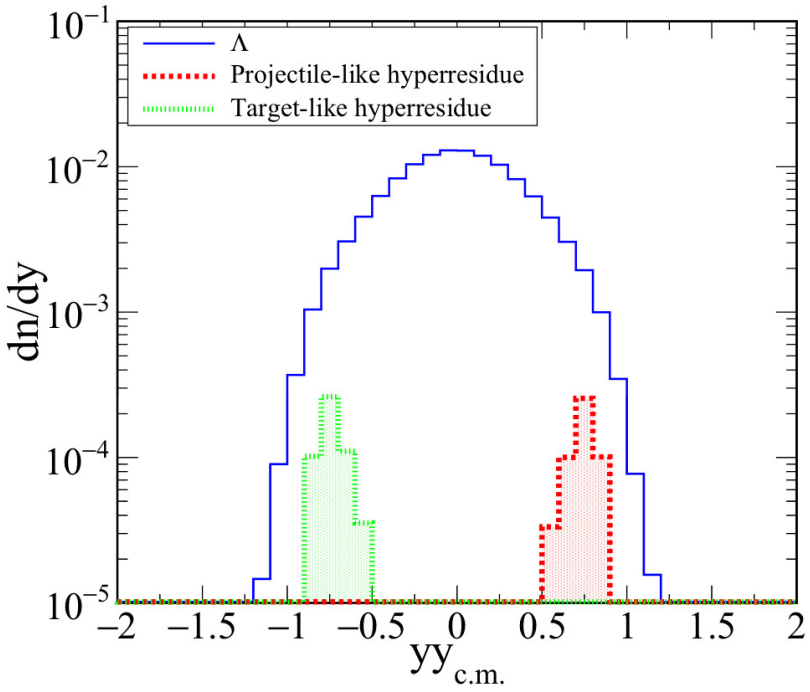

Figure 1.11.: Mid-rapidity distributions of Λ (solid blue line) and hyperresidues in the center-of-mass frame for ^{12}C+^{12}C collisions at 2 AGeV. Red and Green histograms show the rapidity of projectile-like and target-like hyperresidues, respectively. This figure is reprinted from [49] under CC BY 4.0.

strangeness in the form of $K\bar{K}$ pairs [51]. These kaons can interact with the nucleon of the nucleus and, by strangeness exchange reaction i), produce a Λ that if captured by the nucleus forms an hypernucleus. The advantage as compared to the kaon induced reaction i) is that the antiproton remains stable and can be held in a storage ring. This feature enables achieving a relatively high luminosity. Heavy hypernuclei production using this method have been experimentally performed at LEAR (Low-Energy Anti-proton Ring) to study the lifetime of hypernuclei in the region of uranium [52]. At FAIR, in the future, the PANDA (antiProton ANnihilation at DArmstadt) collaboration aims at using $\bar{p}$ beam to produce double-Λ hypernuclei to explore the YY interaction [53].

Once the hypernucleus is formed, it is unstable to the weak decays of the Λ, which in free space has a lifetime of $\tau_\Lambda = 263.2 \pm 2.0$ ps [54]. For light hypernuclei the decay mode is dominated by weak mesonic decays (Γ_M) and the two channels are:

$$(\Gamma_{\pi^-}) \quad \Lambda \rightarrow \pi^- + p + 38\,\text{MeV} \qquad p_N \sim 100 \ \text{MeV}/c, \tag{1.19}$$

$$(\Gamma_{\pi^0}) \quad \Lambda \rightarrow \pi^0 + n + 41\,\text{MeV} \qquad p_N \sim 100 \ \text{MeV}/c, \tag{1.20}$$

where p_N is the momentum of the outgoing nucleon. The branching ratio (BR) of Eq. 1.19 is 64.1±0.5% [54] and Eq. 1.20 is 35.9±0.5% [54]. This is compatible with the $\Delta I = 1/2$ isospin rule, observed experimentally, which states that the charged BR is twice the neutral one. This rule is observed in all other known strangeness-changing non-leptonic weak decays [55]. However, the mesonic weak decay (MWD) when the Λ is bound in the nucleus, for increasing mass number A, is suppressed by the Pauli principle, because the momentum

of the outgoing nucleon ($p_N \sim 100$ MeV/c) is lower than the typical Fermi momentum in the nucleus ($p_F \sim 270$ MeV/c). Therefore, the so-called non-mesonic weak decay (NMWD) dominates, that originates from the fact that the Λ interacts with one or more of the surrounding nucleons (Γ_{NM}):

$$(\Gamma_1) \qquad \Lambda + N \rightarrow N + N + 176 \text{ MeV} \qquad p_N \sim 420 \text{ MeV}/c, \tag{1.21}$$

$$(\Gamma_2) \qquad \Lambda + N + N \rightarrow N + N + N + 176 \text{ MeV} \qquad p_N \sim 340 \text{ MeV}/c, \tag{1.22}$$

where the ratio is estimated Γ_2/Γ_1 ~0.2 for A >4 [56]. Finally, the total decay rate of Λ-hypernuclei is:

$$\Gamma_T = \Gamma_M + \Gamma_{NM} = \Gamma_{\pi^-} + \Gamma_{\pi^0} + \Gamma_1 + \Gamma_2. \tag{1.23}$$

Figure 1.12 shows the weak decay rate relative to the free Λ (Γ_Λ^{free}) as a function of the total number of baryons, comparing the theoretical predictions with the available experimental data.

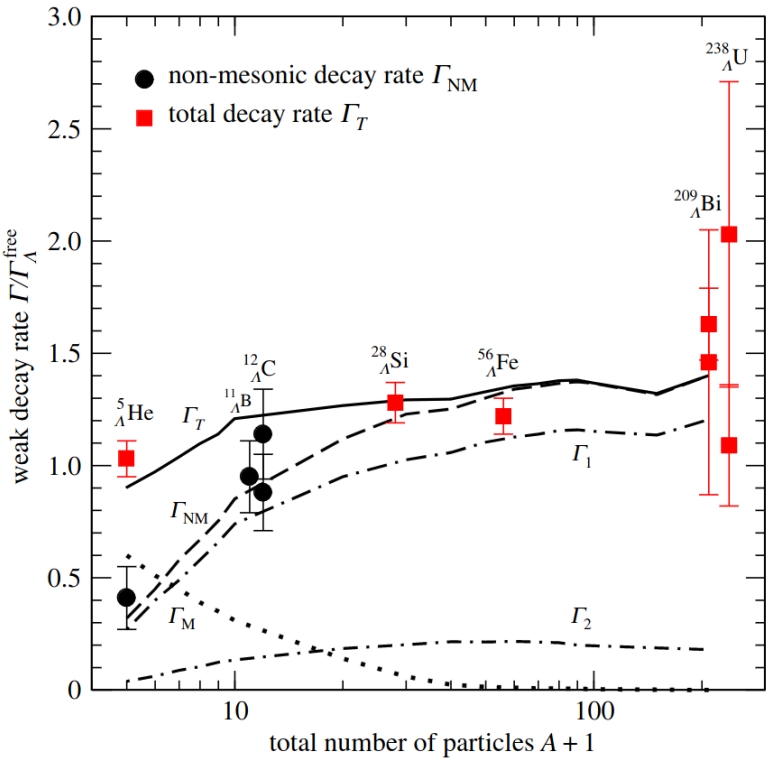

Figure 1.12.: Weak decay rate Γ as a function of the total number of particles in units of the weak decay rate of the Λ in free space Γ_Λ^{free}. Details are in the text. This figure is reprinted with permission from [57]; permission conveyed through Copyright Clearance Center, Inc..

The only way to study a particle that decays before reaching the detector is by using the so-called *invariant mass* technique. The invariant mass m_0 represents the mass of the particle in its rest frame. It can be computed using the particle's energy E and momentum $\vec{p}$ measured in any frame thanks to the energy-momentum conservation law. The reconstruction of the invariant mass of a particle that has undergone decay (known as the mother particle) can be

achieved through its decay products present in the final state (known as daughter particles). This approach is feasible since the invariant mass relies on quantities that remain constant during the decay process. Hence, the invariant mass of the mother particle can be calculated as follows:

$$(m_0 c)^2 = \left(\sum_i^{N_{tot}} E_i\right)^2 - \left|\sum_i^{N_{tot}} \vec{p}_i c\right|^2 , \tag{1.24}$$

where c is the speed of light, N_{tot} is the total number of daughter particles, E_i and $\vec{p}_i$ are the energy and momentum of the i-*th* daughter particle.

1.4.2. Halo and hyper-halo nuclei

The remarkable glue-like role of the Λ particle leads to the formation of more bound states. When a Λ is added to a halo nucleus, a loosely bound system at the dripline, the resultant hypernucleus will become substantially stable against the neutron decay. Therefore, there is a new possibility to produce a hypernuclear neutron (proton) halo state if the core nucleus has a weakly unbound state with an appropriate energy above the particle decay threshold, e.g. a candidate is the ${}^{6}_{\Lambda}$He which has an ^{5}He core. In this way, hypernuclei can extend the neutron (proton) drip-line from that obtained in ordinary nuclei [58].

Halo nuclei are, by definition [59], loosely bound systems at the dripline that satisfy two important conditions:

1. There must be a large probability f_c (>50%) of finding a cluster component in the total many-body wave function.

2. A large fraction f_h (>50%) of the probability density of the halo nucleon(s) must be in the classically forbidden region outside the cluster potential.

These conditions are realised for a low separation energy, typically less than about 1 MeV. In a one-body potential, the size dependence on the separation energy can be found analytically by solving the Schrödinger equation for a loosely bound state in the region far outside of the nuclear surface ($r \gg R$) where the potential $V(r)\rightarrow$0. One can show that the mean square radius of the wave function will be dominated by the contribution in this region:

$$\langle r \rangle^2 \propto \frac{1}{k^2} , \tag{1.25}$$

where $k = \sqrt{2\mu|\varepsilon|/\hbar^2}$ is the separation energy of the orbital, ε is the single particle energy, and μ the reduced mass. For $|\varepsilon| \rightarrow$0, the mean square radius of s-wave (l=0) state diverges, while, for $l >$1, the centrifugal barrier prevents any divergent behaviour, suggesting that the halo phenomenon occurs only in nuclei with $l \leq$1 [60]. It is possible to see this dependence by comparing systems at finite binding energy through the use of dimensionless scaling variables, see left panel of Fig. 1.13. For a two-body system (core+halo particle(s)) the classical turning point of the particle can be used in which its potential energy is equal to its total energy ($\sim R$). Therefore, the ratio $\langle r \rangle^2/R^2$ gives the dimensionless mean square radius used for the y-axis. While, the x-axis represents the dimensionless binding energy $\mu|\varepsilon|R^2/\hbar^2$. The conditions presented above for the halo have as a direct consequence that these nuclei

have a larger root-mean-square (r.m.s.) matter radii, compared to that of spherical nuclei which are approximated by

$$R(A) = r_0 A^{1/3}\,, \tag{1.26}$$

where $r_0 = 1.25$ fm.

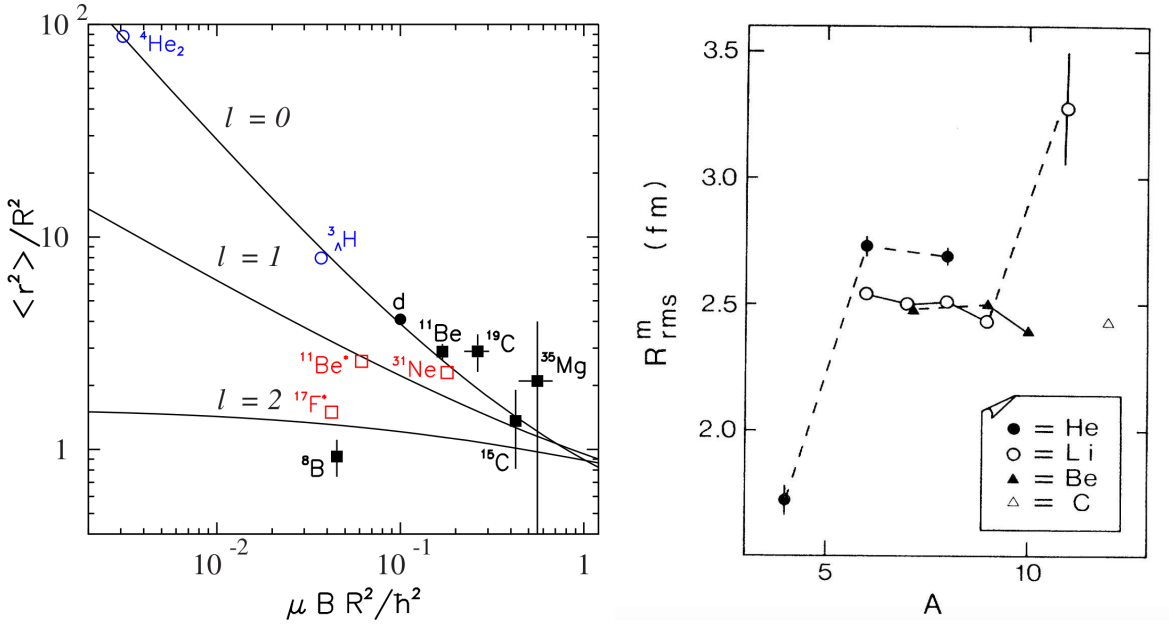

Figure 1.13.: Left. Scaling plot for two-body halo systems. The filled circle denotes the deuteron, the filled squares denote nuclei where radii were extracted from experimental interaction cross-sections, the open squares are simple model estimates and the open circles are theoretical calculations. This figure is reprinted with permission from [61]; permission conveyed through Copyright Clearance Center, Inc.. Right. Matter radii of He, Li, Be, and C isotopes extracted from interaction cross-section measurements. This figure is reprinted with permission from [62] ©2024 by the American Physical Society.

There are several methods to probe the halo nature of a nucleus. The experiment that gave birth to this field is the one performed by Tanihata *et al.* in 1985 [62]. As can be seen from the right panel of Fig. 1.13, a systematical study of the nuclei radius of those elements along their isotopic chains has been performed for He, Li, Be, and C. The interaction radii have been extracted by measurement of interaction cross sections σ_I of the isotopes impinging on Be, Ca, and Al targets:

$$\sigma_I(p,t) = \pi[\mathrm{R}_I(p) + \mathrm{R}_I(t)]^2\,, \tag{1.27}$$

where $\mathrm{R}_I(p)$ is the projectile radius and $\mathrm{R}_I(t)$ is the target radius. To relate (more) quantitatively σ_I to the r.m.s. radius it has been used a Glauber-type calculation assuming different model density distributions. The lithium case revealed unexpected results: the isotopic chain $^{6-9}$Li follows the trend from Eq. 1.26, ^{10}Li is unbound, while ^{11}Li exhibits a jump in size with a radius of 3.27±0.24 fm. This long tail of the nuclear density profile was later explained as a two-neutron halo system (^{9}Li+2n) [63]. Other ways to assess the halo nature of nuclei are

determining the transverse momentum distribution of the core, which is expected to be a narrow distribution [64], proton-nucleus elastic scattering [65], and others. An exhaustive overview is given in Ref. [66].

Hypernuclei presenting a halo have been predicted, e.g., the ${}^{3}_{\Lambda}$H ($S_{\Lambda d}$=0.13 MeV) [67], and the ${}^{6}_{\Lambda}$He (S_n=0.17 MeV) [68]. However, the size of hypernuclei has not been yet measured. New information on exotic hypernuclei would reveal aspects of the *YN* and *YNN* interactions and would be an important benchmark for *ab initio* theories [36].

1.4.3. Hypertriton ${}^{3}_{\Lambda}$H

As introduced in Sec. 1.3.3, determination of the hypertriton (${}^{3}_{\Lambda}$H) size is crucial for understanding the nucleosynthesis mechanism in relativistic HIC. Over the past decades, there has been a vivid interest in characterizing ${}^{3}_{\Lambda}$H, the lightest hypernucleus (npΛ). It is a loosely bound system with the Λ bound only by B_Λ = 130(50)(40) keV to the deuteron core [69], a reference value from emulsion analyses. Meanwhile, as shown in the left panel of Fig. 1.14, there are two recent measurements that differ significantly, though with large uncertainties. The STAR collaboration in 2020 found a value of B_Λ= 410(120)(110) keV [70], while, according to ALICE in 2022 B_Λ= 72(63)(36) keV [30].

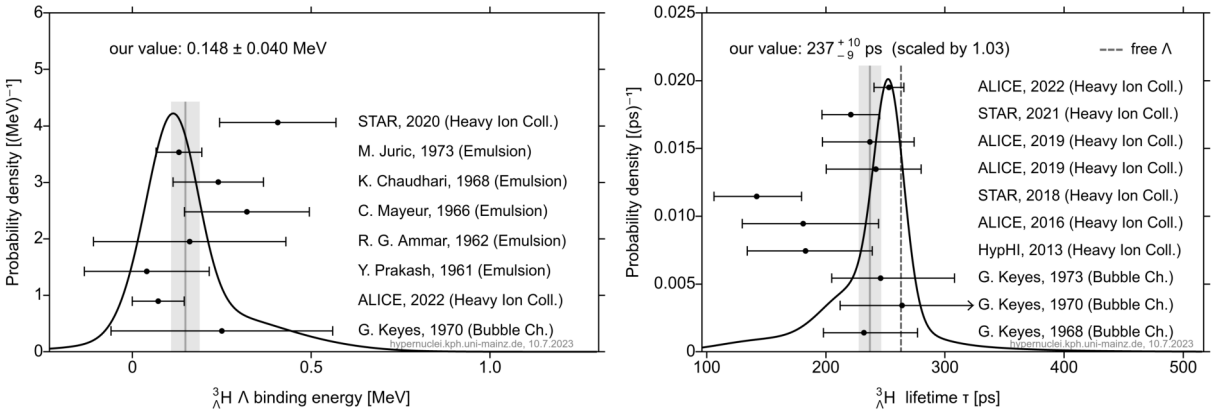

Figure 1.14.: Left. Experimental Λ binding energy values in ${}^{3}_{\Lambda}$H obtained by different experiments, the grey band represents the weighted average. Right. Experimental ${}^{3}_{\Lambda}$H lifetime values, the grey area represents the weighted average, and the dashed line the lifetime of the free Λ. Figure is taken from [71].

The consequences of a weak binding between the Λ and the deuteron are twofold. First, the lifetime of the ${}^{3}_{\Lambda}$H is expected to be compatible with that of the free Λ (τ_Λ=263 ps). Nonetheless, the right panel of Fig. 1.14 summarizes values from different measurements that are shorter, leading to what is known as the *hypertriton lifetime puzzle*. However, the latest value reported by the ALICE collaboration in 2022 is consistent with the lifetime of the free Λ and is the most precise one so far, 253(11)(6) ps [30]. Second, the ${}^{3}_{\Lambda}$H is predicted to be a hyperhalo nucleus. Using the $\not\pi$EFT (pionless Effective Field Theory) a strong correlation has been found between separation energy B_Λ and the matter r.m.s. radius of the ${}^{3}_{\Lambda}$H [72].

In particular, as it can be seen from Fig. 1.15, lower binding energy leads to larger spatial extension, up to 10 fm, *i.e.*, a Λ halo. So far, no experimental observation on its size has been obtained.

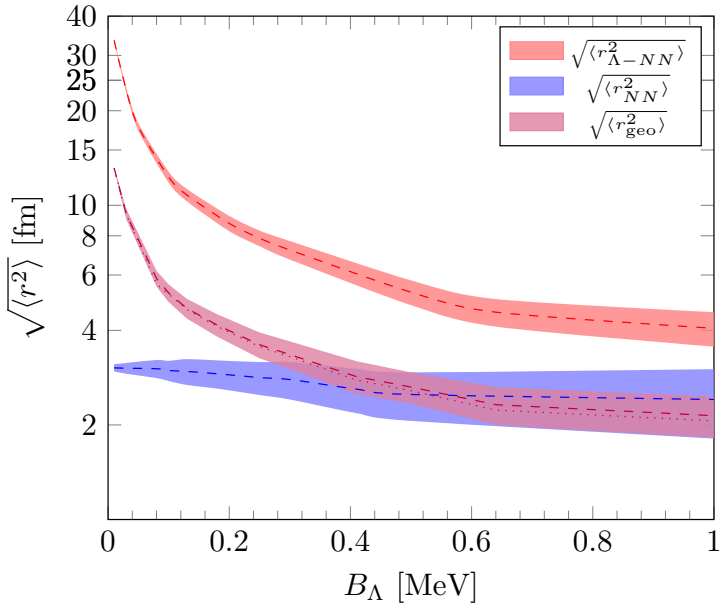

Figure 1.15.: Matter radii for the Λnp system as function of the Λ binding energy. The orange curve represents the separation of the Λ from the c.m. of the two nucleons ($\Lambda - NN$). The violet one is the interparticle distance of the two nucleons (NN). Finally, the red one is the geometric combination according to the constituent masses (*geo*) [73]. The bands width are (propagated) EFT errors given by the power counting from Ref. [72]. Figure is taken from [74].

In contrast to heavier hypernuclei, where mesonic decays are Pauli blocked, in ${}^{3}_{\Lambda}$H they are by far the dominant ones. Table 1.1 shows the mesonic decay channels of the ${}^{3}_{\Lambda}$H, where according to the empirical $\Delta I = 1/2$ rule, all the decay rates into π^- are a factor of 2 larger than the ones into π^0.

Channel	$\Gamma(\text{sec}^{-1})$	Γ/Γ_Λ
^{3}He+π^- and ^{3}H+π^0	0.46×10^{10}	0.384
d+p+π^- and d+n+π^0	0.235×10^{10}	0.619
p+p+n+π^- and p+n+n+π^0	0.368×10^{8}	0.0097
all mesonic channels	0.385×10^{10}	1.01

Table 1.1.: Partial and total mesonic decay rates of the ${}^{3}_{\Lambda}$H. Table is from [75].

In this introduction, the importance of the discovery of the strange quark has been shown, in particular the advantages in studies of hypernuclei. They can form more neutron-rich nuclei and extend the dripline. Study of their internal structure allows to characterize the YN and YY interactions, that are not possible to study directly due to the short lifetime of

hyperons. As such, they can also help understand better the nuclear EoS and consequently the structure in the inner core of NSs. Among the various hypernuclei, the ${}^{3}_{\Lambda}$H and in particular its size, has been indicated as a key probe to understand the nucleosynthesis in HIC, to better constrain the prediction from the coalescence models.

This thesis focuses on the strangeness production at GSI/SIS18 energies (few GeV). In the first part, the concept of a new accepted experiment at GSI that will be performed in 2025 at the R^{3}B setup is detailed. The experiment will focus on the estimation of the ${}^{3}_{\Lambda}$H size through reconstruction of its invariant mass and by using a new experimental method to extract the interaction cross section, see Chapter 2 for the details of the method. Chapter 3 and 4 present the experimental setup including GEANT4 simulations performed for its design optimization.

In the second part of the thesis, the focus shifts to ${}^{3}_{\Lambda}$H production at heavy-ion collisions in the HADES setup, exploring different energies and in-medium conditions. Chapter 5 provides an overview of the HADES detector setup and its configurations during the 2012 (Au+Au at 1.23 AGeV) and 2019 (Ag+Ag at 1.23 and 1.58 AGeV) experimental campaigns which where analyzed. The methodology employed for analyzing HIC data to study the ${}^{3}_{\Lambda}$H production and ensure a clear signal and background separation can be found in Chapter 6. While, the experimental results including the invariant mass spectra and the production cross-sections are presented in Chapter 7. Finally, conclusions and perspectives are drawn.

Part I.

HYDRA- HYpernuclei Decay at R^{3}B Apparatus

2. The two-target method

The first experiment in the HYDRA (Hypernuclei Decay at R^{3}B Apparatus) program within the FAIR Phase-0 stage is scheduled for 2025, with the aim to extract the matter radius of hypertriton through measurement of its interaction cross section (ICS) with a two target measurement with ^{12}C nuclei. As it was introduced in the previous Chapter, the determination of the size of the hypertriton has been indicated as a key probe for understanding the nucleosynthesis in HIC. However, accessing the matter radius of hypernuclei is challenging due to two main reasons: their low production cross section and their sub-nanosecond lifetime. Although there are different experimental methods to determine the matter radius of a nucleus, in the case of very low intensities, the measurement of interaction or reaction cross sections of a projectile with an ion target can provide a quantitative assessment of its matter radius. This method was historically pioneered by I. Tannihata *et al.* for the two neutron-halo ^{11}Li [62]. In the following Chapter, the hypernuclear version of this method is presented including a detailed study of its sensitivity for the specific case of the hypertriton. A paper describing the method and its realistic implementation was recently published in Eur. Phys. J. A [76].

2.1. General description

The method allows for the measurement of the interaction cross sections of hypernuclei ($^{A}_{\Lambda}$X) with a target nucleus, which can then be further analyzed to infer their matter radii. In this context, the term 'interaction cross section' refers to all reactions that result in a final state that is different from the initial hypernucleus in a bound state.

The population of hypernuclei $N_\Lambda(x)$, inside a material of density $n(x)$, depends on the following processes:

- the beam population $N(x)$ interacts with the target and according to the *production cross section σ_Λ of the hypernuclei* (unknown, little data with large uncertainties [77]), a certain yield of hypernuclei is produced:

$$dN_\Lambda(x) = n\sigma_\Lambda N(x)dx\,; \tag{2.1}$$

- the beam impinging on the target nuclei produces projectile-like fragments. Further interaction of a fragment with the target can produce hypernuclei, *i.e.*, a *two-step strangeness production*:

$$dN_\Lambda(x) = \sum_i n\sigma_{\Lambda i}N_i(x)dx \tag{2.2}$$

where N_i is the number of i secondary particles produced in the fragmentation with an associated hypernuclei production cross section $\sigma_{\Lambda i}$. Note that the production of hypernuclei implies $A \geq 3$ and $E_{kin} > 1.58$ AGeV. The contribution of this mechanism strongly depends on the initial conditions of beam and target nuclei and cannot be generalized. Therefore, it has to be evaluated case by case.

- the yield of the produced ${}^{\mathrm{A}}_{\Lambda}\mathrm{X}$ is then attenuated by two main processes:
  1. decay of the hypernucleus, according to its short lifetime ($\tau \sim 200$ ps). Considering β the velocity of the ${}^{\mathrm{A}}_{\Lambda}\mathrm{X}$ in the laboratory frame, γ its Lorentz factor and *c* the speed of light, gives:
  $$dN_{\Lambda}(x) = -N_{\Lambda}(x)\frac{dx}{\gamma\beta c\tau}\,; \tag{2.3}$$
  2. its interaction with the target nuclei, according to the *interaction cross-section* $\sigma_{\Lambda R}$ *of* ${}^{A}_{\Lambda}X$ *with the target* (unknown) reducing its population by:
  $$dN_{\Lambda}(x) = -n\sigma_{\Lambda R}N_{\Lambda}(x)dx\ . \tag{2.4}$$

To obtain the two unknown cross sections, it is proposed to perform two separate measurements. In principle, several experimental configurations can be considered to reach this objective. The first possibility includes a single measurement using two targets of thicknesses, d_1 and d_2, separated by a flight gap *L*. This configuration requires less beam time since the measurement from both targets is done only once. However, distinguishing whether the primary vertex is allocated inside target 1 or 2 is technically challenging, and would require a high-granularity high-rate tracking detector placed in between the two targets. The second configuration introduces two independent measurements using the same beam and two targets of the same material but with an increasing thickness. Although it requires a longer beam time, reconstruction of the decay vertex can be obtained with high accuracy as it is done with two independent measurements. The third configuration includes two independent measurements using the same target but two different beams with different hypernuclei production cross section. It implies a long beam time and since the hypernuclei production cross section is low ($\sim \mu$b) such an option would require a measurement with one production cross section significantly lower than the other, *i.e.*, extremely beam-time consuming. For these reasons, I focus here on a method based on two separate measurements with identical beam and with two different target thicknesses of the same material, which will allow to access both σ_{Λ} and $\sigma_{\Lambda R}$.

As a first step, we make the assumption that the interaction cross section of ${}^{\mathrm{A}}_{\Lambda}\mathrm{X}$ with a target ${}^{\mathrm{A}}\mathrm{Y}$ can be expressed by the geometrical cross section. In the black-disc model, the projectile and target nuclei are treated as structure-less spheres with radii $\mathrm{R}({}^{\mathrm{A}}_{\Lambda}\mathrm{X})$ and $\mathrm{R}({}^{\mathrm{A}}\mathrm{Y})$, respectively, as illustrated in Fig. 2.1. A reaction occurs when these spheres overlap in a collision and the cross section can be expressed as

$$\sigma_{\Lambda R} = \pi[\mathrm{R}({}^{\mathrm{A}}_{\Lambda}\mathrm{X}) + \mathrm{R}({}^{\mathrm{A}}\mathrm{Y})]^2\,, \tag{2.5}$$

where $\mathrm{R}({}^{A}\mathrm{Y}) = R_0\,A^{\frac{1}{3}}$ and $R_0 = 1.25$ fm. For the ${}^{3}_{\Lambda}\mathrm{H}$ case, the interaction cross section will be analysed in Sec. 2.3 within the eikonal formalism to obtain a microscopic connection to

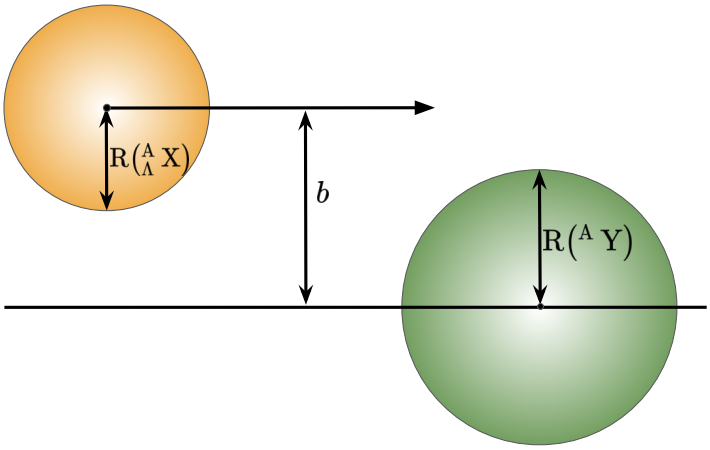

Figure 2.1.: Sketch of a hard-sphere projectile of radius R($^{A}_{\Lambda}$X) approaching a hard-sphere target of radius R(^{A}Y), with impact parameter b. A collision occurs only for $b <$ R($^{A}_{\Lambda}$X) + R(^{A}Y).

its matter radius.
Hypernuclei produced will be reconstructed via the invariant-mass method by measuring the weak decay products in the final state. The mesonic decay vertex ditribution (DVD) along the flight path downstream the target will be used as an observable to determine the interaction cross section. Figure 2.2 illustrates the sensitivity of the DVD to $\sigma_{\Lambda R}$ (and thus to the matter radius) for a generic $^{A}_{\Lambda}$X, assuming: τ =200 ps, $\sigma_{\Lambda} = 1.8\,\mu$b (see Sec. 2.3) and different interaction cross sections $\sigma_{\Lambda R} = 0$ b, 1 b, 5 b. A sudden drop in the DVD can be observed due to the interaction downstream the target.

Below, the analytical formulation of the method is presented, as well as its sensitivity for the specific case of $^{3}_{\Lambda}$H by estimating the uncertainties of its interaction cross section.

2.2. Analytical formulation

In the following, the second experimental configuration will be analyzed: the first measurement is done using a single cylinder of thickness d_1 and a second with two cylinders of thicknesses, d_1 and d_2, separated by a flight gap L. For L=0, this corresponds to two independent measurements with a target thickness d_1 and a target of thickness $d_1 + d_2$. It is assumed that all particles propagate along the beam axis (z). Under the above conditions, the beam population $N(z)$, when considering a stable beam (e.g. ^{12}C), depends only on the interaction of the projectile particles with the target nuclei:

$$dN(z) = -\delta\Big(n\sigma_R N(z)\Big)dz\,, \tag{2.6}$$

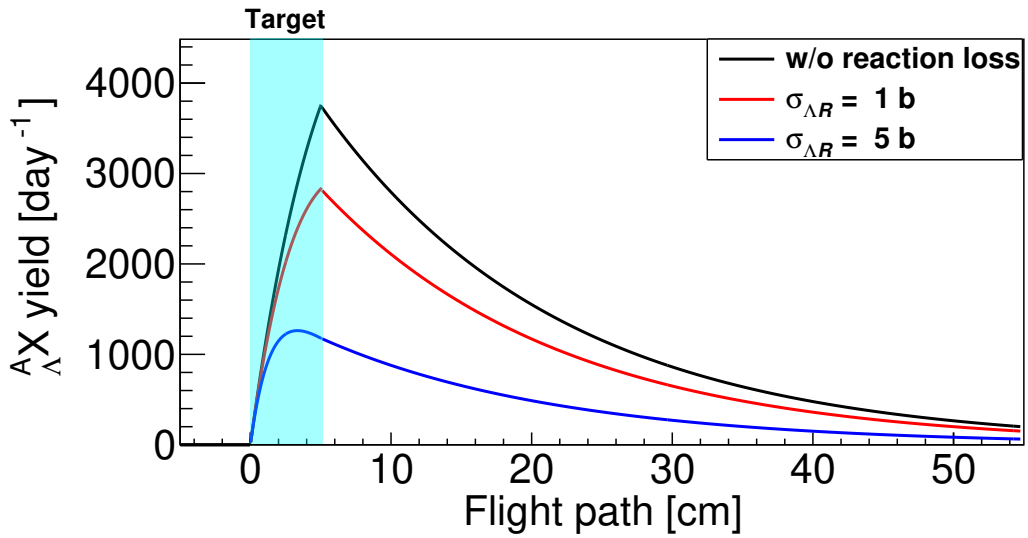

Figure 2.2.: Yield of hypernucleus ${}^{A}_{\Lambda}$X along the flight path assuming different interaction cross sections (different curves), and a ^{12}C beam at 1.9 AGeV with intensity of 10^6 particle per second (pps) impinging on a 5 cm thick carbon target (blue shaded band). This figure is reprinted from [76] under CC BY 4.0.

where, σ_R is the reaction cross section of the beam projectiles with the targets, and $\delta = 0, 1$ (0 in free space and 1 inside a target). The trends of the beam population at different regions are:

$$N(z) = \begin{cases} N_0 = I \cdot t & z \leq 0 \\ N_0\, e^{-n\sigma_R z} & 0 < z \leq d_1 \\ N_1 = N_0\, e^{-n\sigma_R d_1} & d_1 < z \leq d_1 + L \\ N_1\, e^{-n\sigma_R (z - d1 - L)} & d_1 + L < z \leq d_1 + L + d_2 \\ N_2 = N_1\, e^{-n\sigma_R (d_2)} & z > d_1 + L + d_2 \end{cases} \tag{2.7}$$

where I is the beam intensity and t is the total measurement time. These trends are visualized by the red line on Fig. 2.3.

The population $N_\Lambda(z)$ of hypernuclei can be formulated analytically by taking into account the contributions from Eqs. (2.1, 2.3, 2.4):

$$dN_\Lambda(z) = -\frac{N_\Lambda(z)}{\gamma\beta c\tau} dz + \delta\Big(n\sigma_\Lambda N(z) - n\sigma_{\Lambda R} N_\Lambda(z)\Big) dz\,, \tag{2.8}$$

with the different trends of the hypernuclei population:

$$N_\Lambda(z) = \begin{cases} 0 & z \leq 0 \\ \frac{n\sigma_\Lambda N_0}{B}\left(1-e^{-Bz}\right)e^{-n\sigma_R z} & 0 < z \leq d_1 \\ N_\Lambda(d_1)e^{-\left(\frac{z-d_1}{\gamma\beta\tau c}\right)} & d_1 < z \leq d_1+L \\ \left[\frac{n\sigma_\Lambda N_1}{B}\left(1-e^{-B\,z'}\right)+N_\Lambda(d_1+L)\,e^{-B\,z'}\right]e^{-n\sigma_R\,z'} & d_1+L < z \leq d_1+L+d_2 \\ N_\Lambda(d_1+L+d_2)e^{-\left(\frac{z-d_1-L-d_2}{\gamma\beta\tau c}\right)} & z > d_1+L+d_2 \end{cases} \tag{2.9}$$

where $z' = z - d_1 - L$ and $B \equiv \left(\frac{1}{\gamma\beta c\tau} + n\sigma_{\Lambda R} - n\sigma_R\right)$ includes all the processes that affect the ${}^{A}_{\Lambda}$X population. The trends are shown by the black line in Fig. 2.3. The contribution from the two-step processes (Eq. 2.2) is addressed in Sec. 2.4.2.

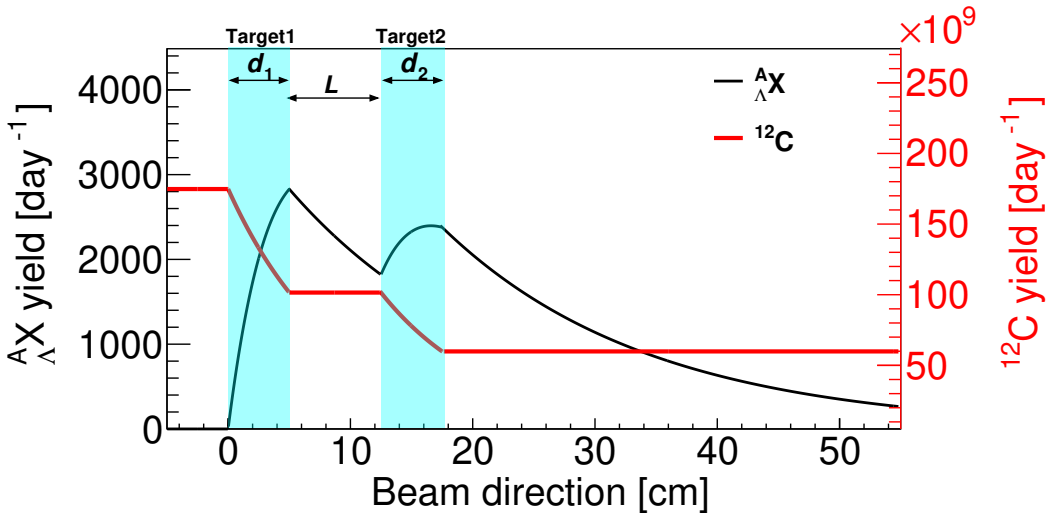

Figure 2.3.: Yield of particles per day. The left black y-axis represents the decay vertex distribution of ${}^{A}_{\Lambda}$X assuming $\sigma_{\Lambda R} = 1$ b. The right red y-axis represents the yield of ^{12}C at 1.9 AGe with intensity of 10^6 pps along the beam direction. The shaded light-blue bands depict two carbon targets with thicknesses, d_1 and d_2, separated by a gap L.

Once the DVD of ${}^{A}_{\Lambda}$X along the beam axis (z) has been extracted, it is of particular interest to extrapolate the populations at the exit of the two targets, where the contribution from their interaction is the largest, *i.e.*, $N_\Lambda(d_1)$ from the first measurement and $N_\Lambda(d_1+L+d_2)$ for the second one. The two populations can be expressed using Eqs. (2.7, 2.9) as:

$$N_\Lambda(d_1) = \frac{n\sigma_\Lambda N_{0,d_1}}{B}\left(1-e^{-Bd_1}\right)e^{-n\sigma_R d_1}\,, \tag{2.10}$$

$$N_\Lambda(d_1+L+d_2) = \left[\frac{n\sigma_\Lambda N_1}{B}\left(1-e^{-B\,d_2}\right)+N_\Lambda(d_1+L)\,e^{-B\,d_2}\right]e^{-n\sigma_R\,d_2}\,, \tag{2.11}$$

where $N_{0,d_1} = I \cdot t\,\alpha$ is the number of beam projectiles that impinges on the first target ($z = 0$) for the first measurement, $N_1 = N_{0,d_2}\, e^{-n\sigma_R d_1}$ is the number of primary beam nuclei $N_{0,d_2} = I \cdot t\,(1-\alpha)$ that reaches the second target ($z = d_1 + L$) for the second measurement. The additional parameter α represents the share of the total beam time among the two measurements, *i.e.*, $0 < \alpha \leq 1$.

By taking the ratio between the two and re-arranging the terms it is possible to get the analytical formulation of the ${}^{A}_{\Lambda}$X interaction cross section:

$$A\,(1 - e^{-B\,d_1})e^{-\left(\frac{L}{\gamma\beta\tau c} + B\,d_2\right)} - A\,e^{-B\,d_2} + e^{-B\,d_1} + A - 1 = 0\,, \tag{2.12}$$

where to help the readability of the equation, the ratio between the two populations is contained in the variable

$$A \equiv \frac{N_\Lambda(d_1)\; N_{0,d_2}}{N_\Lambda(d_1 + L + d_2)\; N_{0,d_1}} \cdot e^{-n\sigma_R\, d_2}\,. \tag{2.13}$$

Note that for the case $L = 0$, Eq. 2.12 is simplified into:

$$e^{-B\,d_1} - A\,e^{-B\,(d_1+d_2)} - 1 + A = 0\,, \tag{2.14}$$

where $A \equiv \dfrac{N_\Lambda(d_1) N_{0,d_2}}{N_\Lambda(d_1 + d_2) N_{0,d_1}} \cdot e^{-n\sigma_R\, d_2}$.

2.3. Method sensitivity

The sensitivity of the method is investigated for the case of the hypertriton (${}^{3}_{\Lambda}$H), where the considered production and decay channels are ^{12}C + ^{12}C $\rightarrow$ X + ${}^{3}_{\Lambda}$H and ${}^{3}_{\Lambda}$H $\rightarrow$ ^{3}He + π^- (branching ratio, *BR*=26% [75]), respectively. As presented in Chapter 1, it is of particular interest to study the size of ${}^{3}_{\Lambda}$H, the lightest predicted hyperhalo. In such a case, we cannot consider here the traditional geometrical interaction cross section of hypernucleus (Eq. 2.5), since the hypertriton is expected to be a dilute object for which the black-disk limit may not be suited. Instead, the correlation between the measured interaction cross section and the matter radius of ${}^{3}_{\Lambda}$H will be analysed with microscopic wave functions and the eikonal formalism, valid at the considered incident energies, beyond the simplistic geometrical ansatz.

2.3.1. Eikonal approximation and matter radius

The eikonal approximation offers a semi-classical framework for calculating reaction probabilities based on the distance between the colliding projectile and target nuclei. One common approximation is to assume that the ejectile particle propagates along the beam direction (z) in a straight-line. This approximation is effective for high energy projectile as it simplifies the Schrödinger equation into a single-variable differential equation. The essential inputs for the calculation are the density distributions of the projectile and target nuclei, and the prerequisite for a nuclear-induced reaction is the overlapping of the nuclei.

The total reaction cross section is obtained by integrating the total reaction probability over the impact parameter b. Assuming the target density distribution is well-known, the density distribution of the projectile can be adjusted to reproduce a cross section obtained from experimental data. Extracted matter r.m.s. radii $< r_m^2 >^{1/2}$ are usually based on a harmonic oscillator or Fermi parametrization of the density distribution, as presented for example in Ref. [78].

For the case of the interaction cross section of ${}^{3}_{\Lambda}$H with ^{12}C target, the required inputs for the calculation are (i) the density distribution of ^{12}C, (ii) the density distributions of the Λ and the deuteron in the center of mass of ${}^{3}_{\Lambda}$H, (iii) proton-neutron and proton-proton total cross sections, (iv) Λ-nucleon total cross sections. Nucleon-nucleon cross sections at energies of ~ 2 GeV have been measured [79], and the density distribution of ^{12}C can be considered well known, in particular, its charge density distribution from precision (e, e) measurements [80]. The neutron density distribution can be considered identical, as a good approximation. The Λ-nucleon total cross sections have been measured [81, 82] and show a flat behaviour over a large range of energies. The measured values, fitted over momentum p in GeV/*c*, of $\sigma(\Lambda p) = (34.3 \pm 1.5)$ mb $- p^{-1}(-3.8 \pm 17.6)$ mb GeV/*c* and $\sigma(\Lambda n) = (34.1 \pm 3)$ mb $- p^{-1}(33 \pm 35)$ mb GeV/*c* are close to the nucleon-nucleon total cross sections. Note that at the energies relevant in this thesis, the total cross section is expected to reflect the size of the colliding baryons, and show little momentum dependence (less than 1%), consistent with the above mentioned measurements. The radial density distributions for the neutron, proton and Λ in ${}^{3}_{\Lambda}$H are taken from theory. In the case of the pionless EFT, the rms radius of ${}^{3}_{\Lambda}$H can be tuned by modifying the Λ separation energy, as illustrated in [72]. As the separation energy for the ${}^{3}_{\Lambda}$H has not been determined experimentally precisely three values were considered in the calculation: 50 keV (rms radius = 7.9 fm from pionless EFT), 130 keV (rms radius = 4.9 fm) and 410 keV [70] (rms radius = 2.8 fm). The obtained cross sections are 1062 mb, 861 mb and 645 mb, respectively.

2.3.2. Parameters optimization

In this sub-section, the different scenarios for the ${}^{3}_{\Lambda}$H rms matter radius, and consequently interaction cross section ($\sigma_{\Lambda R}$), are analyzed assuming detection efficiency $\varepsilon_{det} = 100\%$ for the weak decay products, where in the next section realistic conditions are considered. The purpose of this analysis is to conclude on an optimal configuration that minimizes the resulting uncertainty when extracting the interaction cross section.

The statistics of the experiment plays a fundamental role in the proposed method and determines the choice of the beam and targets. For the purpose of this sensitivity study, we consider realistic beam conditions at GSI/FAIR [83]: beam intensity $I = 10^6$ pps, beam energy $E_{beam} = 1.9$ AGeV, and assuming a total beam time $t = 1$ day. At this energy the measured reaction cross section ^{12}C+^{12}C equals $\sigma_R = 888 \pm 19$ mb [84]. The method is general and applicable to other beams and different energies under the condition that it is above the Λ production threshold of 1.58 GeV (elementary process $NN \to \Lambda KN$). In terms of the experimental setup, the parameters taken into consideration are: the target thicknesses (d_1 and d_2), the flight gap (L), and the share of total beam time among the two measurements (α). The mean free path of ^{12}C in the target is calculated to be $\lambda = 1/(\sigma_R n) = 10$ cm. In

the case of a pronounced halo, the mean free path of the hypertriton is expected to be also in the order of 10 cm, which therefore, limits the maximum target thickness to avoid too many reactions. The contribution of these parameters to the uncertainty of the $\sigma_{\Lambda R}$ ($\delta\sigma_{\Lambda R}$) is analyzed considering a lifetime $\tau(^3_\Lambda\mathrm{H}) = 237^{+9}_{-7}$ ps [71]. The sensitivity study presented in this section is not affected by the choice of the lifetime, such that the conclusions drawn from the method will remain unchanged. Note that Eqs. (2.12, 2.14) cannot be solved analytically, therefore the numerical bisection method [85] was used.

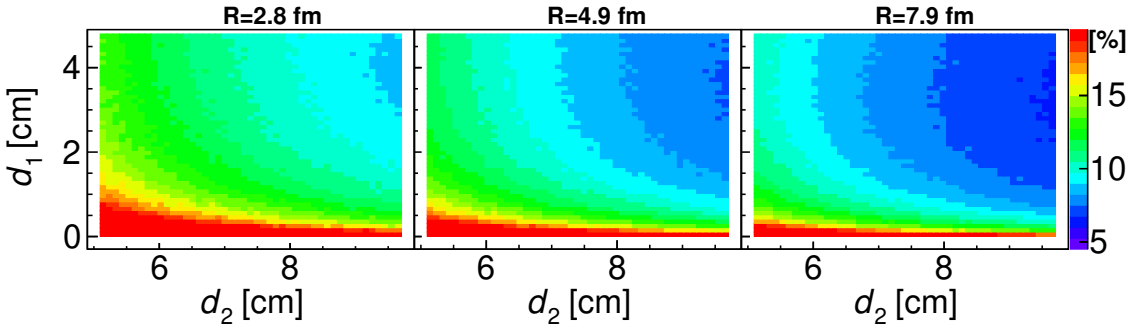

Figure 2.4.: Relative uncertainty of hypertriton interaction cross section $(\delta\sigma_{\Lambda R}/\sigma_{\Lambda R})$ with ^{12}C for several matter radii as a function of the target thicknesses d_1 and d_2, for $L = 0$ and $\alpha = 50\%$. This figure is reprinted from [76] under CC BY 4.0.

Figure 2.4 shows the resulted relative uncertainty of $\sigma_{\Lambda R}$ ($\delta\sigma_{\Lambda R}/\sigma_{\Lambda R}$) as a function of the target thicknesses for different matter radii, for the case of L =0 and $\alpha = 50\%$. A minimum is reached, where the lowest values of $\delta\sigma_{\Lambda R}/\sigma_{\Lambda R}$ are obtained using a thin target for the first measurement, $d_1 \sim 3 - 4$ cm, and a thicker target for the second one, $d_1 + d_2 \sim 8 - 11$ cm. Values of $d_1 = 3$ cm for the first measurement and $d_1 + d_2 = 11$ cm for the second one will be used in this section.

The left panel of Fig. 2.5 shows the dependence of $\delta\sigma_{\Lambda R}/\sigma_{\Lambda R}$ as a function of α, considering $L = 0$, where a minimum is reached for $50\% \leq \alpha \leq 70\%$. The right panel of Fig. 2.5 shows the trend of $\delta\sigma_{\Lambda R}/\sigma_{\Lambda R}$ as a function of the flight gap (L) for a fixed $\alpha = 50\%$. The introduction of a gap between the two targets will only degrade the uncertainty as the yields of $^3_\Lambda$H will be reduced due to its decay.

To conclude, the optimal configuration obtained with the proposed method is: no gap between the two targets ($L = 0$), the same beam conditions for the two measurements $\big(N_0(d_1) = N_0(d_1 + d_2)\big)$, and a large difference between the two target thicknesses. Specific values for the last parameters cannot be given as they strongly depend on the experiment, and therefore have to be evaluated accordingly.

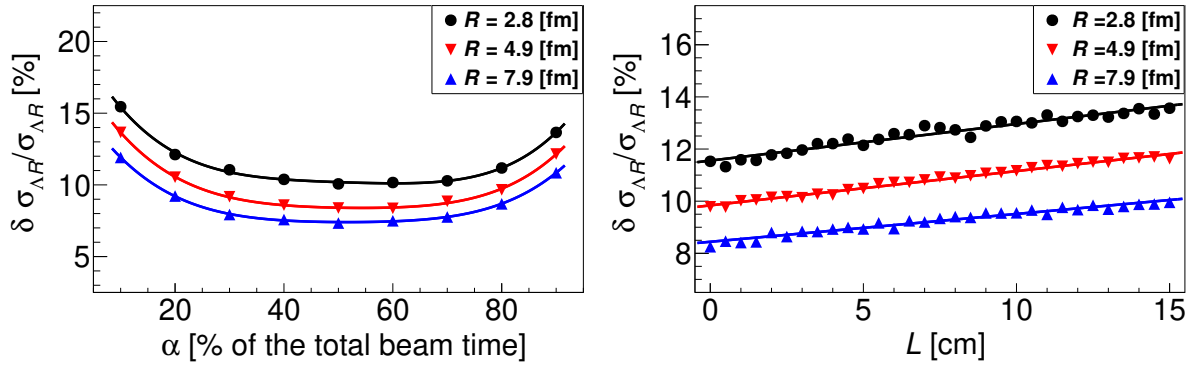

Figure 2.5.: Left. Relative uncertainty of hypertriton interaction cross section $(\delta\sigma_{\Lambda R}/\sigma_{\Lambda R})$, considering $L = 0$, $d_1 = 3$ cm and $d_1 + d_2 = 11$ cm, for several hypertriton radii and a given amount of total beam time (1 day) as a function of α. Right. $(\delta\sigma_{\Lambda R}/\sigma_{\Lambda R})$ as a function of the flight gap *L*, considering $\alpha = 50\%$. These figures are reprinted from [76] under CC BY 4.0.

2.4. Application of the method: the HYDRA day-1 experiment

2.4.1. Measurement sensitivity

The R^{3}B setup at GSI/FAIR has the potential for a world-unique contribution to the study of Λ-hypernuclei using relativistic stable and radioactive beams [49, 77].

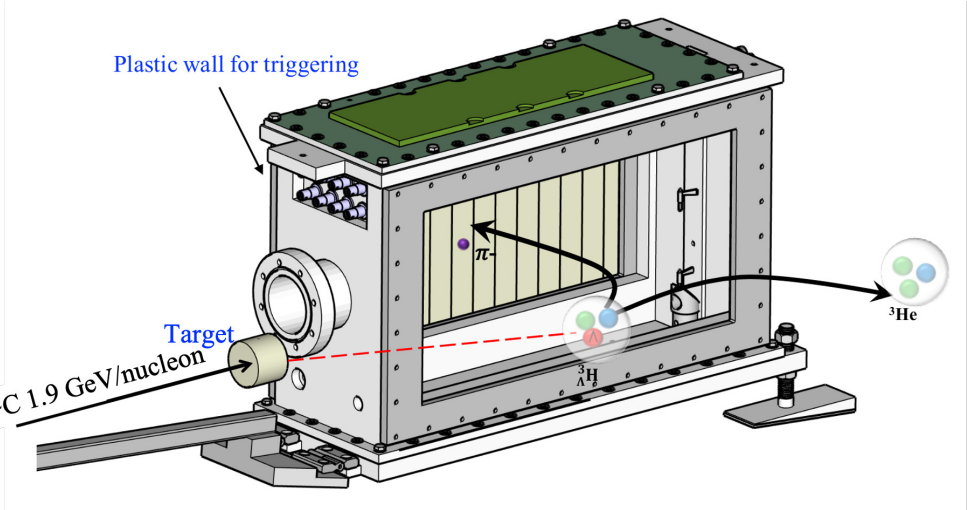

Figure 2.6.: Sketch of the HYDRA TPC prototype geometry and the experimental concept. The TPC aims at measuring π^- from the mesonic decay of light hypernuclei. The trajectory of the π^- is deflected in the GLAD magnetic field around 2 T. This figure is reprinted from [76] under CC BY 4.0.

The first experiment foreseen at the R^{3}B setup in 2025 will utilize the mini-HYDRA Time Projection Chamber (TPC) to detect pions emerging from hypernuclear decay, as shown in Fig. 2.6. Detailed information about the R^{3}B experimental setup can be found in Chapter 3. The experiment aims to determine the interaction cross section (and consequently

the matter radius) of the hypertriton, employing the two-target method introduced here. The production and decay channels are those described in the previous section: ^{12}C + ^{12}C $\rightarrow$ X + $^{3}_{\Lambda}$H and $^{3}_{\Lambda}$H $\rightarrow$ ^{3}He + π^-, respectively. Real experimental conditions determine several limitations that cannot be neglected and are detailed in Chapter 4: (i) π^- detection efficiency in the TPC of 25%, (ii) fragment detection efficiency of 69%, (iii) dead time, spill structure and acceleration duty 40%, (iv) analysis loss 20%. The beam conditions which will be used are: ^{12}C with $I = (1-5)\cdot 10^6$ pps (trigger rate limitation, see Sec. 4.3) and $E_{beam} = 1.9$ AGeV (maximum energy accessible at GSI currently). Since the production cross section of the hypertriton is predicted to be very low 1.8 μb [49], high intensity beam, $\mathcal{O}(10^6$ pps) is necessary, and when combined with a thick target, will lead to a high production of secondary particles and consequently a high trigger rate. Monte-Carlo simulations (using INCL++[86] + Dubna [87] cascade model) for a 6 cm thick ^{12}C target and beam of 10^6 pps result in a trigger rate (coincidence between the trigger wall and TOFD, see Sec. 4.3) of 30 kHz. This is at the limit of the possible accepted rate by the R^{3}B setup, and as a consequence the maximum target thickness has to be fixed to $d_{max} = 6$ cm. With this constraint the minimum uncertainty for the interaction cross section is obtained for $d_1 = 1$ cm and $d_2 = 5$ cm. Using this initial condition it is possible to estimate the total amount of beam time necessary to accumulate sufficient statistics that will ensure good accuracy for the interaction cross section. As can be seen from Fig. 2.7, using the HYDRA prototype, it is

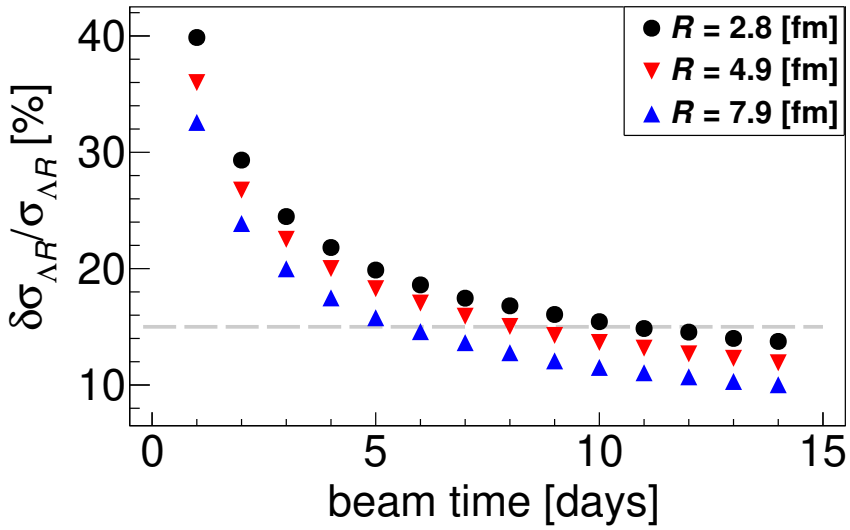

Figure 2.7.: Relative uncertainty of $\sigma_{\Lambda R}$ ($\delta\sigma_{\Lambda R}/\sigma_{\Lambda R}$) as a function of beam time using a ^{12}C beam at 1.9 AGeV impinging on ^{12}C targets with increasing thickness of 1 and 6 cm. The grey dashed line represents 15% relative uncertainty.

possible to obtain a precision of 15% or better, in the case of a halo hypernucleus, within 8 days of beam time. Table 2.1 summarizes the relative uncertainties for the interaction cross section.

While several background contributions (for the complete study see Sec. 4.3) are taken into account in the above, the *two-step strangeness production* is not included, *i.e.*, the

production of hypertriton from interaction of fragments formed in the primary collision. The contribution from such processes is investigated below.

Radius (rms) [fm]	$\sigma_{\Lambda R}$ [mb]	$\delta\sigma_{\Lambda R}/\sigma_{\Lambda R}[\%]$
2.8 (no halo)	645 ± 106	17
4.9	861 ± 129	15
7.9	1062 ± 134	13

Table 2.1.: Interaction cross sections for ${}^{3}_{\Lambda}$H with ^{12}C using Eq. 2.14, assuming two independent measurements with 1-cm and 6-cm thick carbon targets and 8 days of beam time.

2.4.2. Background estimate from two-step processes

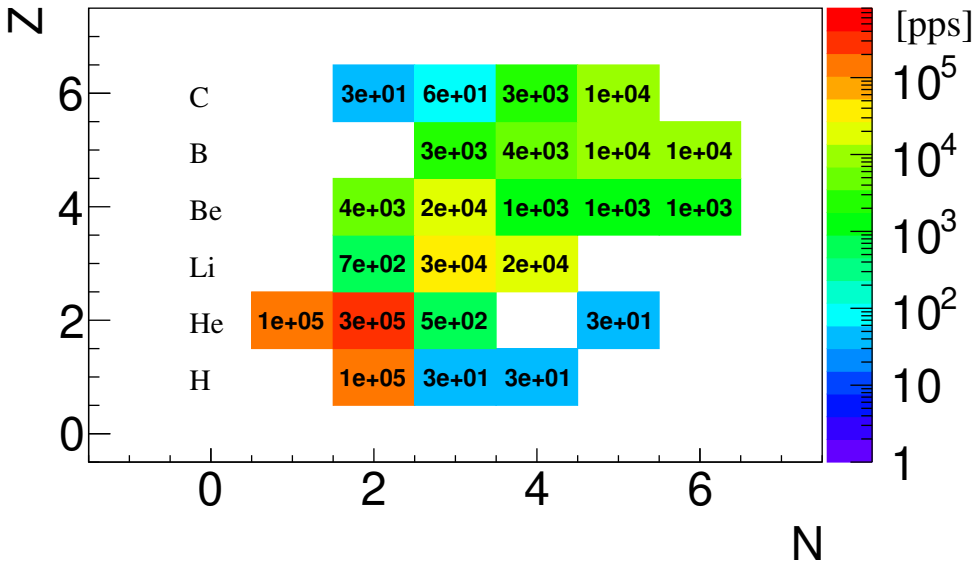

Figure 2.8.: Production rates [pps] of various fragments from ^{12}C+ ^{12}C collisions for incoming beam rate of 10^6 pps and a 6 cm thick target. Only fragments that can lead to the production of a hypertriton are shown, *i.e.*, $A \geq 3$ and E_{kin}>1.58 AGeV.

In order to estimate the upper limit of the two-step production of hypertriton, two assumptions were made: (i) all fragments are produced at the center of the target, (ii) fragments with mass number $A \geq 5$ have a production cross section of 1μb, while for other fragments, the production cross sections are estimated using the method in Ref. [49], which gives values smaller than 1μb. Using INCL++, the rate of fragments produced in ^{12}C+^{12}C collisions was estimated, for beam intensity of 10^6 pps and a 6 cm thick target, as shown in Fig. 2.8. Here only fragments that could lead to the production of hypertriton are considered, *i.e.*, $A \geq 3$ and $E_{kin} > 1.58$ AGeV. Under these assumptions, the maximal number of ${}^{3}_{\Lambda}$H, produced from such two-step processes is estimated to be 1.4% of the total amount of ${}^{3}_{\Lambda}$H produced

by the primary interaction. This therefore justifies to neglect this contribution as it was done in the previous section.

The objective of this Chapter was to introduce a novel, comprehensive approach for estimating interaction cross sections of hypernuclei. This approach involves a two-target measurement strategy. The Chapter began by providing a detailed analytical derivation of this method. Subsequently, the method's sensitivity was analyzed, and the parameters necessary for its execution were optimized under an ideal scenario. Finally, the method was applied to a realistic case to demonstrate its feasibility. The following Chapter provides an in-depth description of the experimental setup that will be used for the execution of the realistic case.

3. Experimental setup

HYDRA (HYpernuclei Decay at R^3B Apparatus) is a physics program within the R^3B (Reactions with Relativistic Radioactive Beams) collaboration to study the production of hypernuclei from heavy-ion collisions and perform their invariant-mass spectroscopy at GSI-FAIR (Gesellschaft für Schwer-Ionenforschung- Facility for Antiproton and Ion Research). The program aims at measuring with high resolution the in-flight pionic decay of light- and medium-mass hypernuclei. To achieve that, a dedicated pion tracker is conceived as a time projection chamber (TPC) inside the GLAD (GSI Large Acceptance Dipole) [88] magnet of the R^3B setup. This Chapter gives a general overview of the facility, the R^3B experimental setup, and the newly developed pion tracker.

3.1. The GSI-FAIR facility

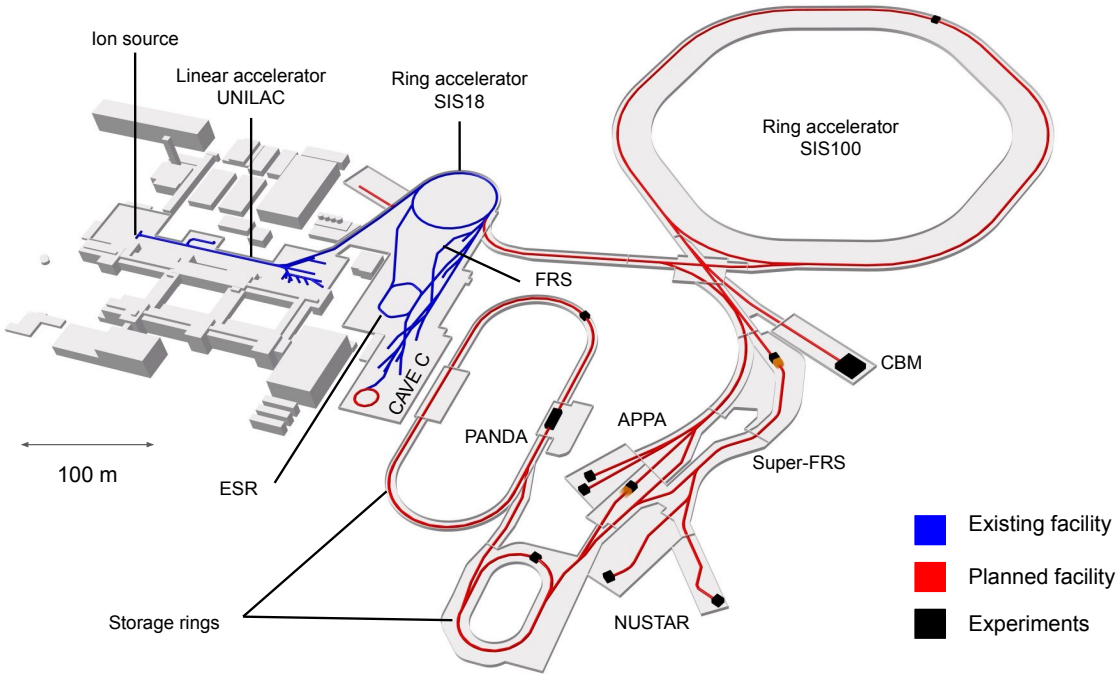

Figure 3.1.: Schematic view of the future GSI-FAIR facility. Figure is taken from [89].

The upcoming FAIR accelerator facility is being built at GSI Helmholtzcenter for Heavy-Ion Research, enlarging the existing GSI accelerator complex, see a schematic view of the project on Fig. 3.1. The scientific program is spread into four collaborations that will benefit

from the higher energies and intensities accessible by SIS100 synchrotron (SchwerIonen Synchrotron[1]), 29 GeV for protons and from 2.7 to 10 AGeV for ^{238}U depending on the charge state [90], that are: APPA (Atomic, Plasma Physics and Applications) [91], CBM (Compressed Baryonic Matter) [92], NUSTAR (NUclear STructure Astrophysics and Reactions) [93] and PANDA (antiProton ANnihilation at DArmstadt) [94].

The existing GSI accelerator facility will serve as the first acceleration stage. Its main components are: (i) ion sources that provide primary stable ion beams from p to ^{238}U. (ii) :inear accelerator UNILAC (UNIversal Linear ACcelerator) up to energy of 11.4 AMeV[95]. (iii) The ring accelerator SIS18 synchrotron where ions can be accelerated up to magnetic rigidity of 18 Tm, *i.e.*, energy of 1.9 AGeV for ^{238}U [96]. The primary beam can then be injected into the storage ring ESR (Experimental Storage Ring) [97], delivered directly to the experimental halls or transported to the fragment separator (FRS), which is also limited to magnetic rigidity of 18 Tm [96]. At the FRS, secondary radioactive-ion beams are produced either from projectile-fragmentation or in-flight fission, and selected using magnetic separation. For HYDRA day-1 experiment a stable beam of ^{12}C will be used, delivered directly from SIS18, with no need of the FRS, to the R^{3}B experimental hall, located in cave C.

At FAIR, the primary beams will be injected from the SIS18 into the SIS100 (maximum magnetic rigidity of 100 Tm) ring accelerator. The accelerated ions will either be used directly for experiments, such as CBM or APPA, or be delivered into the Super-FRS for production of radiactive-ion beams with a maximum magnetic rigidity of 20 Tm. The secondary beams can be transported to NUSTAR experiments including the R^{3}B setup that will be located in a new high energy cave. The Early Science stage at FAIR using SIS18 beams with the Super-FRS is foreseen for 2027, while the first beams from SIS100 at the First Science Stage are expected in 2028.

In 2019 FAIR Phase-0 stage has started, its main objectives are to allow for fore-front research in advance of FAIR by employing detector components developed for FAIR and exploiting the upgraded GSI accelerator facility [98]. The first HYDRA physics proposal has been accepted in 2022 as a FAIR Phase-0 experiment with the following remark made by the GSI-GPAC (General Program Advisory Committee) "*[...] the proposal is very well aligned with the efforts in hypernuclei physics as one of the pillars of the FAIR physics program, taking advantage of the R^{3}B setup and a new dedicated HYDRA TPC prototype recently built.*". The experiment will therefore take place within the phase-0 program and is foreseen for 2025.

3.2. R^{3}B standard setup

The experimental approach of the R^{3}B collaboration involves using high-energy radioactive-ion beams, ranging from few hundred AMeV kinetic energy to about 1 AGeV, depending on the physics case. The physics program is very rich including spectroscopy by quasi-free scattering, fission, shell structure, short range correlations and more, employed using various reactions of the incoming beam with a target nucleus. The strength of the R^{3}B setup is the

[1]It translates in English as: Heavy ion synchrotron

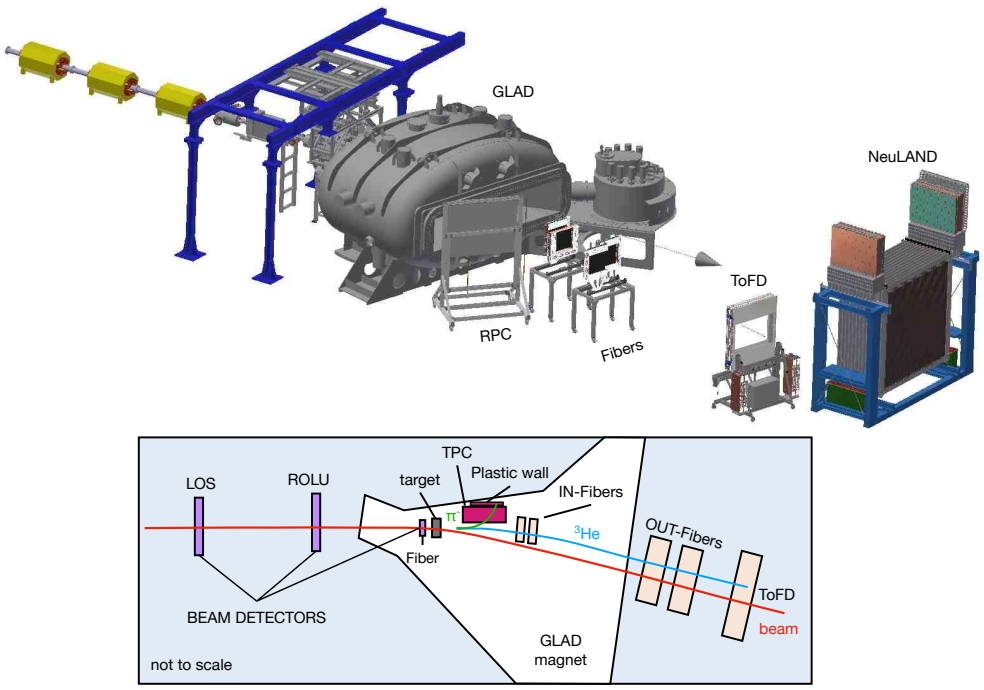

Figure 3.2.: Top. Schematic of the standard R^{3}B setup. Bottom. Schematic of the setup for invariant-mass spectroscopy of hypernuclei. A typical event corresponds to the weak decay of ${}^{3}_{\Lambda}$H into π^- (green) and ^{3}He (blue) after being produced from ^{12}C+^{12}C collisions at 1.9 AGeV is shown, the beam particle is shown in red.

ability to perform kinematically complete measurement of reactions, *i.e.*, detecting all reaction products as well as gamma-rays emitted with velocities close to the beam velocity [99].

The top panel of Fig. 3.2 shows the standard R^{3}B configuration schematically. The incident beam is identified on an event-by-event basis using energy loss and time-of-flight (ToF) measurements, by employing dedicated beam detectors. Similarly, the fragments produced from interactions of the incoming beam with the reaction target are identified. Charged particles are deflected then by the magnetic field (B) of the large-acceptance dipole magnet called GLAD, positioned behind the target, according to their magnetic rigidity, defined as:

$$B\rho = \frac{\gamma m v}{q} \propto \frac{A}{Z}\,, \tag{3.1}$$

where ρ is the trajectory curvature, γ, m, v, q, A and Z are the lorentz factor, the mass, the velocity, the charge, the mass number and the proton number of the particle, respectively. The magnetic rigidity is determined by analyzing position measurements, before and after the magnet that allow to extrapolate the trajectory curvature. Additional energy loss and ToF measurements allow for the identification and momentum determination of the outgoing fragments. For this purpose, various detectors, including a ToF wall, fiber detectors, silicon detectors, and ionization chambers, have been developed. Recoil protons, which have lower magnetic rigidity, and therefore larger bending angles, can be measured in a multi-gap RPC (Resistive Plate Chamber) [100]. The detection of gamma-rays produced by the high-energy beams, is done using the large acceptance CALIFA (CALorimeter for In-Flight detection of

gamma-rays and high energy charged pArticles) detector, a complex array of scintillation crystals surrounding the target area. It serves as a gamma-ray calorimeter and spectrometer, as well as detector for light charged particles. For example, high-energy protons resulting from quasi-free (p,2p) scattering reactions can be measured using CALIFA together with a dedicated tracking system surrounding the target. The main properties of this device are high efficiency and good angular resolution [101]. Finally, a unique feature of the R^3B experimental setup is the possibility to detect neutrons in the energy range from 100 to 1000 MeV, with high ToF resolution and high detection efficiency, by using the NeuLAND (New Large-Area Neutron Detector) neutron detector. The momenta of the detected neutrons are determined based on ToF and position information [102].

For the first HYDRA experiment (S073), the setup will include the detectors to monitor the beam, and to detect the recoil ions (^{3}He) and the π^- from the $^3_\Lambda$H decay (see bottom panel Fig. 3.2), each of them will be described in the following subsections.

3.2.1. Beam detectors

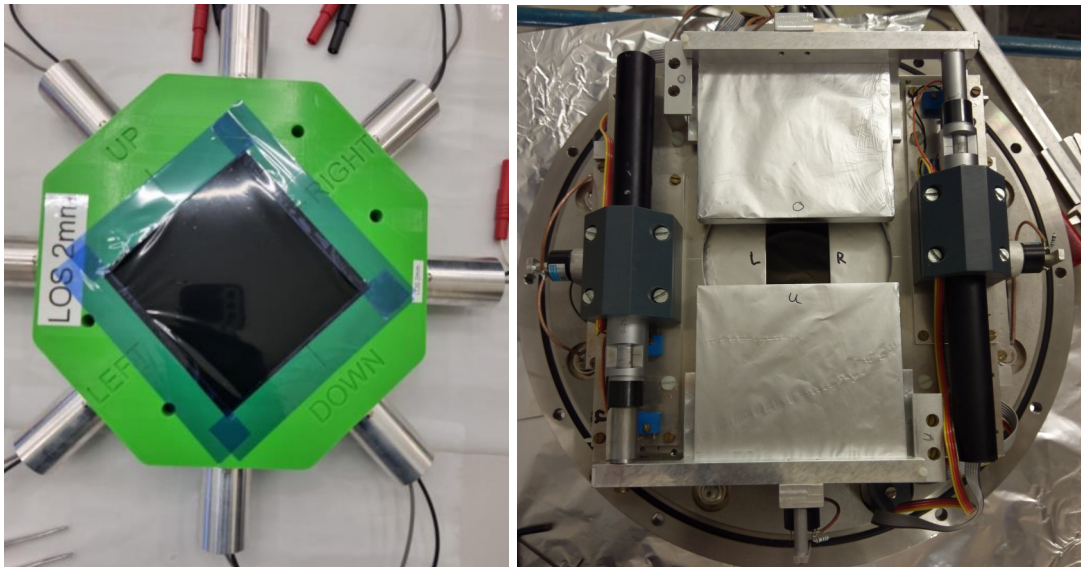

Figure 3.3.: Beam monitor detectors: LOS (left) and ROLU (right).

Beam intensity and beam-timing information will be measured by the start detector LOS. It is made of 8 plastic scintillators EJ204 [103] with a thickness of 2 mm. It has an octagonal shape of 130.4 mm width and height, and an active area of 65 mm in diameter, see left panel Fig. 3.3. The signals are read-out by PMTs (PhotoMultiplier Tube), which are positioned on the back side of the each scintillator. LOS is placed at the beginning of the beam line, and serves as a start detector for ToF measurements. The start time is the average of all 8 time measurements. Moreover, the detector can be used for a position measurement of the incoming ions by utilizing the time difference of opposite PMTs, and for charge identification of the ions by measuring the energy loss in the scintillator.

To verify that the beam is centered/focused a veto detector is used, ROLU (Rechts, Oben, Links, Unten)[2]. It consists of four rectangular scintillators, each read out by a PMT. The four scintillator paddles can be moved and thus adjusting the size of the detector window in the plane perpendicular to the beam axis, see right panel Fig. 3.3.

For beam tracking, a small fiber detector with dimension of 3x3 cm^2 and fiber thickness of 1 mm will be placed 5 cm upstream the target (placed inside GLAD) providing (x, y) position measurement, to ensure that the beam hits the target. It is currently been developed at TU Darmstadt.

3.2.2. Recoil ions detectors

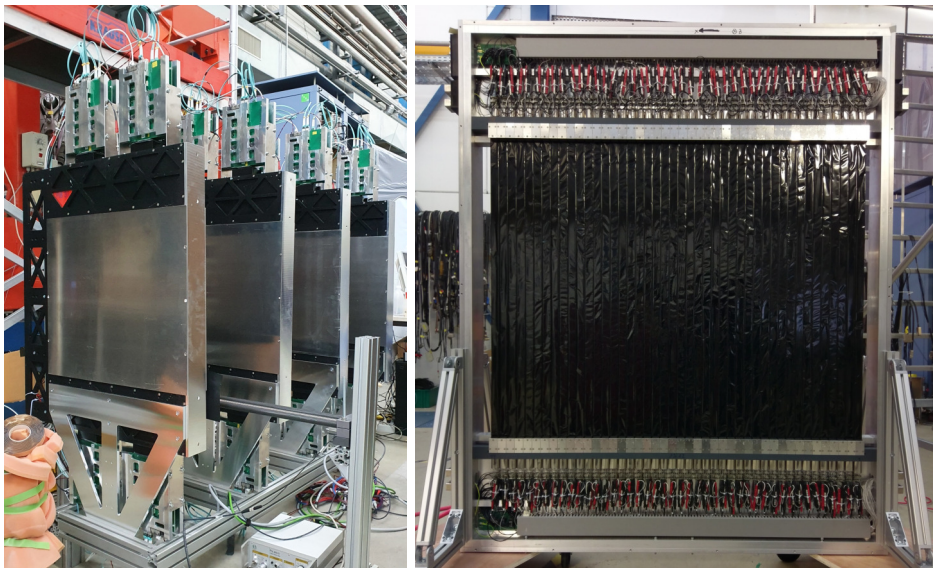

Figure 3.4.: Recoils tracking detectors. Left. The fiber detector planes placed outside GLAD. Right. One plane of the TOFD wall.

The recoil ^{3}He from the decay of $^3_\Lambda$H will be tracked at three different positions: i) inside GLAD downstream the TPC, 4 small-size fiber detectors (13$\times$13 cm^2) with 1-mm-thick fibers and square cross section, will provide two (x, y) positions after the decay. They are currently under development at TU Darmstadt. ii) Just after the magnetic field region, where the particle is not being bent anymore, by utilizing 4 large-area fiber detectors (50$\times$50 cm^2), with 512 1-mm-diameter fibers and square cross section, see left panel of Fig. 3.4. The signal is read-out by Multi-anode PMTs since they are less sensitive against fringe magnetic field of GLAD. These fibers provides two (x, y) positions just after GLAD. iii) The last detector is the ToF wall, named TOFD, placed around 8 m downstream GLAD, which consists of two frames. Each frame has two planes of 44 scintillator paddles with the dimensions 1000 x 27 x 5 mm^3, each of them read-out by PMTs at the two ends, see right panel Fig. 3.4. It is used for energy loss and ToF measurements, allowing for charge identification of fragments, and together with the fibers detectors for mass identification and momentum reconstruction.

[2]It translates to English as: Right, Up, Left, Down.

3.2.3. Target holder

The experiment, as explained in Chapter 2, requires two measurements with two different target thicknesses. Therefore, a rotary target holder has been developed, see Fig. 3.5. It consists of a rotary stage with three possible configurations: 2 different target holders, for the measurements with 1 cm and 6 cm ^{12}C targets and an empty slot for empty target run used for calibration measurements. The rotation of the rotary stage is done with a stepper motor (3200 micro-steps) controlled remotely that transmits the rotation to a planetary gear with a ratio of 1:4.5, allowing a precision in the rotation of 0.44 mrad. The operability of the stepper motor inside the GLAD magnetic field has been simulated using the COMSOL [104] software. It showed that the stepper motor case itself acts as a magnetic shield avoiding any magnetic interference to the stator. To enhance the shielding an additional Bismuth case will be added. Finally, to ensure a light weight most of the components have been 3D-printed.

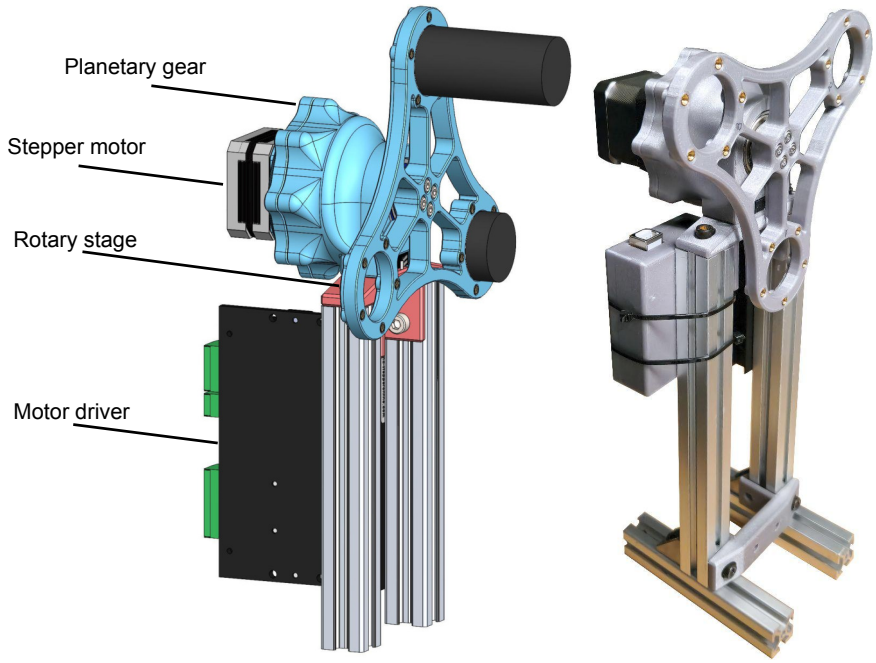

Figure 3.5.: Left. 3D visualization of the target holder. Right. Picture of the target holder. Details are given in the text. Courtesy of A. Enciu, TU Darmstadt.

3.2.4. GLAD magnet

The R^{3}B-GLAD superconducting magnet is a large acceptance dipole (see Fig. 3.6), with a butterfly-shape set of coils. The design includes six superconducting coils: two main coils and four lateral coils provide a magnetic field of up to 2.2 T in the working space. The side coils are optimized to reduce the fringe field, and guarantee a low magnetic field where the detectors have to be placed (20 Tm at 3 m distance). The magnet key features include: i) A large vertical gap that grants an angular acceptance range of $\pm$80 mrad for neutrons; ii) A maximum bending angle of 40° for protons at 1 GeV, ensuring an acceptance close to 100% even for experiments with very different magnetic rigidities of the beam and the fragments; iii) A high field integral of about 5 Tm, which allows a bending angle of 18° for a 15 Tm beam

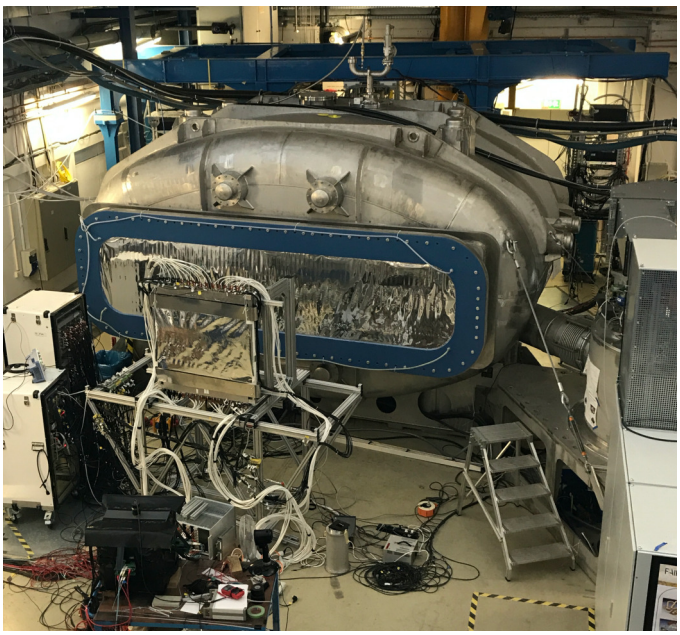

Figure 3.6.: The GLAD magnet dipole inside Cave C at GSI.

(e.g. 1 AGeV ^{132}Sn or 500 AMeV ^{8}He). A momentum resolution $\Delta p/p$ of around 10^{-3} can be achieved by tracking the particles with high resolution. However, the large acceptance of GLAD leads to significant fluctuations of the magnetic field amplitude inside the bore. In the central region of the magnet bore, the vertical component of the field varies by several tens of percents, as illustrated in the left panel of Fig. 3.7, where in a homogeneous magnetic field $\vec{B} = (0,\ B,\ 0)$. Moreover, the magnetic field shows non-vertical components, see right panel of Fig. 3.7. The parallel components of the magnetic field are typically $\pm$(3-10)% of the maximum vertical component inside the magnet bore. These inhomogeneities might conflict with the high resolution (in momentum and position) required for HYDRA to reach the targeted invariant-mass energy resolution of $\sim$2 MeV. Therefore, a laser system has been developed to produce reference tracks inside the TPC which will be used to correct for these effects, see next section.

3.3. Pion tracker

To fully characterize the light hypernuclei decay via the pion emission, it was necessary to add to the standard R^{3}B experimental setup, inside GLAD, a dedicated pion tracker with sufficient acceptance and efficiency for the low rigidity pions. This is achieved by using a Time Projection Chamber (TPC). In addition to the TPC, a plastic wall behind the exit window of the TPC is employed as a start of the drift time measurement and for triggering, see next section.

The TPC is called mini-HYDRA and is a gas-filled detector that provides precise three-dimensional tracking of charged particles and gathering information about their energy loss. While a comprehensive review of a TPC can be found in reference [105], this section summarizes the general working principle and highlights specific features of the mini-HYDRA

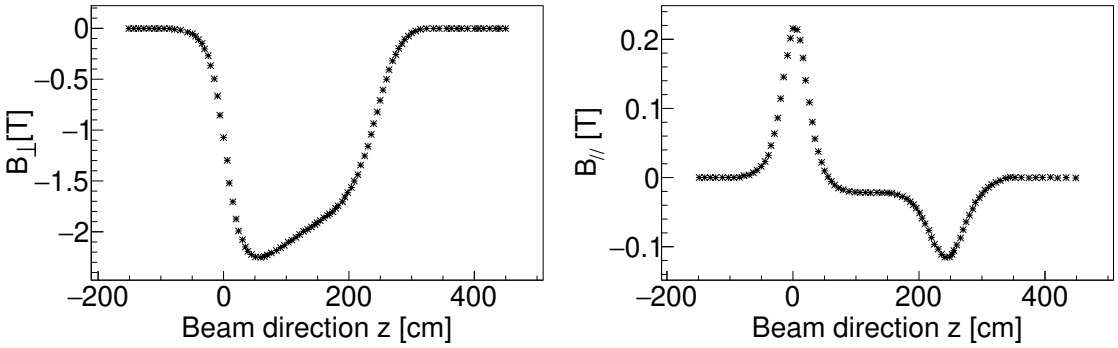

Figure 3.7.: Magnetic field profiles of the GLAD dipole of the R^{3}B setup along the beam direction (z), where z =0 corresponds to the entrance flange. Left. Amplitude of the vertical (main) component. Right. Transverse component along a line traversing the magnet along the z axis through the (x= 0, y= 0) point.

TPC.

3.3.1. TPC- Working principle

The operational principle of a TPC can be schematically described as follows:

- A charged particle traverses the gas-filled volume of the detector, causing ionization along its path by creating pairs of electrons and ions.
- If the ionization occurs in the presence of an electric field ($\mathcal{O}$(100 V/cm)), known as the drift region, which is established by applying different potentials to the ground-Cathode and negative-Anode, and maintained uniform by a field cage[3], the electrons will follow the electric field lines drifting towards the segmented anode (each segment is called pad).
- As the cloud of drifted electrons approaches the anode, it enters the amplification region, where a high electric field ($\mathcal{O}$(40 kV/cm)) amplifies the signal using the avalanche principle.
- The amplified electron cloud induces a current on the pad, which is then pre-amplified, shaped, and converted into a digital signal for transmission to the Data Acquisition system (DAQ).

See Fig. 3.8 for visualizing the working principle of the mini-HYDRA TPC.

Therefore, the pad provides the transverse position (x, z), while the longitudinal one (y) is obtained from the time the electrons need to reach the anode, the so called drift time. Finally, an external magnetic field that bends the trajectory of a charged particle is needed to extract its momentum and charge sign.

[3]A field cage is a set of conductors, e.g. wires, connected to one another through a resistor chain. As a consequence, a linearly decreasing potential is created within which the electrostatic field lines show an overall straight path from anode to cathode in the active volume of the TPC.

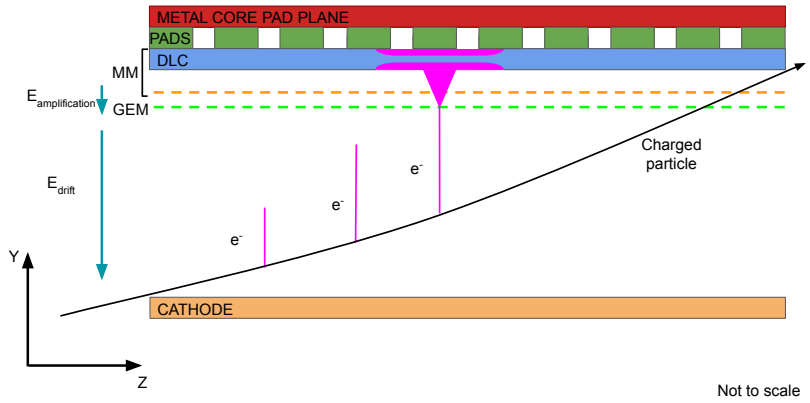

Figure 3.8.: Sketch of the working principle of the mini-HYDRA TPC. Details are given in the text.

3.3.2. The mini-HYDRA TPC

For the first experiment of the HYDRA program (S073) a new TPC, namely the mini-HYDRA, has been constructed. The mini-HYDRA TPC is a prototype of the planned full HYDRA TPC foreseen for FAIR experiments in the future [106] and is about one third of its size. It is meant to demonstrate the proof-of-principle, where all components and technical features foreseen for the full HYDRA are implemented in the prototype and described below, see Fig. 3.9.

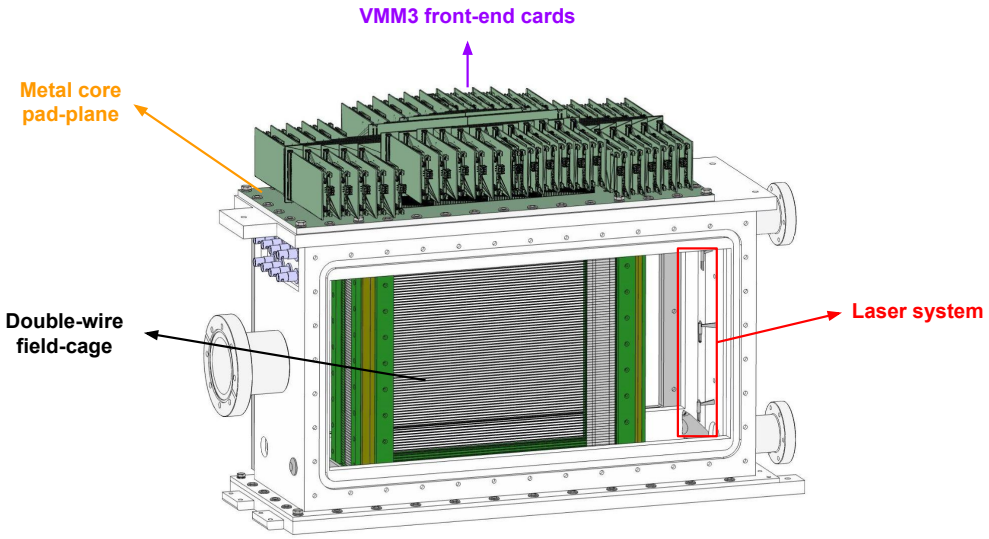

Figure 3.9.: Schematic view of the mini-HYDRA TPC. Details are give in the text.

The main objective of the TPC is to detect π^- from the mesonic decay of hypernuclei after their production from ion beam and fixed target collisions. The trajectories of the pions will be measured, and their momentum will be extracted from the curvature. To

compensate for the low production cross section of hypernuclei, predicted to be few μb [49], the beam will not pass through the TPC but aside (see Fig. 3.2) allowing to use a high intensity beam $\mathcal{O}(10^6$ pps). Since the pions will have to enter inside the detector, in order to reach high momentum and position resolution, the TPC has thin entrance and exit windows to minimize the energy and angular straggling. To further reduce the budget material for the pions entering the active area, the electric field is held homogeneous by two layers of wires, the field cage. The wires have a diameter of 75 μm and they are distributed along the drift direction with a pitch size of 3 mm and the two planes are shifted by half pitch size. Therefore, the area covered by the wires represents only 5% of the total area and adds negligible amount of material for the pions.

The TPC covers an active area of 88 $\times$ 256 mm^2 and has a drift region of 300 mm long. The anode pad plane consists of 5,632 pads, each with a dimension of 2$\times$2 mm^2. Above the drift region, the amplification is done using a Micromegas (MICRO-MEsh GAseous Structure) [107] embedded with a DLC (Diamond-Like-Carbon) resistive layer inside a metal core pad plane (197$\times$497.8 mm^2) [108] combined to a GEM (Gas Electron Amplification) [109] layer, for reducion of the ion back flow[4] (IBF). A signal gain factor of 4k is expected, while the IBF will be considerably reduced compared to a standalone Micromegas mesh. An IBF lower than a 1% will be achieved [110]. The resistive layer of the Micromegas and the combination with a GEM detector will quench the spark rate. The TPC is readout using the high-rate capability VMM3 front-end electronics, integrated with the Scalable Readout System (SRS), that can allow a readout rate as high as 3.6 MHz/channel [111]. A technical review paper of the mini-HYDRA TPC is currently under preparation (*L. Ji et al.*, TU Darmstadt).

The selection of a filling gas is guided by several factors: low operating voltage, high gain, and high rate capability. For a minimum operating voltage, noble gases are favored since they require the lowest electric field (E) for initiating an avalanche process. In addition, noble gases are typically chosen for their negative electron affinities, that translate to low electron attachment (loss of signal due to the formation of negatively charged molecules by absorption of drifting electrons). However, considering for example pure Argon, it cannot operate with gain greater than 10^3-10^4 without continuous discharge occurring. To work at higher gains a quencher is needed. These polyatomic gases, such as methane (CH_4) or isobutane (C_4H_{10}), absorb the radiated photons and then dissipating this energy through dissociation or elastic collisions. A small percentage already produces a significant change allowing to reach gain up to 10^6 [112]. Finally, to increase the drift velocity, a small percentage of CF_4 will have a great impact [113]. Therefore, the gas mixture used for the mini-HYDRA TPC is 96% Argon + 2% CF_4 + 2% C_4H_{10}. For E = 250 V/cm and B = 2 T (the experimental conditions), the calculated drift velocity is 7 cm/μs and the transversal diffusion is 90 μm/cm$^{1/2}$ while the longitudinal diffusion is 125 μm/cm$^{1/2}$. The TPC will be operated at an absolute pressure of 1.1 bar to avoid oxygen and water contamination.

Finally, a laser system is implemented to correct for the inhomogeneities of the GLAD

[4]Ion backflow refers to the migration of positive ions that are generated during the avalanche process, moving from the amplification region towards the drift volume. This can create the so-called space charge effects: the accumulation of charge generates an electric field that could distort the drift field.

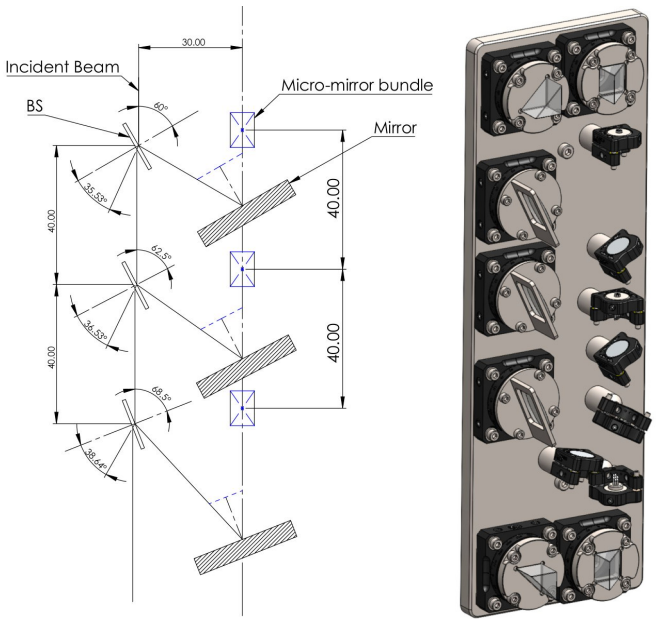

Figure 3.10.: Laser system to correct for GLAD magnetic field inhomogeneities. Left. Sketch of the beam splitter system to produce the reference tracks inside the TPC. 21 horizontal reference laser tracks will be created by the 3 micro-bundle mirrors into the drift volume. Dimensions are given in centimeters and degree. Right. 3D model of the beam splitter. Courtesy of A. Enciu, TU Darmstadt.

magnetic field, which will generate reference tracks inside the TPC allowing for drift velocity calibration and monitoring the TPC performance, see Fig. 3.10. The technique has previously been used in the STAR [114] and ALICE TPCs [115]. The laser (266 nm and 20 Hz) will be introduced from the downstream side of the TPC, going through a quartz window, then reflected by a mirror towards upward. The laser is then segmented by micro-mirror bundles such that 1 mm narrow laser beams are guided into the active region with different angles. Non-reflected laser will be guided out of the TPC and monitored by a CMOS (Complimentary Metal-Oxide Semiconductor) camera with a UV converter. Laser tracks are particularly suited for detectors calibration since they have no multiple scattering and are not sensitive to magnetic fields. Therefore, straight tracks are produced via the two-photon absorption of the chamber gas impurities. The energy of laser light in the visible and near ultraviolet range is considerably lower than the ionization energies of the molecules. This implies that multiple laser photons, usually two or more, are needed to ionize the organic molecules found in the gas within the chamber. The basic process is: a first photon excites the molecule to a usually virtual state with a cross-section σ_1 of the order of 10^{-16} cm^2. This virtual state lives for a time $\tau \sim 10^{-16}$ s. If a second photon arrives during that time, it can ionize the virtual state with a cross-section $\sigma_2 \sim \sigma_1$. However, the regular components of the chamber gas mixture (Ar, CH_4) are not easily ionizable (ionization potential, I_p>11.65 eV) while the impurities, complex organic molecules, have lower ionization potential and represent the main responsible of the photo-ionization by the double photon absorption [116].

In the following sub-section estimation of the pion momentum resolution is performed using an analytical approach, showing the importance of the entrance window to the TPC.

3.3.3. Momentum resolution and multiple scattering

This section demonstrates the importance of the entrance window to the TPC for the pions measurements to ensure a high momentum resolution, which, in the case of the mini-HYDRA TPC, mainly depends on the multiple-scattering (MS) effect. In fact, in addition to inelastic collisions with atomic electrons (*i.e.* ionization - Bethe Bloch), charged particles passing through matter also experience frequent elastic Coulomb scattering from atomic nuclei. This type of scattering leads to a shift of the particle direction without causing a substantial loss of energy. This change in direction caused by MS affects the accuracy of momentum measurements.

As a particle passes through a material, combination of a very large number of small deflections results in a significant net deviation, see Fig. 3.11. In the simplest model of multiple scattering, large scattering angles are ignored. In this approximation, the distribution of scattering angle θ_{plane} after traveling a distance x through a material with radiation length X_0[5] is approximately Gaussian:

$$\frac{dp(\theta_{plane})}{d\theta_{plane}} = \frac{1}{\theta_0\sqrt{2\pi}} \mathrm{e}^{-\frac{\theta_{plane}^2}{2\theta_0^2}} , \tag{3.2}$$

with:

$$\theta_0 = \frac{13.6 \cdot 10^{-3}\,\mathrm{GeV}}{\beta c p}\, z \sqrt{\frac{x}{X_0}} \left[1 + 0.038 \ln\left(\frac{x z^2}{X_0 \beta^2}\right)\right] , \tag{3.3}$$

where p, βc, and z are the momentum, velocity, and charge number of the incident particle. The average scattering angle is $\langle\theta_{plane}\rangle$ =0, but the rms scattering angle is $\langle {\theta_{plane}}^2 \rangle^{1/2} = \theta_0$. Equation 3.3 describes the scattering effect from a single material. In order to get an accurate description of the MS of a particle traversing different layers and materials it is necessary first to find x and X_0 for the combined scatterer [54]. The radiation length for a compound medium is:

$$\frac{1}{X_0} = \sum_i \frac{w_i}{X_{0,i}} , \tag{3.4}$$

where w_i and $X_{0,i}$ are the fractional weight and the radiation length for the ith element.

The TPC measures the projection of the particle trajectory on the pad plane through the detection of the drifted electrons. Therefore, if one considers

$$p = \frac{p_T}{\sin\phi} = p_T\sqrt{1 + \cot^2\phi} , \tag{3.5}$$

where p_T is the transverse momentum and ϕ is the angle formed between the particle trajectory and the drift axis (y). By considering the two quantities independently, the total relative error is:

$$\left(\frac{\sigma_p}{p}\right)^2 = \left(\frac{\sigma_{p_T}}{p_T}\right)^2 + \left(\cot\phi\,\sigma_\phi\right)^2 . \tag{3.6}$$

[5]The radiation length (X_0) is a characteristic of a material and is defined as the mean length (in cm) in the material at which the energy of an electron is reduced by the factor 1/e.

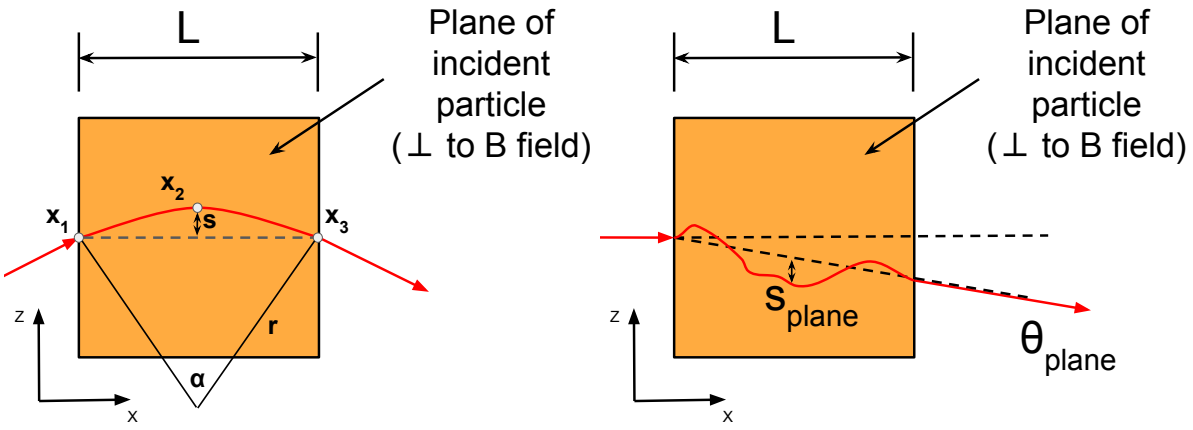

Figure 3.11.: Left. Sagitta (s) representation for a charged particle in a homogeneous magnetic field of length L, details are given in the text. Right. Illustration of the multiple scattering effect on a charged particle passing through a material of thickness L.

The relative uncertainty of the transverse momentum depends on two different contributions: the spatial resolution of the TPC (*TPC*), which is determined by the pad size and the electronics time resolution and the multiple Coulomb scattering (*MS*):

$$\left(\frac{\sigma_{p_T}}{p_T}\right)^2 = \left(\frac{\sigma_{p_T}}{p_T}\right)^2_{TPC} + \left(\frac{\sigma_{p_T}}{p_T}\right)^2_{MS} . \tag{3.7}$$

To measure the momentum of a charged particle a homogeneous magnetic field (**B**=(0, B, 0)) is needed, which will bend the particle trajectory. From the Lorentz and the centripetal force it is possible to extract the transverse momentum assuming a particle with $|q| = 1$:

$$p_T(\text{GeV}/c) = 0.3B\rho\,, \tag{3.8}$$

where ρ is the curvature of the particle trajectory. The expression is valid only if B is expressed in Tesla and ρ in meter. In experimental physics the radius of curvature (ρ) of an accelerated particle is used, along with chord length (L), the sagitta (s) (see left panel Fig. 3.11), the distance from the center of the arc to the center of its base. For small angles ($\alpha \simeq L/\rho$), the sagitta can be expressed as:

$$s = \rho\left(1 - \cos\frac{\alpha}{2}\right) \simeq \rho\frac{\alpha^2}{8} = \frac{0.3BL^2}{8p_T}\,, \tag{3.9}$$

where α is the angle subtended by the chord of the circle at the center. To extrapolate the sagitta are necessary at least 3 position measurements (x_1, x_2, x_3):

$$s = x_2 - \frac{x_1 + x_3}{2}\,, \tag{3.10}$$

with a common uncertainty on the position σ_x. Therefore, the uncertainty on the sagitta is $\sigma_s = \sqrt{3/2}\sigma_x$, which can be used to extrapolate the momentum resolution for three position

measurements:

$$\left(\frac{\sigma_{p_T}}{p_T}\right)_{TPC} = \frac{\sigma_s}{s} = \sqrt{\frac{3}{2}}\sigma_x \frac{8p_T}{0.3BL^2}\,. \tag{3.11}$$

It is possible to see that the momentum resolution degrades linearly with the transverse momentum, increases linearly with increasing B field and quadratically with the geometrical extension of the detector. In the case of N ($\geq$ 10) equidistant measurements, the resolution is [117]:

$$\left(\frac{\sigma_{p_T}}{p_T}\right)_{TPC} = \frac{\sigma_x p_T}{0.3BL^2}\sqrt{\frac{720}{N+4}}\,. \tag{3.12}$$

As discussed above, the MS changes the trajectory of the charged particles and, therefore, limit the momentum resolution. The apparent sagitta due to MS is [54]:

$$s^{rms}_{plane} = \frac{1}{4\sqrt{3}} L\theta_0 = 1.96 \cdot 10^{-3} \frac{zL}{\beta cp}\sqrt{\frac{L}{X_0}}\left[1 + 0.038 \ln\left(\frac{Lz^2}{X_0\beta^2}\right)\right]\,. \tag{3.13}$$

Therefore, the momentum resolution is given by the ratio between the apparent sagitta due to MS and the one according to the bending in B field (Eq. 3.9):

$$\left(\frac{\sigma_{p_T}}{p_T}\right)_{MS} = \frac{s^{rms}_{plane}}{s} = \frac{0.0523\, z}{\beta cB\sqrt{LX_0}}\left[1 + 0.038 \ln\left(\frac{Lz^2}{X_0\beta^2}\right)\right]\,. \tag{3.14}$$

Due to the dependence to $1/\beta$, this term is dominant for low energy particles. Finally, by substituting Eq. 3.12 and Eq. 3.14 into Eq. 3.7, one gets the following expression for the total momentum resolution:

$$\left(\frac{\sigma_{p_T}}{p_T}\right)^2 = \left(\frac{\sigma_x p_T}{0.3BL^2}\sqrt{\frac{720}{N+4}}\right)^2 + \left(\frac{0.0523\, z}{\beta cB\sqrt{LX_0}}\left[1 + 0.038 \ln\left(\frac{Lz^2}{X_0\beta^2}\right)\right]\right)^2\,. \tag{3.15}$$

The pions coming from the ${}^{3}_{\Lambda}$H decay have momentum $200 \leq p \leq 800$ MeV/c, and experience MS by Air (from the decay point to the TPC), the entrance Mylar (BoPET)[6] window, and the TPC gas. An average pion total track length is L_{TOT} =45.132 cm, which is divided into the three regions: length in air L_{AIR} = 25 cm (X_0(Air)=3039 cm), in Mylar front window L_{FW} =0.132 cm (X_0(FW)=28.54 cm), and in TPC L_{TPC} =20 cm (in the active region L_{AR} = 16 cm). Considering the 2 T GLAD magnetic field as homogeneous, a pad resolution σ_x =300 μm, a gas mixture called P10 (X_0(P10)=1282.6 cm), that corresponds to the gas mixture described in the previous section, at 1.1 bar, it is possible to analytically estimate the p_T resolution of the pions, using Eq. 3.15, as a function of p_T, see Fig. 3.12. For 200 MeV/c pions the relative uncertainty due to MS is 0.94%, to be compared with the one passing through the TPC chamber, in 1 cm Aluminum (X_0=8.897 cm) frame 2.36%, *i.e.*, no entrance window.

In conclusion, by letting the pions pass through the Aluminium frame without using an entrance window the transverse momentum resolution will degrade by 251%. The mylar plastic film has been chosen for its useful properties, including: chemical and dimensional stability, electrical insulation, impermeability, and high tensile strength. In particular, the latter allows to manufacture very thin (few tens of μm) sheet but very resistant.

[6]Biaxially Oriented PolyEthylene Terephthalate.

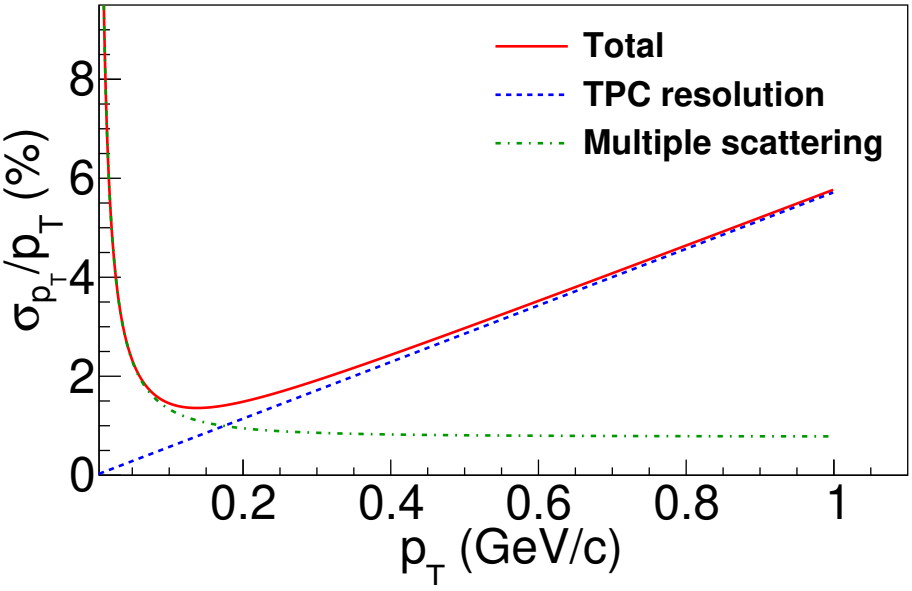

Figure 3.12.: Total transverse pion momentum resolution (solid red line), the TPC resolution component (dashed blue line), and the MS component (dot dashed green line). Details are given in the text.

3.4. Trigger wall

The second detector used to measure pions is the HYDRA plastic wall, a scintillation detector. It serves the dual purpose of triggering the DAQ and initiating the drift time measurements for the TPC. This detector operates based on the property of certain organic materials to emit scintillation light when interacting with particles or radiation. By coupling these materials to an amplifying device like a photomultiplier, the emitted light can be converted into electrical pulses. These pulses are subsequently analyzed and electronically counted to infer information about the incoming particle or radiation. In this section the design, construction and testing of the HYDRA plastic wall to be used in the experiment will be detailed.

3.4.1. Scintillation detector- Working principle

Scintillator materials exhibit a property known as *luminescence*, which involves the emission of photons (such as visible light, UV, or X-rays) after the absorption of a certain form of energy, such as light, heat, or radiation. When this emission occurs shortly after absorption, typically within 10 ns, the process is referred to as *fluorescence*. In contrast, if the emission is delayed, sometimes up to several hours, because the excited state which decays into light emission is metastable, the process is called *phosphorescence*. The time evolution of the emission process ($N(t)$) can be described by a two-component exponential:

$$N(t) = A\, e^{-\frac{t}{\tau_f}} + B\, e^{-\frac{t}{\tau_s}}, \tag{3.16}$$

where τ_s and τ_f are the decay constants for the slow and fast emission, respectively, and *A* and *B* are constants that depend on the material [118].

There are several types of scintillator materials commonly used in various applications: organic crystals, organic liquids, plastics, inorganic crystals, gases, and glasses. In the case of the HYDRA plastic wall, since a fast signal response is required, the best option is the plastic scintillator: it has a fast signal response with a decay constant typically in the range of 2-3 ns. Additionally, plastic scintillators offer a high light output($\gtrsim 10^4$ photons/MeV), enabling efficient detection of scintillation photons and high flexibility, allowing them to be easily shaped into the desired form for specific experimental setups or detector designs [118].

Once the scintillation light is generated, it propagates in all directions within the scintillator material. Along its path, several phenomena can occur, including absorption by the material, internal and external reflection, or escape through the scintillator boundaries. In the case of small detectors, absorption can be neglected, as it depends on the attenuation length[7], typically on the order of 1 m or more. To prevent the light from escaping the scintillator the simplest approach is to redirect the light by internal and/or external reflection. With plastic scintillators, internal reflection can be achieved by polishing the surface of the plastic, turning it into a specular surface that reflects the light at the same angle of incidence. While, the external reflection can be done by wrapping the scintillator with aluminium foil (acting as an external specular surface) and then applying an external light-tight layer of black tape. Additionally, the external layer should be loosely applied in order to have a thin gap of air, which, due to its small refractive index ($n_{\text{air}} = 1.0003$), maximizes internal reflection [118]. Therefore, only a fraction of the total light produced can be collected and converted into an electrical signal for further analysis.

The conversion is done using photomultiplier (PM) devices that are coupled to the scintillator. The PM device serves as an interface between the scintillator and the electronic readout system. These devices, such as photomultiplier tubes (PMTs) or silicon photomultipliers (SiPMs), operate based on the fundamental principle of the photoelectric effect [119], where incident photons liberate electrons from a photosensitive surface. Therefore, it converts the scintillation light emitted by the scintillator into a measurable electrical signal, which can be processed, analyzed, and recorded by the DAQ. For the HYDRA case, the PM device has two main requirements to fulfill: compact design, due to the space limitation inside the GLAD dipole bore, and immunity to the effects of magnetic field. For these reasons the suitable option is the SiPM [120, 121]. It is an array of small avalanche photodiode cells, usually called pixels, each with dimensions of only tens of microns. Ideally, the size of each cell is small enough that the probability of a given cell being hit by a scintillation photon during a scintillation pulse is low, with at most a single photon impacting a cell. In this way, the number of cells fired is then proportional to the number of incident scintillation photons providing energy loss measurements. The output of each cell when operated in Geiger mode[8] is very close to the same amplitude, set by the uniformity of the cells and

[7]The length after which the light intensity is reduced by a factor 1/e.

[8]The applied voltage is above the breakdown threshold voltage (voltage that exceeds the dielectric strength of an insulator that turns into a conductor), and even a single electron–hole pair can trigger a strong avalanche.

the individual quenching resistors that are implemented on the silicon for each cell. Then simply adding their outputs by connecting them in parallel produces an analog pulse whose amplitude is proportional to the number of detected photons.

3.4.2. HYDRA plastic wall

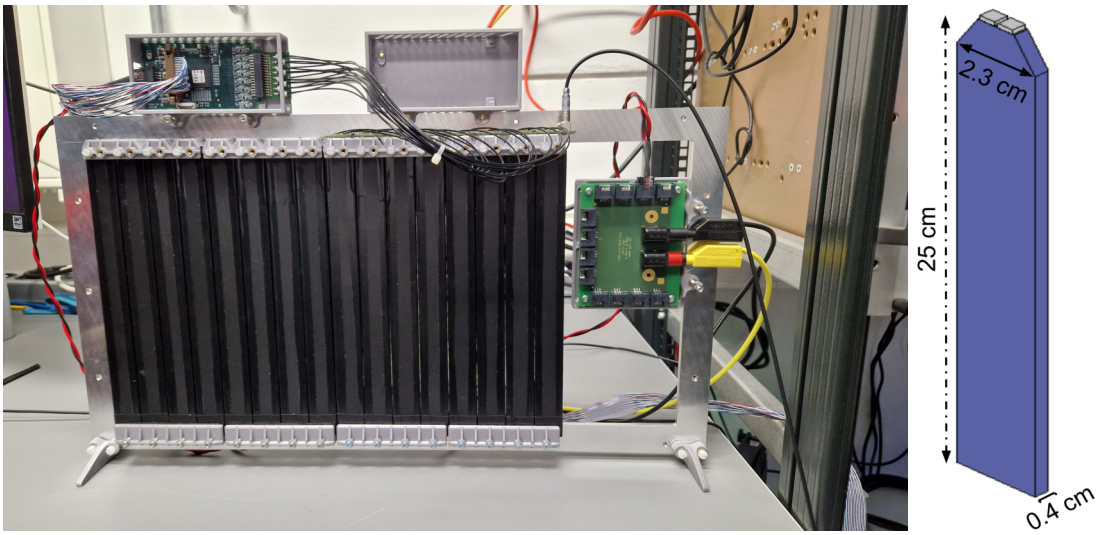

Figure 3.13.: Left. HYDRA plastic wall assembled. Right. Sketch of one detection module, not to scale. The purple bar represents the plastic scintillator and the two grey parallelepipeds on top the SiPMs.

The HYDRA plastic wall (PW) consists of sixteen wrapped EJ-200 [103] plastic scintillator bars (see left panel Fig. 3.13), which dimensions are given on the right panel of Fig. 3.13. This material exhibits useful properties such as fast timing (rise time 0.9 ns), and an emission spectrum that matches the sensitivity of the most commonly used PM devices (wavelength of 400-510 nm), see Fig. 3.14. The thickness of the bars has been chosen based on the energy deposit (E_{dep}) by pions in this material: with 4 mm, the most probable value of E_{dep} is 1 MeV [122], which results in the production of around 10,000 photons within the scintillator. While, the height and width are connected to the size of the exit window of the TPC: 220 mm in height and 400 mm in width. With 16 bars, the total covered width is 400 mm, as the exit window. The width of a plastic bar is 23 mm. Accounting for approximately additional 2 mm for each bar due to wrapping, the maximum width for a bar becomes 25 mm. The wrapping consists of two layers: an inner aluminized Mylar foil for light reflection and an external black vinyl light-tight layer to prevent cross-talk with adjacent bars. In addition, in order to minimize the amount of light coming from external sources, the entire HYDRA PW is also wrapped with black vinyl light-tight layer. The number of bars are tied to the readout electronics (detailed in the next section), which is divided into group of 16 channels. Since each bar necessitates two channels, the total number of channels is 32.

Since the HYDRA plastic wall does not need to provide particle position information, the scintillator signal is exclusively read from the top side, reducing the required number of channels. Each bar features a trapezoidal shape on one side, which functions as a light guide

for photons. Each bar is connected to two Hamamatsu SiPMs (S13360-3050PE [123]) with dimensions of 3×3 mm^2 through optical grease. At a later stage closer to the experiment the connection will be fixed using optical cement. This SiPM couples well with the plastic in terms of wavelength response. In fact, as can be seen in Fig. 3.14 the wavelength range of the scintillator output corresponds to the wavelength of the SiPM's maximum quantum efficiency[9] ($\sim$40%). Finally, to ensure a light weight the supports for the scintillator bars and the front-end electronics have been 3D printed.

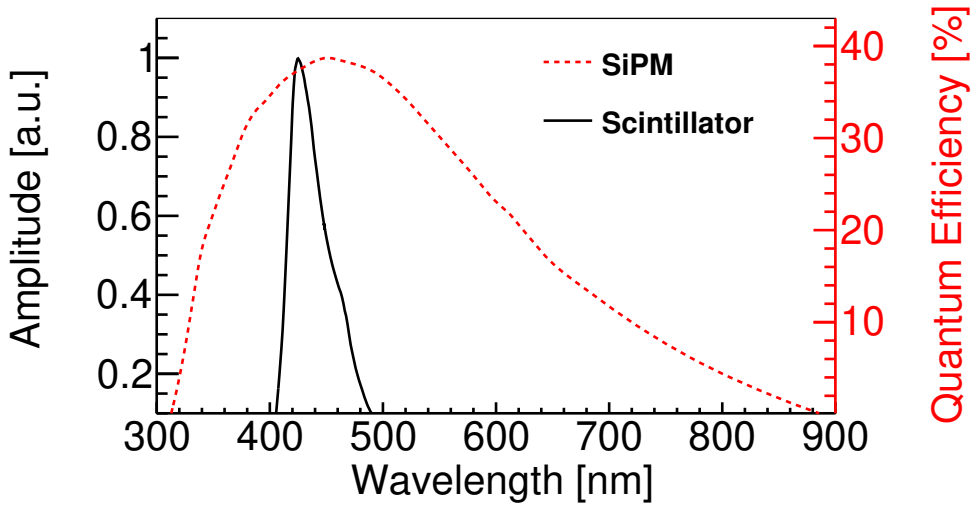

Figure 3.14.: Properties of the EJ-200 plastic scintillator and S13360-3050PE Hamamatsu SiPM as a function of the wavelength. The left black y-axis represents the amplitude of the scintillator light output. The right red y-axis represents the quantum efficiency of the SiPM.

3.4.3. PW electronics

The light produced by a charged particle within a plastic bar is converted to an electrical signal by the SiPM and then sent to the readout electronics, see schematic in Fig. 3.15. The initial phase involves transferring the analog signal from the SiPM to the front-end electronics (FEE). The SiPMs are housed on one face of a PCB (Printed Circuit Board) that has been designed (U. Bonnes, TU Darmstadt) in order to: i) efficiently power all 16 SiPMs through a single LEMO cable, drawing from a 55 V power source, a feasibility owing to the purchased batch's 54.7 ± 0.2 V operational voltage. ii) Using MML cables (microminiature coaxial cable) the signal is extracted from the SiPM and directed to the FEE, the PADIWA3, responsible for converting the analog signal to a logical one, see Fig. 3.15. PADIWA3 [124] is a single card developed at GSI with pre-amplifiers and a FPGA (Field Programmable Gate Arrays) programmed as a discriminator and requires an operational voltage of $+5$ V. With 16 channels on each board, it captures both rising and falling edge signal information. For

[9]The probability to convert incident photons into detectable electrical signals which depends on the wavelength.

establishing connectivity between the 16 SiPM outputs and the FEE, an adapter known as the concentrator board has been developed (U. Bonnes, TU Darmstadt). Once the signal reaches the PADIWA3 board it is pre-amplified and then the discriminator returns a LVDS (Low Voltage Differential Signaling) signal whose leading edge corresponds to the arrival time of the photon and the width to the Time-over-Threshold (ToT) [124]. The LVDS output is subsequently transmitted to the back-end electronics using a 16-way rainbow ribbon cable.

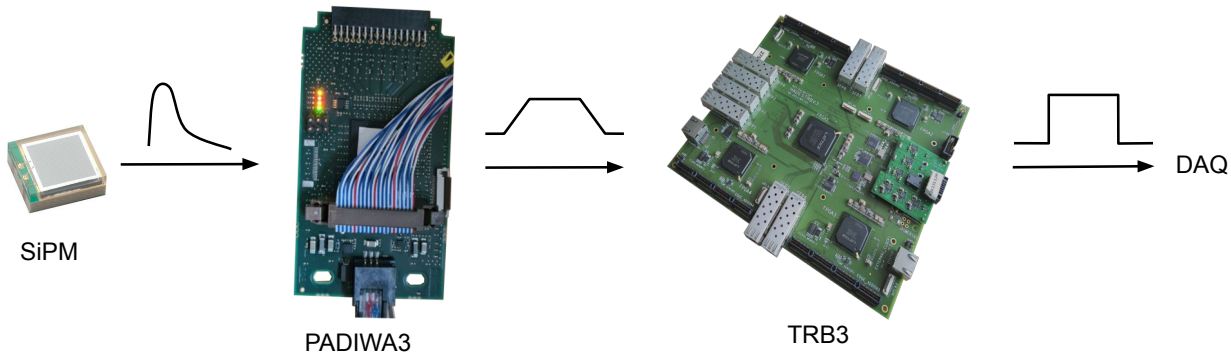

Figure 3.15.: Scheme of the HYDRA plastic wall electronics. The analog signal produced by the SiPM is transmitted to the PADIWA3 for amplification and conversion into an LVDS signal. Subsequently, the signal is directed to the TRB3 electronics, which verifies the fulfillment of trigger conditions. In the event of successful validation, details regarding the rising and falling edge of the signal are encoded into a TTL signal and sent to the DAQ system.

The back-end is the TRB3 [125] (TDC Readout Board) electronics (developed at GSI), see Fig. 3.15. The board has 5 FPGAs, the central one is used for data acquisition, slow control and trigger. While, the 4 peripheral FPGAs are programmed to provide 64 TDC (Time-to-Digital-Converter) channels each and a synchronisation time (total of 260 channels). The TDCs of the TRB3 module are composed of two counters: the coarse counter, incremented at a frequency of 200 MHz within a sub-event, and the fine counter, which initiates upon hit detection and operates within a 5 ns time-frame. The fine counter's step sizes are not fixed. In fact, a TCD calibration needs to be performed to determine their size in order to obtain precise time measurements, see next subsection. The trigger signal for the DAQ from the HYDRA PW is provided when at least in one bar both SiPMs fired simultaneously. Asking for the coincidence between two channels reduces the number of fake triggers due to non-physical events. The data are then sent as a TTL (Transistor–Transistor Logic) signal to a computer via Ethernet cable and are communicated to the DAQ framework DABC (Data Acquisition Backbone Core) [126]. This framework writes the file in the HLD (HADES List mode Data) format that needs to be "unpacked" (converted) to be analyzed. The unpacker used is the object-oriented system Go4 (GSI Object Oriented On-line Off-line system) [126], which is based on ROOT [127] and allows to convert the HLD format into ROOT files.

3.4.4. Test results

The validation of the HYDRA PW has been performed using comprehensive measurements utilizing both a pulser signal and cosmic rays. Additionally, a full test with beam conditions including triggering the mini-HYDRA TPC is scheduled at GSI for the upcoming year (2024). A ^{12}C beam at 1.9 AGeV will be delivered and used to validate the combined operation of the mini-HYDRA TPC and PW, via pion measurements.

The first step necessary in the operation of the PW is a time calibration of the TDCs. It is done using the statistical approach. The internal pulser (30 ns pulse width) of the TRB3 board generates signals randomly distributed across each channel (approximately $\mathcal{O}(10^6)$ hits per channel), constructing a distribution for fine-counter values. The amount of signals in each time step is a direct measure of the width of the corresponding bin [128]. This calibration file is saved and is then used to unpack the experimental data. Figure 3.16 presents the calibration results. The left panel displays the ToT measurements for all 32 channels, featuring a prominent peak at 30 ns, which corresponds to the internal pulser value. The right panel illustrates the ToT distribution for a single channel, where the width has a value of 0.02 ns, which remains constant across all 32 channels.

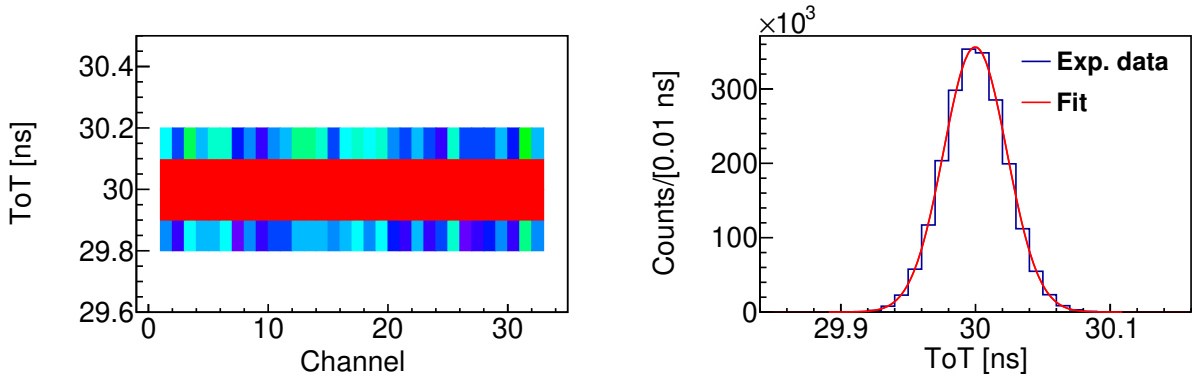

Figure 3.16.: TRB3 TDC calibration results. Left. The ToT distribution measured for the 32 channels. Right. ToT distribution for channel 16, together with a Gaussian fit (red).

In order to measure the internal time precision of the TRB3, for the first test performed with the HYDRA PW electronics, a pulser signal (amplitude of 0.8 V and frequency of 1 kHz) has been used. The signal is split into two, see left panel of Fig. 3.17, and connected to two channels of the PADIWA3 (channel 0 and 6). By fitting a Gaussian function to the histogram obtained by measuring the time difference between the two leading edges of the signals a width of $\sigma_t = 21.8$ ps is found, see right panel of Fig. 3.17. By assuming that both channels have the same contribution to the measured time precision, for a single channel the time precision is:

$$\sigma_{\Delta t} = \frac{\sigma_t}{\sqrt{2}} = 15.4\,\text{ps}\,, \tag{3.17}$$

in agreement with the designed value [129]. Value obtained with FPGA temperature around 45 °C. The temperature is key for the electronics, since it has been observed that the time

precision of the FPGA-TDC in the FPGAs degrades dramatically (up to 200 ps r.m.s.) if the FPGA temperature decreases below roughly 30 °C [130]. Therefore, to keep a constant behaviour of the electronics is necessary to avoid active cooling.

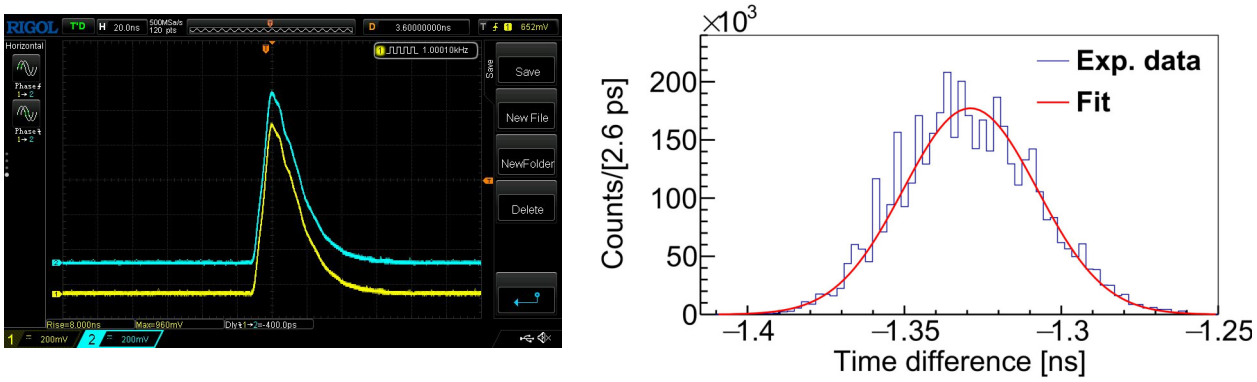

Figure 3.17.: Result from the pulser test. Left. Oscilloscope visualization of the pulser signal splitted into two identical signals, the baseline has been shifted to visualize them simultaneously. Right. Time difference distribution of two channels connected to the PADIWA3, together with a Gaussian fit (red).

The information available for each channel is the rising and falling edge of the signal from which the ToT can be determined as the time difference between these two values. The ToT measurement serves to estimate the energy deposition of the particle in the scintillation material. The second test has been performed by recording data with cosmic rays over a time-window of one day. The aim was to identify and measure cosmic muons, which are minimum ionizing particles and therefore have a constant energy deposition in the plastic material of 2 MeV cm^2 g^{-1} [131], and to ensure a uniform response of all channels. The thresholds of all channels were adjusted in order to minimize the contribution from low energetic background and enhance the signal from cosmic muons, where the same offset from the baseline has been applied to all of them. The left panel of Fig. 3.18 shows the hits distribution for each bar using the trigger configuration introduced before. The distribution is rather constant, as expected from cosmic muons, that hit the different bars uniformly. It is possible to notice how the bars have a maximum variation from the mean hits value of $\pm$10%. The middle and right panels of Fig. 3.18, show the ToT for each channel and for the two channels of a specific bar, *i.e.*, the two SiPMs respectively. It exhibits a distinct peak at approximately 8.5 ns across all channels, attributed to cosmic muons. In particular from the right panel it is possible to see that the response of the SiPMs is equivalent. However, slight variations are noticeable. These differences may arise from the uniform voltage applied to all SiPMs, resulting in minor disparities in gain. Additionally, the adoption of a common offset value for all channels can contribute to these deviations. Finally, the distribution presents a tail, due to: i) hit position of the light along the bar (which cannot be measured with the PW configuration), where the photons travel different distances inside the plastic bar and as result have different measured times. ii) Low energetic background cannot be completely suppressed by the threshold applied.

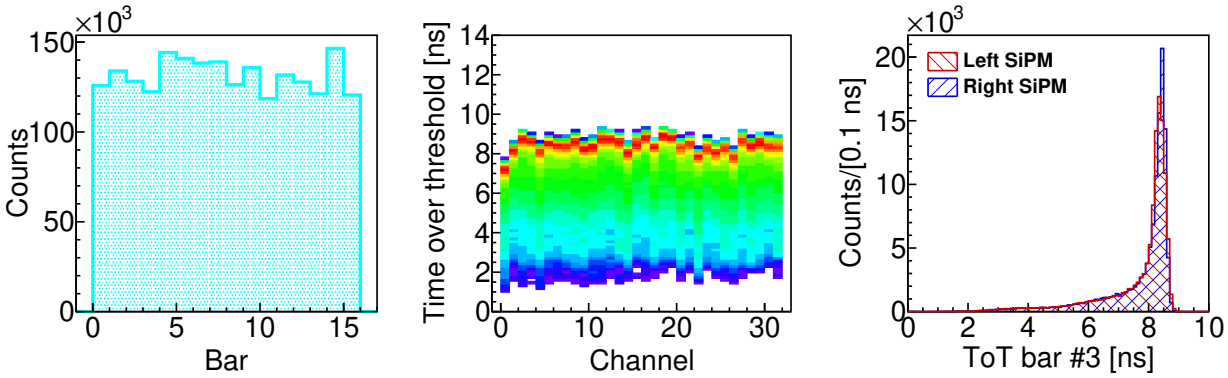

Figure 3.18.: Results from the cosmic ray test. Left. Counts distribution for each bar. Center. Time-of-Threshold (ToT) per channel. Right. Comparison of the ToT of two SiPMs from the same bar.

In conclusion, the HYDRA plastic wall has been tested successfully, and is ready to be used for upcoming experiments at GSI/FAIR.

This Chapter has presented an overview of the accelerator facility GSI/FAIR and outlined the experimental setup that will be used in the forthcoming HYDRA experimental campaign (S073), scheduled to take place in 2025. The initial segment of the Chapter provided a general overview of the different detectors in the R^{3}B setup. While, the main focus of the second part has been dedicated to provide information about the specific detectors that will be used to reconstruct the invariant mass spectrum of the ${}^{3}_{\Lambda}$H by the detection of the π^-, using the mini-HYDRA TPC and the HYDRA plastic wall, and the ^{3}He by using fibers detectors inside and outside the GLAD dipole magnet, and the TOFD wall.

4. Simulation

This Chapter highlights the realistic simulation developed both to assess the feasibility and to optimize the first HYDRA experiment. The simulation was implemented in the R3BROOT [132] framework, a modular software package developed at GSI. R3BROOT serves as a versatile tool for conducting simulations and analyzing data from R^3B experiments. Its core features are inherited from the FairRoot [133] framework, and it adds on top the R^3B setup geometries, detectors response, and calibration procedures. Both of these frameworks are built upon ROOT [127] for data storage and analysis, while GEANT4 [134] software is the transport engine of the simulation. The simulation package includes the GLAD magnet and standard R^3B detectors. To account for the non-uniformity of the GLAD magnetic field used in the simulation, a field map is incorporated into R3BROOT calculated for the maximum field strength. To include the pion tracker, the HYDRA simulation package (called *glad-tpc*) has been developed, described through this Chapter and is available on Github [135].

4.1. Event generators

The core of the simulation process lies in a realistic event generator that provides the input data for the simulation. With the aim of maximizing the detection efficiency of the experimental setup and enhancing the signal arising from the hypernucleus of interest, while rejecting background contributions, a comprehensive exploration of three distinct scenarios was conducted: i) ${}^{3}_{\Lambda}$H as well as ${}^{4}_{\Lambda}$H decay events were examined to enhance the geometrical acceptance of the experiment. The main measurement channel for the experiment S073 is the ${}^{3}_{\Lambda}$H decay, hence, the main efforts have been directed into optimizing its detection. Additionally, the ${}^{4}_{\Lambda}$H will be reconstructed through its two-body decay channel (${}^{4}_{\Lambda}\mathrm{H} \rightarrow \pi^{-}+{}^{4}\mathrm{He}$) as a benchmark for the experimental method introduced in the second Chapter, since the ${}^{4}_{\Lambda}$H is not expected to exhibit halo-like characteristics (B_{Λ}=2.169$\pm$0.042 MeV [71]). ii) Fragmentation events from ^{12}C+^{12}C collisions were studied to evaluate the expected trigger rate in the experiment, the occurrence of ion back flow within the TPC, and to estimate potential background contributions. The beam characteristics considered in all simulations are according to typical ^{12}C beam profile that can be delivered from SIS18 to Cave C, with a full width half maximum of 4 mm in the transverse direction. iii) An analysis of the combined occurrence of both cases was performed to assess the signal-to-background ratio. In the event generator several strangeness channels including, hypernuclei, free-Λ and K^0_S were generated alongside other fragments, following the procedure outlined in case (ii), based on their production cross-section. Subsequently, the decay of the hypernuclei was simulated, following the method described in case (i), where finally the decay products are used as an input for the GEANT4 simulation.

4.1.1. Hypernuclei production and decay

In order to enhance the geometrical acceptance of the experimental setup for detecting the unique signal signature involving a coincident π^- and ^{3,4}He originating from the ${}^{3,4}_{\Lambda}$H decay, it is essential to use a dedicated event generator. It employs the ROOT class *TGenPhaseSpace* [136], incorporating initial inputs such as angular spread and kinetic energy distributions of the ${}^{3,4}_{\Lambda}$H produced in ^{12}C+^{12}C collisions at 1.9 AGeV. These inputs are derived from the Dubna intra-nuclear Cascade Model (DCM) coupled with Fermi Break-up de-excitation Model (FBM) [49].

The DCM is particularly suitable for describing elementary collisions involving relatively light nuclei (A<16) at SIS18 energies. It incorporates a wide spectrum of baryonic species (up to 70), including all the essential conservation laws inherent in the elementary binary interactions of hadrons. This encompasses both scattering and the production of new particles including hypernuclei [137]. As described in Sec. 1.4.1, the hypernuclei are formed when the produced hyperons are captured by neighboring nucleons or residual fragments.

The FBM is used to describe the de-excitation of the formed hot hyperresidues. It assumes that the excited hypernucleus breakups simultaneously into cold and slightly excited fragments, which have a lifetime longer than the breakup time ($\sim$100 fm/c). It includes all possible breakup channels, which satisfy the mass number, strangeness number, charge, and energy and momentum conservations, and the competition between these channels [138].

Based on these models the ${}^{3}_{\Lambda}$H (${}^{4}_{\Lambda}$H) is produced with kinetic energy that is Gaussian distributed around 1.55 AGeV (1.58 AGeV) with a width of 0.134 AGeV (0.112 AGeV), see right panel of Fig. 4.10. The primary production vertex of the hypernuclei in z-direction is uniformly distributed within the target length (6 cm). The lifetime assigned to the ${}^{3}_{\Lambda}$H is τ=237 ps [71], while that for the ${}^{4}_{\Lambda}$H is 208 ps [71]. After the production it propagates according to its velocity and after a time t at the secondary vertex it decays into π^-+^{3}He (π^-+^{4}He) modeled by a phase-space decay. Due to difference in mass, the typical momentum of ^{3}He is $\sim$7 GeV/c, while that of the π^- is $\sim$500 MeV/c. Finally, the momentum and position vectors of the charged particles are used as the initial conditions for the GEANT4 simulation. Through this methodology, a substantial sample of 10,000 decay events were generated, resulting in a statistically meaningful sample. Figure 4.1 visualizes 50 ${}^{3}_{\Lambda}$H decay events within the GLAD magnet.

4.1.2. Fragmentation

The fragmentation event generator utilizes the Liège intra-nuclear cascade model (INCL++) [86] and the ablation stage model (ABLA07) [139] to generate the reactions inside the target that do not lead to the production of hypernuclei.

INCL++ is a Monte-Carlo event generator for nuclear reactions induced by nucleons, pions or light ions on any nucleus with mass numbers between 4 and 250. The reactions follow a sequence where high-energy projectiles initiate a series of binary collisions within

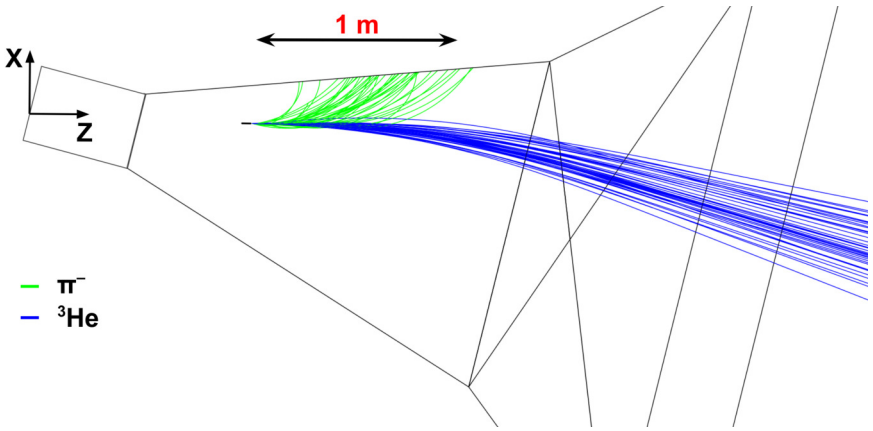

Figure 4.1.: Cut view of the GLAD magnet inner xz-plane. The trajectories represent the daughter particles arising from 50 generated ${}^{3}_{\Lambda}$H decay events. π^- are shown in green, while ^{3}He in blue.

the target nucleus. Each particle, including nucleons and pions, is tracked individually and assumed to move within a spherical calculated volume. The particle-particle interaction is then computed with the individual momenta, and Pauli blocking is tested. After this, the process allows for the emission of nucleons, pions and light clusters. The light clusters, in particular, are formed when nucleons at the surface coalesce with other nucleons close in phase space.

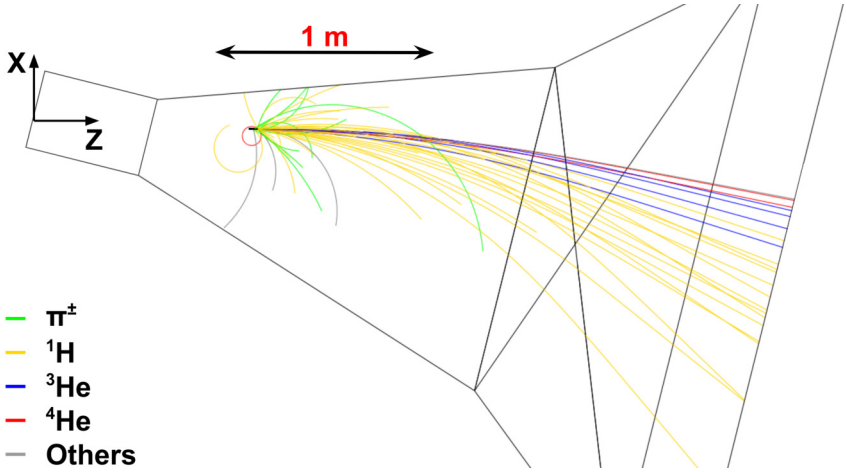

Figure 4.2.: Cut view of the GLAD magnet inner xz-plane. The trajectories represent the fragments coming from 5 ^{12}C+^{12}C at 1.9 AGeV generated events. Only the charged particles are shown. $\pi^{\pm}$ are shown in green, protons in yellow, ^{3}He in blue, ^{4}He in red, and other charged particles in grey.

At the end of the intranuclear-cascade stage, the nucleus has yet to evacuate some of its excitation energy. To de-excite the nucleus the ABLA07 model is used. It is a dynamic code designed to depict the de-excitation process of a thermalized system through a combination of simultaneous breakup, particle emission, and fission. This model has been widely used and compared with experimental data, and in particular reproduces GSI and RIKEN (RIkagaku

KENkyūsho)[1] experimental data relatively well [140].

The reaction considered is ^{12}C beam at 1.9 AGeV with a beam intensity of 10^6 pps impinging on a 6 cm ^{12}C target. Figure 4.2 shows the light charged particles produced by 5 of these collisions.

4.2. Setup optimization

The optimization of the experimental setup was approached in two ways. For the existing R^{3}B detectors, such as the fibers outside GLAD and TOFD, adjustments were made to their positions to maximize geometrical acceptance for the intended experiment. On the other hand, for the new detectors that were not yet built, such as the fibers within GLAD, the HYDRA PW, and the mini-HYDRA TPC, the focus was on simultaneous optimization of their sizes and positions. This was therefore an essential step in the design phase of these detectors.

The total efficiency (ε_{tot}) is defined as the product between two efficiencies: i) the total pion detection efficiency (ε_π), see Fig. 4.3, which is in turn the product of three efficiencies:

$$\varepsilon_\pi = \varepsilon_1 \times \varepsilon_2 \times \varepsilon_3 \,, \tag{4.1}$$

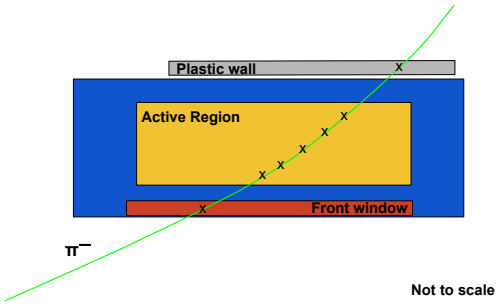

Figure 4.3.: Schematic view of ε_π.

where ε_1 is the fraction of pions that pass through the front window of the TPC, ε_2 the fraction with track length inside the active region > 1 cm (at least 5 pads fire), and ε_3 the fraction that hit the plastic wall with an E_{dep} > 0.5 MeV (see next section). Each fraction is calculated with respect to the total number of simulated pions. In this way it is possible to maximize the number of pions that can be reconstructed with low relative-momentum uncertainty. ii) The total recoil efficiency ($\varepsilon_{\mathrm{He}}$), which is the product of two efficiencies:

$$\varepsilon_{\mathrm{He}} = \varepsilon_I \times \varepsilon_{II} \,, \tag{4.2}$$

where ε_I is the fraction of ^{3,4}He that pass through all the fiber detectors (inside and outside GLAD), and ε_{II} the fraction that hit TOFD with an E_{dep} >2.5 MeV with the exclusion of 12 bars (see next section). Each fraction is calculated respect to the total number of simulated ^{3,4}He.

4.2.1. Pion detectors

The initial focus of the setup optimization was on the central detector, the mini-HYDRA TPC, for detecting the pions from the weak decay of the hypernuclei (similar results are obtained for $^{3,4}_{\Lambda}$H) and the position of the HYDRA PW. Following that, optimization efforts were extended to find the proper targets position.

[1] It translates to English as: Institute of Physical and Chemical Research.

Mini-HYDRA TPC

The GLAD magnetic field has its main component along the y-axis directed into the page and it bends the negative charged particles towards positive x-direction following the beam direction along the z-axis. Therefore, to detect the π^- the TPC has to be located in the orange region shown in the left panel of Fig. 4.4, in order to avoid that the beam goes through the TPC (see Chapter 3). The analysis of particles' momentum relies on assessing its curvature in the magnetic field. Equation 3.11 demonstrates that the relative uncertainty in p_T momentum diminishes in direct proportion to the magnetic field's strength. Consequently, the ideal placement for the mini-HYDRA TPC is as near as feasible to the GLAD entrance flange (point O in the left panel of Fig. 4.4) where the magnetic field is the strongest. However, this is the region where the spatial width available is limited, see right panel of Fig. 4.4. To reach a compromise between the available space and high magnetic field strength, the settled positioning for the TPC is 1.4 m downstream the entrance flange. This choice allows for a chamber size of 20×36×54 cm^3 and an active region of 9×30×26 cm^3. The limitation on the TPC length is mainly related to budget constraints (to limit the amount of electronics channels). Hence, for the active region it was decided to cover the corresponding length of 2 times the free-Λ half-life[2], *i.e.*, ∼26 cm.

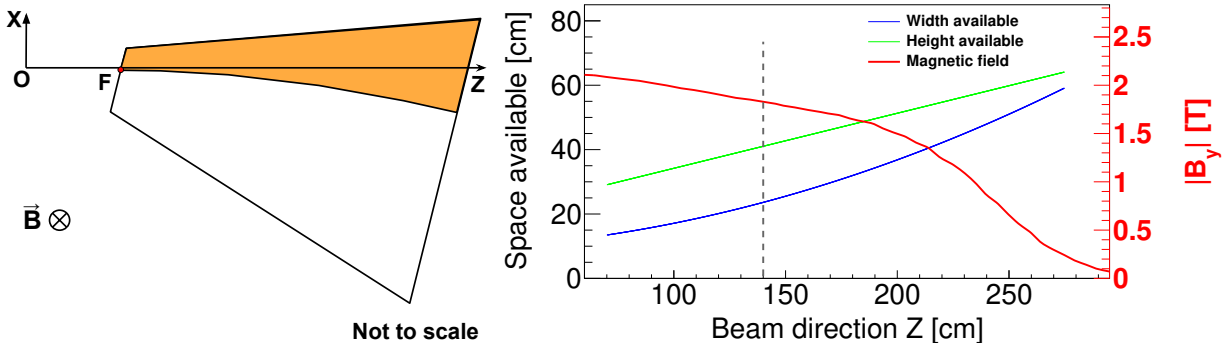

Figure 4.4.: Spatial overview of mini-HYDRA TPC placement in GLAD. Left. Cross-sectional slice through the GLAD inner xz-plane, featuring its reference system with origin at O(0,0,0), the entrance flange. The point F(-0.5,0,71) [cm] represents the first point of the beam trajectory inside the inner part of GLAD where the TPC can be allocated. The delineated orange region marks the permissible allocation space for the mini-HYDRA TPC. Right. The left black y-axis represents the available space, starting from point F along the z-direction. The green curve represents height, while the blue curve signifies width, and the grey dashed line represents the chosen position of the TPC side. The right red y-axis and curve denote the magnitude of the y magnetic field component.

[2]Half-life ($t_{1/2}$) is the interval of time required for one-half of the sample to decay: $t_{1/2} = \tau \ln(2)$. In order to convert it to the corresponding decay length the following relation is used: $L_{1/2} = c\gamma\beta t_{1/2}$.

HYDRA PW

The dimensions of the HYDRA PW are given in Sec. 3.4.2. Concerning its placement, the goal was to maximize the collection of pions fulfilling conditions outlined in Eq. 4.1. To determine its optimal positioning, since it has to be attached to the back side of the mini-HYDRA TPC, a plane with dimensions matching this side was employed. As depicted in Fig. 4.5, centering the plastic wall (red box) approximately 1.74 m downstream the entrance flange allows for a collection of 99.6% of pions that satisfy the previous conditions, *i.e.*, passing through the front window and fire at least 5 pads. It is important to note that this position also reduces the impact of charged particles produced in the target by fragmentation that reach the HYDRA PW, thereby decreasing the experimental trigger rate.

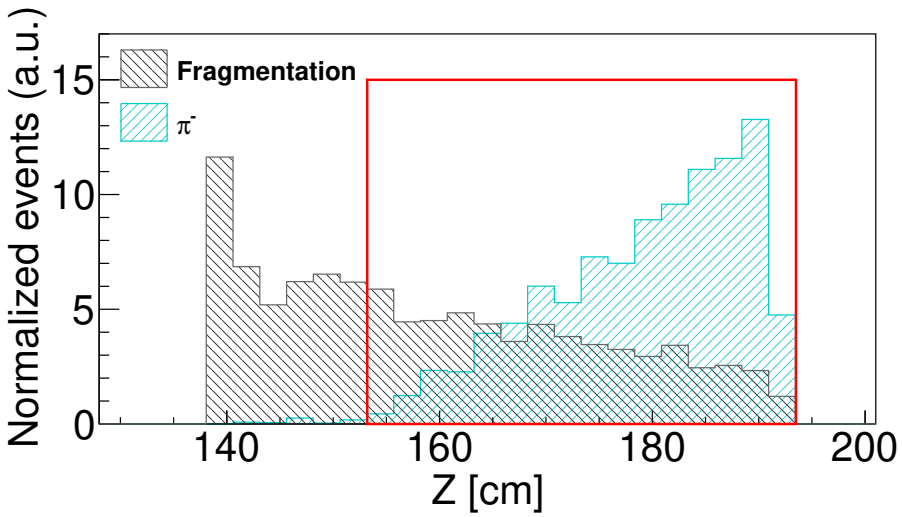

Figure 4.5.: Comparison between fragments (grey) reaching the back side of the mini-HYDRA TPC and pions (cyan) coming from the ${}^{3}_{\Lambda}$H decay passing through the front window and the active region for more than 1 cm, and satisfying the trigger conditions. The distributions are normalized to the same value. The red box represents the chosen HYDRA PW position.

Target

The hypernuclear decay occurs within a relatively short distance, typically spanning tens of centimeters in the laboratory frame. Consequently, the placement of the target cannot be too far away from the active region of the mini-HYDRA TPC. To determine the optimal target position, a study was conducted by systematically varying the target position in steps of 10 cm starting from the F point defined above while the position of the TPC and the PW are fixed. The results, depicted in the left panel of Fig. 4.6, reveal that the highest geometrical detection efficiency for pions (ε_π) is achieved when the target is situated approximately 1.31 m downstream the entrance flange.

Another important aspect to consider is the uniformity of efficiency across different decay vertex positions, extending from the exit of the target to one $t_{1/2}$. This minimizes the

impact of geometrical effects on the measurements. By comparing efficiency distributions for various target positions, it was found that the only configuration exhibiting a nearly uniform efficiency around 33% is for target position of 1.31 m downstream the entrance flange, illustrated in the right panel of Fig. 4.6.

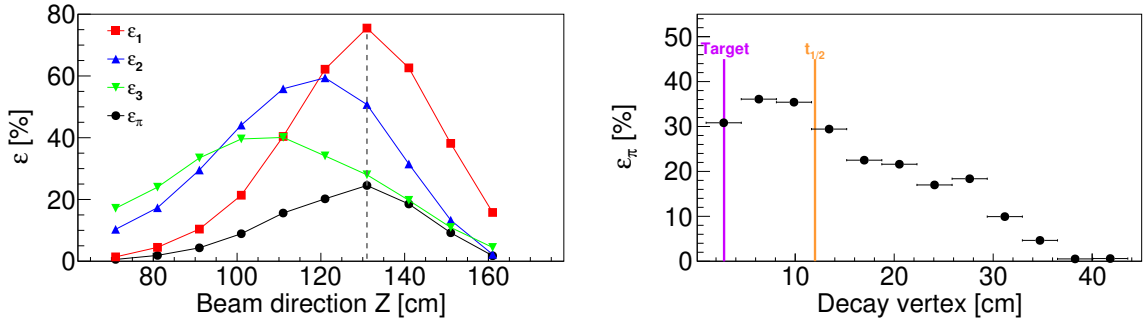

Figure 4.6.: Left: Total pion detection efficiency ε_π (black) as a function of the target position and its components: ε_1 (red), ε_2 (blue), and ε_3 (green). The grey dashed line represents the chosen target position. Details are given in the text. Right: Total pion detection efficiency as a function of the decay vertex for a fixed target position. The violet line represents the exit of the target (1.34 m downstream the entrance flange) and the orange line represents the distance after one half-life ($t_{1/2}$).

4.2.2. Recoil fragment detectors

The positioning of recoil fragment detectors inside and outside GLAD has been determined to maximize the overall geometrical acceptance for detecting ^{3}He particles originating from the ${}^3_\Lambda$H decay (ε_I), as defined in Eq. 4.2.

The dimensions of the fibers inside GLAD need to fit within the orange region, shown in the left panel of Fig. 4.4. It is crucial that their dimensions do not exceed this area at the negative x-axis side to avoid intersection with the beam, as the high beam intensity would affect the functionality of the fibers. To optimize the collection of more than 90% for both ^{3,4}He particles resulting from the decay processes, a size of 13x13 cm^2 has been selected. It is important to note that the limiting factor in this scenario is the presence of the beam on the negative x-axis side. While it is possible to extend the fiber wall further towards the positive x-axis side, it will have a negligible effect on the ^{3,4}He acceptance (see Fig. 4.8) and would primarily capture fragments from fragmentation events, which is unwanted.

The first inner fiber (X-Y planes) is placed 1.9 m downstream the entrance flange, in this way the amount of pions from the decay hitting the fibers is less than 1%. The second inner fiber (X-Y planes) is placed 20 cm behind the first one, allowing for angular measurement without significant loss in acceptance.

The outer fibers provide the position measurement outside the GLAD magnetic field and, therefore, have been placed 4.7 m downstream the entrance flange with the center

aligned to the center of the inner fibers. Also the TOFD center has been aligned with the other fibers and it is 7.4 m downstream the entrance flange. Figure 4.7 shows the position distribution of the recoils in TOFD with $E_{dep} > 2.5$ MeV (no further conditions), where 85% of the simulated ^{3}He will reach TOFD while from the ^{4}He distribution it is 74%. For the detectors outside GLAD it is not possible to select a region where the beam will not intersect the detectors. Therefore, to prevent cross talk, the bars in TOFD hit by the beam will be switched off, whereas for the fibers outside it should not affect their operation, and only those who cover the beam region will not be used later for the data analysis.

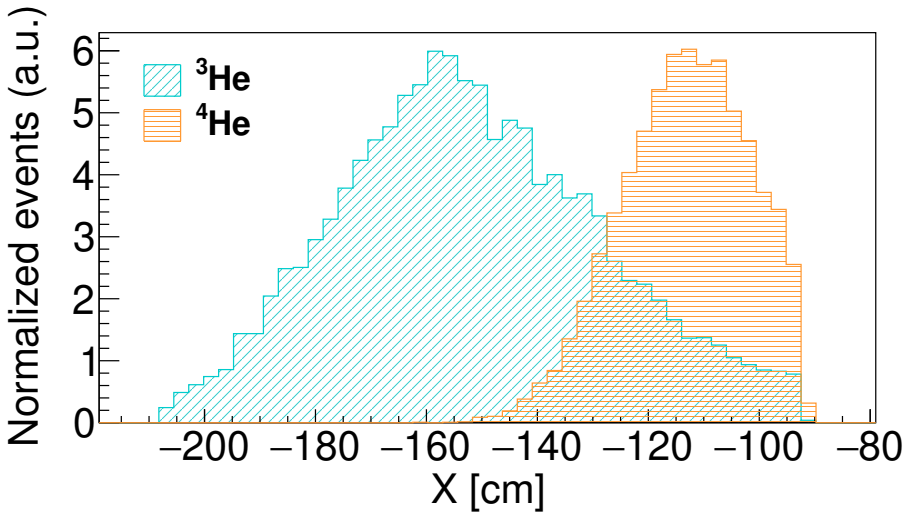

Figure 4.7.: Comparison between ^{3}He (cyan) coming from the ${}^3_\Lambda$H decay and ^{4}He (orange) coming from the ${}^4_\Lambda$H decay reaching TOFD. The distributions are normalized to the have the same maximum.

The final configuration of the detectors discussed in this section together with 25 simulated ${}^3_\Lambda$H decay events is shown in Fig. 4.8. It provides for the ${}^3_\Lambda$H(${}^4_\Lambda$H) a total recoil efficiency $\varepsilon_{\mathrm{He}}$=69%(18%, see next section), total pion efficiency ε_π=25%(31%), and overall detection efficiency of ε_{tot}=17%(6%).

4.3. Background and trigger estimation

Two important parameters requiring precise evaluation are the background and the trigger rate. If the trigger rate becomes excessive for the detectors to handle, it could lead to data loss due to increased dead-time in the electronics. In parallel, the background contribution needs to be suppressed. It leads to unwanted events that are mistakenly reconstructed as signals and potentially obscuring the real ones.

4.3.1. Trigger

To evaluate the trigger rate, the fragmentation event generator described in this Chapter is used, with a beam intensity of 10^6 pps and a 6 cm target. With this configuration it gives a

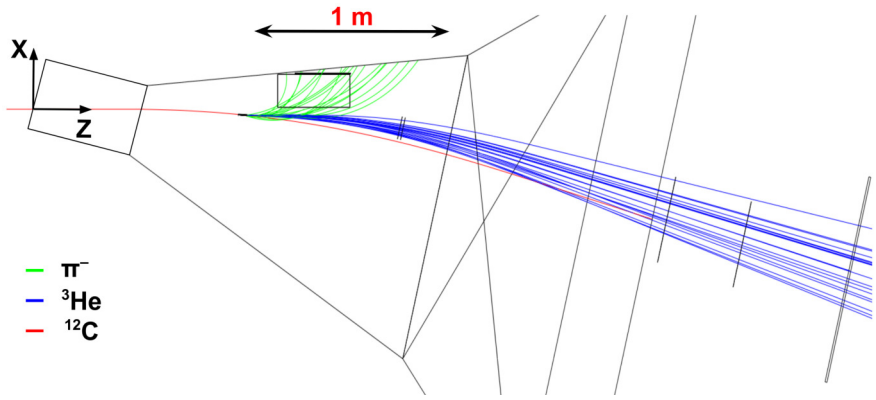

Figure 4.8.: Cut view of the GLAD magnet inner xz-plane. The trajectories represent the daughter particles arising from 25 generated ${}^{3}_{\Lambda}$H decay events. π^- are shown in green, while ^{3}He in blue. All the detectors necessary for the ${}^{3}_{\Lambda}$H reconstruction are shown.

rate of charged particles inside the TPC of 217 kHz, mostly with $|q|=1$ spread over the full active volume of the TPC, resulting in a mean space charge of 40 fC·cm^{-3} (local maximum of 50 fC·cm^{-3}) inside the TPC due to the ion back flow (1%) and considering a gain of 4k. These space charge values are to be compared to the 30-140 fC·cm^{-3} encountered in the ALICE TPC for a 50 kHz interaction rate and a 2k gain [141]. These values will lead to sub-millimetric deviations in the projection of drift electrons onto the pad plane. Therefore, since each pad has an area of 4 mm^2 it can be neglected.

The simulated rate of charged particles reaching the plastic wall at the exit window of the TPC is 102 kHz. Further coincidences with R^{3}B detectors (TOFD for the fragments) leads to a final rate of requested triggers of 30 kHz, limit set by the R^{3}B detectors readout electronics. Finally, by considering a deadtime of the DAQ of 50%, this leads to a rate of $\sim$ 15 kHz that can be handled by the mini-HYDRA TPC, HYDRA PW, fibers and TOFD readouts. From this limitation comes the maximum target thickness and beam intensity used in Sec. 2.4.

The trigger signal is sent to the DAQ when there is a coincidence between at least one bar of the HYDRA PW, which requires a coincidence between the two SiPMs on top, and at least one bar of the TOFD wall, which is given by the coincidence of the PMTs at the two ends. To reduce the trigger signal produced from other particles, a threshold for the energy deposit in the two trigger walls has been considered. As it can be seen from the left panel of Fig. 4.9, the threshold for the π^- coming from the hypertriton decay generator in the HYDRA PW is 0.5 MeV, while, for the ^{3}He in TOFD is 2.5 MeV. In particular the cut on TOFD reduces the trigger rate by 60%. In addition, following the results from the right panel of Fig. 4.9, 10 TOFD bars on the right and 2 on the left are removed from the trigger scheme since they will not trigger decay events. Due to the limited size of the HYDRA PW, it selects a limited region of the decay vertex distribution, as it can be seen from the right panel of Fig. 4.6. This selection is translated into a reduced region in TOFD where the recoils coming from the hypernuclei decay can hit it. Therefore, this reduces the TOFD acceptance for ^{3}He from 85% to 75%, while for the ^{4}He it is much more significant from 74% to 17%. This reduction will not affect the experimental output. The ${}^{4}_{\Lambda}$H production cross section is expected to be almost

twice as higher, 2.9 μb [49], than ${}^{3}_{\Lambda}$H, its ratio decay into two-body branching almost double, 49% [142], and the interaction cross section with the target is lower 645 mb (calculated using Eq. 2.5). Overall, the total amount of statistics that can be collected in 8 days with both targets configurations is still comparable for the two hypernuclei $\sim$4000$\pm$80 (number of reconstructed hypernuclei).

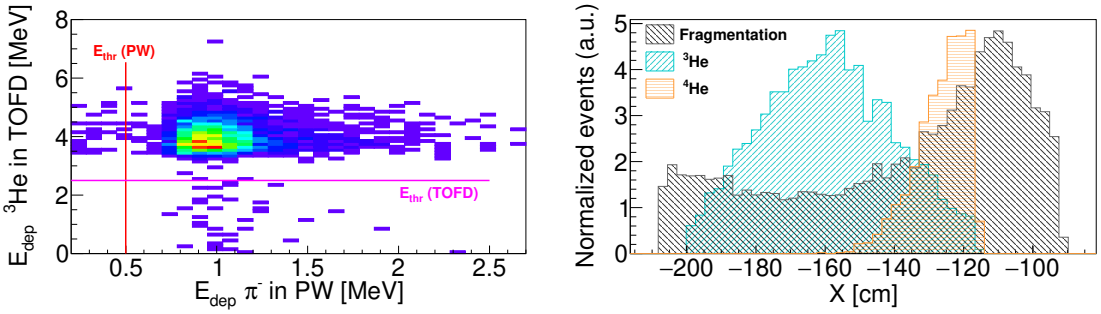

Figure 4.9.: Left. Energy deposit of π^- in the HYDRA PW and ^{3}He in the TOFD wall. The vertical and horizontal lines represent the energy threshold applied to the two detectors. Right. Comparison between fragments (grey), ^{3}He (cyan) coming from the ${}^{3}_{\Lambda}$H decay and ^{4}He (orange) coming from the ${}^{4}_{\Lambda}$H decay events that reach the TOFD and have at least one HYDRA PW bar fired in coincidence. The distributions are normalized to the have the same maximum.

4.3.2. Background

The produced hypertritons are tagged and identified by the invariant mass from their weak decay channel π^-+^{3}He. However, the interaction of the ^{12}C beam with the two ^{12}C targets used for the measurement can produce a π^- and a ^{3}He which do not emerge from the decay of ${}^{3}_{\Lambda}$H, and can therefore lead to the so-called combinatorial background in the invariant-mass spectrum. The possible background contributions are: (1) the coincidence of π^- and ^{3}He both produced from the fragmentation of ^{12}C, (2) the decay of a heavier hypernucleus which decays via pion emission together with a multi-ion final state that includes ^{3}He, and (3) a π^- from the decay of a free Λ, a K^0_S or a heavier hypernucleus and ^{3}He produced in coincidence from the fragmentation of the ^{12}C projectile.

The background from (1) can be mostly removed by selecting the decay vertex position downstream the target [49]. The other two sources of background involve a weak decay, and, therefore, the pion emission is outside the target as in the case of hypertriton decay and it cannot be eliminated via the selection of the vertex position. The background from (2) is quantified assuming a mesonic decay of the heavier hypernucleus, followed by the Fermi breakup of the decayed heavy residue. The relative kinetic energy between π^- and ^{3}He from such background will be always few MeV smaller than 43 MeV, that is the Q-value for the decay of ${}^{3}_{\Lambda}$H and, hence, it is well separated from the region of interest in the invariant-mass spectrum and the effect of background (2) can be considered as negligible.

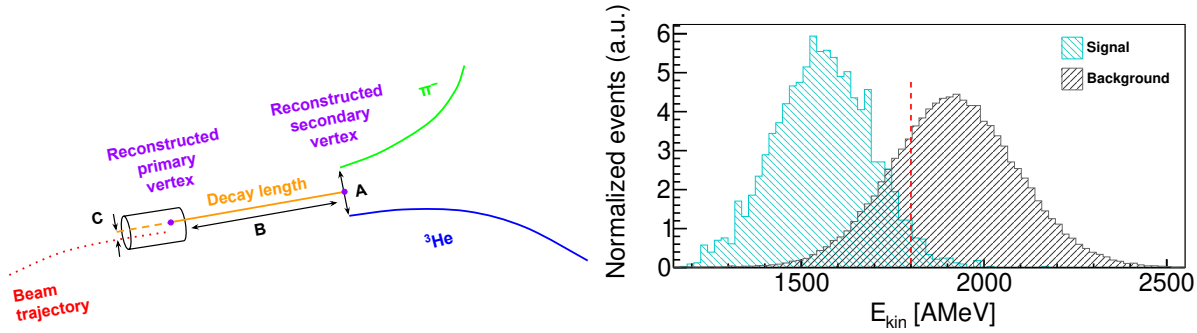

Figure 4.10.: Left. Representation of the ${}^{3}_{\Lambda}$H topological decay variables. Details are given in the text. Right. Comparison between the mixed events background and the simulated ${}^{3}_{\Lambda}$H signal kinetic energy per baryon distribution. The red dashed line represents the selected cut. The distributions are normalized to the same value.

Therefore, the main source of background in the invariant-mass spectrum originates from (3). These background events can be reduced by applying specific topological cuts to the ${}^{3}_{\Lambda}$H decay, see left panel of Fig. 4.10 for their graphical representation. Given that the two daughters emerge from the same secondary vertex, the tracks of the detected decay pion and ^{3}He intersect, with a distance of closest approach (DCA) of less than 5 mm (A<5 mm). To ensure the reconstructed decay vertex belongs to a weak decay, it needs to be located more than 10 mm outside the target (B>10 mm). Similarly, to confirm that the reconstructed hypertriton track originates from the primary interaction beam-target, the DCA between the two trajectories should be less than 5 mm (C<5 mm). Lastly, the kinetic energy of the reconstructed hypertriton should not exceed 1.8 AGeV. The cut on kinetic energy was determined through a comparison of the mixed background events and simulated signal distribution, as shown in the right panel of Fig. 4.10.

Implementing the above cuts yields in a signal-over-background of ∼3, as shown in the simulated spectrum of Fig. 4.11. However, this reduces the statistics of good events by 20%. The primary factors that contribute to the reduction of the background are the topological cuts A and B, which are based on estimation of the vertex reconstruction precision of 5 mm, see next section for the tracking procedure. Yet, to test the sensitivity the values have been varied by a factor of 2, *i.e.*, setting A<10 mm and B>5 mm. The resulted signal-over-background ratio will decrease by a factor of 2.

4.4. Tracking

In the simulation, an invariant-mass resolution of 2 MeV (sigma) based on the momenta of $\pi^- + {}^{3}$He is estimated. Measuring pions in the TPC is challenging and demands a dedicated algorithm for the GLAD magnet's non-uniform magnetic field. Since it forces the electrons to drift under the influence of an additional Lorentz force caused by the non parallel alignment of the magnetic field, and the drift electric field.

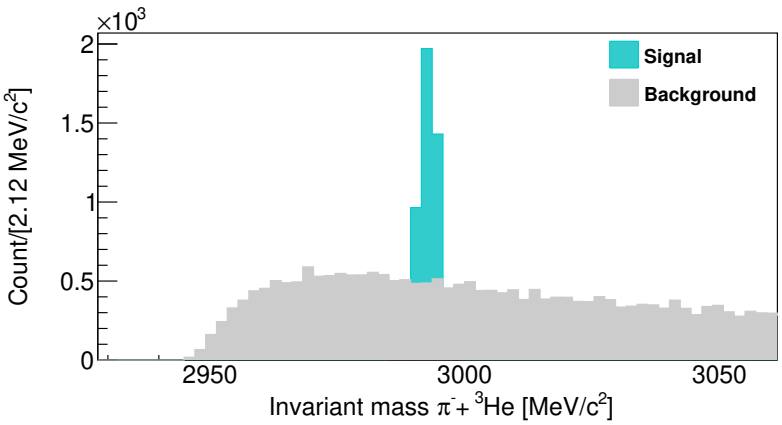

Figure 4.11.: Simulated invariant mass spectrum for 8 days of beam time.

Using the Langevin[3] description of the drift, which takes into account the non-uniform magnetic field, the electrons drift velocity and diffusion are calculated and applied to each electron. The drift parameters are recalculated several times along the drift path according to a configurable length step until they reach the pad plane. A realistic pad plane response is then produced (see next sub-section), recording the number of electrons and their drift time in each pad.

The inverse process, the reconstruction of the real trajectories from the pad plane response, uses again the Langevin equation to calculate the drift parameters. In this case, they are calculated at the end of each step and applied to the starting point to improve the accuracy. The procedure is again performed in steps until the drift time is over, producing a three-dimensional hit pattern reflecting the pad plane information.

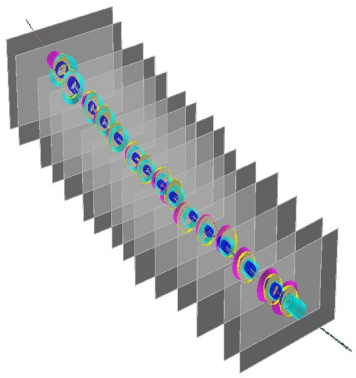

Figure 4.12.: Reconstruction of a π^- track at 800 MeV/c with a homogeneous magnetic field inside the TPC using the GENFIT package. Figure is taken from [143].

The fitting of the individual trajectories involves a pattern recognition algorithm that

[3]The Langevin equation is a stochastic differential equation used to describe the evolution of a system subjected to both deterministic and fluctuating forces.

clusters hit pattern points for each track (see Fig. 4.12) setting initial conditions for the fitting algorithm based on track topology. The Kalman filter [144], commonly used in high-energy physics [145], minimizes the error between measured and estimated state, is well-suited for evolving systems with noisy measurements. GENFIT package [146] provides a complete Kalman filter fitter, accommodating the complex GLAD field map for accurate particle track model propagation and it has been integrated into the HYDRA simulation package. Preliminary results of simulated π^- at 800 MeV/c with a 2 T homogeneous magnetic field, yield around 0.6% momentum resolution, suitable for inferring reaction channel kinematics. In addition, a Runge-Kutta representation of each track can be used to extrapolate the track back to the target position out of the TPC and reconstruct the vertex with an intrinsic resolution of about 2 mm (sigma). While, for the ^{3}He with momentum distributed around 7.1 GeV/c and considering the GLAD magnetic field the relative momentum resolution obtained is <2%. According to these relative momentum resolutions the ${}^3_\Lambda$H invariant-mass resolution is estimated as $\sim$1.7 MeV/c^2(σ) with vertex precision less than 4 mm (sigma). To be conservative a smearing of 2 MeV/c^2 has been applied for the signal distribution in Fig. 4.11.

4.4.1. AGET Electronics response

As presented in sec. 3.3.2 the TPC will be readout using the high-rate capability VMM3 electronics. Yet, for various ongoing test measurements, and validation of the laser system the AGET electronics [147], with limited trigger capability of about 1 kHz, is used. In order to simulate the electronic response realistically, a multi-step process has been implemented following the procedure described in [148]. The first step in the simulation includes generation and tracking of electrons that are produced by gas ionization when charged particles passing through it. The number of these primary electrons is determined by :

$$N_{e^-}^{tot} = \frac{\Delta E}{I}\,, \tag{4.3}$$

where ΔE is the energy deposited at the interaction point and I is the average energy required to create an electron-ion pair ($\sim$30 eV for Ar based mixtures). This number can fluctuate and follows a Gaussian distribution, which is defined by a central value $N_{e^-}^{tot}$ and a deviation:

$$\sigma_{e^-} = \sqrt{F N_{e^-}^{tot}}\,, \tag{4.4}$$

where F is the Fano factor[4] (0.2 for Ar mixture)[149]. Afterwards, these electrons are drifted to the pad plane using the Langevin approach described above. Subsequently, the detector's response is calculated. Within the amplification region, the electrons are multiplied, in a statistical process that is described by the Polya distribution:

$$P_G(G/\bar{G};\theta) = \frac{(\theta+1)^{\theta+1}}{\Gamma(\theta+1)}\left(\frac{G}{\bar{G}}\right)^{\theta} \exp\left(-(\theta+1)\left(\frac{G}{\bar{G}}\right)\right)\,, \tag{4.5}$$

[4]The Fano factor is a measure of the dispersion of a counting process.

where G ($\bar{G}$) is the gain (average gain), Γ is the gamma function and θ is a scale parameter set to 1. The amplified signal is then sampled N times over time (t) using a specific mathematical function:

$$N(t) \propto \sum_{i=1}^{N} G_i \cdot \exp\left(-3\frac{t-t_i}{\tau}\right) \sin\left(\frac{t-t_i}{\tau}\right)\left(\frac{t-t_i}{\tau}\right)^3 , \tag{4.6}$$

where G_i is the gain of the i-th sample, and τ the electronics shaping time taken as 300 ns. To ensure accuracy, white noise is added to each sample. A threshold is applied to the pads, taking into account a signal-to-noise ratio greater than five times the r.m.s. noise value. This ensures the effective detection of signals.

To analyze the signal the following mathematical function is used:

$$f(t) \propto Q_{pad} \cdot \exp\left(-3\frac{t-t_{pad}}{\tau}\right) \sin\left(\frac{t-t_{pad}}{\tau}\right)\left(\frac{t-t_{pad}}{\tau}\right)^3 , \tag{4.7}$$

where Q_{pad} is the total number of electrons collected by the pad, t_{pad} is the trigger time of the pad converted in a drift distance. See Fig. 4.13 for the visualization of a signal. The number of electrons is converted into digital value ADC (Analog to Digital Conversion):

$$ADC = \frac{n_{e^-}\, n_{ch}}{\left(\frac{d_{range}}{q_{e^-}}\right)} + \text{Offset} , \tag{4.8}$$

where n_{ch} is the number of channels, that for a 12 bit electronics is 4096, the d_{range}=120 fC is the electronics dynamic range, q_{e^-}=1.6·10^{-19} C is the charge of the electron, n_{e^-} is the number of collected electrons, and Offset=100 is set to avoid negative ADC values.

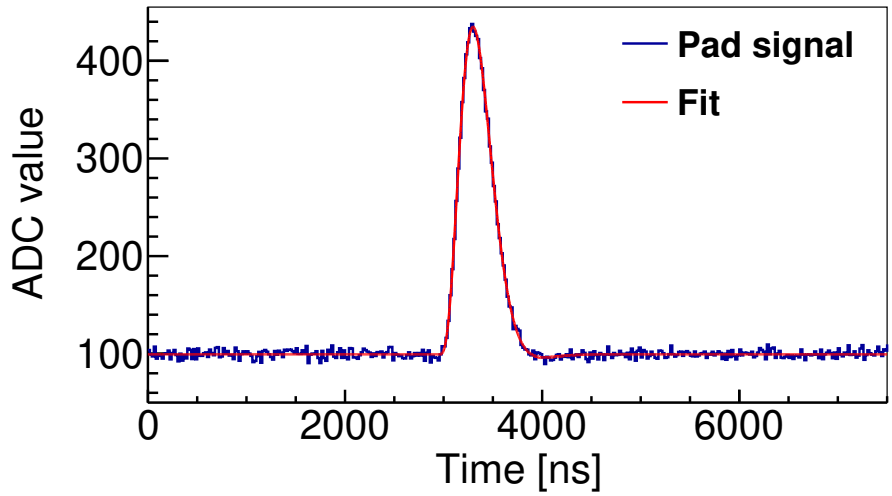

Figure 4.13.: Visualization of a signal from one mini-HYDRA TPC pad converted in ADC values, together with a fit (Eq. 4.7) in red.

This Chapter presented the developed simulation aimed at assessing the feasibility and refining the setup for the first HYDRA experiment. The first part detailed the event generators

used to achieve these goals. In the second part, the use of these generators is highlighted, with a focus on enhancing the geometrical efficiency for detecting the ${}^{3}_{\Lambda}\mathrm{H}$ decay events and suppressing other background events. Additionally, the tracking method and the simulated electronics response were overviewed briefly.

This Chapter concludes the first part of the thesis, where the different steps necessary for the upcoming experiment to be performed at GSI/FAIR has been detailed. The following second part will focus on the analysis of existing data from different experimental HADES campaigns, aiming at characterizing the strangeness production mechanisms at and below the threshold energies (1.6 AGeV).

Part II.

Strangeness production

5. HADES- High Acceptance DiElectron Spectrometer

HADES (High Acceptance DiElectron Spectrometer) is a large acceptance detector setup designed to investigate medium modifications of light vector mesons such as ρ, ω, and ϕ through their leptonic decays into pairs of $e^+ - e^-$. Along this line, the prime objective of the HADES collaboration is to understand QCD matter under extreme temperature and density conditions via HIC. Photons and dileptons possess a unique characteristic of being emitted throughout the evolution of the collision zone and reach the detector almost undistorted since they are not affected by the strong interaction, allowing to probe the hot and dense phase of the HIC [150].

The HADES experiments are performed in a fixed-target setup located at GSI and utilize primary ion beams from the SIS18 synchrotron. Therefore, the typical energies for HIC are at the order of 1-2 AGeV. Owing to its large acceptance, a full characterization of a collision event is possible, by detecting light charged particles ($Z \leq 2$). Therefore, besides its main goal, it can be used as a multi-purpose setup enabling the study of complex systems, in particular those which include strangeness such as the ${}^{3}_{\Lambda}$H. Among the various HADES experimental campaigns, those conducted in 2012 (Au+Au at 1.23 AGeV) and 2019 (Ag+Ag at 1.23 AGeV and 1.58 AGeV) can be used to gain insight on the light-hypernuclei production mechanism in HIC, both at threshold (1.58 AGeV), as shown in Eq. 1.18, and below.

This part focuses on data analysis from the experimental campaigns presented above. In this Chapter, the main sub-detectors employed for the reconstruction of ${}^{3}_{\Lambda}$H through its decay products will be briefly outlined. A more detailed description can be found in Ref. [151].

5.1. Experimental setup

The detector system comprises six identical sectors rotated by 60° relative to each other in azimuth angle, symmetrically surrounding the beam axis. Figure 5.1 provides an exploded view of the spectrometer, facilitating the visualization of the various sub-detectors. The system offers an azimuthal acceptance of 85% and covers polar angles within the range of 18° to 85°.

The relevant sub-detectors used in the analysis will be described in more details in the following sub-sections, following their arrangement along the beam-line. While the experimental setup for the two campaigns is quite similar, the main focus will be on the 2019 campaign, with specific differences highlighted along the text.

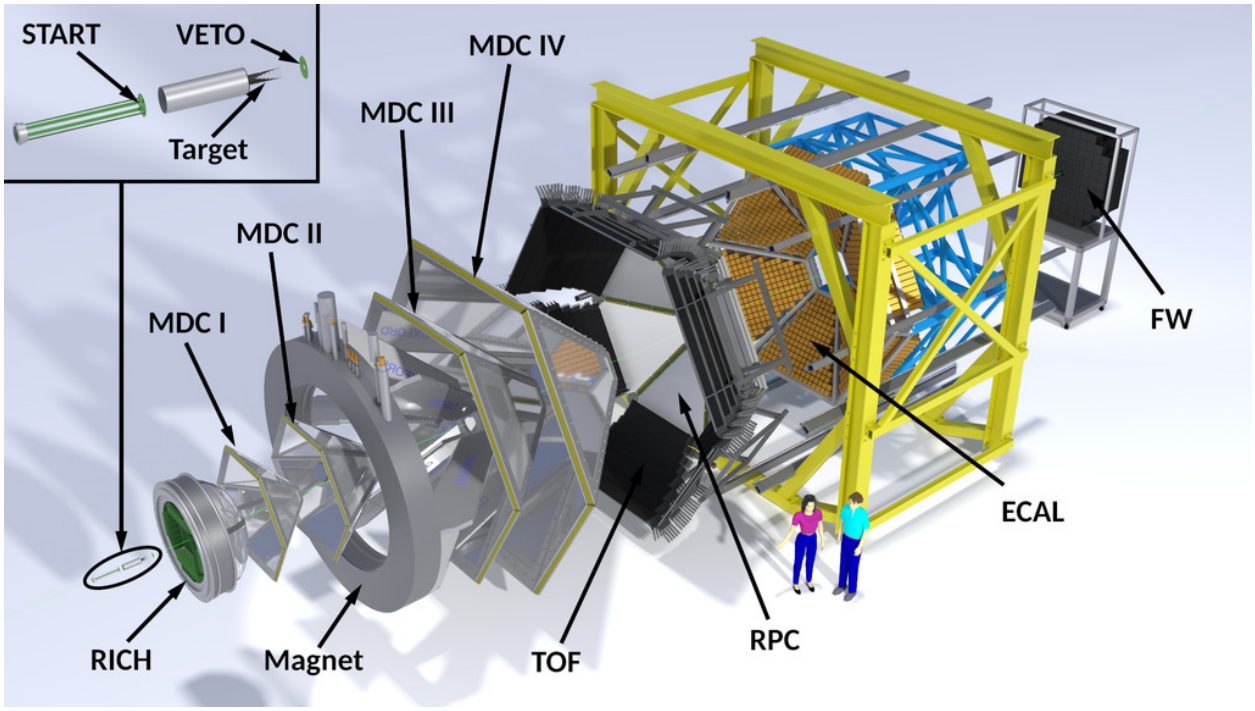

Figure 5.1.: Exploded view of the HADES detector setup used for the experimental campaign in 2019. Figure is taken from [152].

5.1.1. Beam detectors

The beam intensity, position, and its time structure are monitored employing two diamond-based sensors created using the scCVD (single-crystal Chemical Vapor Deposition) technique. Diamonds are chosen for their radiation hardness and fast timing response. The first sensor, known as the START detector, is positioned 2 cm upstream the reaction targets. The second sensor, called VETO, is situated 70 cm downstream from the target [153, 154]. See Fig. 5.2 for the close-up pictures of the two detectors, together with a schematic view of their placement along the beam line.

The START detector primarily serves for beam diagnostics and starts the Time-of-Flight (TOF) measurements, with a time precision σ<50 ps. It has dimensions of 4.7 $\times$ 4.7 cm^2 with a thickness of 70 μm. The detector is equipped with 16 double-sided strips oriented in both the x- and y-directions, each separated by 300 μm from the next one [154]. This configuration enables precise determination of the beam position. Details regarding the characteristics and arrangement of the START detector used in the 2012 campaign can be found in Ref. [155].

The VETO detector features an active area of 8 $\times$ 8 mm^2 and a thickness of 107 μm, with data read-out through 8 pads. Its primary purpose is to reject triggered events in which no collision occurred.

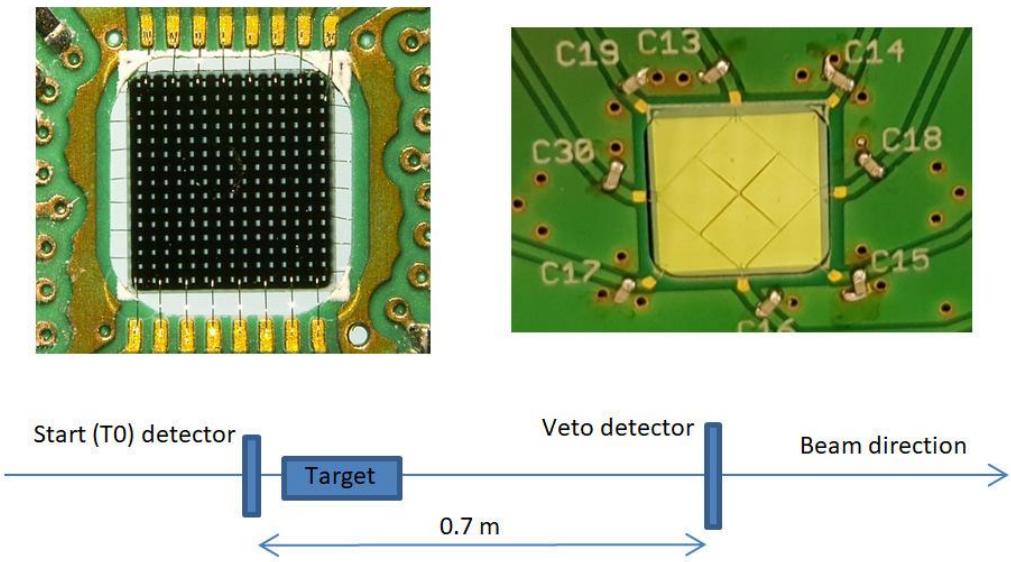

Figure 5.2.: Pictures of the beam detectors. Left. The START detector. Right. The VETO detector. Bottom. The schematic view of their placement along the beam line. Figures are reprinted from [154] under CC BY 3.0.

5.1.2. Segmented target

The target used during the HIC experimental campaigns consists of 15-fold segmented Ag-disks with a radius of 1.1mm and Au-disks with a radius of 1.5mm. These disks are mounted on thin Kapton strips and held in place by a carbon fiber tube, as shown in the right (left) panel of Fig. 5.3. This arrangement minimizes the conversion of photons (produced within

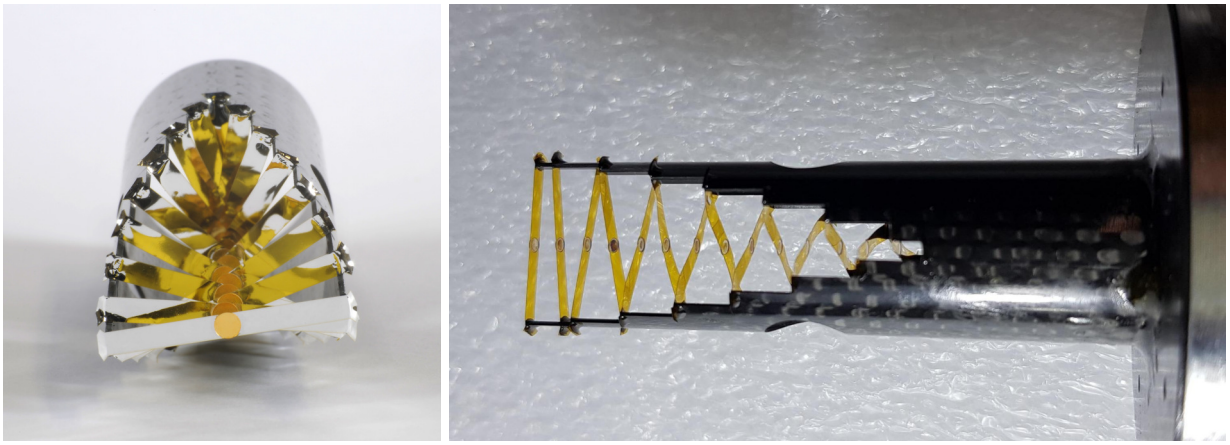

Figure 5.3.: Pictures of the segmented targets, the same holding structure has been used for the two campaigns. Left. Frontal view of the 15-fold Au target. Picture is taken from [156]. Right. Side view of the 15-fold Ag target. Picture is taken from [157].

the fireball) with the target, as the individual target thickness is low 40 μm (25 μm) and with a 3 mm (4 mm) gap between them. This configuration results in a total nuclear interaction probability of 1.5% (1.35%), while maintaining the photon conversion probability at less

than 1% [158]. The strips are arranged in a staggered manner to ensure overlap only where the beam interacts with the target. However, interactions of the beam with the Kapton strips are inevitable and lead to carbon contamination in the data. To address this issue, event selection criteria must be applied during the analysis phase, as discussed in the next Chapter.

5.1.3. Magnet

The ILSE (IronLess Superconduction Electromagnet) magnet (see left panel of Fig. 5.4) is utilized to bend charged particles, enabling the determination of their momenta and charge from their curvature. For electrons a relative precision of σ_p/p=(1.5-2)% can be obtained [151]. It consists of six superconductive coils made of aluminum-stabilized Cu(Nb)Ti, which generate an inhomogeneous toroidally shaped magnetic field ranging from 0.9 to 3.6 T [159]. These coils surround the beam axis and are aligned with the detector frame to minimize any additional loss of solid angle for the detector. An important feature of the beam field geometry is that it provides a field-free region around the target and within the active region of the RICH (Ring Imaging Cherenkov) detector, allowing the electrons identification [151].

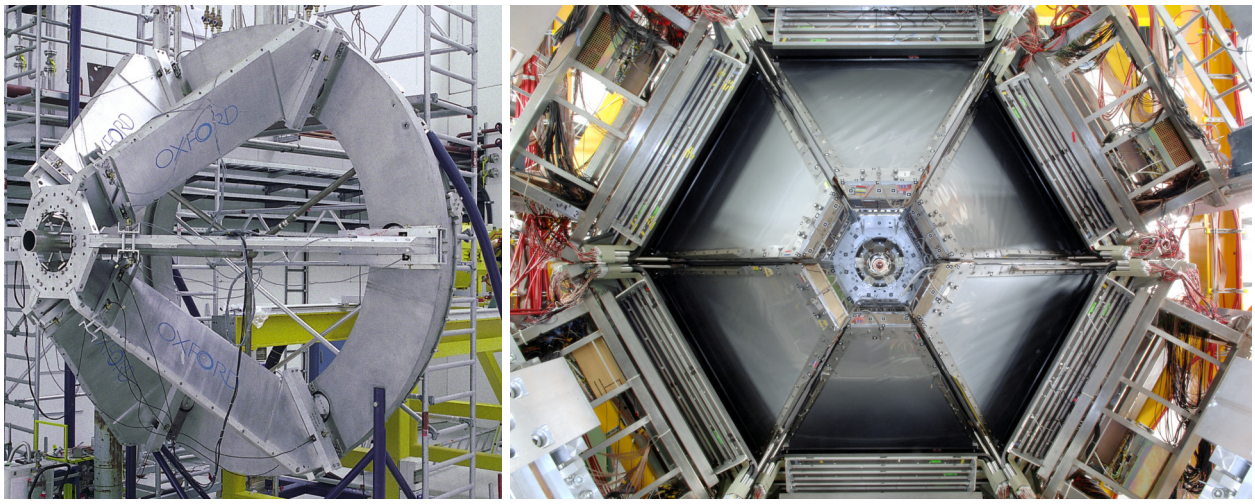

Figure 5.4.: Left. Picture of the ILSE magnet before being mounted in the HADES setup. Right. MDCs mounted on the detector frame. Pictures are taken from [156].

5.1.4. Tracking system

Charged particles are tracked using two sets of gaseous detectors before and two after the ILSE magnet, known as the Multi-layer Drift Chambers (MDCs). Each of the six sectors features four MDCs of increasing size, each composed of six trapezoidal inner planes (see right panel of Fig. 5.4). This configuration provides full azimuthal-angle coverage and spans the polar-angle range between 18° and 85°. The two inner planes (MDC I-II) track particle positions in front of the magnetic field, while the two outer planes (MDC III-IV) provide position measurements after particles have been bent by the magnetic field. These position measurements allow for the reconstruction of the particle's trajectory and the extraction of

information such as its momentum and charge sign.

The MDC chambers are constructed using lightweight materials, including 12 μm Aluminized Mylar windows and Aluminum wires. The wires, which serve as cathode and field wires, have radii of 40 μm (MDC I-III) and 60 μm (MDC IV) and are tensioned at 0.8 N and 1.2 N, respectively. The sense wires are 20 μm (MDC I-III) and 30 μm (MDC IV) gold-plated tungsten wires, tensioned at 0.4 N and 1.1 N, respectively. For MDC I, the gas mixture is Ar-CO_2 (70-30%), while for MDC II-IV, it is Ar-CH_4 (84-16%). This configuration results in a total detector thickness of $5{\cdot}10^{-4}$ radiation length, ensuring minimal multiple scattering and allowing for a position resolution of 100-200 μm. In addition to position information, these detectors allows to extract energy loss information used for charged particles identification [151, 160].

5.1.5. Time-of-Flight system

The time-of-flight system, also known as the META (Multiplicity Electron Trigger Array) detector, comprises two sub-detectors: a scintillator array referred to as the TOF wall (see left panel of Fig. 5.5) and the RPC (Resistive Plate Chamber) detector (see right panel of Fig. 5.5). These detectors are positioned after MDC IV, in beam direction, covering the polar angles between 44° and 85° for the TOF wall and between 18° and 44° for the RPC detector.

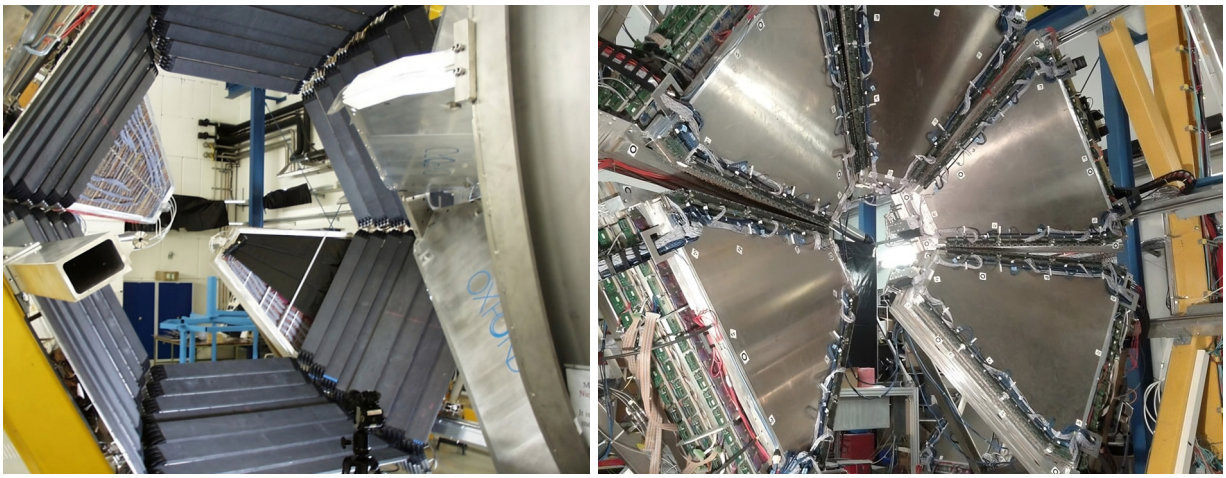

Figure 5.5.: Pictures of the Meta detector. Left. Picture of the TOF wall taken from [161]. Right. Picture of the RPC detector taken from [162].

The TOF wall is divided into six sectors, each consisting of eight modules. Each module, in turn, comprises eight BC-408 scintillator bars (384 rods), all enclosed in a carbon fiber case. The first 192 bars at small polar angles have a cross-section of $20{\times}20$ mm^2, while the remaining 192 bars at large polar angles measure $30{\times}30$ mm^2. The length of these rods varies from 1 m for the innermost rods to 2 m for the outermost ones. Each rod's signal is read-out by PMTs at both ends, providing the following information: i) time-of-flight measurement with a resolution of $\sigma_{TOF}{<}150$ ps. ii) The hit position along the bar, with an average position resolution between 25-27 mm for the different bars in the azimuthal

direction. In the polar direction, the resolution is limited by the size of the scintillator itself. iii) Energy deposition, which can be extracted from the signal shape and used for particle identification. The higher energy deposited in the plastic scintillator, compared to the MDC gaseous detectors, allows for more accurate identification [151, 163].

The RPC is also divided into six sectors, each comprising two overlapping layers. These layers are composed of 93 cells arranged in three columns, with dimensions increasing as the polar angle increases. The dimensions range from 12×2.2 cm^2 for the innermost part to 52×5 cm^2 for the outermost one, with a total thickness of 18 mm. Each cell contains three stacked aluminum electrodes of 2 mm thickness, separated by two 2 mm thick glass plates. The gaps between the plates are filled with a gas mixture of $C_2H_2F_4$-SF_6 (90-10%). When charged particles traverse the detector, they ionize the gas, triggering an avalanche of electrons. These electrons drift due to the electric field created by applying high voltage of 6 kV to the central aluminum plate (anode), which is connected to the two outer aluminum plates (cathode) at ground potential. The intrinsic time resolution for a single hit is 77 ps, and 83 ps for double hits. The transverse position resolution depends on the cell size, while the longitudinal resolution is less than 6 mm [164–166].

The integration of time-of-flight measurements from the META detector, momentum determination from the tracking system, and energy loss measurements allows for precise particle identification, as elaborated in the forthcoming Chapter.

Furthermore, due to the rapid timing response and high granularity of both detectors, it becomes possible to determine the charged particles multiplicity event-by-event, which is utilized for triggering purposes as well as centrality determination of the collision. This information is employed to establish a first-level trigger decision based on the number of hits identified in the META detector.

Two additional systems placed downstream to the META detector, not used in the analysis presented here are the ECAL (Electromagnetic CALorimeter) and Forward Wall (FW). The ECAL is used for photon measurement as well as separation of $e^{\pm}$ from $\pi^{\pm}$. The FW, located at the end of the beam line, is used to measure spectators, allowing to determine the centrality of the collision in a complementary way to the META detector.

5.2. Beam settings

The focus of the analysis presented in this part of thesis is to determine of the ${}^{3}_{\Lambda}$H production cross section at and below threshold energy (1.58 AGeV), and from that to infer about the production mechanisms at different energies, as well as different systems (Ag and Au). For that, existing data from HIC at HADES experimental campaigns is used.

In 2012, the collaboration conducted its first experiment involving collisions of heavy systems. Au+Au collisions were studied with projectile kinetic energy E_{kin} = 1.23 AGeV, corresponding to a center-of-mass energy available for the nucleon-nucleon collision of

$\sqrt{s_{NN}}$ = 2.41 GeV[1], and beam intensity of I_{beam} = (1.2-1.5) MHz. The physical trigger (PT) was set to select events with N_{hits}>20 in the META detector, resulting in a trigger rate of 8 kHz with a 50% duty cycle. This setup allowed to record $N_{rec} = 7.31 \cdot 10^9$ events during 33 days of data taking.

In 2019 the Ag+Ag experimental campaign was conducted at two beam energies. The first and main measurement (26 days) is that at higher energy E_{kin} = 1.58 AGeV ($\sqrt{s_{NN}}$ = 2.55 GeV). This energy is exactly the threshold for strangeness production in a single nucleon-nucleon collision, see Eq. 1.18. The beam intensity was I_{beam} = (1.5-3.5) MHz. Two PTs were defined, PT2 requires 5 hits and PT3 20 hits in the META detector leading to a trigger rate of 8.8 kHz, allowing to record N_{rec}=13.64·10^9 events.

A second Ag+Ag run was carried out to get a sample of events directly comparable to the Au+Au data from 2012. Therefore, the same beam energy of E_{kin} = 1.23 AGeV ($\sqrt{s_{NN}}$ = 2.41 GeV) was used for three additional days of data taking. The same beam conditions were used leading to N_{rec}=1.32·10^9 events.

The main specifications for the experimental campaigns used during the analysis phase are summarized in the Table 5.1.

This Chapter presented an overview of the HADES experimental setup used in the two experimental campaigns 2012 and 2019, including the different detectors in the HADES setup and the beam time conditions.

The next Chapters detail the analysis procedure followed to study the production of ${}^{3}_{\Lambda}$H. In particular, Chapter 6 accurately describes the event selection and the various techniques used to extract the signal. Chapter 7 explains the method for extracting the cross sections for different datasets, and for the Ag1.58Ag datasets, it is possible to study the cross section differentially. Finally, Chapter 8 highlights the results obtained and provides a comparison with simulations.

[1]The Mandelstam variable *s* is one of the three invariant quantities used to describe two-body kinematics. It represents the squared value of the total energy for the colliding system in the center of mass. For fixed-target experiments, it is calculated as:

$$\sqrt{s_{NN}} = \sqrt{2m_N^2 + 2E_{TOT}m_N}\,,$$

where m_N is the nucleon mass, $E_{TOT} = E_{kin} + m_{beam}c^2$ is the total beam energy, E_{kin} the beam kinetic energy, and m_{beam} is the beam rest mass.

Experimental campaigns	Au1.23Au	Ag1.23Ag	Ag1.58Ag
Beam	$^{197}_{79}$Au^{69+}	$^{107}_{47}$Ag	$^{107}_{47}$Ag
E_{kin} [AGeV]	1.23	1.23	1.58
$\sqrt{s_{NN}}$ [GeV]	2.41	2.41	2.55
I_{beam} [MHz]	1.2-1.5	1.5-3.5	1.5-3.5
y_{cm}	0.74	0.74	0.82
Magnet current [A]	2496	2496	3195
Target	$^{197}_{79}$Au	$^{107}_{47}$Ag	$^{107}_{47}$Ag
Segment distance [mm]	4	3	3
Segment disk radius [mm]	1.5	1.1	1.1
Segment disk thickness [μm]	25	40	40
Density [g/cm^3]	19.32	10.49	10.49
σ_{tot} [mb]	6833$\pm$430	4537$\pm$248	4575$\pm$257
N_{rec} [10^9]	7.31	1.32	13.64

Table 5.1.: Characteristic of beam settings for the HADES experimental campaigns (2012 and 2019) analyzed in this thesis [152]. The segment distance represents the distance between individual targets along the beam direction. The total cross-section σ_{tot} is estimated via Glauber Monte Carlo simulation [167, 168].

6. Data Analysis

The recorded HADES data are analyzed using the HYDRA[1] (Hades sYstem for Data Reduction and Analysis) framework [169], which is based on ROOT, and kept in a DST (Data Summary Tape) format. This framework features a modular structure for each sub-detector as well as global ones for a collision event, that allow to treat the complexity of the setup and the high particle multiplicities. Its primary purpose is to process raw data and provide calibrated and reconstructed data, prepared for further physics analysis. To enhance readability, this Chapter exclusively presents results from the Ag+Ag at 1.58 AGeV dataset using only the data from one day of beam-time which is representative for all events analyzed in this thesis. Results for the other systems can be found in Appendix A for Au+Au at 1.23 AGeV and in Appendix B for Ag+Ag at 1.23 AGeV.

After the event reconstruction, further selection criteria are applied to choose the event of interest and filter out non-physical events that may have been stored. These events are identified by combining information from all detectors, as will be elaborated in Sec. 6.1.1. To facilitate the reconstruction of ${}^{3}_{\Lambda}\mathrm{H}$, which is the central focus of this thesis, the invariant-mass technique is applied to candidate tracks that meet specific selection criteria detailed in Sec. 6.2, 6.3. Subsequently, the obtained spectra are refined to eliminate background events (Sec. 6.4), and simulations are employed to correct the results for the HADES detector acceptance and efficiency (Sec. 6.5). Finally, an artificial neural network has been trained to better differentiate the signal (S) and background (B) and maximize the S/B ratio (Sec. 6.6).

6.1. Event Selection

6.1.1. Pre-selection cuts

In order to exclude non-physical, pile-up, and faulty events not originating from A+A collisions, a set of nine initial criteria is employed. These criteria are consistently applied across different datasets, with some minor modifications highlighted in the text: i) *kGoodTRIGGER* criterion selects events that meet the PT3 condition. For Ag+Ag (Au+Au) collisions, this corresponds to requiring 20 hits in the META (TOF) detector. This criterion serves as a coarse selection, roughly representing events in the (0-55%) (0-45%) centrality range. ii) *kGoodSTART* criterion is applied to ensure the presence of at least one hit in the START module, which is crucial for accurate time-of-flight measurements. iii) The *kNoVETO* criterion is employed to eliminate events in which a START hit was detected but no actual collision occurred. This is achieved by searching within a time window of $\pm$15 ns around the START time and ensuring that no VETO hit is present. iv) The *kNoSTART* criterion (referred to as

[1]To not be confused with the R^{3}B scientific program introduced in the first part of the thesis.

kNoPileUpSTART for the Au+Au campaign) is specifically applied to the START detector. This criterion is crucial for event rejection if, within a time window of ±15 ns, a second START hit is detected, which could indicate pile-up or other undesirable events. v) The *kGoodSTARTVETO* criterion serves to safeguard the selected events from contamination by secondary reactions. For Ag+Ag, this implies that in the case of a second START hit it has no corresponding VETO hit within a narrow time window of ± 2 ns to be discarded. In contrast, for Au+Au, the criterion is applied differently, rejecting events in which a second START hit is found with no corresponding VETO hit within a broader time window of 15-350 ns. vi) The *kGoodSTARTMETA* criterion is essential because of the moderate efficiency of the VETO detector. To account for this, a condition similar to that in the previous criterion is applied, but in this case, it concerns the relationship between the START and META detectors. Specifically, if a second START hit is detected within a time window of 80-350 ns and more than 4 META hits are found within a time frame of 7-12 ns after the second START hit, the event is discarded. vii) *kGoodVertexClust* ensures that at least one track has been successfully reconstructed, and it validates that the vertex position corresponds to one of the 15 targets, with a minimum Z value of -70 mm in order to remove events originating from the beam interaction at the START detector. viii) *kGoodVertexCand* is the same condition but for at least two tracks. Finally, ix) *kNoFlashMDC*, which is not present in the Au+Au campaign, is employed to ensure that events in which more than 20 sense wires inside one MDC fired are excluded from the analysis. This *flash* in the MDC is not linked to any physical event and is therefore removed.

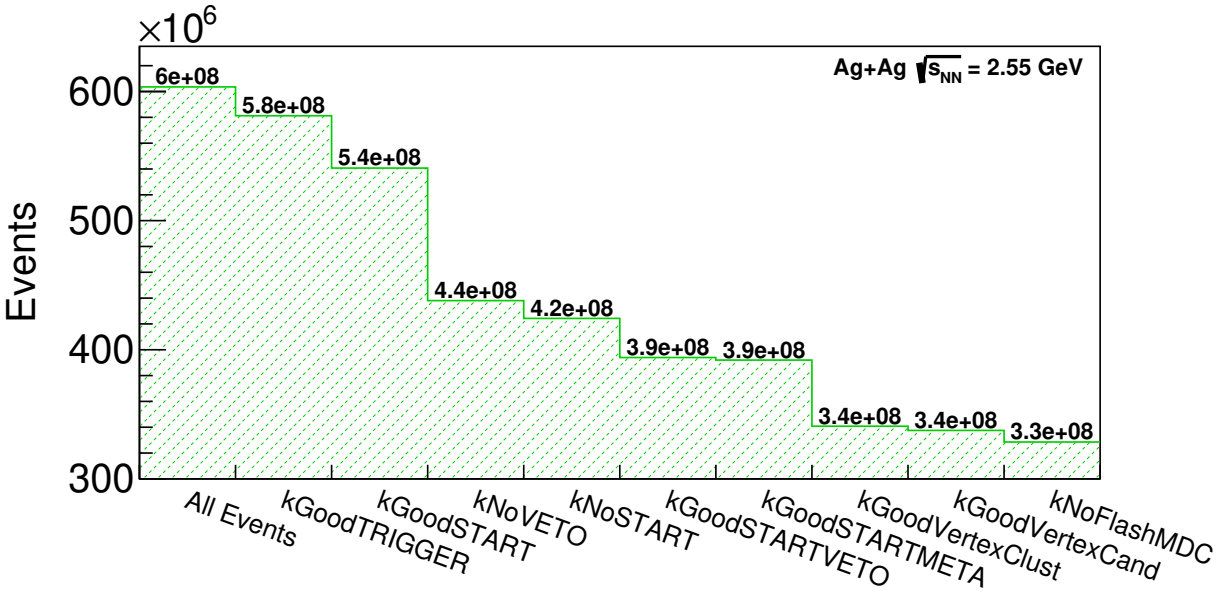

Figure 6.1.: Number of events after subsequently applying the different selection criteria. Plot generated using one day (83) of data. For details on the criteria see text.

The application of all these selection criteria results in halving the number of recorded events for further analysis, as demonstrated in Fig. 6.1. The following subsections provide details on additional selections necessary to ensure the purity of Ag+Ag (or Au+Au) collisions among the remaining events.

6.1.2. Centrality

In the context of HIC, due to the large spatial extension of the colliding systems the determination of the centrality is key for understanding various physical observables. Centrality relies on the impact parameter (b), which represents the distance between colliding nuclei in the transverse plane to the beam axis (see Fig. 2.1). However, this parameter cannot be directly measured in experiments, necessitating the use of a theoretical framework. The HADES collaboration employed an eikonal model known as the *Glauber Monte Carlo* to establish a connection between the impact parameter and physically measurable quantities, such as the charged particle multiplicity (N_{ch}) [167, 170]. Figure 6.2 illustrates the correlation obtained. This correlation is obtained under the assumption that the probability for particles production increases monotonically with the number of participating nucleons (A_{part}) in more central collisions.

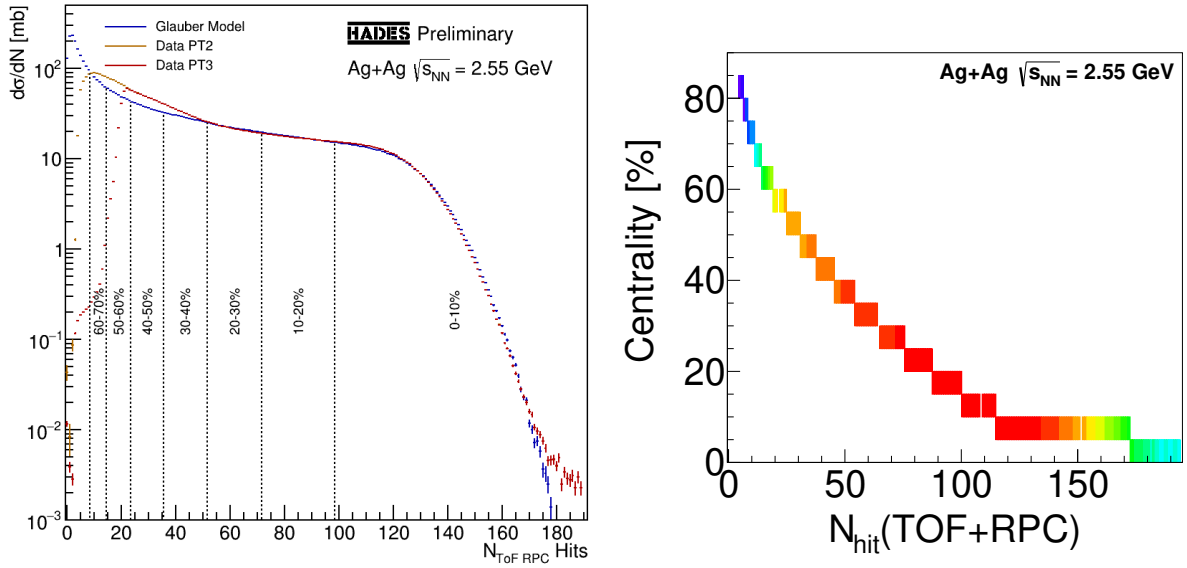

Figure 6.2.: Centrality Estimation. Left. Comparison of the differential cross-section as a function of N_{hit} in TOF and RPC detectors between the Glauber MC model and the PT2/3 trigger data divided in centrality classes of 10%. Figure is taken from [152]. Right. Correlation between N_{hit} in TOF and RPC detectors and Glauber model predictions for the centrality in classes of 5%. The most peripheral events are discarded by the PT3.

The Glauber Monte Carlo (MC) model conceptualizes a HIC as a superposition of independent nucleon-nucleon collisions and uses Gaussian distributions to extrapolate N_{ch} for each event. The parameters of these distributions, including the mean ($N_{mean} = \mu A_{part}$) and sigma ($\sigma = k\sqrt{N_{mean}}$), are determined by comparing a group of various simulated multiplicity distributions with the measured one obtained using the number of hits in the META (TOF+RPC) detectors. The parameters μ and k take into account detector acceptance and efficiency. The agreement between the distributions is quantified using the χ^2 technique, and the combination with the smallest χ^2 value is ultimately selected.

The left panel of Fig. 6.2, shows the differential cross section as a function of the number of hits (N_{hit}) in TOF and RPC detectors. As it can be seen there is an overshooting of the data compared to the Glauber model beyond the 30% centrality interval. This discrepancy is attributed to carbon contamination (Ag+C) that survives the event selections. This contamination results from the beam interaction with the target tube and the Kapton strips. Therefore, in the analysis presented in this thesis, to ensure the purity of Ag+Ag (Au+Au) collisions, only the 0-30% most central collisions are considered, by applying N_{hit}>64 cut. Furthermore, it's worth noting that PT3 trigger condition doesn't impose a hard cut on N_{hit}=20, but values below this threshold are still present in the data. This is because PT3 operates on raw data, and the correct N_{hit} values are determined during subsequent offline reconstruction and calibration.

6.1.3. Primary vertex

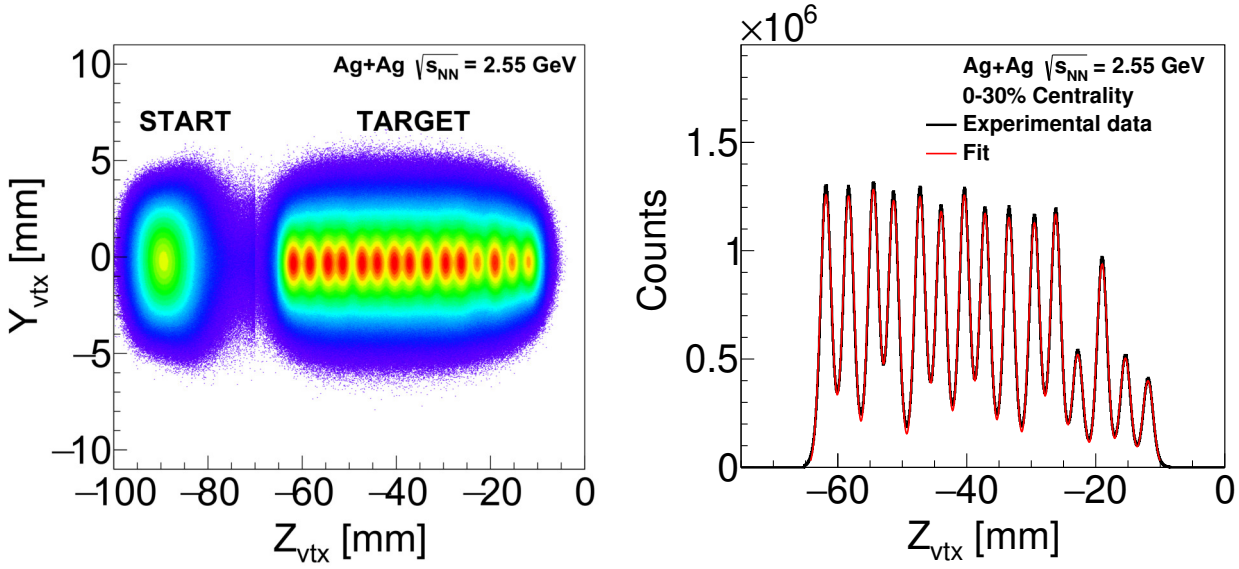

Figure 6.3.: Distribution of the reconstructed primary vertex. Left. The START detector together with the 15-target segments can be clearly distinguished in the YZ plane. Right. The Z component after the event selection together with a 15-Gaussian fit in red.

The study of decaying particles necessitates precise knowledge of the collision's primary vertex. This primary vertex is reconstructed using information from the tracking system. As charged particles traverse the tracking detectors, they generate signals in the wires along their paths. By projecting the fired wires within a single MDC onto a common plane and finding the intersection of these wires, the particle's position in the MDC can be determined. The ILSE magnet, which provides a negligible magnetic field between MDC I-II and between MDC III-IV, allows to model a straight-line trajectory as a first approximation. The curvature between MDC II-III is determined using a Runge-Kutta fit [171], which takes into account the ILSE magnetic field map. This approach enables the reconstruction of the track between MDC I-IV and the determination of the particle's charge sign and momentum. However,

in HIC, especially in central collisions, a high track multiplicity is inherent, leading to the presence of numerous spurious tracks, often referred to as *fake tracks*. These must be eliminated through a process known as *META matching*, where the full track must be associated with a hit position on the META detector. For the resulting trajectory, a parameter known as MMQ (META Matching Quality) is extrapolated, which can be interpreted as the distance between the intersection point of the trajectory and the META hit expressed in standard deviations (σ) [151]. In this analysis, only tracks with an MMQ value less than 3σ are considered.

To reconstruct the primary vertex, various methods can be employed, but the one that offers the highest precision involves using fully reconstructed tracks obtained through the Runge-Kutta method, described above. Track candidates from MDC I are back-propagated toward the target region, and the vertex is extrapolated as the average point of closest approach for all the tracks. The left panel of Fig. 6.3 shows the vertex distribution of the events before applying the events selection from Sec. 6.1.1 and demonstrates the effectiveness of this method in differentiating the individual target segments and the START detector (around Z_{vtx}= -90 mm). To filter out the latter, a geometrical cut on the vertex is applied (kGoodVertexClust) in Sec. 6.1.1. The quality of the reconstructed vertex is assessed using the χ^2_{RK} parameter, and for this analysis, based on results from previous analysis [172] only tracks with χ^2_{RK}<400 are considered.

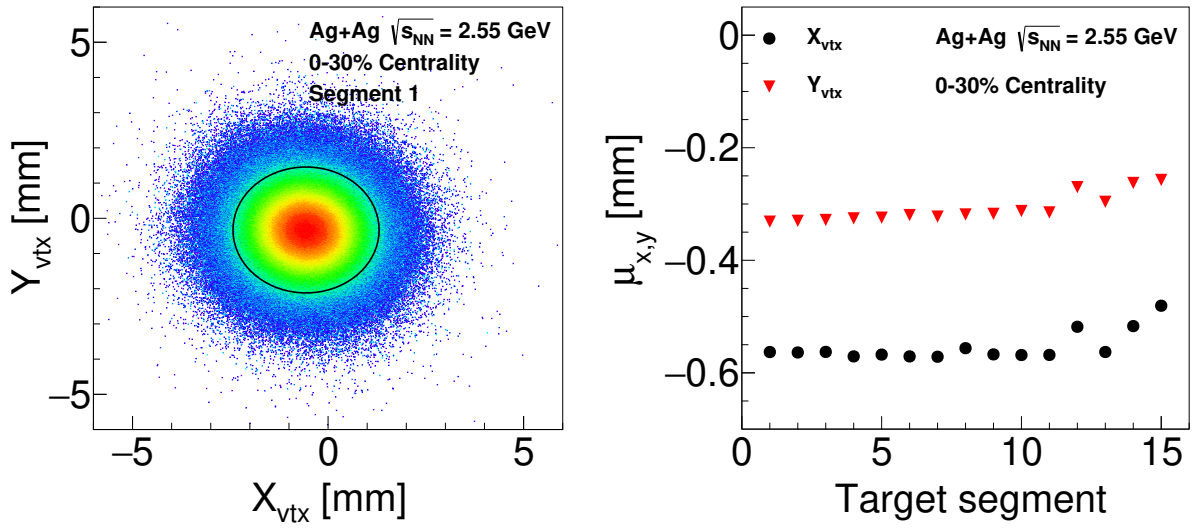

Figure 6.4.: Components (x, y) of the primary vertex. Left. The 2D distribution for the first target segment. The black ellipse represents the 3σ selection cut for the vertex. Right. The mean value from a Gaussian fit for each of the 15 targets.

The left panel of Fig. 6.3 displays the vertex distribution in the YZ plane, revealing 15 distinct peaks. Each of these peaks needs to be assigned to one of the 15 target segments. To achieve this, a 15-Gaussian fit function has been employed for the projected Z_{vtx} distribution, as shown in the right panel of Fig. 6.3. The mean values extracted from these fits serve as the positions of the vertex segments, with the separation point between two consecutive

Gaussians defined as the z position located 3σ away from the mean value. In addition, to ensure that the collisions occurred between the beam and the target discs, a Gaussian fit to the X and Y components has been applied for each target segment separately. Only events falling within 3σ were included in the analysis. The left panel of Fig. 6.4 provides an example for the first target segment, while the right panel shows the mean values for X and Y component of the vertex across all 15-target segments. Notably, these means average align at around -0.55 mm and -0.32 mm, respectively, indicating a slight misalignment of the beam, with an almost constant width of σ_x=0.66 mm and σ_y=0.69 mm.

Both the right panel of Fig. 6.3 and the right panel of Fig. 6.4, clearly reveal that target segments 12, 14, and 15 exhibit deviations from the general behavior, with a noticeable 30% lower collected statistics. Consequently, these particular targets have been excluded from the analysis.

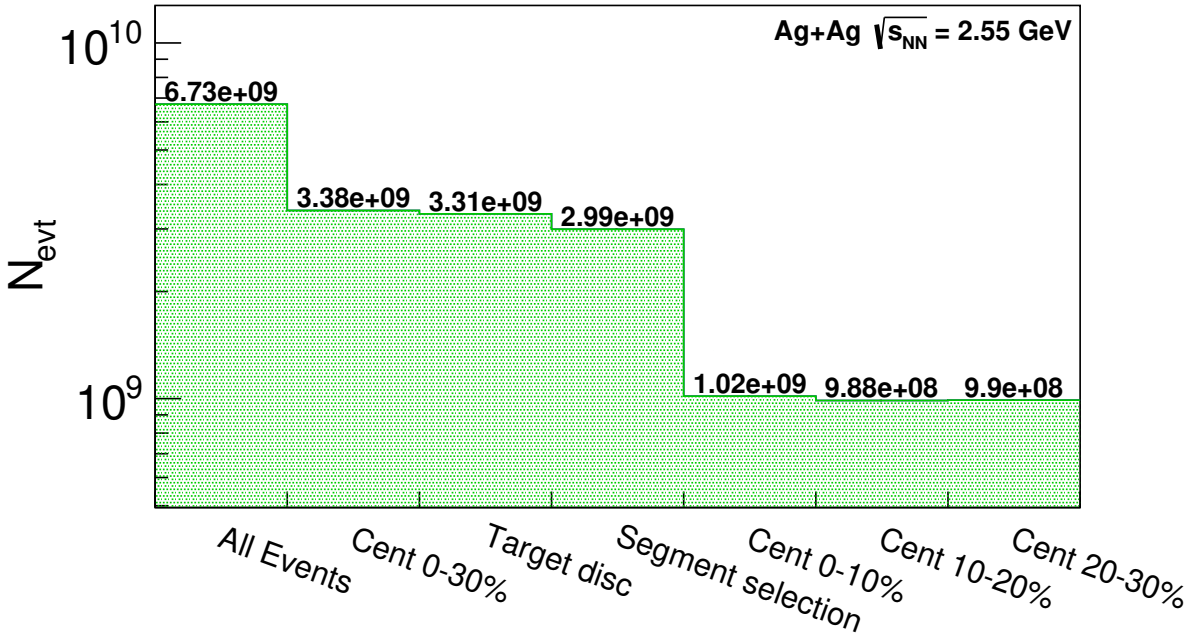

Figure 6.5.: Number of events after subsequently applying the events selection criteria defined in the previous sub-sections. For details on the bin content see text.

The event selection criteria used in the analysis have been detailed above and are summarized in Fig. 6.5. The bin labeled as *All Events* shows the number of events that survive the pre-selection described in Sec. 6.1.1. The second bin, *Cent 0-30%*, illustrates the total number of events that passed the previous selection criteria and are within the 0-30% most central collision events. The third and fourth bins are related to the targets. The *Target disc* bin depicts 0-30% central events in which the Primary Vertex (PV) is located inside the target disc (in all 3 dimensions), while the *Segment selection* bin shows the number of events where the anomalous targets are excluded. The last three bins represent the events from bin four that are within three centrality intervals: 0-10%, 10-20%, and 20-30%, respectively.

The sample corresponding to Segment Selection is used in the next Chapter.

6.2. Particle identification

The Particle IDentification (PID) process is crucial for associating reconstructed tracks with their corresponding particles. In the HADES detector, the identification of hadrons involves the utilization of two distinct techniques: time-of-flight and specific energy loss.

Once the complete track has been reconstructed using the Runge-Kutta fit, it becomes possible to determine the total distance traveled by the particle by integrating its trajectory from the primary vertex to the recorded META hit. This, along with the flight time, allows for the calculation of the particle's velocity (β). Additionally, the fitting process provides information about the momentum-to-charge ratio (p/q). It is possible to express the momentum in terms of the velocity using the following equation:

$$p/q = \frac{\beta c\, m/q}{\sqrt{1-\beta^2}}, \tag{6.1}$$

where c is the speed of light and m the particle mass.

Figure 6.6 displays the velocity distribution for reconstructed tracks as a function of their momentum over charge. The top panel represents tracks with a META hit in the RPC, while the bottom panel corresponds to tracks in the TOF detector. It is important to note that, for some tracks, β values greater than 1 are observed. This is primarily due to uncertainties in time-of-flight and/or momentum measurements. Within the distribution, there are clearly pronounced bands around the nominal mass-to-charge ratio (m/q) values of different particles labeled in the plots. The pink curves represent the theoretical relation, using Eq. 6.1, to highlight the expected position of the hadrons and it is possible to notice that HADES is able to identify particle up to Z=2 (He). The selection of hypertriton decay candidate events requires identification of π^- and ^{3}He. A graphical cut has been applied to select the π^- band (shown in red), with the cut criteria determined by [172] that corresponds to a 3σ cut. However, for ^{3}He, applying a graphical cut on those variables is not feasible since it can not be fully separated from other particles such as protons or deuterons.

In order to identify ^{3}He, the specific energy loss technique is employed, which involves studying the energy deposited by charged particles in the MDCs. The energy deposit in the gaseous volume is described by the Bethe-Bloch (BB) formula [54].

Figure 6.7 illustrates the measured p/q values for tracks within a mass-to-charge range 1.27 < m/q [GeV/c^2] < 1.58. The distribution is presented separately for particles detected in the RPC (top panel) and TOF (bottom panel) detector. Within this distribution, three distinct bands are evident. The higher-energy band corresponds to ^{3}He, as the Bethe-Bloch equation is dependent on the charge of the particle and increases with z^2. The bands located below are associated with protons, deuterons, and kaons. To remove contaminations from the ^{3}He mass region, a graphical cut has been applied shown in red. The cut depicted in the dis-

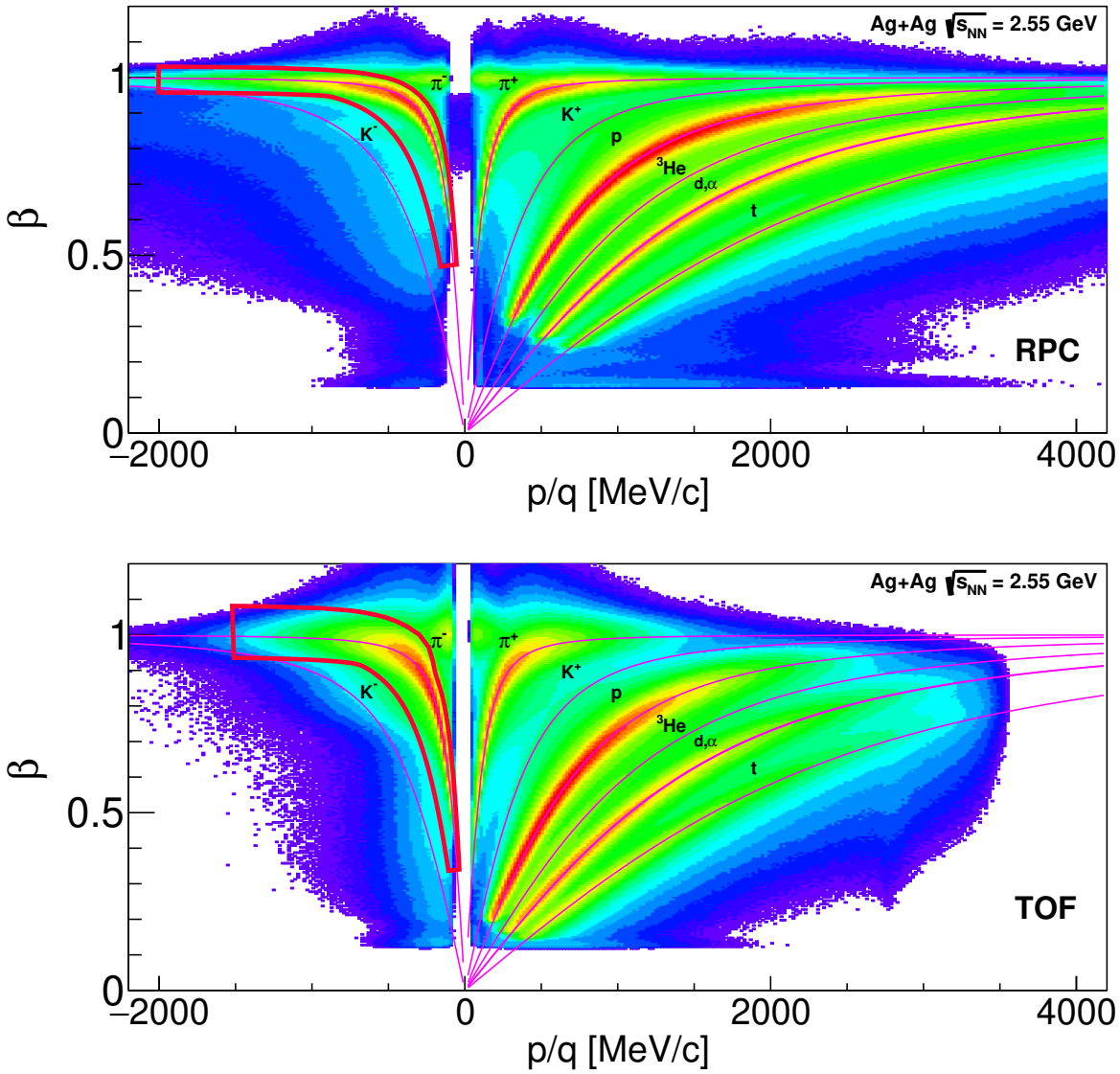

Figure 6.6.: Correlation between the p/q and β for all selected tracks, shown separately for RPC (top) and TOF detectors (bottom). The graphical cut (red) for the π^- has been taken from [172], while the pink lines represent the theoretical curves for the hadrons using Eq. 6.1.

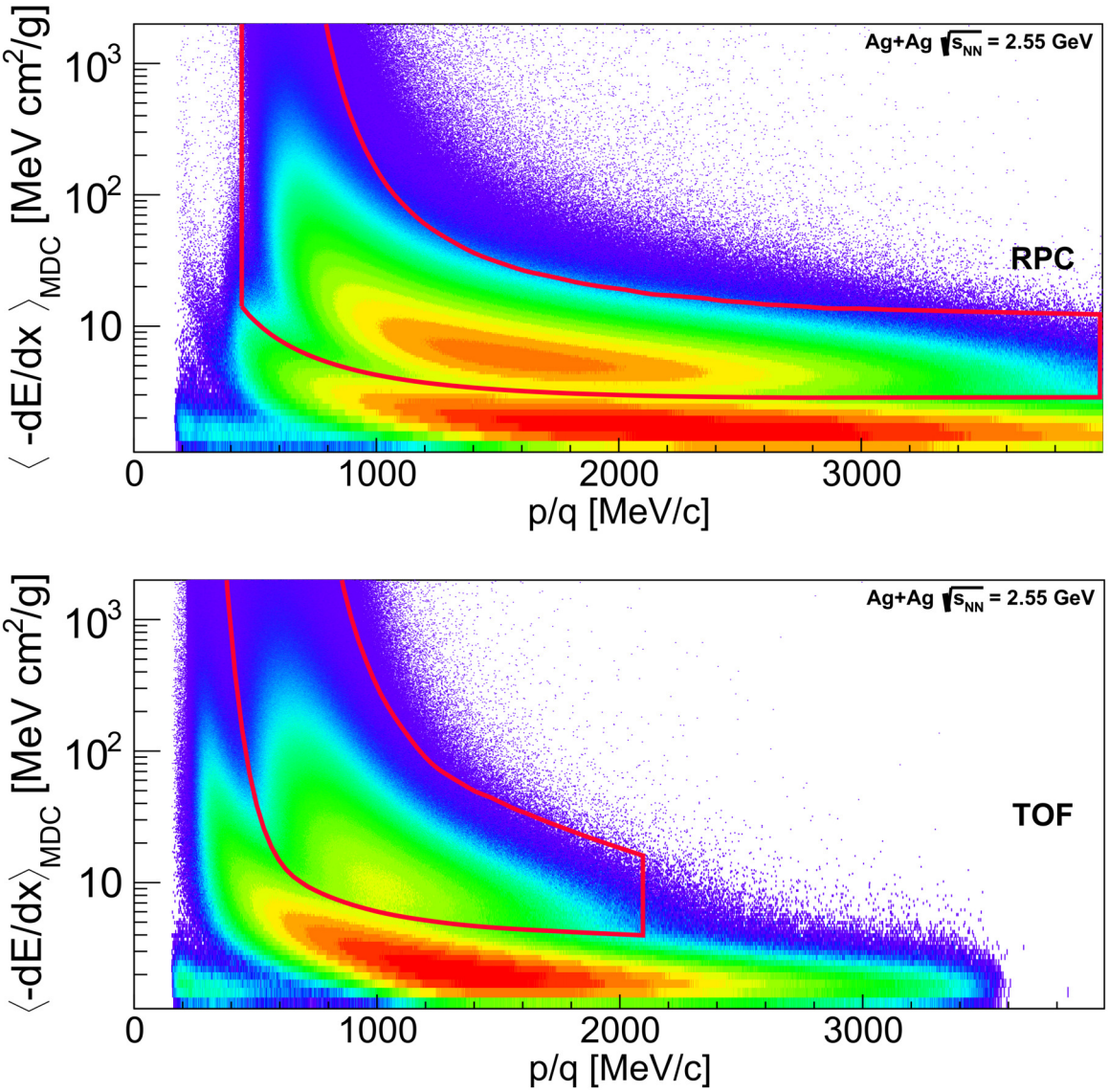

Figure 6.7.: Correlation between the specific energy loss in the MDC and the p/q measured in RPC (top) and TOF (bottom) for tracks with a mass over charge between 1.27 GeV/c^2 and 1.58 GeV/c^2. The graphical cuts (red) are taken from [172].

tribution has been determined by [172] that corresponds to 3σ cut relative to the BB formula.

Figure 6.8 shows the mass-to-charge ratio before and after applying the identification cuts. It clearly illustrates the effectiveness of all the cuts and selections applied in isolating π^- and ^{3}He particles up to this point.

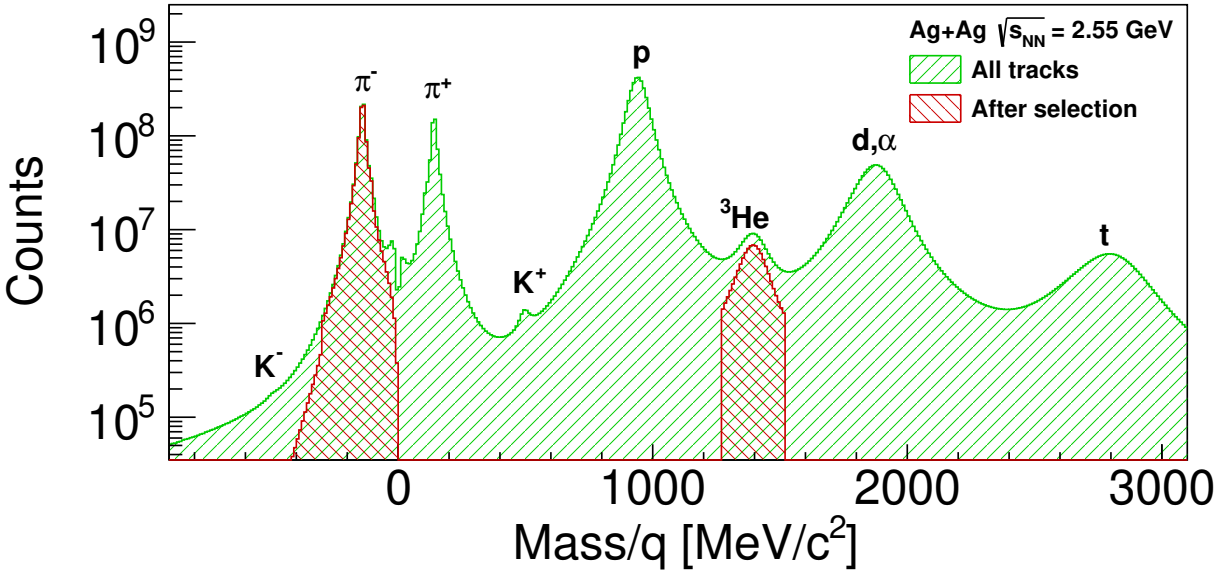

Figure 6.8.: Mass distribution of all selected tracks before and after particle identification for the π^- and ^{3}He, combined for TOF and RPC tracks.

6.3. $^3_\Lambda$H reconstruction

The study of the $^3_\Lambda$H, a weakly decaying particle, is conducted using the invariant mass technique, following Eq. 1.24. This technique relies on the knowledge of the four-momentum vectors $P = (p_x, p_y, p_z, E)$ of the daughter particles. In this analysis, the focus is on reconstructing the $^3_\Lambda$H through its two-body charged decay:

$$^3_\Lambda\mathrm{H} \rightarrow {}^3\mathrm{He} + \pi^- \, .$$

For each event, the reconstructed four-momentum vectors of all possible daughter pairs of the π^- and ^{3}He particles are combined to yield $^3_\Lambda$H candidates. Due to the high particles multiplicity (see Sec. 6.4), the majority of candidates do not originate from the $^3_\Lambda$H decay, leading to the inclusion of uncorrelated pairs in the invariant mass spectrum. These uncorrelated pairs contribute to what is known as the *combinatorial background*. To mitigate the presence of these pairs, a set of cuts on topological decay variables is required.

Figure 6.9 provides an illustration of the event topology and the different variables that can be constrained. The particle of interest is produced at the Primary Vertex (*PV*) of the collision

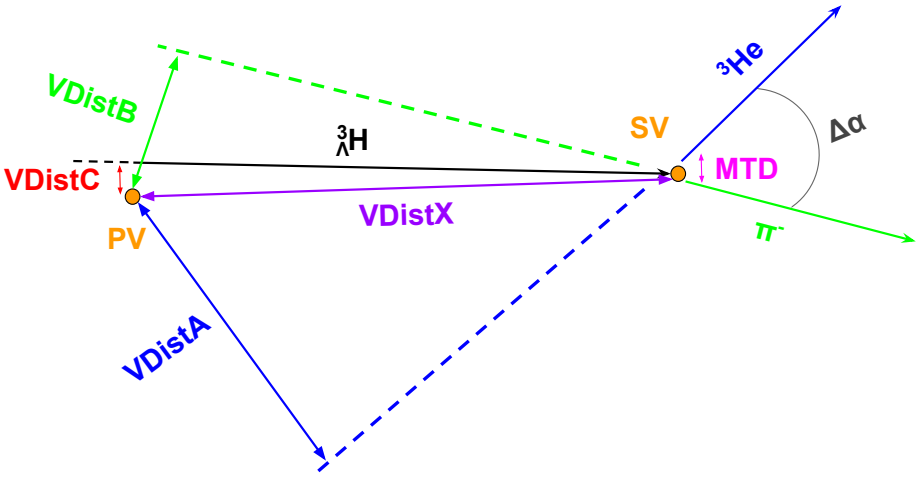

Figure 6.9.: Sketch of the $^3_\Lambda$H decay topology. The variables are described in the text.

event, and then decays at the Secondary Vertex (*SV*). *VDistX* represents the flight length of the mother particle and is determined as the distance between *PV*-*SV*. The secondary vertex is calculated as the midpoint of the vector connecting the daughter particle trajectories at their point of closest approach. The variable *VDistC* is defined as the distance of closest approach (DCA) between the reconstructed particle candidate track and *PV*. *VDistA* and *VDistB* describe the DCA between the daughter particle trajectories and *PV* for ^{3}He and π^-, respectively. In addition, also the opening angle between the two daughter tracks ($\Delta\alpha$) is considered. To account for the reconstruction algorithm's resolution limits, a variable to evaluate the DCA between the two daughter tracks, denoted as the Minimum Track Distance (*MTD*), is defined.

Ultimately, to consider the forward momentum of the particles resulting from the collision in the context of the fixed target setup, it is necessary for the decay vertex to be situated downstream of the primary vertex along the longitudinal axis (PV_z-SV_z<0). When plotting the SV_z in function of the PV_z for all possible combinations of π^- and ^{3}He, as shown in Fig. 6.10, three distinct regions can be distinguished: i) PV_z-SV_z=0: In this scenario, the reconstructed particle decays immediately after being produced, which is represented by the black dashed line. ii) PV_z-SV_z>0: In this case, the reconstructed particle decays in the direction opposite to the beam's orientation in the laboratory frame. These points are located below the line. iii) PV_z-SV_z<0: Here, the reconstructed particle decays following the beam's direction in the laboratory frame. These points are located above the dashed line, where the physical events are expected. It is worth noting that by removing the lower portion, nearly 50% of the combinatorial background can be eliminated.

In addition to the topological decay variables, the Armenteros-Podolanski (AP) plot [173] has proven useful for suppressing the combinatorial background [172]. This plot is employed to visualize the kinematic properties of decaying particles and consists of a two-dimensional scatter plot with transverse momentum ($p_t = p_t^+ = p_t^-$ due to momentum conservation) on one axis and the longitudinal momentum (p_l) asymmetry (α) of the oppositely charged

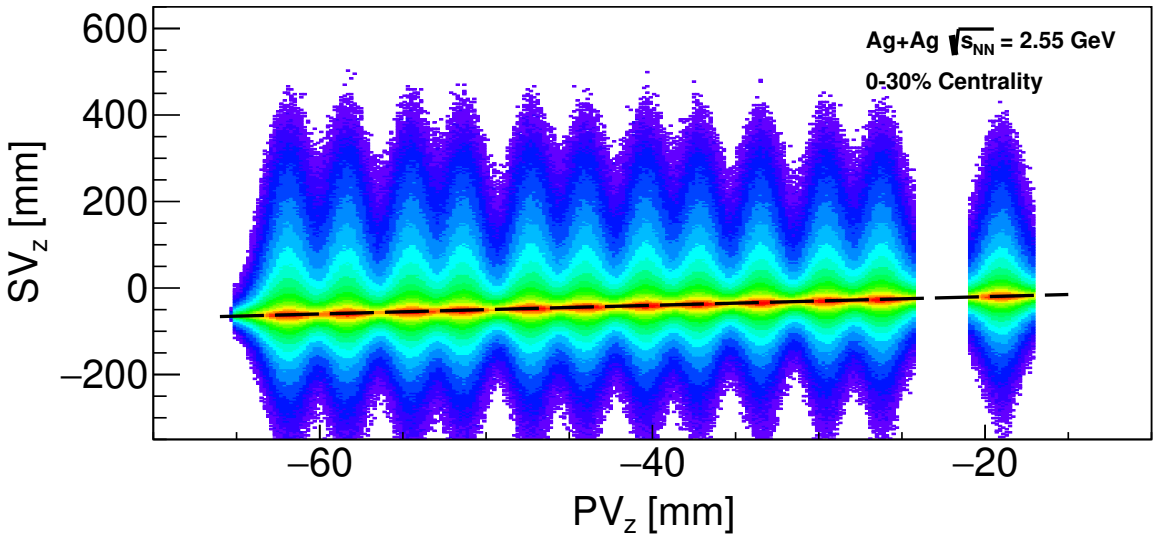

Figure 6.10.: SV_z in function of PV_z along the beam direction z, where the black dashed line represents PV_z-SV_z=0.

decay particles on the other:

$$\alpha = \frac{p_l^+ - p_l^-}{p_l^+ + p_l^-} \,. \tag{6.2}$$

In the AP plot, correlated particles generated from the decay of a heavier mass particle are expected to distribute along an ellipse described by the equation:

$$\left(\frac{\alpha - \alpha_0}{r_\alpha}\right)^2 + \frac{p_t^2}{p_{\text{cm}}^2} = 1 \,, \tag{6.3}$$

where: $\left(\alpha_0 = \frac{m_+ - m_-}{M}, p_t = 0\right)$ is the center of the ellipse, and M is the mass of the mother particle. $r_\alpha = \frac{2p_{\text{cm}}}{M}$ represents the semi-minor axis of the ellipse, with $p_{\text{cm}} = p_{\text{cm}}^{\pm} = \sqrt{\left(\frac{M^2 + m_\pm^2 - m_\mp^2}{2M}\right)^2 - m_+^2}$ is the semi-major axis of the ellipse. It is important to note that this representation is applicable only to ultra-relativistic decaying particles. Therefore, the daughter particles are artificially boosted to $\beta = 0.99$ before constructing the plot. A novel approach to using the AP parameters has been developed in [172]. It involves transforming the ellipse into polar coordinates normalized to the ellipse axes:

$$r_{\alpha p_t} = \sqrt{\left(\frac{\alpha - \alpha_0}{r_\alpha}\right)^2 + \frac{p_t^2}{p_{cm}^2}} \qquad \text{and} \qquad \phi_{\alpha p_t} = \arctan\left(\frac{p_t \, r_\alpha}{p_{cm} \, (\alpha_0 - \alpha)}\right) . \tag{6.4}$$

However, to avoid biasing the invariant mass distribution, only the polar angle ($\phi_{\alpha p_t}$) is considered, as the radius ($r_{\alpha p_t}$) is strongly correlated with the mass of the mother particle. Figure 6.11 displays the AP plot for simulated (see Sec. 6.5) ${}^3_\Lambda$H particles, which have been reconstructed from the boosted daughter particles.

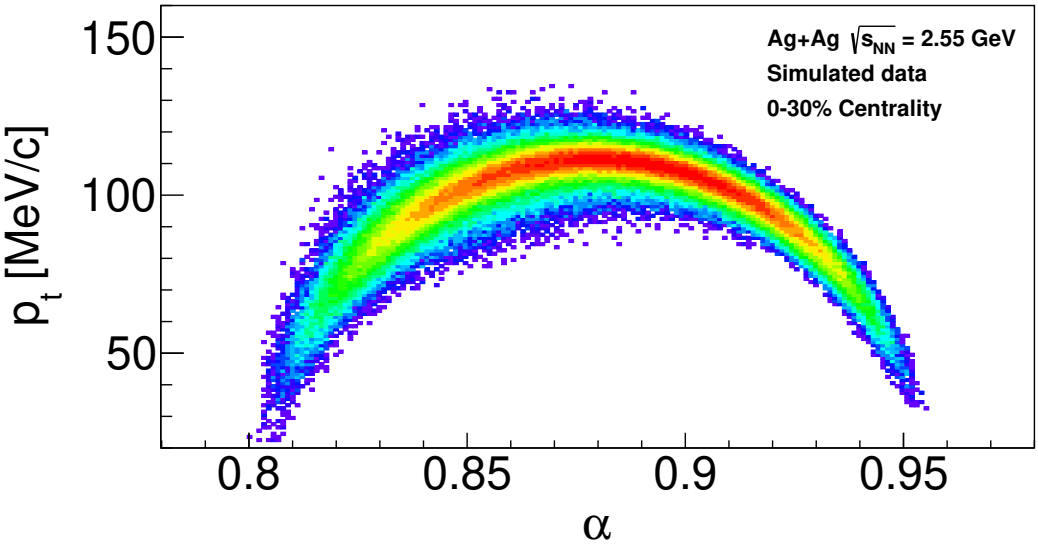

Figure 6.11.: Armenteros-Podolanski plot for reconstructed ${}^{3}_{\Lambda}$H particles from the simulated data.

These variables will be used to apply selection cuts in order to enhance S/B. They can be used as hard-cut directly onto the dataset or they can be optimized via the use of an Artificial Neural Network, found to be more efficient, as detailed in Sec. 6.6 and used in Chapter 7.

6.4. Background estimation

Figure 6.12 displays the multiplicity of ^{3}He (left) and π^- (right) per event, which can lead to as many as 100 ${}^{3}_{\Lambda}$H candidates. Consequently, even after applying cuts to enhance the signal a substantial amount of combinatorial background must be subtracted from the invariant mass spectrum. Various techniques can be employed to replicate the contribution from these candidates and distinguish them from the signal. These techniques rely on the fact that the daughter particles contributing to the background originate from uncorrelated pairs.

In this analysis, the method used is referred to as the *mixed-event* method. Daughter particles are chosen and combined from different events to ensure that they are not correlated. However, to realistically describe the background, specific criteria for the events that can be mixed must be applied: i) only daughters originating from events with the same primary vertex can be mixed, *i.e.*, from the same target segment. ii) The detection efficiency must be consistent to avoid introducing bias. This can be achieved by combining events with similar track multiplicities and from the same day of the beam time, as the detector efficiency might change over time. iii) Furthermore, previous analyses [172, 174] have shown that a minimum opening angle $\Delta\alpha$ greater than 15 degrees between daughter tracks is necessary. This is because, for small opening angles, daughters from the same event cannot be distinguished in the MDC due to the distance between hits being smaller than the

detector's resolution. This effect is not observed for two particles from different events since they are reconstructed independently. Therefore, the mixed-event approach results in an enhanced distribution for low opening angles compared to the combinatorial background that needs to be suppressed.

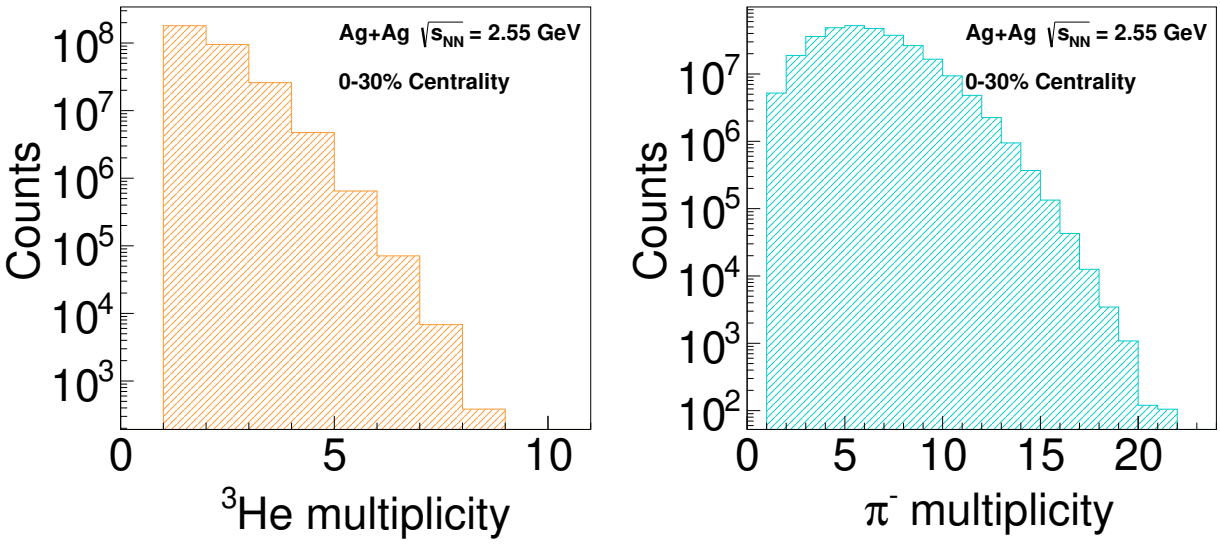

Figure 6.12.: Multiplicity of daughter particles per event, ^{3}He (left) and π^- (right). The analysis is limited to events where at least a pair of daughter candidates is identified.

The combinatorial background reproduced with the mixed-event technique is used to generate the background training sample for the Artificial Neural Network, as discussed in Sec. 6.6.

6.5. Simulated data

The simulated data in HADES experiments is used to correct for detector efficiency and geometrical acceptance, as the experimental setup does not cover the entire phase space. To simulate the production of ${}^{3}_{\Lambda}$H in HIC and its decay, the PLUTO event generator [175] is employed. PLUTO is a collection of C++ libraries designed for simulating particle production at the SIS18 energies. It provides the flexibility to configure particles, reaction channels, and complex reactions while enabling the application of experimental filters on the reaction products.

In HIC, the effective temperature of the system depends on the mass (m) of the system under study and its velocity β:

$$T_{eff} = T_{kin} + \frac{1}{2} m\beta^2 \,, \tag{6.5}$$

where T_{kin} is the kinetic freeze-out temperature. For ${}^{3}_{\Lambda}$H, an effective temperature of 200 MeV has been estimated and used based on previous analysis [172]. To better reproduce the various sources of spurious particles present in experimental data but not accounted for in purely simulated events, an *embedding* procedure is used. This procedure involves embedding the particles generated by PLUTO into experimental data.

The embedding process starts with the use of the HGEANT (Hades GEometry ANd Tracking) package, which is based on the GEANT 3.21 package [176]. HGEANT provides the complete HADES detector geometry and material information necessary to track the generated ${}^{3}_{\Lambda}$H decay daughters through the detector. It also includes a digitizer, which replicates the response of the detector and its electronics. After this step, each real event is embedded with the simulated ${}^{3}_{\Lambda}$H decay, producing a new dataset that is subjected to the same event reconstruction procedure as the original experimental data including all selection cuts and PID. In this way, it ensures that the simulated reconstruction efficiency accurately reflects the real experimental conditions.

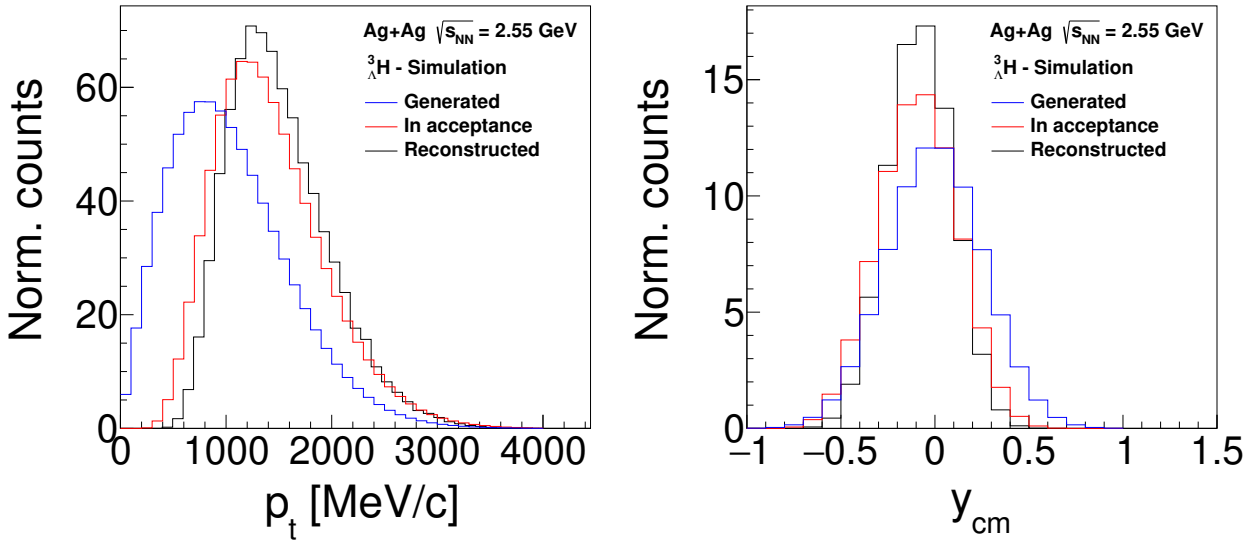

Figure 6.13.: Comparison between the normalized distributions of generated (blue), in acceptance (red) and reconstructed (black) ${}^{3}_{\Lambda}$H from simulated data, separately for the p_t (left) and y_{cm} (right).

The correction for the HADES acceptance and efficiency is performed by calculating the ratio of the initial generated ${}^{3}_{\Lambda}$H from the simulation (N^{sim}_{gen}) to the number of reconstructed (N^{sim}_{rec}) events. This correction accounts for both the total acceptance (a_{tot}) and the efficiency (ε_{tot}). The total acceptance includes the branching ratio (BR) of the decay channel under study and the individual acceptances of the daughter particles. This ensures that the daughter particles traverse the active areas of the detector systems. However, not all particles within the acceptance contribute to the final signal due to the total efficiency. The total efficiency is the product of four different factors: i) *detector efficiency*, accounts for cases where a particle's signal is not recorded because it is either rejected by the electronics threshold or

arrives during the dead time of the detector. ii) *Track reconstruction efficiency*, particularly for high-track multiplicity events, some tracks may not be properly reconstructed. iii) *Track selection efficiency*, assesses the effectiveness of the selection criteria described in Sec. 6.3. iv) *Off-Vertex-Decay topology efficiency*, this accounts for the cuts on the topological variables required to suppress the combinatorial background. The correction for acceptance and efficiency can be summarized by the following equation:

$$\varepsilon_{tot} \times a_{tot} = \frac{N_{rec}^{sim}}{N_{gen}^{sim}} \,. \tag{6.6}$$

This correction can be applied either globally for the full ${}^{3}_{\Lambda}$H data sample, or estimated for different bins of kinematical variables such as p_t and rapidity. The latter is used for the Ag+Ag at 1.58 AGeV data, while the former for the Ag+Ag and Au+Au at 1.23 AGeV due to the lower statistics (see Chapter 7). Figure B.11 shows the effect of the HADES detector acceptance on p_t (left panel) and y_{cm} (right panel). It is particularly noticeable that the acceptance cuts away events with low p_t (<500 MeV/*c*) and those with positive y_{cm} (>0.5).

In addition to correcting for the detector's acceptance and efficiency, the simulated data are also employed to generate the signal training sample for the artificial neural network (ANN), as discussed in the next section.

6.6. Artificial Neural Network

In order to increase the separation between the reconstructed ${}^{3}_{\Lambda}$H and the combinatorial background, an ANN has been employed. ANNs are well-suited for handling multiple inputs, allowing them to capture intricate relationships between different features for making predictions or classifications. Specifically, it has been utilized the MultiLayer Perceptron (MLP) from the ROOT package TMVA (Toolkit for MultiVariate Analysis) [177].

The MLP architecture, illustrated in Fig. 6.14, is composed of multiple layers. In an MLP, the initial layer is the *input layer* (Layer 0), which is designed to accommodate several inputs. Each input neuron represents one input variable (the topological variables presented in Sec. 6.3), and there is also a bias neuron set to 1, which ensures the convergence of the optimization process. Following the input layer, there are one or more layers known as *hidden layers* (Layer 1,2), responsible for processing the input information and learning complex relationships within the data. The final layer, typically referred to as the *output layer*, produces the network's classifications based on the learned patterns. The flow of information in the MLP is called the *Feedforward Process*, which progresses from the input layer to the output layer. Each connection between neurons of different layers, known as a *synapse*, is associated with a weight calculated by the *synapse function x*. In TMVA its implemented the so-called *Sum*:

$$x_j^l = w_{0j}^l + \sum_{i=1}^{n} y_i^l w_{ij}^l \,, \tag{6.7}$$

where j is the index of the neurons executing the function, i the index of the neurons from the previous layer l, w_{0j}^l is the weight of the bias neuron, n represents the number of neurons

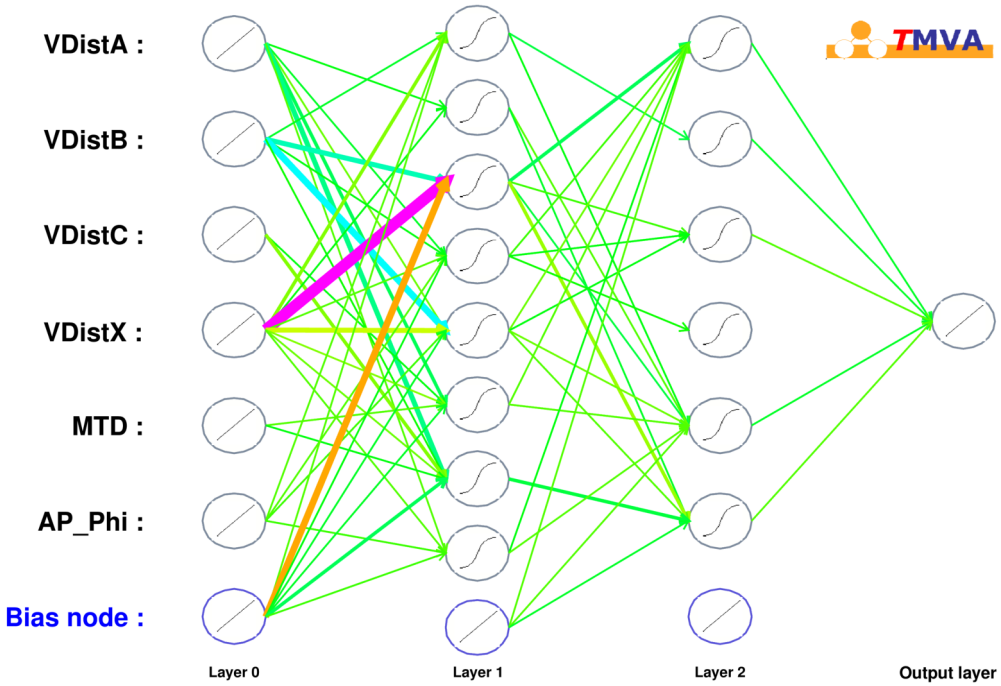

Figure 6.14.: Architecture of the MLP after training the Ag+Ag at 1.58 AGeV data. The thickness of the arrows (synapses) indicates how strong the weights are between the neurons. The straight line in the node indicates a linear function, while the wavy one the sigmoid function.

in the j-layer, y_i^l is the output value of neuron i from the previous layer, and w_{ij}^l is the weight of the synapse connecting neuron i from layer l with neuron j from layer $l+1$. The result from the synapse function (x) is then passed to the *neuron activation function* (α). The different options provided by TMVA return similar results, and the one called *sigmoid* is used for the analysis since it provides the fastest and more reliable results:

$$\alpha(x) = \frac{1}{1+e^{-x}}\,. \tag{6.8}$$

In order to optimize the classification performance of an ANN, it needs to be trained: adjusting the weights through a minimization procedure. The most common minimization algorithm used for this purpose is the *Back Propagation*. It is a supervised learning approach, meaning that the desired outputs are known. For this analysis, the output should clearly distinguish between signal (1) and background (0). Therefore, labeled datasets are used, with a set of 50,000 simulated events for the signal and 50,000 mixed events for the background.

The training process starts with assigning random weights to the neural network. For each training event, the neural network response is computed and compared with the known training samples. An error function (E) measures the agreement between the network response and the desired output. Based on the differences for all training events, the weights are updated according to the gradient of E:

$$\vec{w}^{l+1} = \vec{w}^{l} - \eta\vec{\nabla}_{\vec{w}}E\,, \tag{6.9}$$

where η is the learning rate. The weights are adjusted individually for each event from the training sample. Additionally, the entire training sample is processed multiple times, in what is called a *training cycle* (N_{cycle}).

After the training phase is completed, the ANN's performance is evaluated using an independent test sample of the same size. The results are visualized using *ROC* curves (Receiver Operating Characteristic), where the *x*-axis represents the signal efficiency, *i.e.*, the fraction of events from the signal sample that are correctly classified as signal. The *y*-axis represents the background rejection, *i.e.*, the fraction of events from the background sample that are correctly classified as background. The ROC curve provides a visual representation of how well the ANN is classifying events. The worst case scenario is represented by a line that connects the points (0,1) and (1,0), indicating that the training generated a random response. The ideal scenario is represented by a step function passing through the point (1,1), where the signal is perfectly distinguishable from the background.

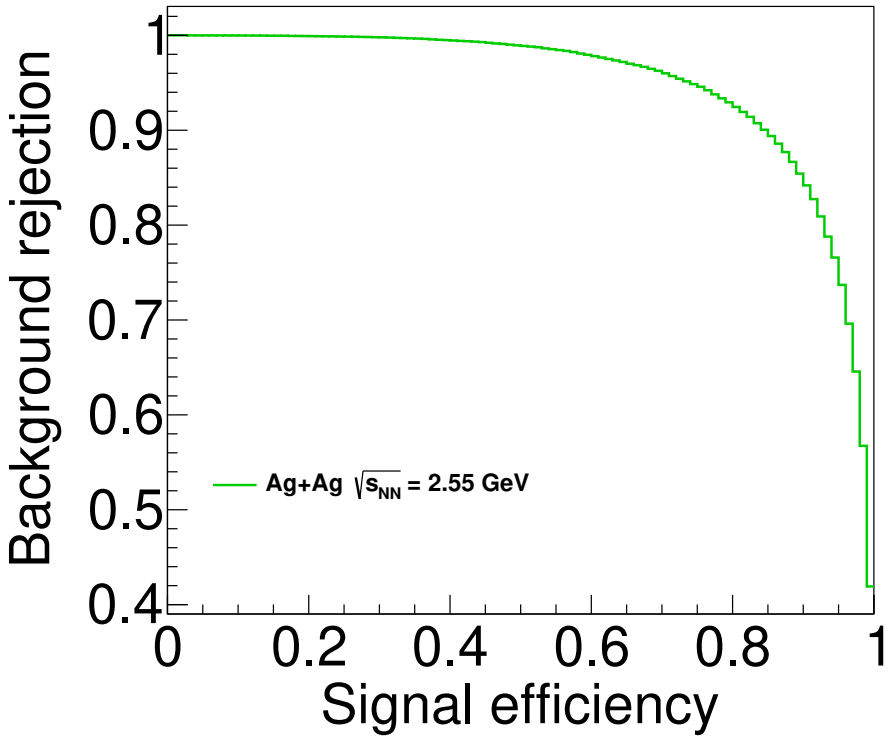

Figure 6.15.: ROC curves for the Ag+Ag at 1.58 AGeV dataset.

In this analysis, a total of seven ($N = 7$) inputs is considered, which include the five topological decay variables VDistA, VDistB, VDistC, VDistX, and MTD, the AP azimuthal angle ($\Phi_{\alpha p_t}$), and 1 bias neuron. The architecture of the neural network consists of two hidden layers. The first hidden layer has *N+2* neurons, and the second hidden layer has *N* neurons. The synapse function used is sum, and the activation function is sigmoid. The Back Propagation algorithm is employed, and N_{cycle} is set to 1500. The ROC curve, as shown in

Fig. 6.15, is close to the ideal scenario, indicating that this configuration provides a good compromise between the performance of the ANN and the time required for training. Various MVA approaches were explored, including different configurations of the MLP method, and all the tested setups provided inferior results.

Another useful way to assess the performance of the MLP is by plotting the distributions of the MLP response for the testing samples separately, as shown in Fig. 7.2 in the next Chapter. This visualization highlights the discriminator power of the MLP, with the majority of the background events concentrated near 0 and the signal events near 1. However, due to the limitations of the MLP, the distributions exhibit long tails. The MLP response parameter can be interpreted as the probability of a given set of input parameter values belonging to the signal category. When the trained MLP is applied to the experimental data, it classifies all the ${}^{3}_{\Lambda}\mathrm{H}$ candidates and assigns an MLP response value to each of them. A cut on this value is then used in the next Chapter to reduce the combinatorial background and extract the signal. The choice of the cut value is a compromise between the purity of the signal and the available statistics. This compromise can be quantified by the *Significance*:

$$Significance = \frac{S}{\sqrt{B}}\,, \tag{6.10}$$

where S is the signal and B the background. The Significance indicates how many standard deviations (σ) the signal exceeds the hypothesis of being a background fluctuation. The optimal MLP response cut value is determined by maximizing the Significance.

This Chapter focused on the detailed methodology employed for analyzing HIC data from the HADES Ag+Ag at 1.58 AGeV campaign to study the ${}^{3}_{\Lambda}\mathrm{H}$ production. Detailed analyses of the same study for datasets from Ag+Ag and Au+Au collisions at 1.23 AGeV can be found in the Appendices. It encompasses a series of steps, including event selection, centrality determination, particle identification, topological cuts, and the utilization of neural networks. The primary objective is to accurately distinguish the signal (${}^{3}_{\Lambda}\mathrm{H}$) from the combinatorial background events. Various selection criteria, such as event quality checks, centrality determination through the Glauber Monte Carlo model, and particle identification techniques like time-of-flight and specific energy loss, are implemented to ensure the purity of the event sample. Additionally, various topological cuts, and mixed-event technique are applied to effectively suppress background events. The role of the simulated data embedded into real data is crucial for accounting for detector efficiency and acceptance, providing a realistic representation of both signal and background events. Finally, Artificial Neural Networks, specifically MultiLayer Perceptrons (MLP), play a central role in the analysis. They are trained to classify events from the different datasets as signal or background, allowing to maximize the significance of the signal.

7. Experimental results and Discussion

The trained ANN is used with the selected track pairs (see previous Chapter) to reconstruct and identify ${}^{3}_{\Lambda}$H events, and extract information about the normalized ${}^{3}_{\Lambda}$H production yield in HIC within the HADES acceptance. Finally, the ${}^{3}_{\Lambda}$H production cross-section at different collision energies and in-medium conditions is extracted.

In the first section, the results from the invariant mass technique obtained with the use of the ANN are detailed for the three systems. In Sec. 7.2, the obtained statistics for Ag+Ag at 1.58 AGeV allow for a differential study of ${}^{3}_{\Lambda}$H production with respect to the transverse momentum and rapidity in the center of mass frame. Subsequently, the obtained yields are corrected for the acceptance and efficiency of the HADES detector. Finally, the production cross-sections are extracted and normalized with respect to the total reaction cross-section beam-target estimated by the Glauber MC model and the systematic uncertainties arising from the use of topological cuts are investigated.

7.1. Invariant mass spectra

Previous analysis [172] showed that to train the ANN for better discrimination between the combinatorial background and the signal, it is necessary to first apply hard cuts to the topological variables. This is because of the exponential nature of weak decays, which predominantly occur close to the primary event vertex where the majority of the combinatorial background occur. In scenarios where the decay vertex is too close to the target, the topological decay variables have limited discrimination power and are therefore not suitable for distinguishing between actual decays and combinatorial background. As a result, a set of pre-cuts is applied for the study of ${}^{3}_{\Lambda}$H which where determined to optimize the ANN training [172], and Table 7.1 displays the ones used for the three datasets. No pre-selection is applied to the Armenteros-Podolanski polar angle since it is a kinematic variable.

	VDistA	VDistB	VDistC	VDistX	MTD
Pre-cuts [mm]	>2	>14	<16	>45	<20

Table 7.1.: Selection criteria used to prepare the training and test samples for the ANN, and as pre-selection for the experimental data. Values are taken from [172].

In the following subsections, the invariant mass spectra obtained by applying MLP response cuts are shown.

7.1.1. Ag+Ag at 1.58 AGeV

Figure 7.1 displays the ANN input variables for the Ag+Ag dataset at 1.58 AGeV with the pre-cuts from Table 7.1. The distributions shown are the ${}^{3}_{\Lambda}\mathrm{H}$ simulated signal and combinatorial background samples, each with 50000 events, such that the shape is compared. Most of the input parameters exhibit strong discrimination power. In particular it can be observed that for the simulation the MTD variable has a peak at 0 while the background data show a flat behavior across the entire range and a similar trend is observed for VDistC. This is why upper limits have been chosen for these two variables. For the other topological variables, it is evident that the background tends to reach its maximum value at small distances, hence lower limits are considered. For $\Phi_{\alpha p_t}$ it can be seen that the simulated distribution is symmetrically centered around 85°, while the background exhibits an asymmetric and wider distribution.

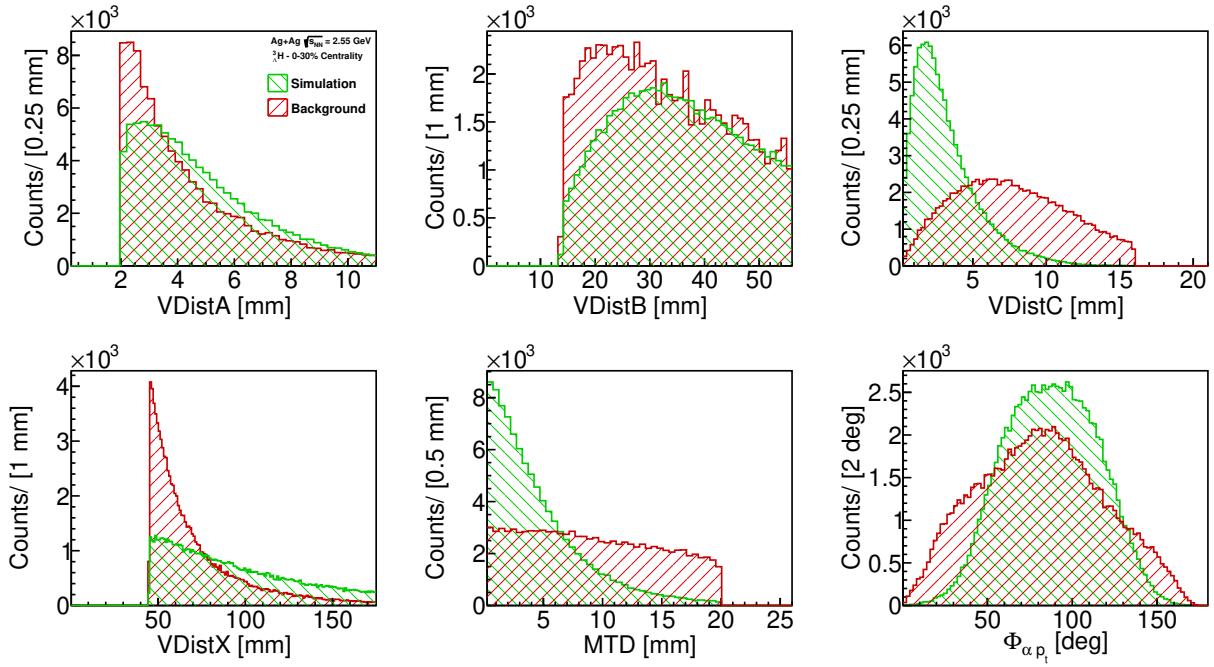

Figure 7.1.: ${}^{3}_{\Lambda}\mathrm{H}$ simulated signal (green) and combinatorial background (red) distributions of the input variables used to train and test the ANN with the pre-cuts from Table 7.1.

After the training procedure the MLP response distribution for simulation and background is produced, see Fig. 7.2. It is possible to observe how strong is the separation between the response parameter for the simulation, which has a peak at 1, and the background which has a peak at 0. It is essential now to choose the cut on the MLP response which will then separate the background on the left side and signal on the right. Once this cut is chosen there are two types of unwanted contributions arising from wrong classification of signal/background events: i) type-I (α), the integral of the red distribution on the right side of the cut represents the background wrongly identified as the signal. ii) Type-II (β), the integral of the green distribution on the left side of the cut represents the signal

wrongly identified as background. In this case, the purity of the sample is enhanced by minimizing α, and this requires high values of MLP response. However, it is possible to observe that in this case the signal efficiency is reduced since β will, on the other hand, increase.

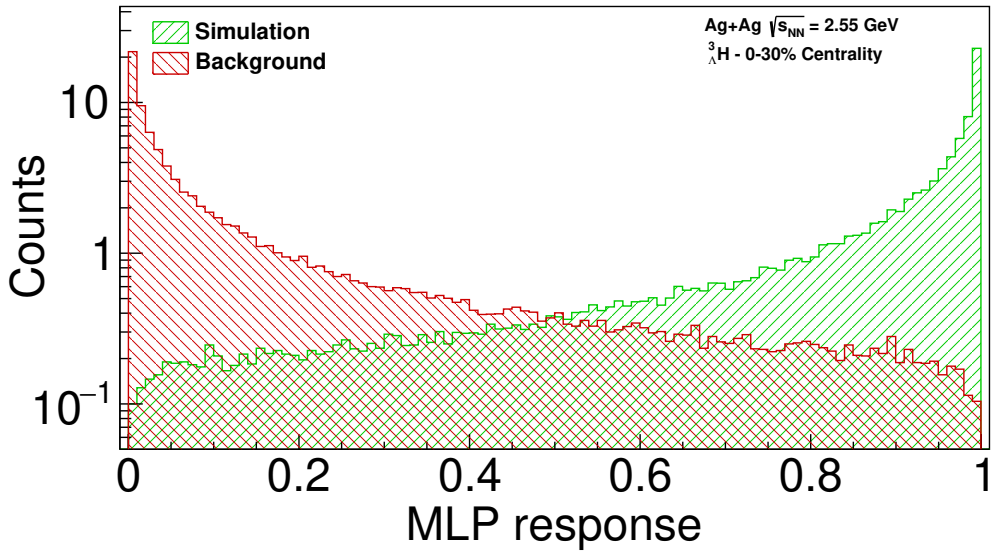

Figure 7.2.: Logarithmic representation of the MLP response distribution for the $^{3}_{\Lambda}$H simulated signal (green) and combinatorial background (red).

To choose the MLP response cut and find the best compromise, as anticipated in Sec. 6.6, it is necessary to maximize the significance of the signal. To determine the significance, the information about the signal (S) and the background (B) is extracted from the invariant mass distributions of the ^{3}He-π^{-} pairs using both experimental and mixed-event data. The number of pairs generated with the mixed-event method is orders of magnitude larger than that of the experimental data. Therefore, it is essential to normalize the mixed-event sample to the experimental data. The normalization procedure involves utilizing the so-called *side-bands*, which are regions located $\pm 6\sigma$ away from the signal region. This approach ensures that only the background is considered when calculating the normalization factor (N_{factor}). The boundaries of the side-bands are determined by fitting a Gaussian function to the signal peak in the invariant mass region expected for the $^{3}_{\Lambda}$H in the experimental data to obtain the mean position (μ) and standard deviation (σ). Finally, the integrals of the side-bands for the experimental (M_{inv}^{exp}) and the mixed-event data (M_{inv}^{mix}) distributions are computed, and the ratio between the two is determined:

$$N_{factor} = \frac{\int_{-\infty}^{\mu-6\sigma} dM_{inv}^{exp} + \int_{\mu+6\sigma}^{+\infty} dM_{inv}^{exp}}{\int_{-\infty}^{\mu-6\sigma} dM_{inv}^{mix} + \int_{\mu+6\sigma}^{+\infty} dM_{inv}^{mix}} \,. \tag{7.1}$$

Once the background has been normalized, as shown in the left panel of Fig. 7.3, the background subtraction can be performed, as depicted in the right panel of Fig. 7.3. For this procedure, the two histograms are subtracted bin wise, and the displayed error is calculated

under the assumption of two independent histograms.

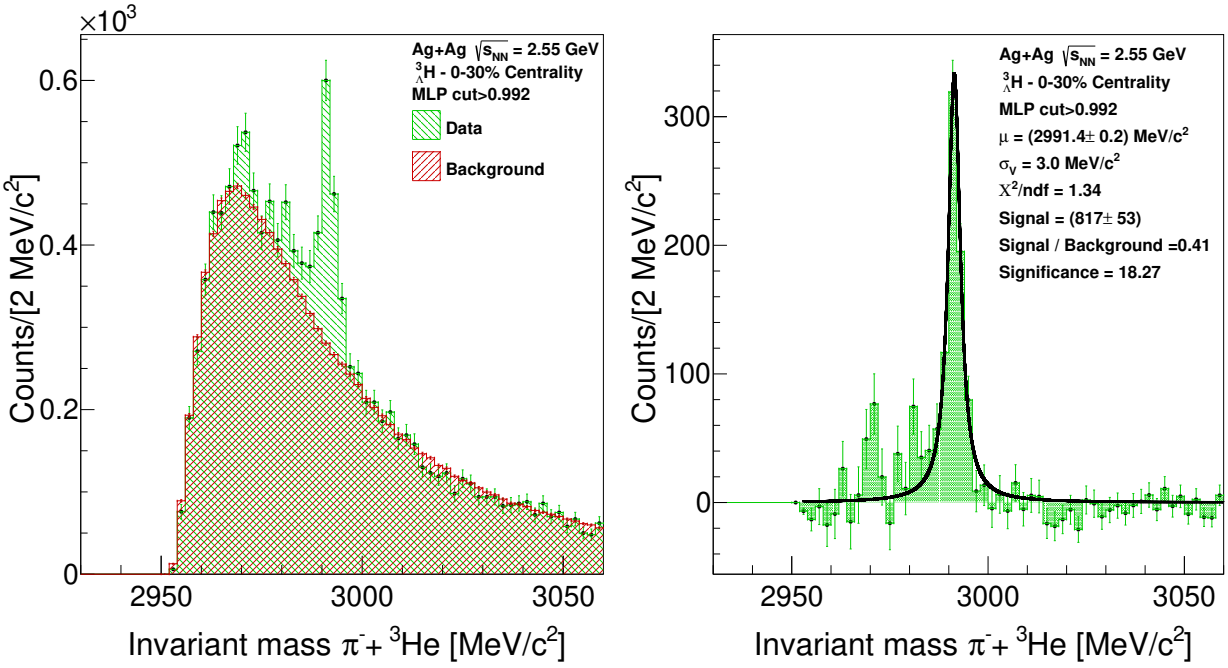

Figure 7.3.: Invariant mass distribution for ^{3}He-π^- pairs. Left. Distribution of the experimental data (green) together with the normalized combinatorial background (red). Right. Experimental data distribution after background subtraction together with the Voigt function fit (black). The fit results are shown on the plot.

After the background subtraction (M_{inv}^{sub}), the signal (S) is calculated by fitting the distribution with a Voigt function, which is a convolution between a Gaussian and a Breit-Wigner (BW) distribution:

$$V(x,\sigma,\Gamma) = \frac{1}{\sigma\sqrt{2\pi}} \int_{-\infty}^{\infty} \frac{e^{-\frac{(x-\mu)^2}{2\sigma^2}}}{\sqrt{2\pi}\Gamma} \frac{1}{1+\left(\frac{x-\mu}{\Gamma}\right)^2} d\mu\,, \tag{7.2}$$

where σ represents the standard deviation of the Gaussian part of the function, Γ represents the full-width at half-maximum (FWHM) of the BW part of the function, and μ represents the peak position. The Voigt function is used because it provides a better description of the distribution tails. For the fit shown in Fig. 7.3 the χ^2_{Voigt}/ndf=1.34 is smaller compares to the one obtained with a Gaussian fit χ^2_{Gauss}/ndf=1.52, where ndf (number of degrees of freedom) is taken as the number of data points minus the number of fit function variables. The standard deviation σ_V from the Voigt fit is estimated by finding the extremes on the left and right side of the peak for which the integrated area gives 68.2% of the total area. The signal (S) is then calculated as:

$$S = \int_{\mu-2\sigma_V}^{\mu+2\sigma_V} dM_{inv}^{sub}\,. \tag{7.3}$$

The same integral range is used to calculate the background (B). In this case, the distribution used is from the mixed-event data after normalization:

$$B = \int_{\mu-2\sigma_V}^{\mu+2\sigma_V} dM_{inv}^{mix} \,. \tag{7.4}$$

From Fig.7.3, in particular after the background subtraction (right panel), it can be noticed that the combinatorial background is well reproduced by the mixed events in the high-mass region (right side of the peak). However, on the left side, around 2700 MeV/c^2, there is an underestimation of the background that needs further investigation. This can be achieved, for example, by examining ^{3}He-π^+ pairs to see if the structure is reproduced.

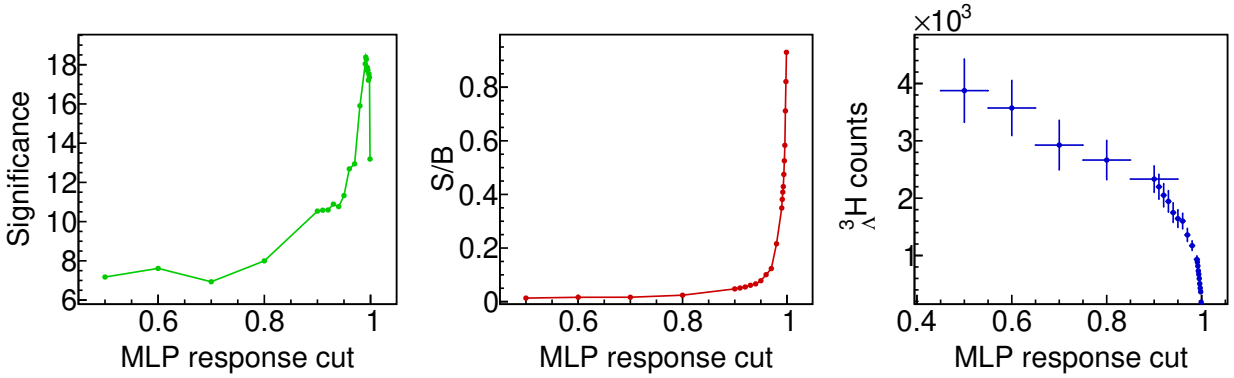

Figure 7.4.: Trends of significance (left), S/B (middle) and $^3_\Lambda$H counts (right) in function of the MLP response cut.

The MLP response cut used for the following analyses has been determined through an optimization procedure aimed at maximizing the significance of the $^3_\Lambda$H peak. The optimization was carried out iteratively, starting from MLP response of 0.5, where α=β, up to 1. Figure 7.4 shows that the maximum significance is obtained for MLP=0.992 with Significance=18.25. This leads to S/B=0.41 and S=816±53 events for reconstructed $^3_\Lambda$H with a mass of 2991.4±0.2 MeV/c^2 and a width of 3 MeV/c^2. The mass found is in agreement with the nominal mass of the $^3_\Lambda$H, which can be obtained from its constituents:

$$M_{^3_\Lambda\mathrm{H}} = M_{^2\mathrm{H}} + M_\Lambda - B_\Lambda = 2991.16 \pm 0.06\,\mathrm{MeV}/c^2\,, \tag{7.5}$$

where $M_{^2\mathrm{H}}$ is the deuteron mass [178], M_Λ is the mass of the Λ [54], and B_Λ is the binding energy $\Lambda-^2$H from the emulsion analyses [69].

The same steps have been followed to obtain the invariant mass spectra for the other systems. To help the readability of the following sub-sections the plots related to the ANN have been placed in the Appendices, and only the results for the MLP response are presented.

7.1.2. Ag+Ag at 1.23 AGeV

The same procedure described in the previous sub-section is applied to the Ag+Ag at 1.23 AGeV dataset. From Fig. B.13, it is possible to see that the topological variables exhibit

a similar behavior as the one described for the higher energy dataset. The MLP response distribution for the simulation and background shows a strong discrimination power for S and B, as it can be seen from Fig. B.14. Finally, the same procedure has been followed to normalize the background (left panel of Fig. 7.5), and after it has been subtracted from the experimental data to obtain the signal peak (right panel of Fig. 7.5). For this dataset, it can be seen that the background is well reproduced in both sides of the peak.

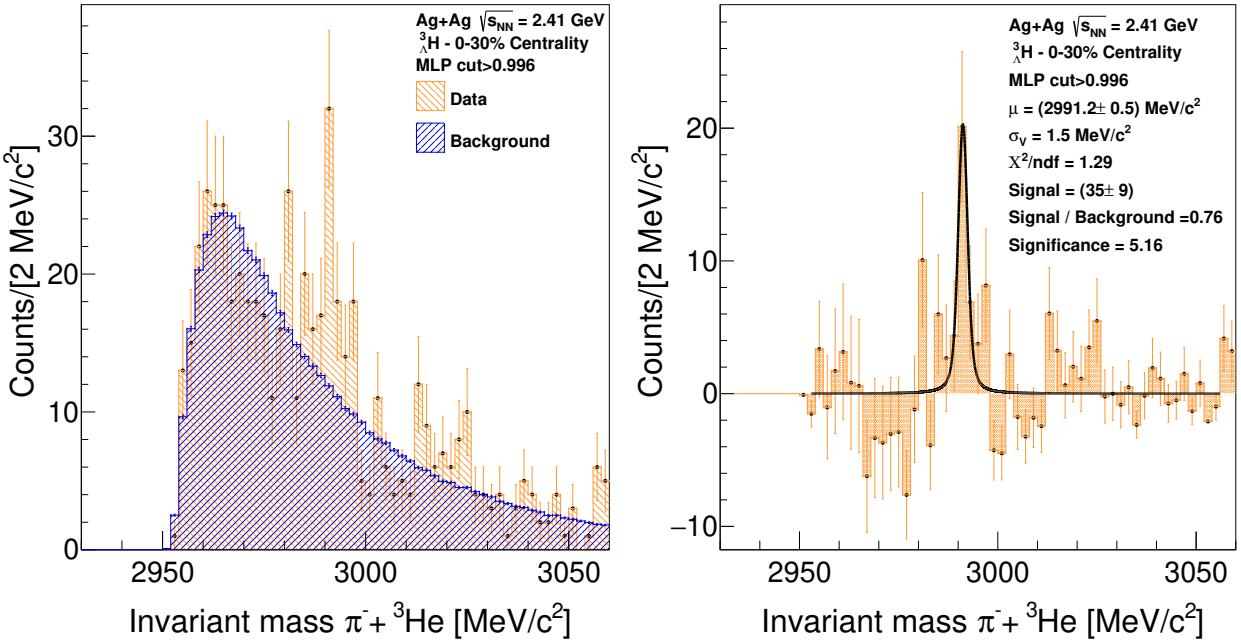

Figure 7.5.: Invariant mass distribution for ^{3}He-π^- pairs. Left. Distribution of the experimental data (orange) together with the normalized background (blue). Right. Experimental data distribution after background subtraction together with the Voigt fit (black). The fit results are shown on the plot.

Figure 7.6 shows that the maximum significance is achieved for MLP response cut of 0.996 with Significance=5.16. This leads to S/B=0.76 and S=35±9 events, for reconstructed $^3_\Lambda$H with a mass of 2991.2±0.5 MeV/c^2 with a width of 1.5 MeV/c^2. The amount of signal found is reduced compared to the Ag+Ag at 1.58 AGeV, by two main factors: i) the amount of beam time for the lower energy system is reduced by a factor 10. ii) The beam energy is below the strangeness production threshold from isolated nucleon-nucleon collisions (1.58 GeV). The fact that the extracted significance for the peak exceeds the 5σ is generally accepted by the particle physics community as a criterion to claim a new discovery [179]. This is because it ensures that the probability of this peak to be random noise is around 0.00006%. In this case, since the production $^3_\Lambda$H has been found below the production threshold, this implies for the importance of other production mechanisms, as will be discussed in Sec. 7.5.

Furthermore, it can be observed in the right panel of Fig. 7.6 that the extracted $^3_\Lambda$H counts for a low MLP response cut (<0.9) fluctuate significantly and have large error bars. This

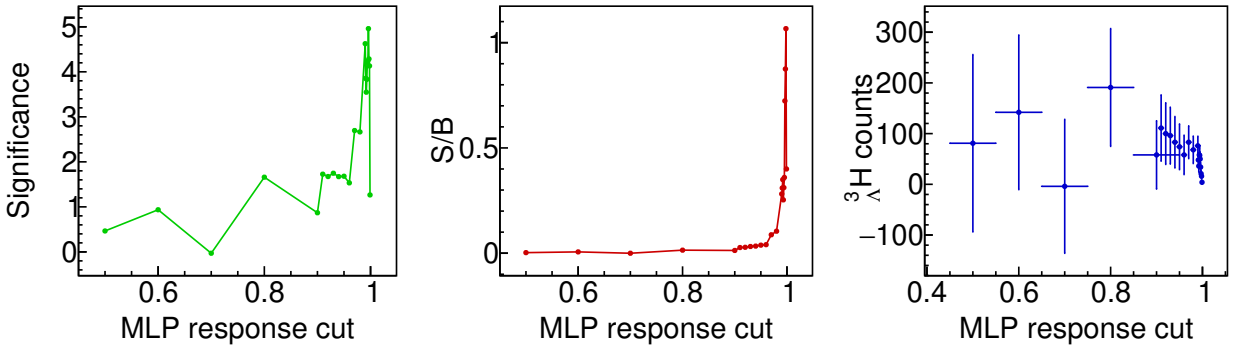

Figure 7.6.: Trends of significance (left), S/B (middle) and count (right) in function of the MLP response cut.

phenomenon is also related to the expected low production cross-section for beam energy below the $^{3}_{\Lambda}$H production energy threshold.

7.1.3. Au+Au at 1.23 AGeV

The same procedure described in the previous sub-sections is applied to the Au+Au at 1.23 AGeV datatset. Figures A.13 and A.14 demonstrate that the ANN trained for this system exhibits similar behavior in discriminating S and B compared with the previous sub-sections. Likewise for this system, the background has been normalized and subtracted from the experimental data, as it is shown in Fig. 7.7.

Figure 7.8 shows that the maximum significance is achieved for MLP response cut 0.995 with Significance=4.0. This leads to S/B=0.12 and S=130±35 events, for reconstructed $^{3}_{\Lambda}$H with a mass of 2991.3±0.6 MeV/c^2 with a width of 2.1 MeV/c^2. Also in this case, the result indicates the $^{3}_{\Lambda}$H production below the threshold. However, here since the significance level is lower than 5σ, a clear conclusion cannot be made, as will be discussed in Sec. 7.5.

7.2. Differential analysis

The study of the $^{3}_{\Lambda}$H production in function of kinematical variables, such as p_t and y_{cm}, is important as it helps to understand the processes leading to its formation. p_t represents the component of momentum perpendicular to the beam direction and, since, before the collision the particles do not carry any perpendicular component, its study provides information about the colliding system. On the other hand, y_{cm} offers insights into particle emission in the direction of the beam relative to the center of mass of the collision, where -1 corresponds to beam-like particles and +1 to target-like particles. Consequently, for the Ag+Ag at 1.58 AGeV dataset, which provides the highest amount of reconstructed signal, it is possible to perform a multi-differential analysis. The data are divided into (p_t, y_{cm}) bins within the available phase-space: 5 p_t bins with a width of 420 MeV/c, ranging from 600 to 2700 MeV/c, and 4 y_{cm} bins with a width of 0.2, ranging from -0.5 to 0.3. The invariant

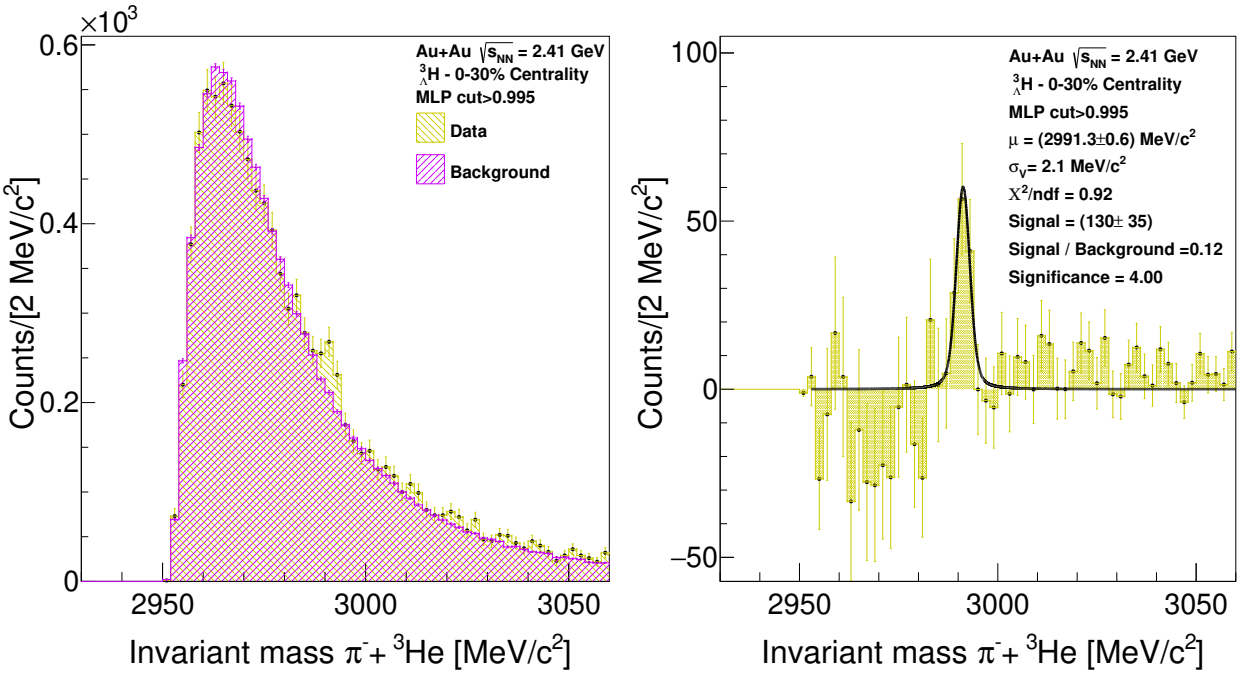

Figure 7.7.: Invariant mass distribution for ^{3}He-π^- pairs. Left. Distribution of the experimental data (yellow) together with the normalized background (pink). Right. Experimental data distribution after background subtraction together with the Voigt fit (black). The fit results are shown on the plot.

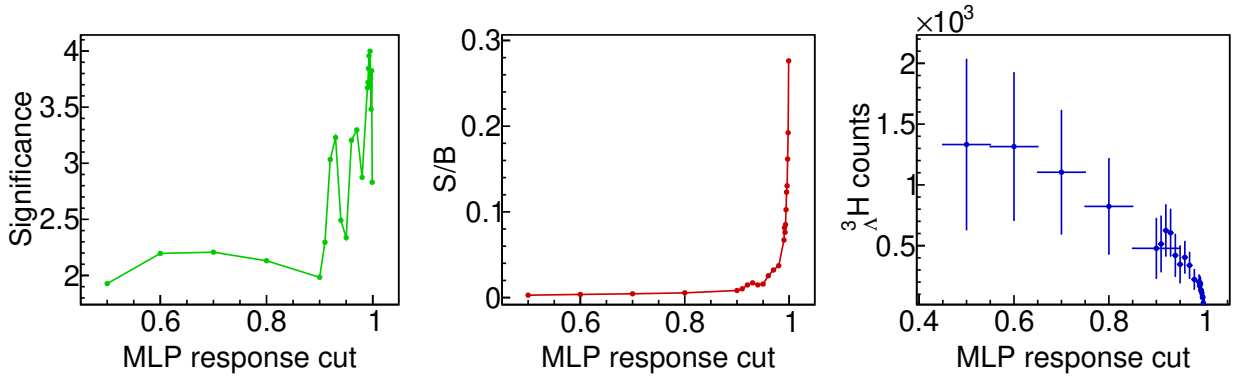

Figure 7.8.: Trends of significance (left), S/B (middle) and count (right) in function of the MLP response cut.

mass spectra corresponding to the 20 (p_t, y_{cm}) intervals can be found in the Appendix C, see Fig. C.1.

The extracted signal and the significance from the experimental data after the background subtraction are presented in Fig. 7.9. For some of the bins, due to reduced statistics, the fitting procedure failed. In these cases, the boundaries for the integral were fixed at 2991.2 MeV/c^2 (the nominal mass of the ${}^{3}_{\Lambda}$H) $\pm 2\sigma_V$ (see Fig. 7.3). Additionally, there are empty bins in the plot that did not meet certain conditions: i) the obtained invariant mass histogram is discarded if the total integral of the experimental spectrum is less than 100 events, as the method explained in Sec. 7.1.1 cannot be applied. ii) Peaks with fewer than 10 counts and a significance less than 1 are not statistically meaningful and, therefore, are discarded.

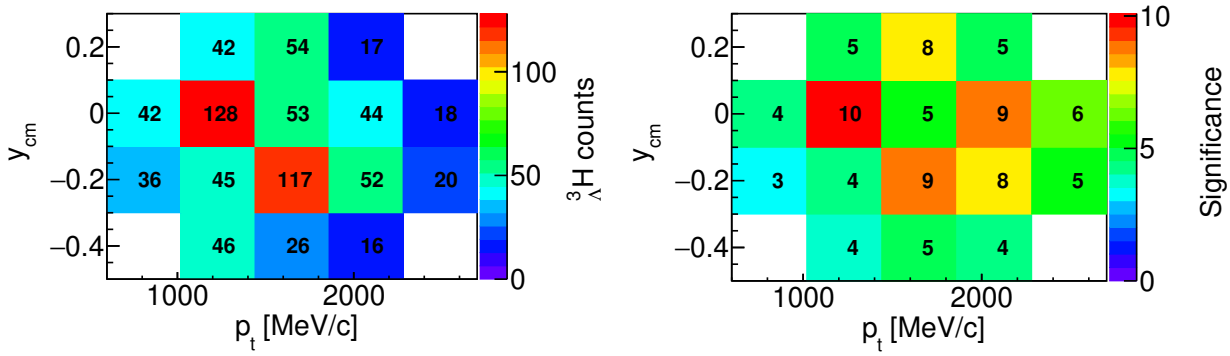

Figure 7.9.: ${}^{3}_{\Lambda}$H differential analysis results for the Ag+Ag at 1.58 AGeV data in the 0-30% centrality region. Left. The reconstructed ${}^{3}_{\Lambda}$H signal. Right. The extracted significance.

The right panel of Fig. 7.9 reveals that all the extracted peaks have a significance larger than 3, ensuring a good quality of the peaks. The left panel of Fig. 7.9 displays the signal counts that will be used to study the production rate kinematics in the following analysis.

7.3. Acceptance and efficiency correction

The data analyzed so far need further consideration before being used to extrapolate physical quantities. In particular, it is necessary to correct the yields for the HADES detector acceptance, since it doesn't cover the full phase space, and for its efficiency, see Sec. 6.5. The correction is done by the use of the simulation, in this way by comparing the amount of generated events with the amount of reconstructed ones it is possible to asses the correction factor as defined by Eq. 6.6. For the analysis that considers only selection on the centrality, one value per system is extracted from the simulation, as summarized in Table 7.2.

For the differential analysis conducted for the Ag+Ag at 1.58 AGeV data the corrections

	Ag+Ag (1.58 AGeV)	Ag+Ag (1.23 AGeV)	Au+Au (1.23 AGeV)
Acc × Eff	4.85×10^{-4}	4.0×10^{-4}	5.2×10^{-4}

Table 7.2.: Acceptance × Efficiency correction factors extrapolated from the simulation for the 0-30% centrality events selected for different datasets.

need to be calculated for the individual bins:

$$\varepsilon_{tot}(p_t, y_{cm}) \times a_{tot}(p_t, y_{cm}) = \frac{N^{sim}_{rec}(p_t, y_{cm})}{N^{sim}_{gen}(p_t, y_{cm})} \,. \tag{7.6}$$

Using this equation it is possible to extrapolate, from the simulation, the correction factors as depicted in Fig. 7.10. The highest correction factors are for low p_t and positive values of y_{cm}. This is due to the acceptance effects, see Fig. B.11.

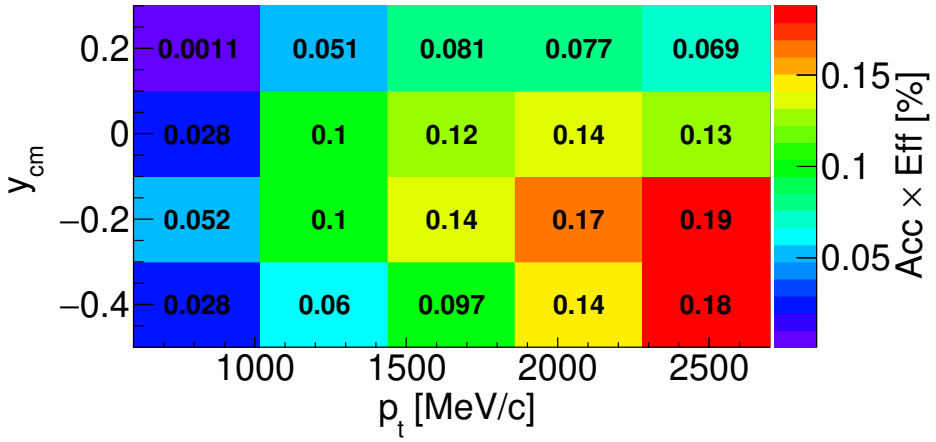

Figure 7.10.: Acceptance × Efficiency correction factors extrapolated from the simulation for the multi-differential analysis.

These correction factors are used in the next section.

7.4. Production cross section

In order to calculate the production cross-section of the ${}^{3}_{\Lambda}\mathrm{H}$, within the HADES acceptance[1], for the different datasets Eq. 2.1 can be utilized. In the following, it is rewritten in terms of the experimental production cross-section of the ${}^{3}_{\Lambda}\mathrm{H}$ from HIC:

$$\sigma_{{}^{3}_{\Lambda}\mathrm{H}} = \frac{N_{MEAS}}{N_{evt} \times n \times t} \,, \tag{7.7}$$

[1]The HADES detector acceptance intervals of p_t and y_{cm} can be found in Fig. 7.9.

where $N_{MEAS} = N_{SIG}/\left(Acc \times Eff\right)$ is the total amount of measured ${}^{3}_{\Lambda}$H corrected for the HADES acceptance and efficiency, N_{evt} is the total amount of events used in the analysis, $n = N_A\rho/M_{mol}$ is the number density of the target, with $N_A[mol^{-1}]$ the Avogadro number, $\rho[g \cdot cm^{-3}]$ the density, and $M_{mol}[g \cdot mol^{-1}]$ the molar mass of the target, and $t[cm]$ is the target thickness. For 12 (15) targets with thickness of 40 μm in Ag data at 1.58 AGeV (1.23 AGeV) amounts to 0.048 cm (0.06 cm). For the Au data at 1.23 AGeV, for 15 targets with a thickness of 25 μm it amounts to 0.0375 cm. The quantities used for the estimation together with the resulted production cross-section for 0-30% most central events including both the statistical and systematical uncertainties (explained below), are summarized in Table 7.3. In addition, the ratio between the production ${}^{3}_{\Lambda}$H for the low-to-high energy Ag+Ag dataset amounts to 0.30±0.08(stat.)±0.04(sys.).

	Ag+Ag (1.58 AGeV)	Ag+Ag (1.23 AGeV)	Au+Au (1.23 AGeV)
N_{evt} [10^9]	2.99	0.42	2.19
N_{MEAS} [10^5]	16.8±1.1	8.5±0.2	2.5±0.7
nt [10^{21} cm^{-2}]	2.84	3.55	2.21
$\sigma_{^{3}_{\Lambda}\mathrm{H}}$ [mb]	199±13±20	59±15±6	52±14±5
$\sigma_{^{3}_{\Lambda}\mathrm{H}}/\sigma_{tot}$ [10^{-5}]	4.34±0.28±0.50	1.30±0.34±0.15	0.75±0.21±0.09

Table 7.3.: Production cross-section estimate of the ${}^{3}_{\Lambda}$H from HIC for the 0-30% centrality region for different datasets, within the detector acceptance (see Fig 7.9 for the (p_t, y_{cm}) intervals), with the first uncertainty being statistical and the second one systematic. The quantity nt for the Ag+Ag 1.58 AGeV dataset differs from the lower energy since the number of segments used is reduced to 12, as opposed to 15 segments used in the Ag+Ag 1.23 AGeV dataset.

Systematic uncertainties can originate from various potential sources, and they must either be assessed for their influence on the analysis results or, when feasible, identified and subsequently eliminated. In the analysis presented in this thesis, a significant contribution comes from applying cuts to the topological variables using the ANN. These cuts are crucial because they effectively reduce the combinatorial background, making it possible to observe and study the signal. Consequently, systematic uncertainties are assessed by comparing results obtained with the ANN against two sets of hard cuts on the topological variables. The evaluation is quantitative, based on differences in results that exceed their respective $\pm 1\sigma$ statistical uncertainties. The specific cut criteria are detailed in Table 7.4. The ANN is excluded due to the complex relationships between input parameters that cannot be adequately captured with hard cuts, potentially introducing additional bias into the analysis.

The sets of topological variable cuts are adjusted to achieve a higher level of suppression of the combinatorial background in one case *Tight* (see Fig. 7.11), and in the other case, they are relaxed to create a broader selection that results in a lower signal-to-background ratio *Loose* (see Fig. C.2). In addition, Fig. 7.11 allows to comprehend better the benefit of using the

	VDistA	VDistB	VDistC	VDistX	MTD
Loose [mm]	>4	>30	<8	>90	<10
Tight [mm]	>8	>40	<4	>110	<6

Table 7.4.: Selection criteria used to evaluate the systematic uncertainties coming from the cuts on the topological variables. Values are taken from [172].

ANN. The use of Tight cut gives barely a Significance of 8.2 and a total of 186±27 ${}^{3}_{\Lambda}$H events for the Ag+Ag at 1.58 AGeV dataset. The acceptance and efficiency correction function for Tight is $1.51 \cdot 10^{-4}$, with an extrapolated production cross-section of 145±21 mb. While, for Loose cut the total number of reconstructed events is 1158±169 with a significance of 7.10, and a correction factor of $8.29 \cdot 10^{-4}$, which leads to a production cross section of 165±24 mb.

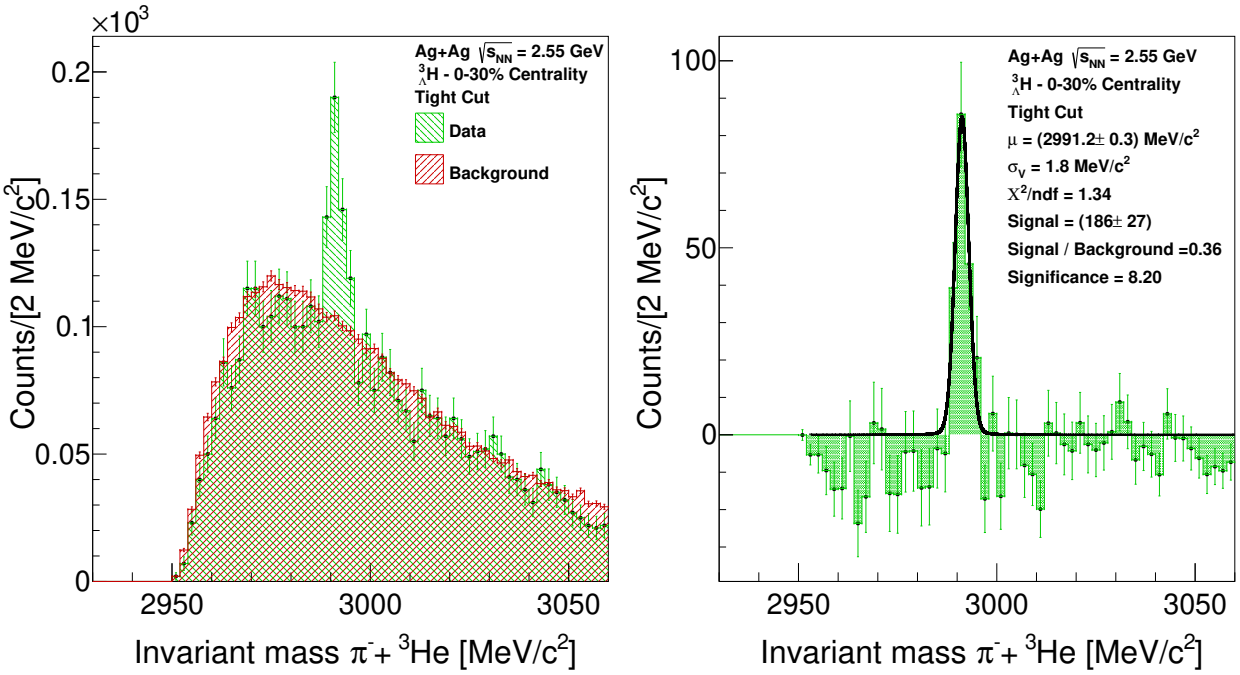

Figure 7.11.: Invariant mass distribution for ^{3}He-π^{-} pairs. Left. Distribution of the experimental data (green) together with the normalized background (red) using Tight topological cuts. Right. Experimental data distribution after background subtraction together with the Voigt fit (black). The fit results are shown on the plot.

This results in a total systematic uncertainty of 10% for Ag+Ag at 1.58 AGeV.For the low-energy systems where the statistical errors without the use of the ANN are too large (see Appendices), the systematic uncertainty found for the high-energy dataset is used instead.

Figure 7.12 shows the production rate of ${}^{3}_{\Lambda}$H, for 20 different (p_t, y_{cm}) intervals, within the HADES detector acceptance and normalized for the total number of analyzed events. This 2D plot shows that the production rate of the ${}^{3}_{\Lambda}$H peaks around mid-rapidity and that is more abundant for low p_t reflecting the fact that the beam energy is at the production threshold. Further interpretation of the yields needs to be performed, by comparing to kinematics distribution from theoretical models.

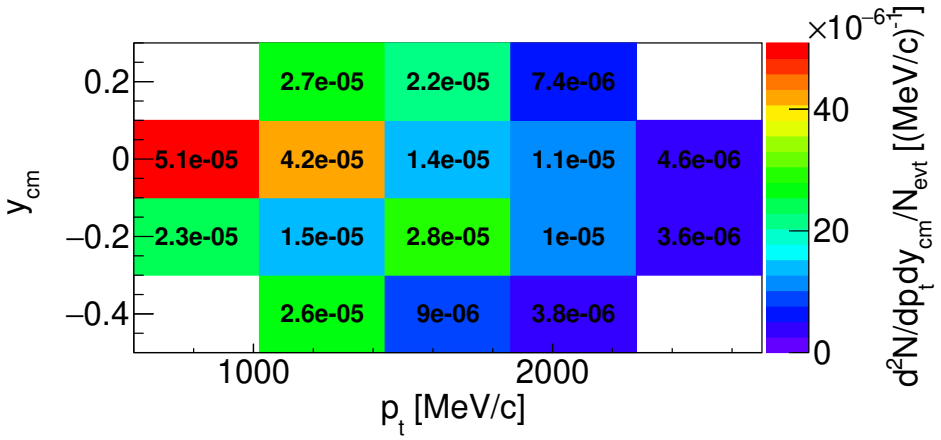

Figure 7.12.: ${}^{3}_{\Lambda}$H differential analysis for Ag+Ag at 1.58 AGeV dataset for the 0-30% centrality region. Each bin (p_t , y_{cm}) is corrected by the acceptance and efficiency and normalized to N_{evt}.

7.5. Discussion

The study of ${}^{3}_{\Lambda}$H production in HIC at HADES provides a unique opportunity to investigate it at the energy threshold for isolated NN collisions (1.58 GeV), as demonstrated by the analysis of the Ag+Ag at 1.58 AGeV data. Additionally, this study allows for an examination of production below the threshold, where the production from elementary NN collisions is expected to be quenched. The analysis of the Ag+Ag dataset reveals a signal peak with significance level reaching the 5σ limit, confirming ${}^{3}_{\Lambda}$H production below the threshold, and sequentially implying for additional production mechanisms. While, for Au+Au at 1.23 AGeV only an indication of its production can be inferred with a significance level of around 4σ. There are several possible mechanisms that can produce hadrons with masses higher than the available energy in the elementary NN collisions. For example, the nucleon intrinsic Fermi momentum before the collision, can lead to relative energies higher than the beam energy. Also, two-step reactions such as $N+N \rightarrow N+N+\pi$ followed by $\pi+N \rightarrow \Lambda+K$ can produce hyperons at sub-threshold energies (<1.58 AGeV). Finally, there is the possibility of accumulation of energy through multi-step processes that result in resonant intermediate states like Δ- or N^*-resonance that decay producing strange particles. Investigations along these lines will be conducted through the comparison of the experimental findings with transport models to understand the dynamics of the complex heavy-ion reactions, such as UrQMD (Ultra-Relativistic Quantum Molecular Dynamics) transport model [180] and SMASH (Simulating Many Accelerated Strongly interacting Hadrons) [181].

8. Conclusion

In this work the focus has been on studies of ${}^{3}_{\Lambda}$H, produced in relativistic ion-ion collisions at GSI/SIS18 energies (up to 2 AGeV). The main objective was to develop a method for extracting its matter radius, which will be realized in the first HYDRA experiment in 2025 using a newly developed pion tracker. Additionally, the thesis aimed to enhance our understanding of the ${}^{3}_{\Lambda}$H production mechanisms at and below the energy threshold (1.58 GeV) in elementary nucleon-nucleon (NN) collisions.

The new experiment (S073), scheduled for 2025 at the R^{3}B setup in GSI using ^{12}C+^{12}C collisions at 1.9 AGeV, is proposed as the hypernuclear version of the groundbreaking experiment led by I. Tannihata *et al.*. This historical experiment resulted in the discovery of the two-neutron halo nucleus ^{11}Li by measuring its interaction cross section. The primary objective of the new experiment is to make the first estimation of the ${}^{3}_{\Lambda}$H's size, which is predicted to be a halo hypernucleus. This will be achieved through an invariant mass measurement of its weak decay products, $\pi^- + {}^3$He. To accomplish this goal, a novel experimental method has been developed. It involves the extraction of the interaction cross-section of hypernuclei with a target nucleus, which is sensitive to their matter radii. This measurement is performed using a two-target setup. The expected precision in determining the interaction cross-section is better than 15%. This will enable the extraction of the unknown matter radius of ${}^{3}_{\Lambda}$H and determining whether it exhibits halo or non-halo characteristics. In preparation for the forthcoming experiment, extensive realistic GEANT4 simulations have been conducted to optimize the design of the experimental setup and reach a total detection efficiency of the two-body decay products of the ${}^{3}_{\Lambda}$H of 17%. As the final step, a new detector, the HYDRA plastic wall, has been constructed, following the design and validation phases, which will employed as a trigger to the main detector, the mini-HYDRA TPC.

Furthermore, the production mechanisms of ${}^{3}_{\Lambda}$H in heavy-ion collisions at the HADES setup in GSI have been investigated. Here, the production has been explored by analyzing existing datasets, taken in 2019 and 2012, with different collision energies and in-medium conditions, *i.e.*, Ag+Ag at 1.58 AGeV and 1.23 AGeV, and Au+Au at 1.23 AGeV. While the first set is exactly at the strangeness production threshold from elementary NN collisions (1.58 GeV), which is considered as the main production mechanism, the others are below it. The data analysis has been carried through a multi-step methodology and the use of an Artificial Neural Network to study the production of ${}^{3}_{\Lambda}$H while ensuring a clear separation between the signal and background. The results obtained include invariant mass spectra for all three systems, where the ${}^{3}_{\Lambda}$H signal is identified in the high-energy Ag+Ag measurement as well the low energy ones Ag+Ag and Au+Au, although located below the production threshold: the significance levels of the observed peaks in the spectra are 18.27, 5.16, and 4.00, respectively. Following that, the associated production cross-sections at and below

the strangeness production threshold are extracted, the value for Ag+Ag at 1.58 AGeV amount to 199±13(stat.)±20(sys.) mb, 59±15(stat.)±6(sys.) mb for Ag+Ag at 1.23 AGeV and 52±14(stat.)±5(sys.) mb for Au+Au at 1.23 AGeV. These findings suggest that the strangeness production cannot be explained only by primary elementary NN reactions inside the reaction zone. Instead, their production may occur due to the nucleon intrinsic Fermi momentum before the collision, providing enough energy to overcome the production energy threshold. Alternatively, secondary or multi-step processes facilitated in the high-density environment formed during the collision could enable sub-threshold production mechanisms. These processes need to be further investigated through a comparison of the experimental results with the predictions of transport models.

A. Supplementary material Au+Au at 1.23 AGeV

The event and track selection, particle identification (PID), background estimation, and training techniques for the ANN described in Chapter 6 are also applied to the Au1.23Au dataset. In this appendix, the relevant plots for the 2012 dataset, divided into their respective sections, are shown.

A.1. Event selection

The event selection criteria for the 2012 and 2019 experimental campaigns exhibit a few differences. Specifically, in the 2012 campaign, the *kNoFlashMDC* criterion is not implemented, and the *kNoSTART* criterion has been renamed to *kNoPileUpSTART*. For detailed information about the specific criteria and their effects on the Au1.23Au dataset see Fig. A.1.

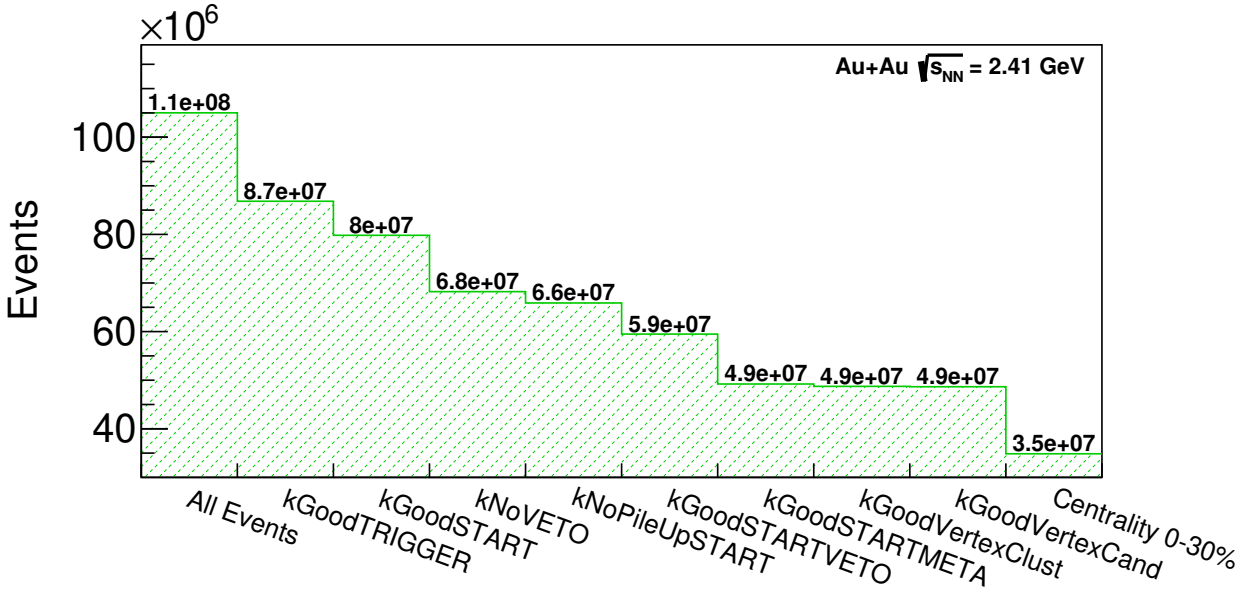

Figure A.1.: Number of events after subsequently applying the different criteria. Plot generated using one day (108) of data. For details on the criteria see Sec. 6.1.1.

A.1.1. Centrality

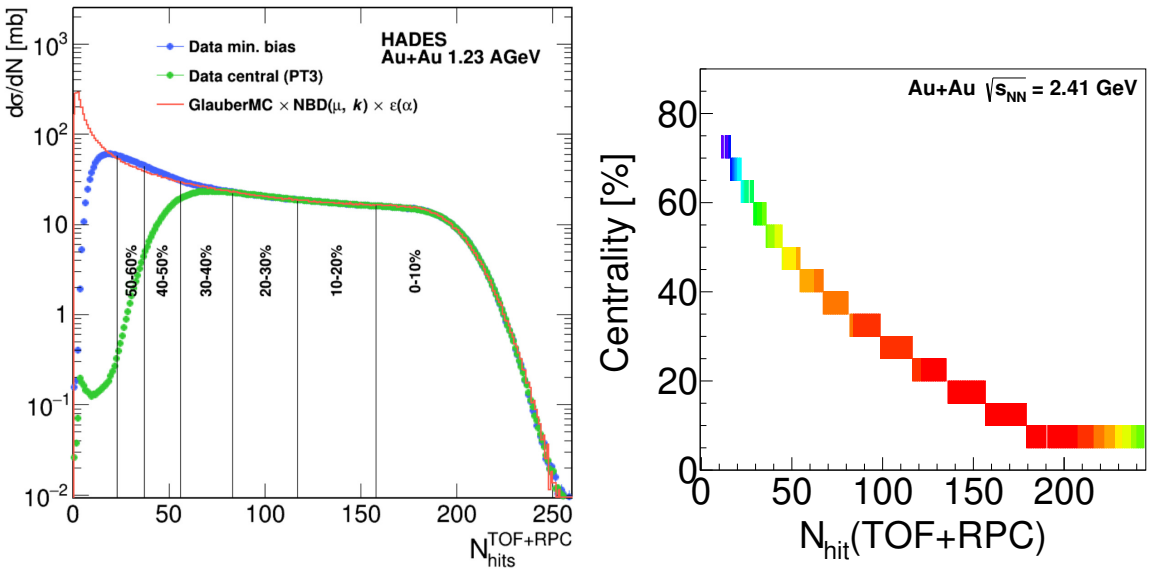

Figure A.2.: Centrality Estimation. Left. Comparison between the Glauber MC Model and experimental data divided in centrality classes of 10%. Figure is taken from [152]. Right. Correlation between N_{hit} in TOF and RPC detectors and Glauber Model predictions. For details see Sec. 6.1.2.

A.1.2. Primary vertex

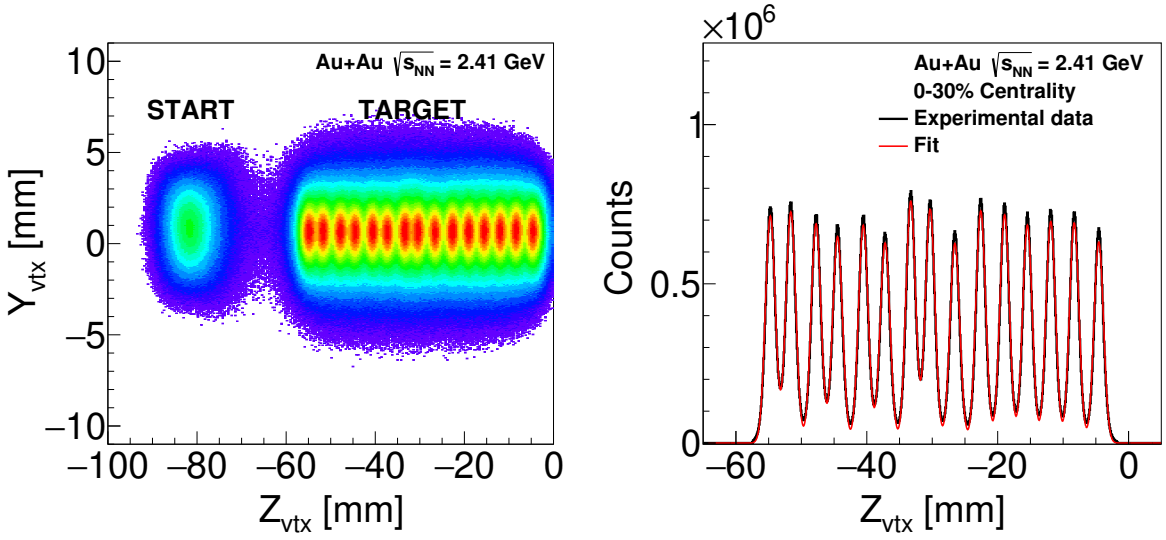

Figure A.3.: Distribution of the reconstructed primary vertex. Left. The START detector together with the 15-target segments. Right. The Z component after the event selection together with a 15 Gaussian fit in red. For details see Sec. 6.1.3.

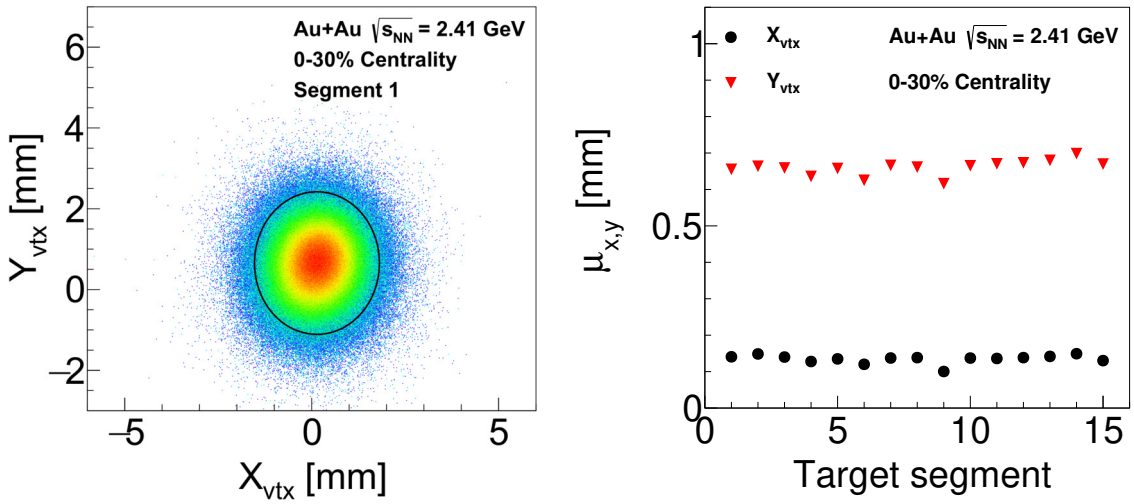

Figure A.4.: Components (x, y) of the primary vertex. Left. The 2-D distribution for the first target segment. Right. The mean value extrapolated using a Gaussian fit for the 15 targets. For details see Sec. 6.1.3.

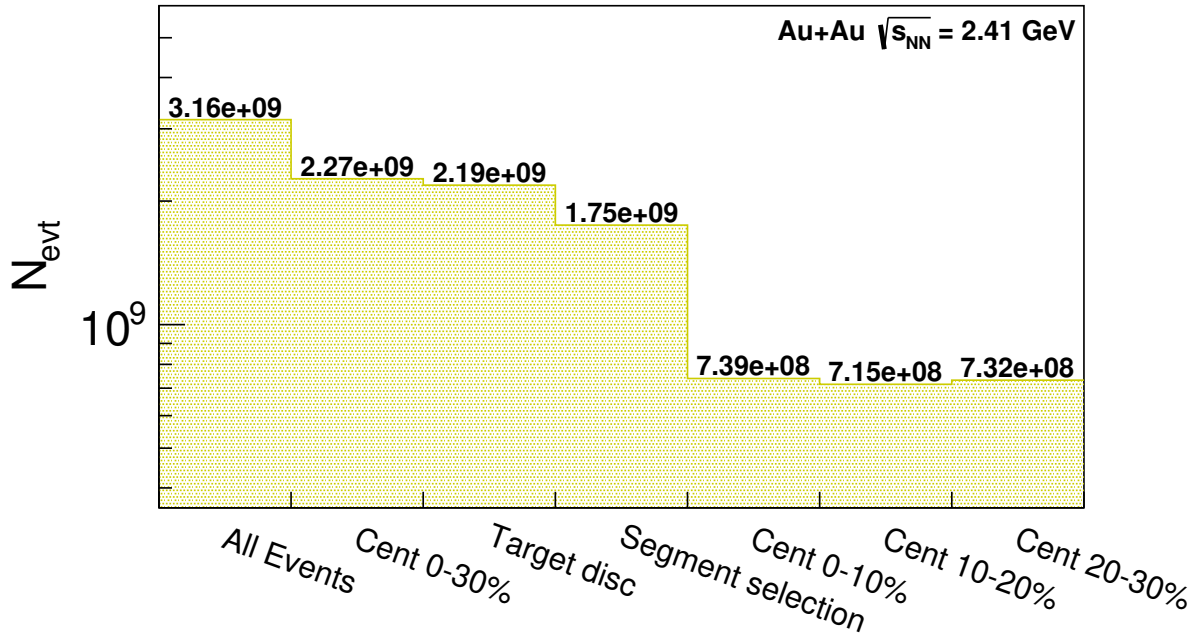

Figure A.5.: Number of events after subsequently applying the events selection criteria. For details on the bin content see Sec. 6.1.3.

A.2. Particle identification

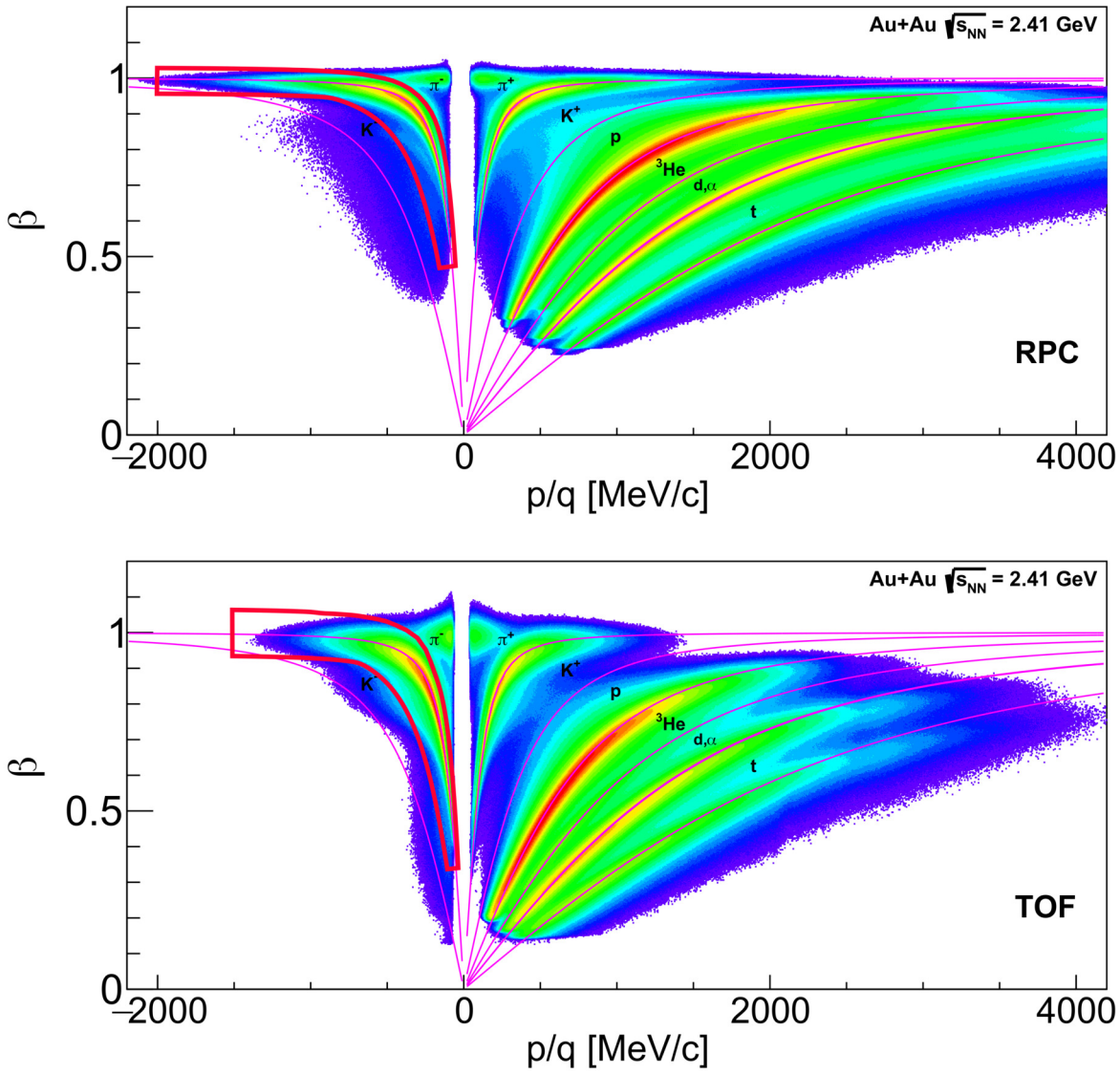

Figure A.6.: Correlation between the p/q and β for all selected tracks. Separately for RPC (top) and TOF detectors (bottom). The graphical cut for the π^- has been taken from [172], while the pink line represents the theoretical curve for the ^{3}He using Eq. 6.1. For details see Sec. 6.2.

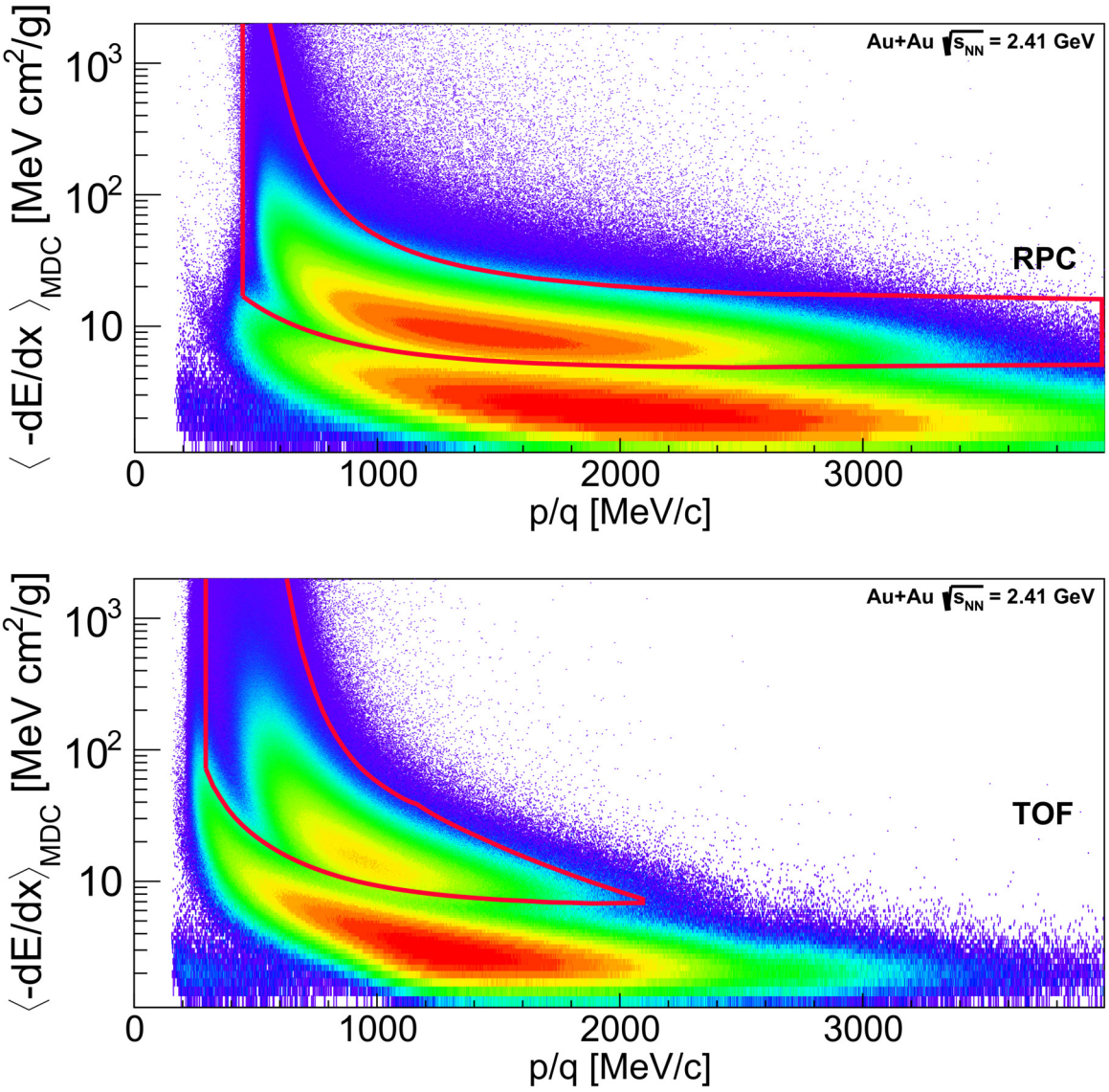

Figure A.7.: Correlation between the specific energy loss in the MDC and the p/q measured in RPC (top) and TOF (bottom) for tracks with a mass over charge between 1.27 GeV/c and 1.58 GeV/c. The graphical cuts are taken from [172]. For details see Sec. 6.2.

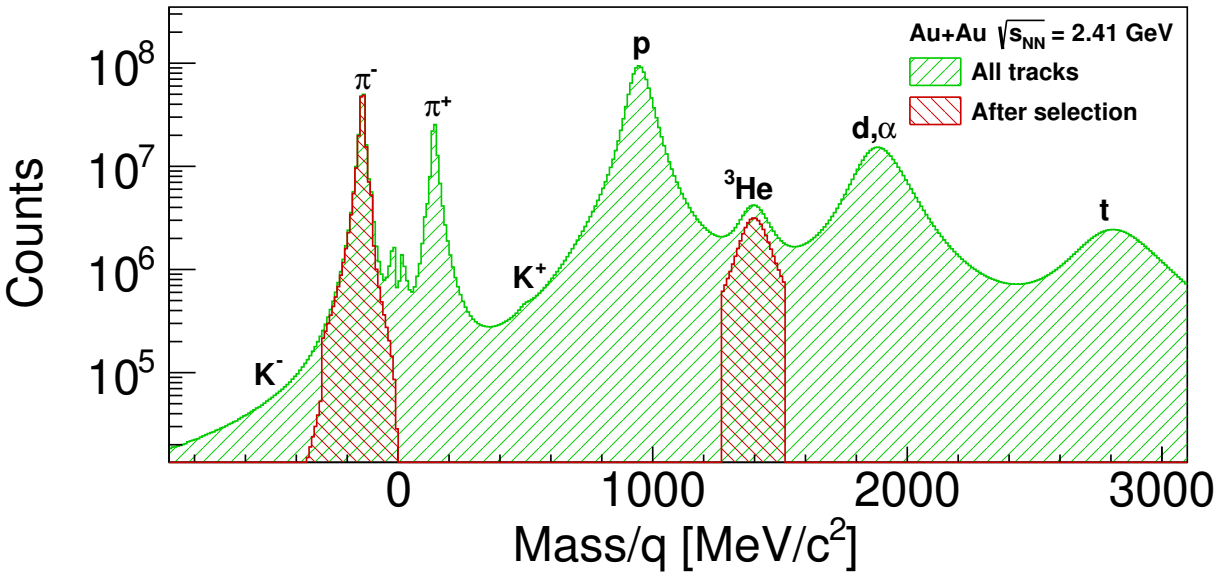

Figure A.8.: Mass distributions of all selected tracks before and after the event and track selection for the π^- and ^{3}He, combined for TOF and RPC tracks. For details see Sec. 6.2.

A.3. ${}^{3}_{\Lambda}$H reconstruction

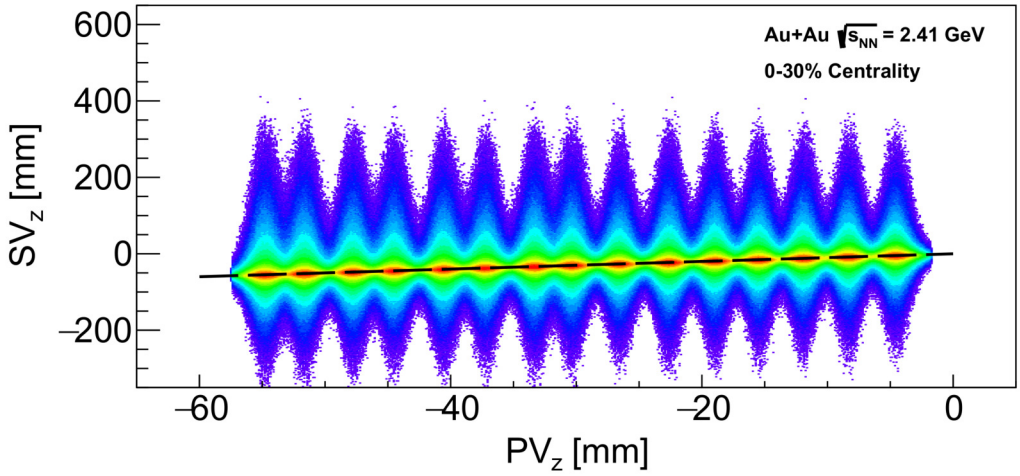

Figure A.9.: SV in function of the PV, the black dashed line represents PV-SV=0. For details see Sec. 6.3.

A.4. Background estimation

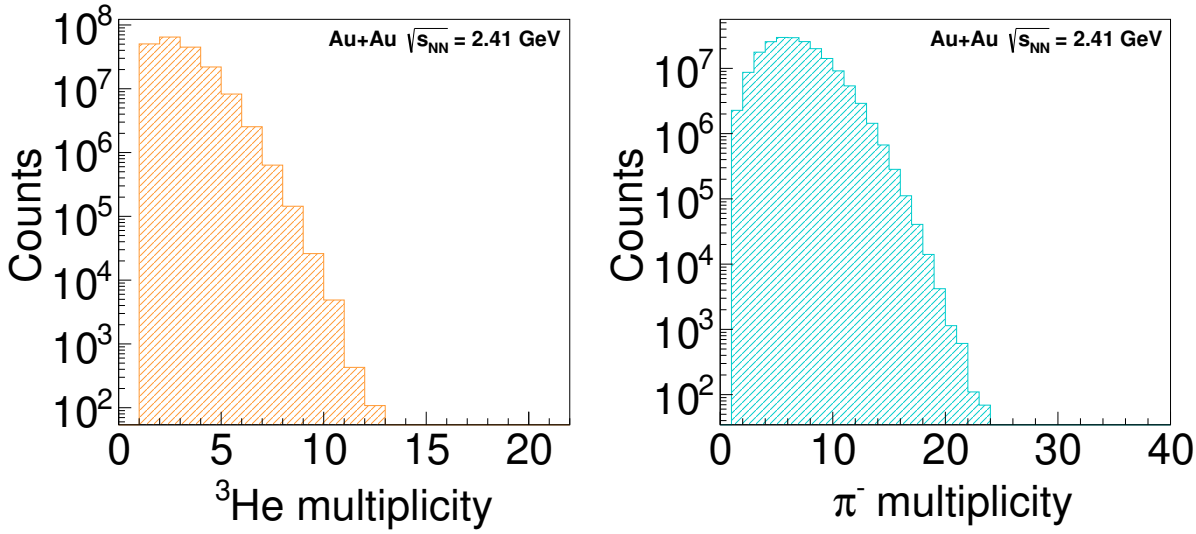

Figure A.10.: Multiplicity of daughter particles per event, π^- (right) and ^{3}He (left). For details see Sec. 6.4.

A.5. Simulated data

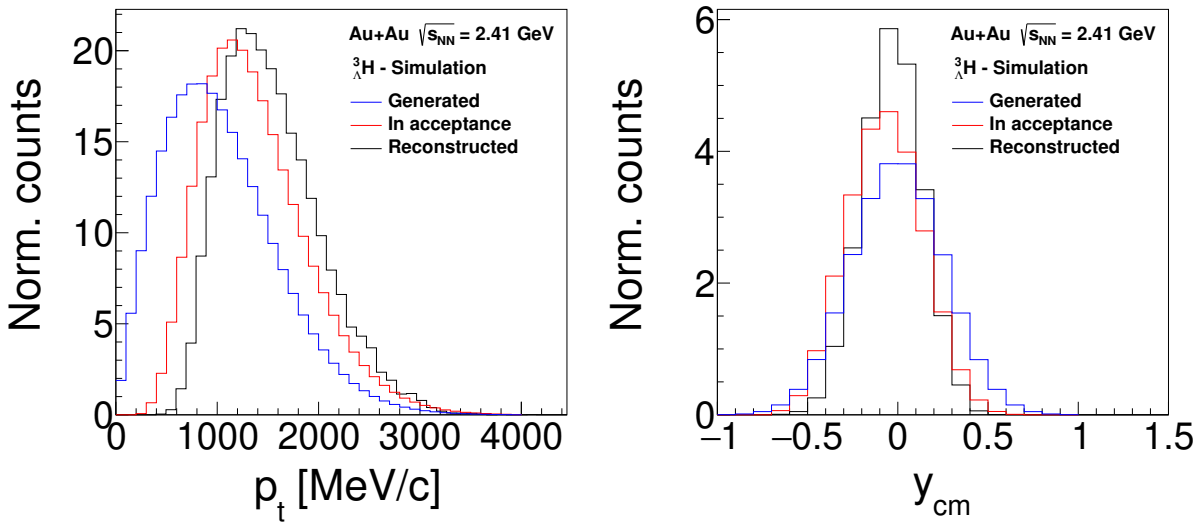

Figure A.11.: Comparison between the normalized distributions of generated (blue), in acceptance (red) and reconstructed (black) $^{3}_{\Lambda}$H from simulated data, separately for the p_t (left) and y_{cm} (right). For details see Sec. 6.5

A.6. Artificial Neural Network

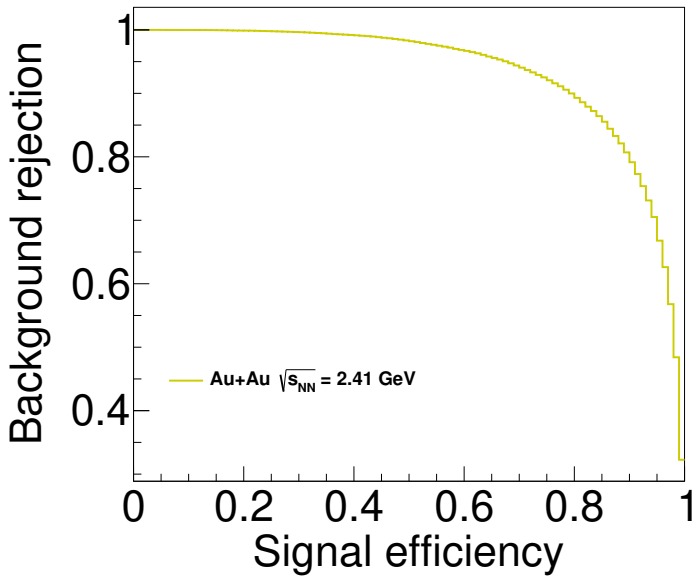

Figure A.12.: ROC curves for the Au+Au at 1.23 AGeV dataset. For details see Sec. 6.6.

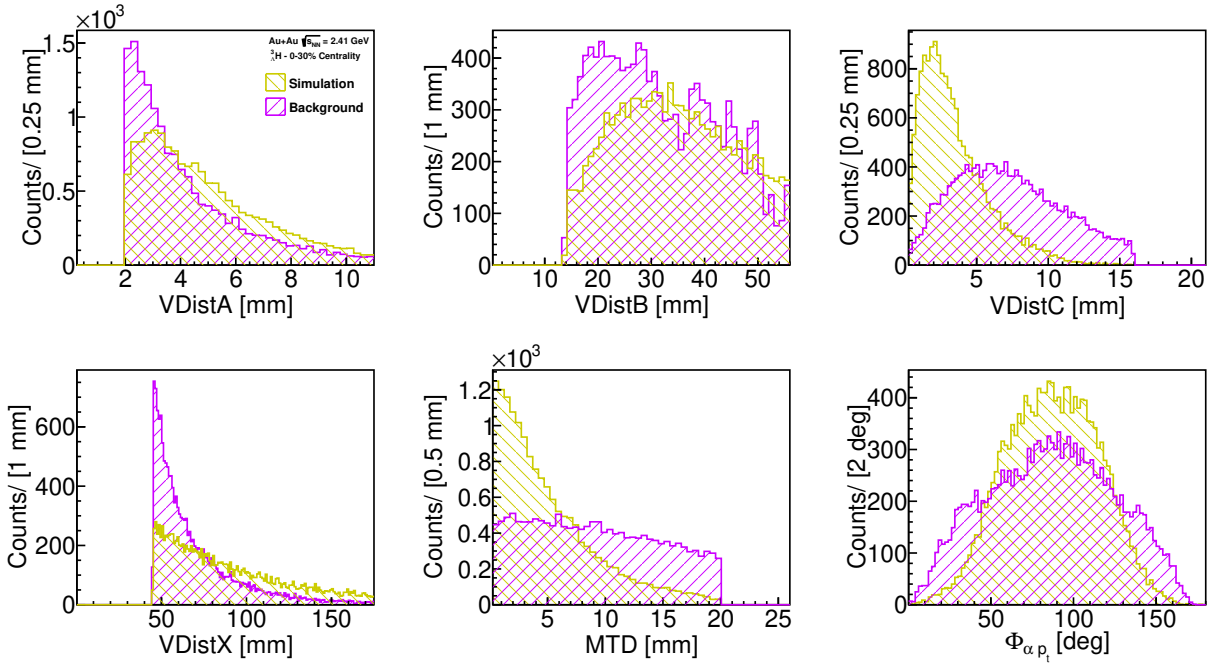

Figure A.13.: ${}^{3}_{\Lambda}\mathrm{H}$ simulated signal (yellow) and combinatorial background distributions used to train and test the ANN with the pre-cuts from Table 7.1. For details see Sec. 7.1.1.

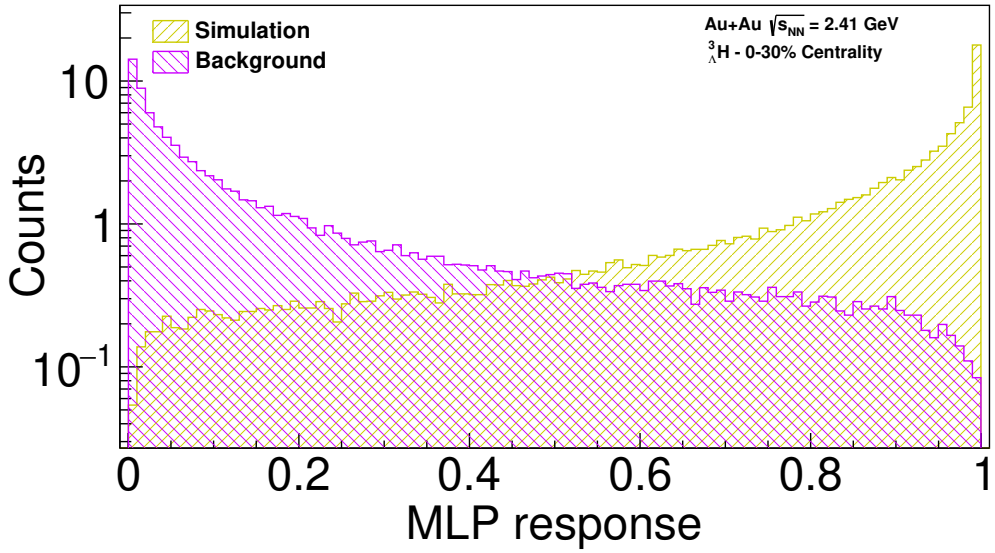

Figure A.14.: Logarithmic representation of the MLP response distribution for the ${}^{3}_{\Lambda}\mathrm{H}$ simulated signal (yellow) and combinatorial background (pink). For details see Sec. 7.1.1.

A.7. Production cross section

Using the topological cuts from Table 7.4 the systematic uncertainty for the ${}^{3}_{\Lambda}$H production cross section are investigated. From the use of Loose cut, for the Au+Au at 1.23 AGeV the peak significance reaches 1.32, for a total of 299±229 signal events with a mass of 2993.0±3.3 MeV/c^2 and a width of 3.4 MeV/c^2. To be noted the mean variable of the fit for this distribution was limited 2989<μ<2993 MeV/c^2. The acceptance and efficiency correction is $9.9 \cdot 10^{-4}$, which gives a ${}^{3}_{\Lambda}$H production cross section of 62±48 mb. While, for Tight cut the peak significance is 1.59, for a total of 44±29 signal events with a mass of 2991.8±1.2 MeV/c^2 and a width of 2.2 MeV/c^2. The acceptance and efficiency correction is $1.8 \cdot 10^{-4}$, which gives a ${}^{3}_{\Lambda}$H production cross section of 50±33 mb.

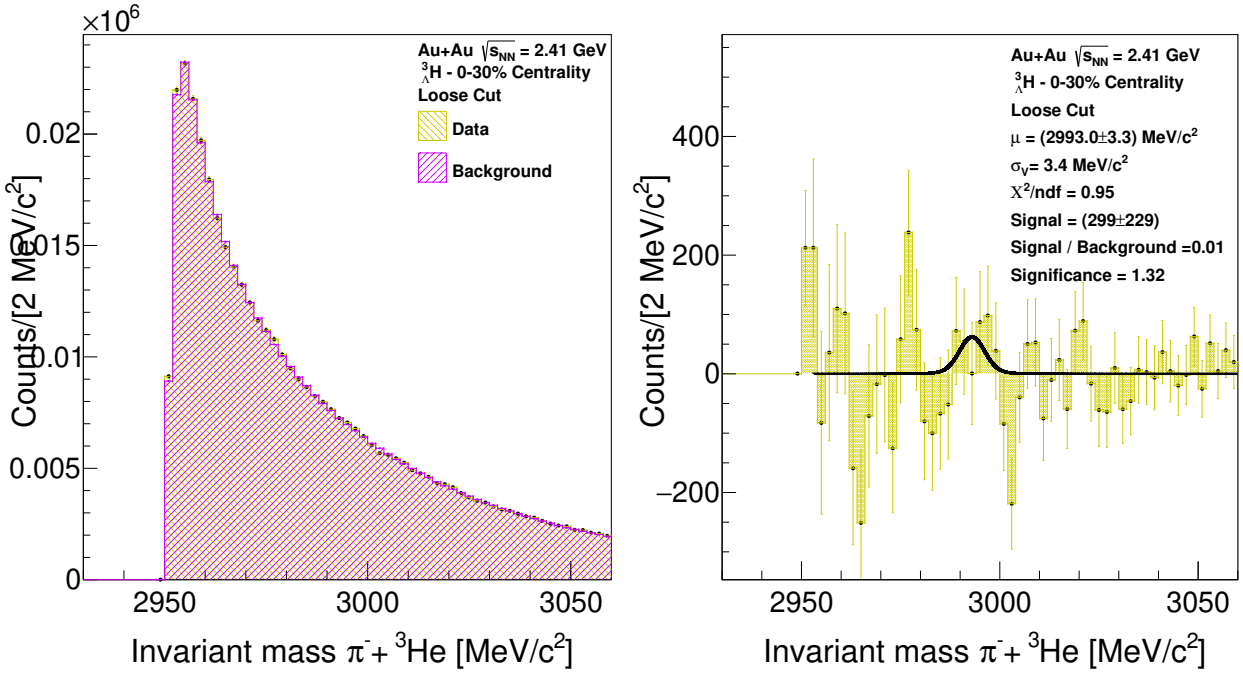

Figure A.15.: Invariant mass distribution for ^{3}He-π^- pairs. Left. Distribution of the experimental data (yellow) together with the normalized background (pink) using Loose topological cuts. Right. Experimental data distribution after background subtraction together with the Voigt fit (black). The fit results are shown on the plot.

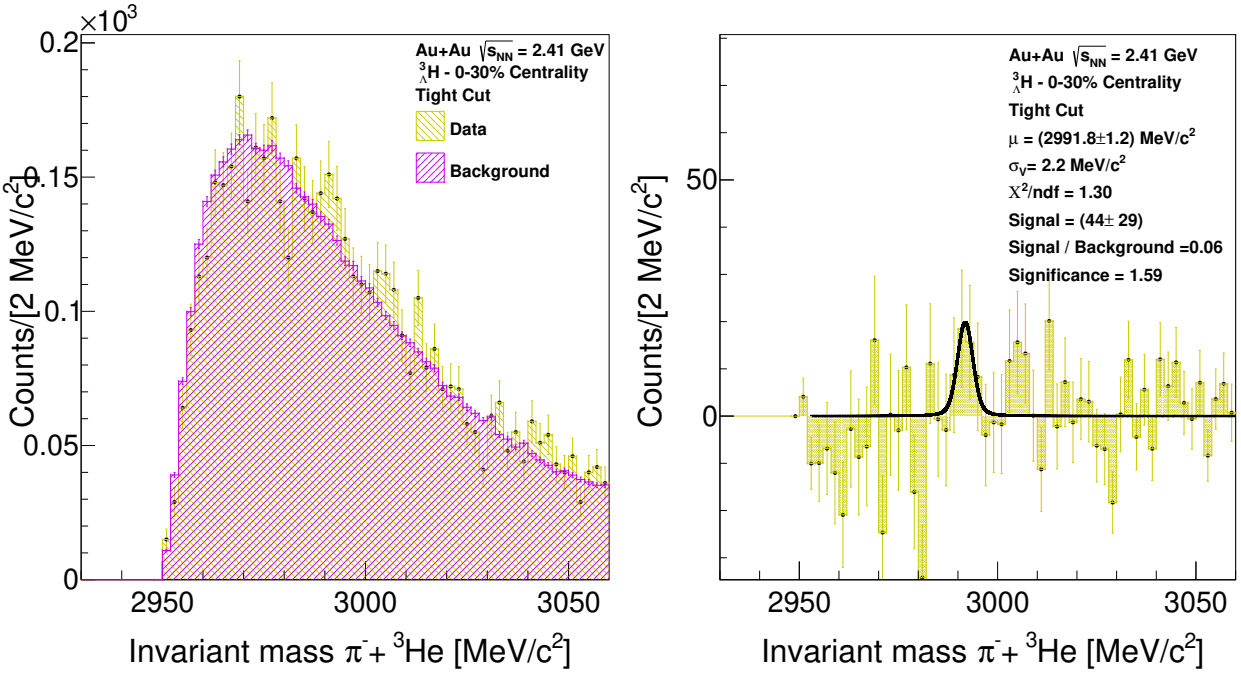

Figure A.16.: Invariant mass distribution for ^{3}He-π^- pairs. Left. Distribution of the experimental data (yellow) together with the normalized background (pink) using Tight topological cuts. Right. Experimental data distribution after background subtraction together with the Voigt fit (black). The fit results are shown on the plot.

B. Supplementary material Ag+Ag at 1.23 AGeV

The event and track selection, particle identification (PID), background estimation, and training techniques for the ANN described in Chapter 6 are also applied to the Ag1.23Ag dataset. In this appendix, the relevant plots for the second part of the 2019 beam time, divided into their respective sections, are shown.

B.1. Event selection

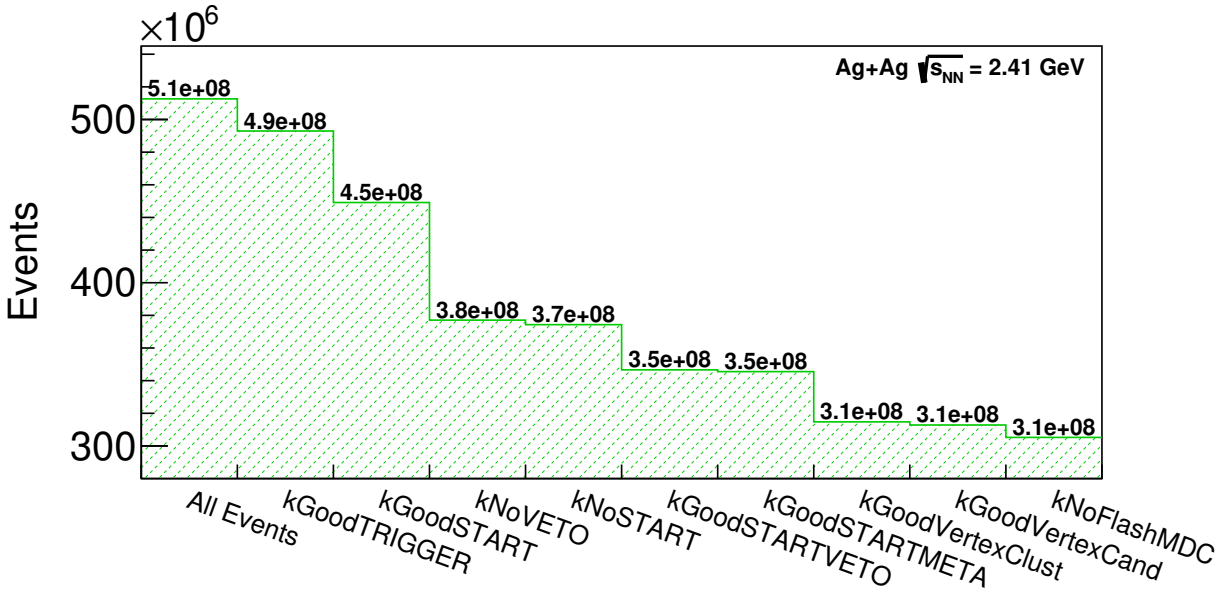

Figure B.1.: Number of events after subsequently applying the different criteria. Plot generated using one day (90) of data. For details on the criteria see Sec. 6.1.1.

B.1.1. Centrality

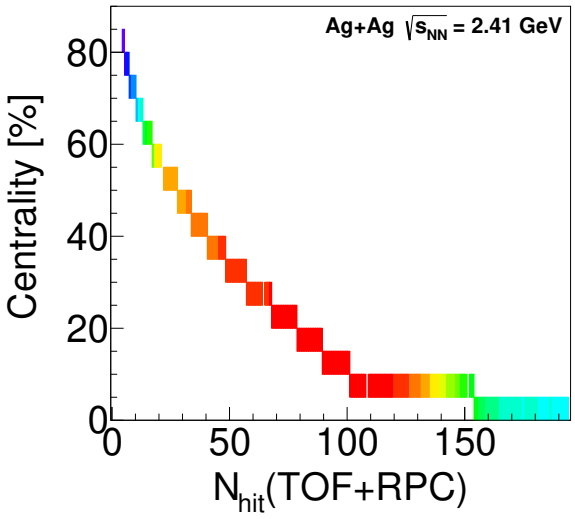

Figure B.2.: Centrality Estimation. Correlation between N_{hit} in TOF and RPC detectors and Glauber Model predictions. The most peripheral events are discarded by the PT3. For details see Sec. 6.1.2.

B.1.2. Primary vertex

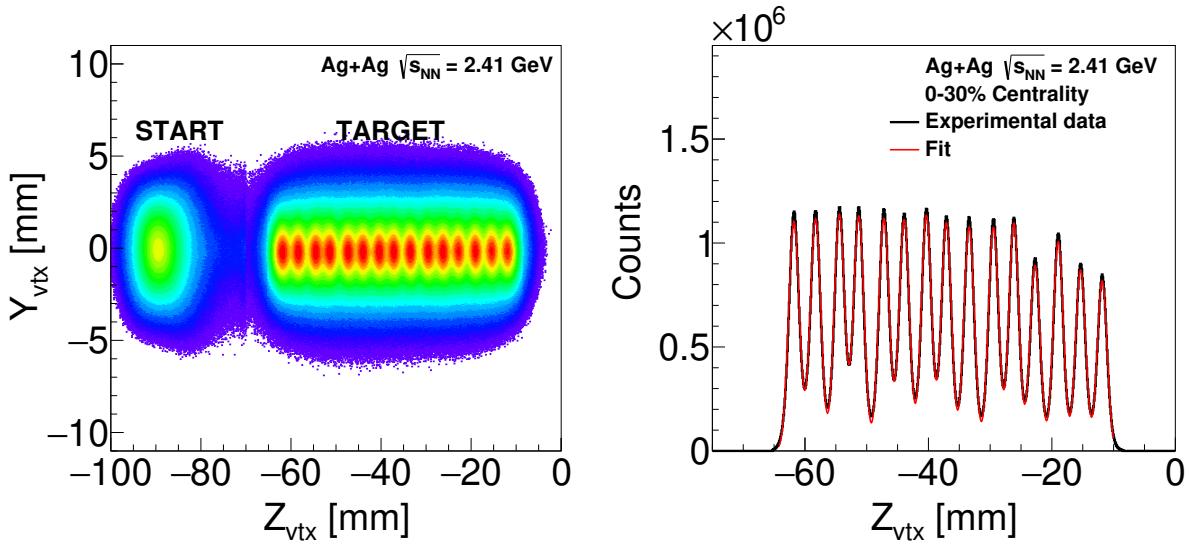

Figure B.3.: Distribution of the reconstructed primary vertex. Left. The START detector together with the 15-target segments can be clearly distinguished. Right. The Z component after the event selection together with a 15 Gaussian fit in red. For details see Sec. 6.1.3.

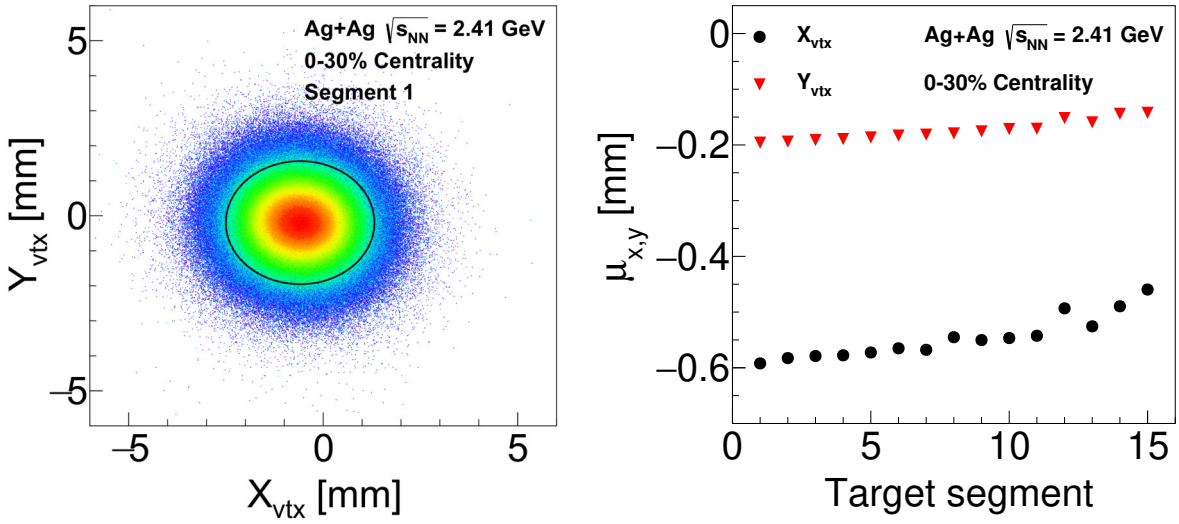

Figure B.4.: Components (x, y) of the primary vertex. Left. The 2-D distribution for the first target segment. Right. The mean value extrapolated using a Gaussian fit for the 15 targets. For details see Sec. 6.1.3.

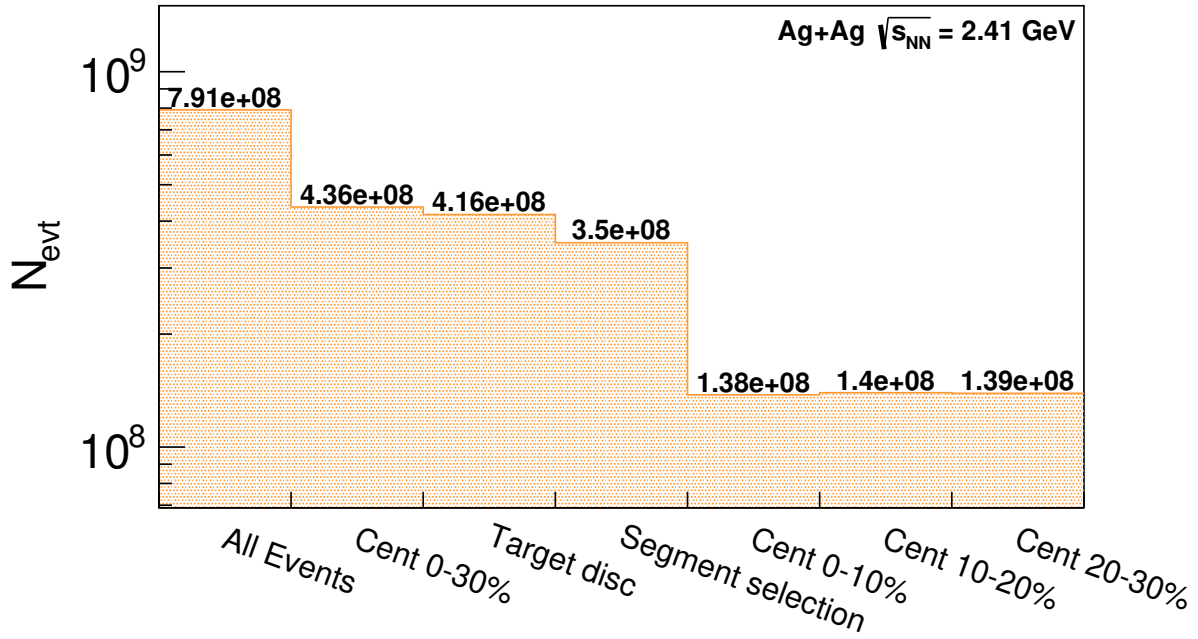

Figure B.5.: Number of events after subsequently applying the events selection criteria. For details on the bin content see Sec. 6.1.3.

B.2. Particle identification

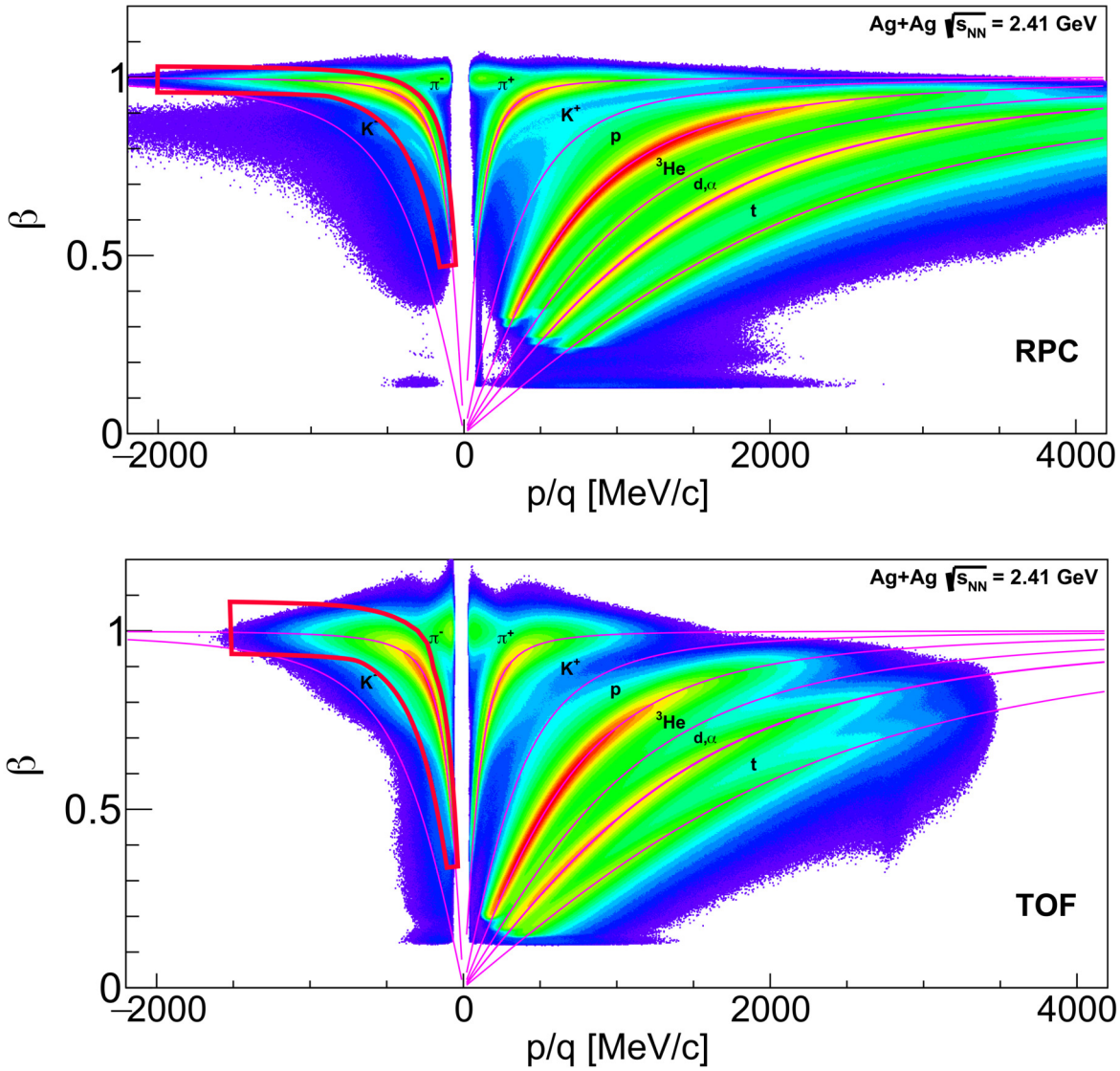

Figure B.6.: Correlation between the p/q and β for all selected tracks. Separately for RPC (top) and TOF detectors (bottom). The graphical cut for the π^- has been taken from [172], while the pink line represents the theoretical curve for the ^{3}He using Eq. 6.1. For details see Sec. 6.2.

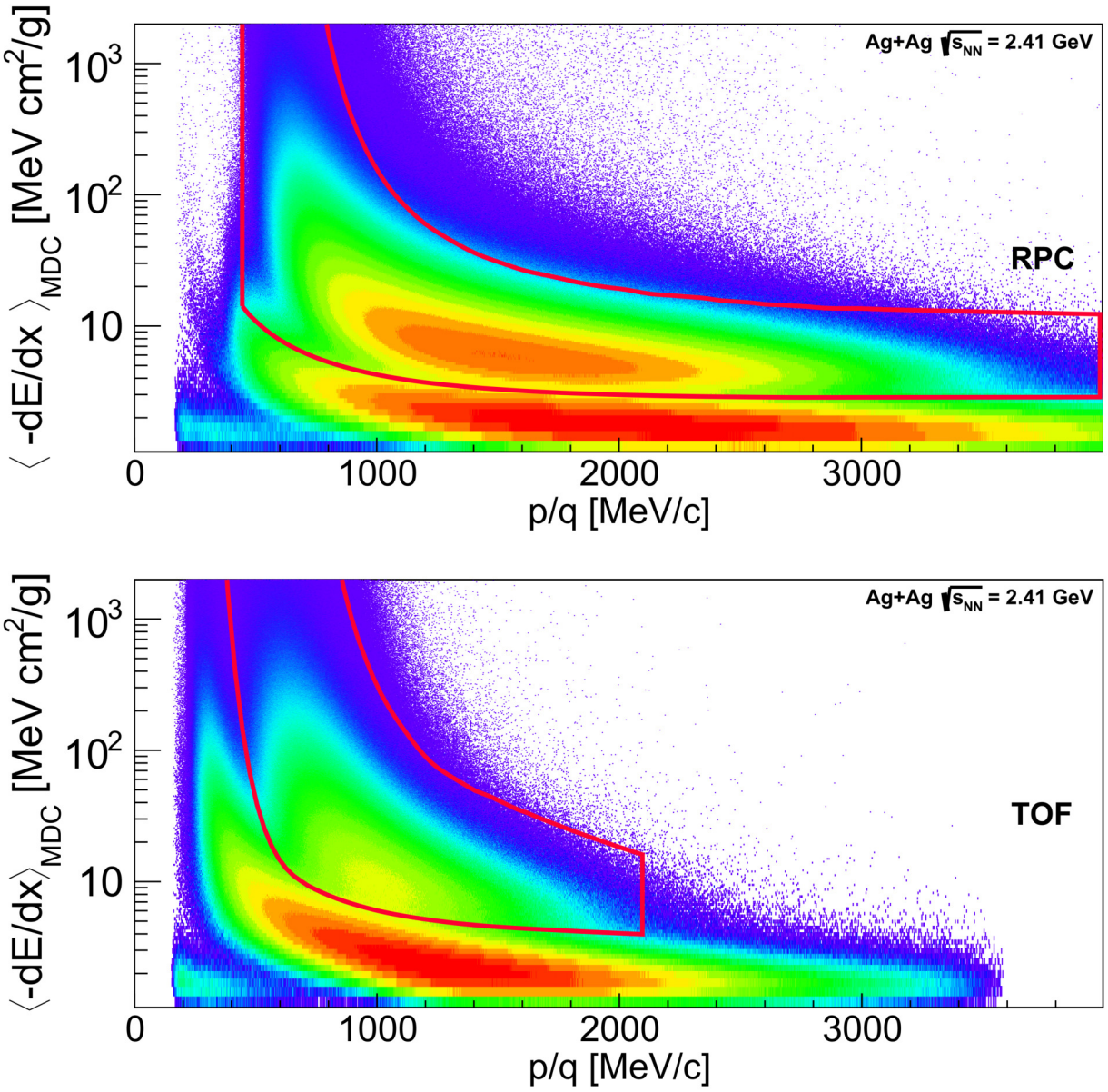

Figure B.7.: Correlation between the specific energy loss in the MDC and the p/q measured in RPC (top) and TOF (bottom) for tracks with a mass over charge between 1.27 GeV/c and 1.58 GeV/c. The graphical cuts are taken from [172]. For details see Sec. 6.2.

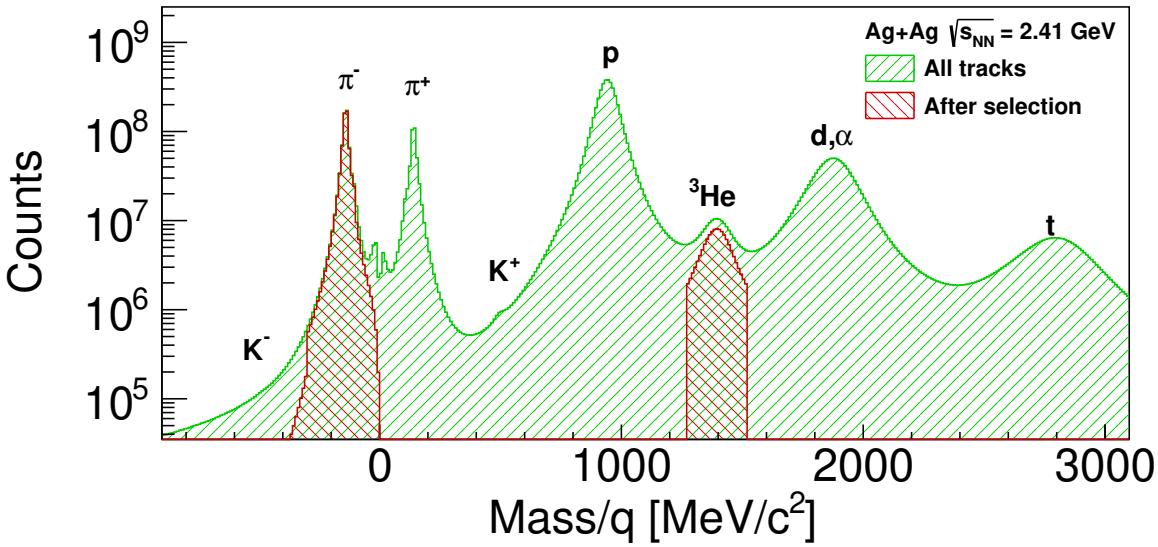

Figure B.8.: Mass distributions of all selected tracks before and after the event and track selection for the π^- and ^{3}He, combined for TOF and RPC tracks. For details see Sec. 6.2.

B.3. ${}^{3}_{\Lambda}$H reconstruction

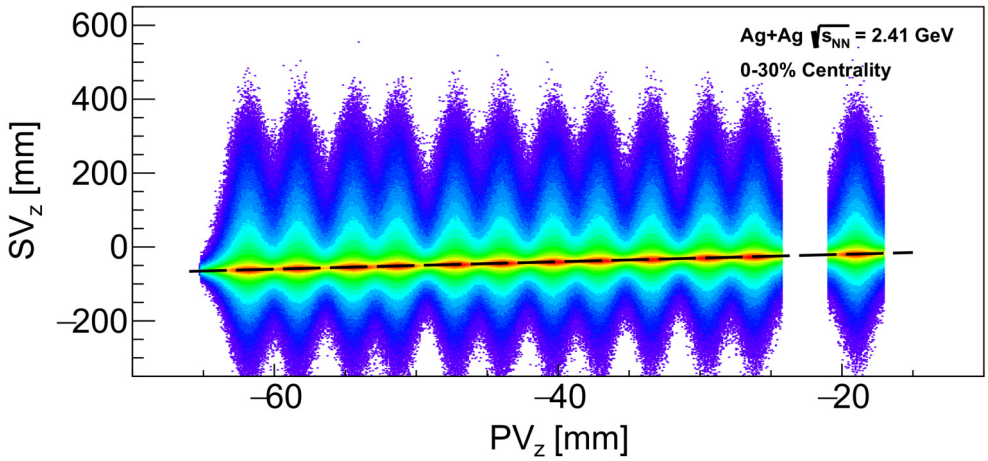

Figure B.9.: SV in function of the PV, the black dashed line represents PV-SV=0. For details see Sec. 6.3.

B.4. Background estimation

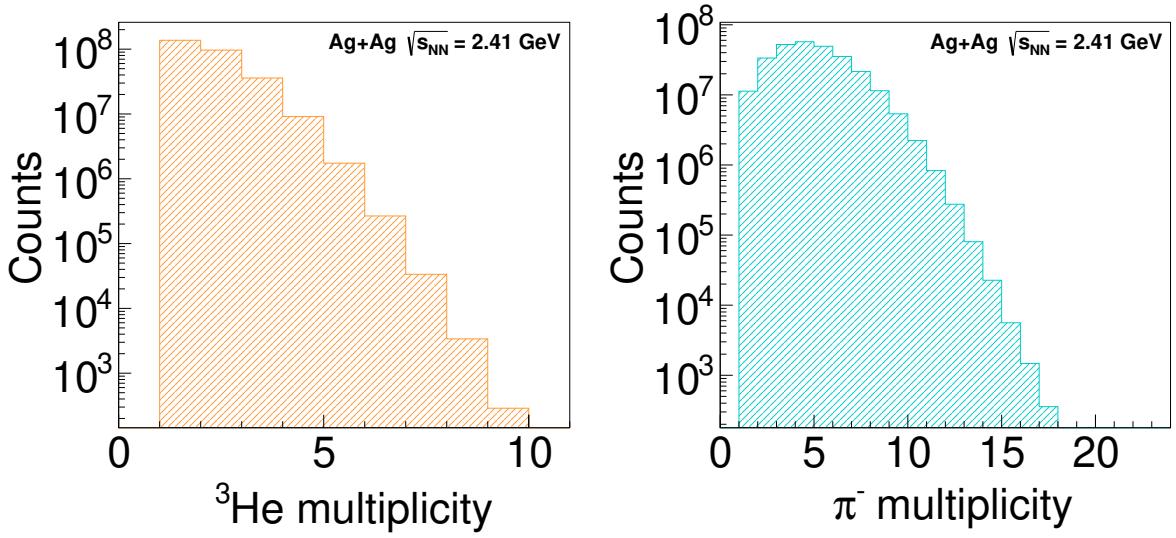

Figure B.10.: Multiplicity of daughter particles per event, π^- (right) and ^{3}He (left). For details see Sec. 6.4.

B.5. Simulated data

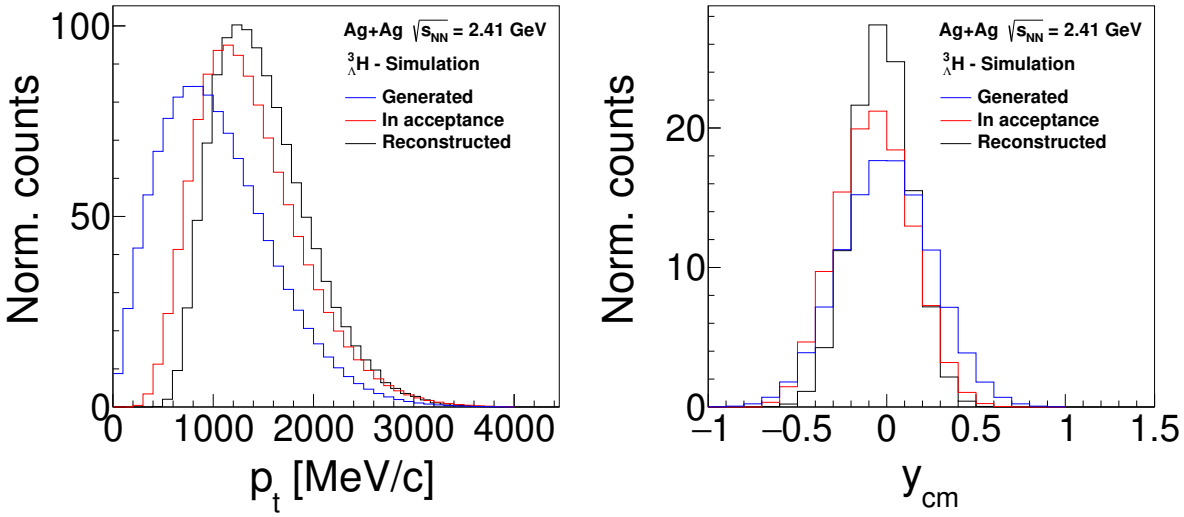

Figure B.11.: Comparison between the normalized distributions of generated (blue), in acceptance (red) and reconstructed (black) $^{3}_{\Lambda}$H from simulated data, separately for the p_t (left) and y_{cm} (right). For details see Sec. 6.5

B.6. Artificial Neural Network

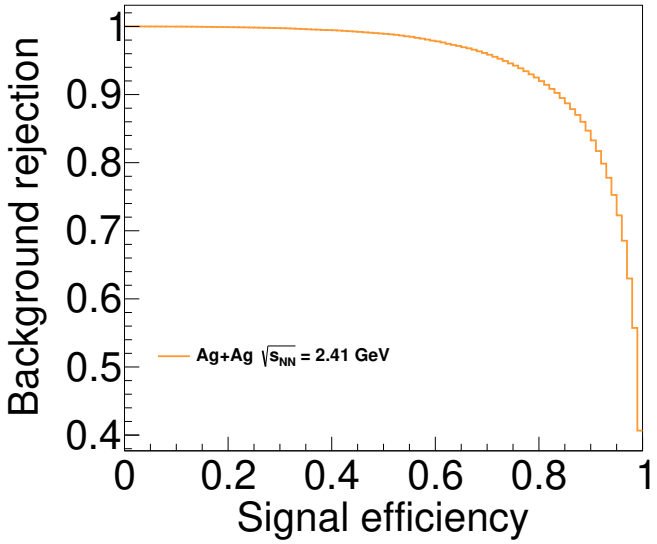

Figure B.12.: ROC curves for the Ag+Ag at 1.23 AGeV dataset. For details see Sec. 6.6.

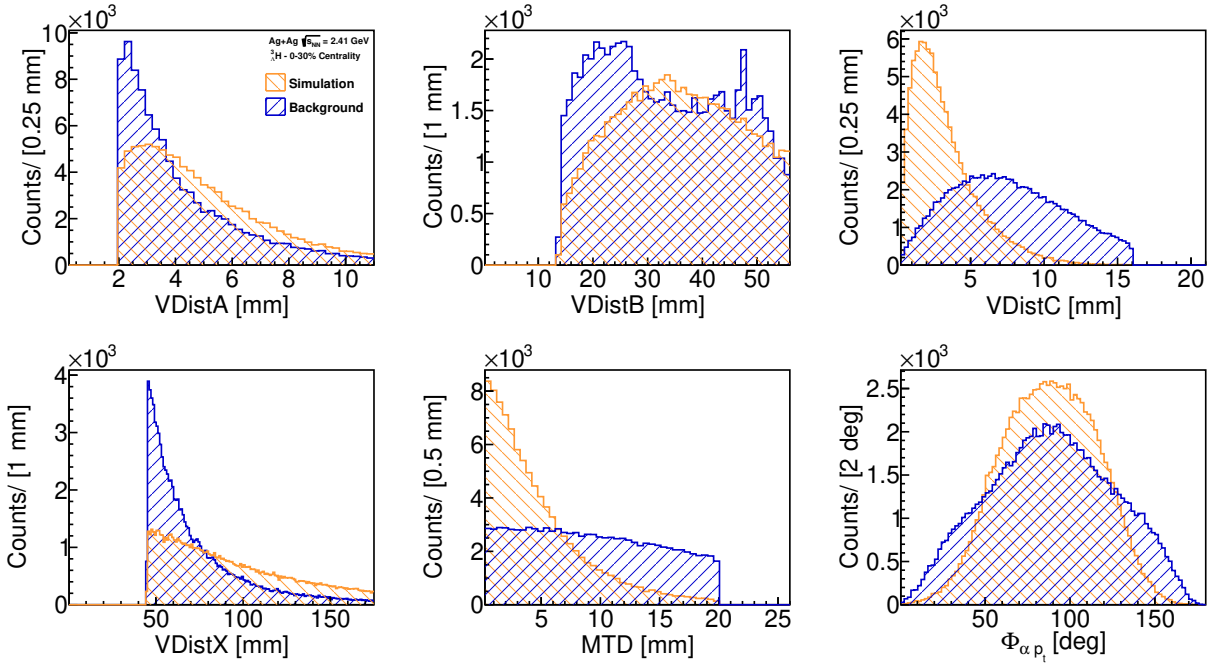

Figure B.13.: ${}^{3}_{\Lambda}$H simulated signal (orange) and combinatorial background (blu) distributions used to train and test the ANN with the pre-cuts from Table 7.1. For details see Sec. 7.1.1.

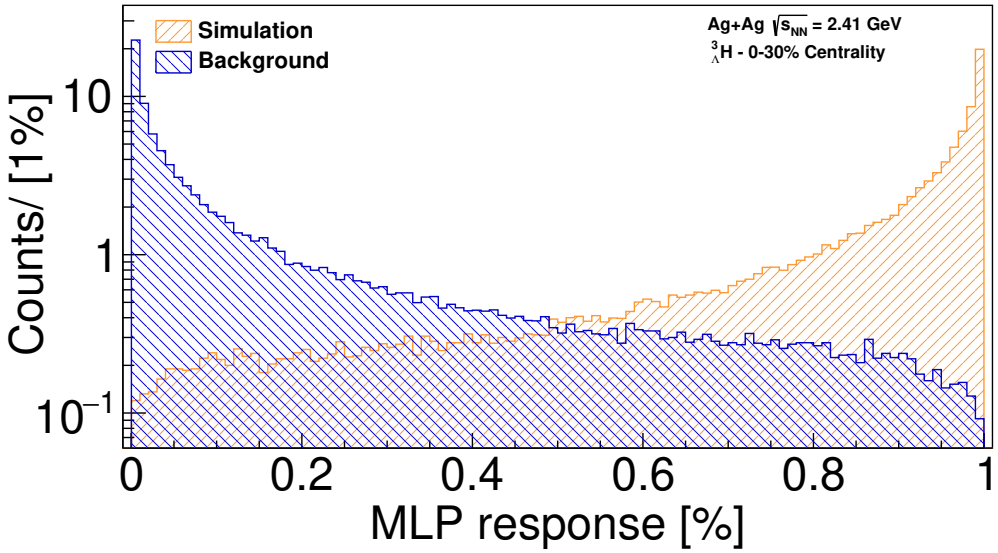

Figure B.14.: Logarithmic representation of the MLP response distribution for the ${}^{3}_{\Lambda}$H simulated signal (orange) and combinatorial background (blu). For details see Sec. 7.1.1.

B.7. Production cross section

Using the topological cuts from Table 7.4 the systematic uncertainty for the ${}^{3}_{\Lambda}$H production cross section can be investigated. From the use of Loose cut, for the Ag+Ag at 1.23 AGeV the peak significance reaches 3.31, for a total of 200±62 signal events with a mass of 2991.7±0.6 MeV/c^2 and a width of 1.5 MeV/c^2. The acceptance and efficiency correction is $12.3{\cdot}10^{-4}$, which gives a ${}^{3}_{\Lambda}$H production cross section of 110±34 mb. While, for Tight cut the peak significance is 2.34, for a total of 19±9 signal events with a mass of 2991.8±0.3 MeV/c^2 and a width of 1.2 MeV/c^2. The acceptance and efficiency correction is $2.4{\cdot}10^{-4}$, which gives a ${}^{3}_{\Lambda}$H production cross section of 54±26 mb.

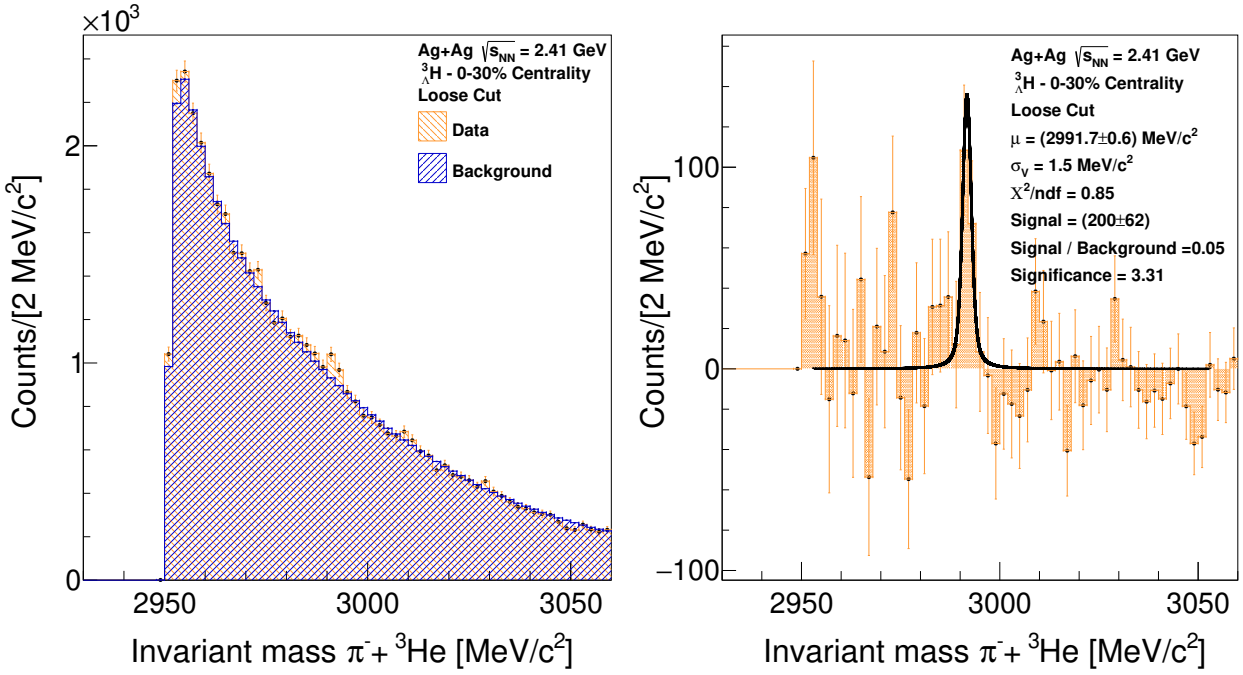

Figure B.15.: Invariant mass distribution for ^{3}He-π^{-} pairs. Left. Distribution of the experimental data (orange) together with the normalized background (blue) using Loose topological cuts. Right. Experimental data distribution after background subtraction together with the Voigt fit (black). The fit results are shown on the plot.

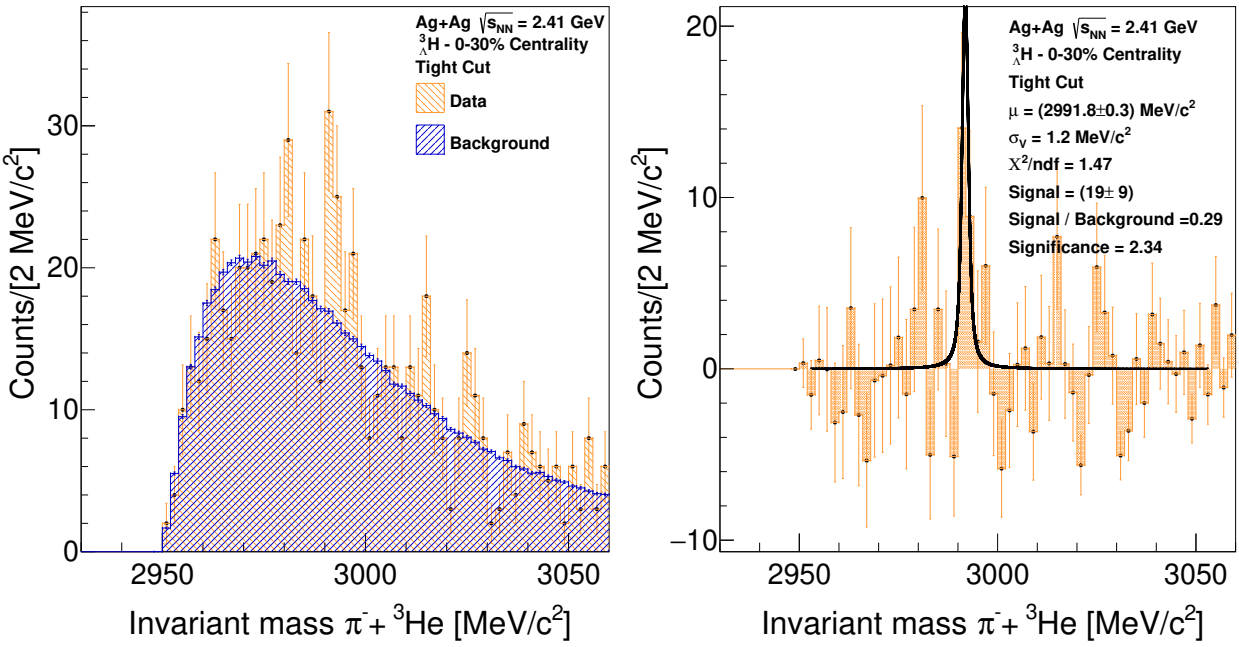

Figure B.16.: Invariant mass distribution for ^{3}He-π^- pairs. Left. Distribution of the experimental data (orange) together with the normalized background (blue) using Tight topological cuts. Right. Experimental data distribution after background subtraction together with the Voigt fit (black). The fit results are shown on the plot.

C. Supplementary material Ag+Ag at 1.58 AGeV

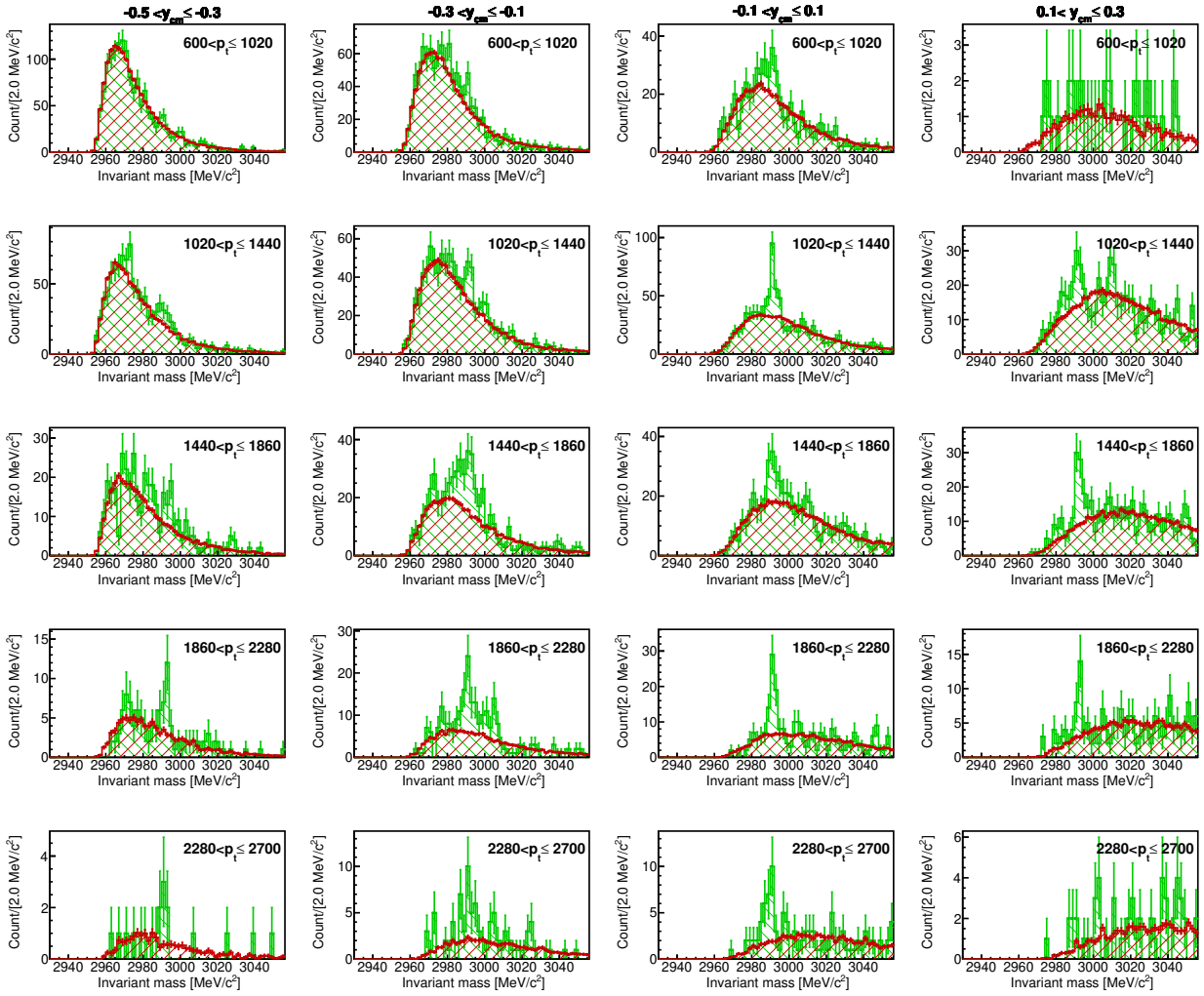

Figure C.1.: Invariant mass distributions for the pair ^{3}He-π^- for different intervals (p_t, y_{cm}) in the 0-30% most central events. Distribution of the experimental data (green) together with the normalized background (red).

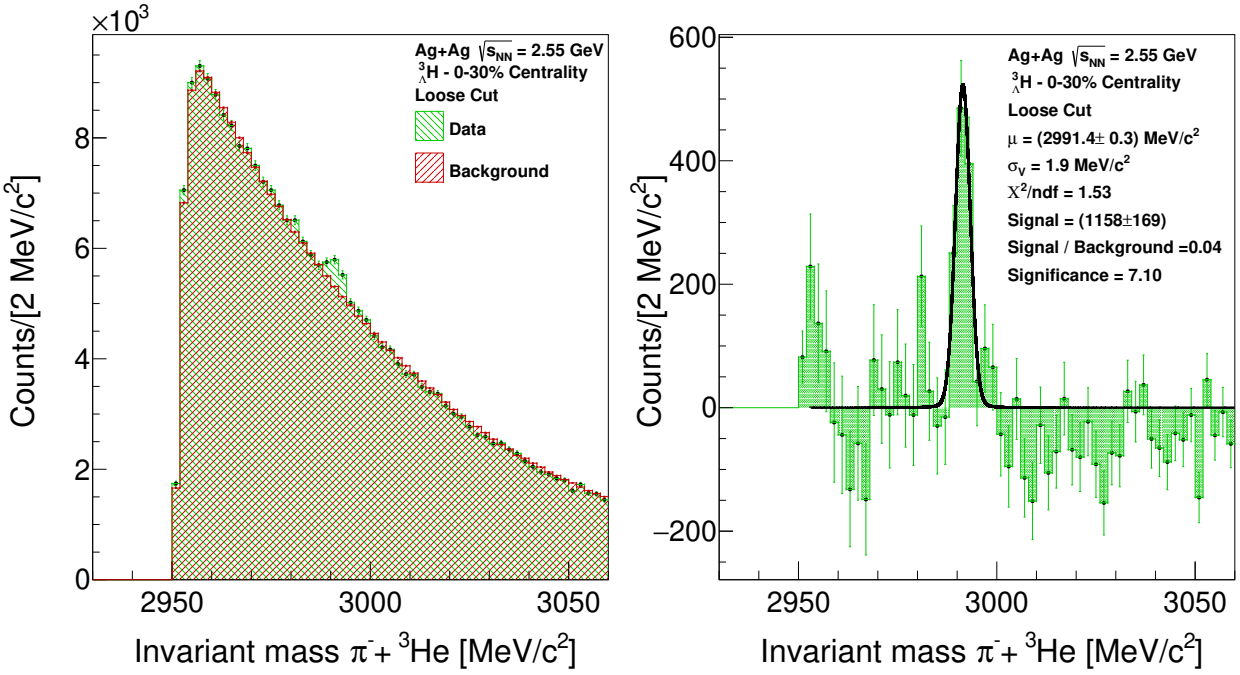

Figure C.2.: Invariant mass distribution for ^{3}He-π^- pairs. Left. Distribution of the experimental data (green) together with the normalized background (red) using Loose topological cuts. Right. Experimental data distribution after background subtraction together with the Voigt fit (black). The fit results are shown on the plot.

Bibliography

[1] L. Matic, *Standard model*, `http://www.physik.uzh.ch/groups/serra/StandardModel.html`.

[2] J. E. Dodd and B. Gripaios, "The Glashow–Weinberg–Salam model", in *The Ideas of Particle Physics*, 4th ed. Cambridge University Press, 2020, pp. 108–111.

[3] ATLAS Collaboration, "Observation of a new particle in the search for the Standard Model Higgs boson with the ATLAS detector at the LHC", *Phys. Lett. B*, vol. 716, no. 1, pp. 1–29, 2012.

[4] CMS Collaboration, "Observation of a new boson at a mass of 125 GeV with the CMS experiment at the LHC", *Phys. Lett. B*, vol. 716, no. 1, pp. 30–61, 2012.

[5] M. Gell-Mann, "Isotopic spin and new unstable particles", *Phys. Rev.*, vol. 92, pp. 833–834, 3 1953.

[6] T. Nakano and K. Nishijima, "Charge Independence for V-particles*", *Prog. Theo. Phys.*, vol. 10, no. 5, pp. 581–582, 1953.

[7] A. Pais, "Some remarks on the V-particles", *Phys. Rev.*, vol. 86, pp. 663–672, 5 1952.

[8] M. Gell-Mann, "The eightfold way: A theory of strong interaction symmetry", 1961.

[9] O. W. Greenberg, "Spin and unitary-spin independence in a paraquark model of baryons and mesons", *Phys. Rev. Lett.*, vol. 13, pp. 598–602, 20 1964.

[10] M. B. Tsang *et al.*, "Constraints on the symmetry energy and neutron skins from experiments and theory", *Phys. Rev. C*, vol. 86, p. 015 803, 1 2012.

[11] I. Vidaña, "A short walk through the physics of neutron stars", *Eur. Phys. J. P.*, vol. 133, no. 10, p. 445, 2018.

[12] L. Tolos and L. Fabbietti, "Strangeness in nuclei and neutron stars", *Prog. Part. Nucl. Phys*, vol. 112, p. 103 770, 2020.

[13] J. R. Oppenheimer and G. M. Volkoff, "On massive neutron cores", *Phys. Rev.*, vol. 55, pp. 374–381, 4 1939.

[14] P. B. Demorest *et al.*, "A two-solar-mass neutron star measured using shapiro delay", *Nature*, vol. 467, no. 7319, pp. 1081–1083, 2010.

[15] J. Antoniadis *et al.*, "A massive pulsar in a compact relativistic binary", *Science*, vol. 340, no. 6131, p. 1 233 232, 2013.

[16] D. Lonardoni *et al.*, "Hyperon puzzle: Hints from Quantum Monte Carlo Calculations", *Phys. Rev. Lett.*, vol. 114, p. 092 301, 9 2015.

[17] A. A. Usmani, "Three-baryon Λnn potential", *Phys. Rev. C*, vol. 52, pp. 1773–1777, 4 1995.

[18] D. Lonardoni, F. Pederiva, and S. Gandolfi, "Accurate determination of the interaction between Λ hyperons and nucleons from auxiliary field diffusion monte carlo calculations", *Phys. Rev. C*, vol. 89, p. 014 314, 1 2014.

[19] L. P. Csernai, *Introduction to relativistic heavy ion collisions*. John Wiley and Sons Ltd, 1994.

[20] K. G. Wilson, "Confinement of quarks", *Phys. Rev. D*, vol. 10, pp. 2445–2459, 8 1974.

[21] D. J. Gross and F. Wilczek, "Ultraviolet behavior of non-abelian gauge theories", *Phys. Rev. Lett.*, vol. 30, pp. 1343–1346, 26 1973.

[22] I. A. Shovkovy, "Two lectures on color superconductivity", *Foundations of Physics*, vol. 35, no. 8, pp. 1309–1358, 2005.

[23] R. Rapp, "Fireball spectroscopy", *Nature Physics*, vol. 15, no. 10, pp. 990–991, 2019.

[24] S. Bass *et al.*, "Microscopic models for ultrarelativistic heavy ion collisions", *Prog. Part. Nucl. Phys*, vol. 41, pp. 255–369, 1998.

[25] T. Galatyuk, Private communication, Nov. 9, 2023.

[26] K. Agarwal and for the CBM Collaboration, "The compressed baryonic matter (CBM) experiment at FAIR—physics, status and prospects", *Physica Scripta*, vol. 98, no. 3, p. 034 006, 2023.

[27] P. Braun-Munzinger, K. Redlich, and J. Stachel, "Particle production in heavy ion collisions", in *Quark–Gluon Plasma 3*, pp. 491–599.

[28] F. Bellini and A. Kalweit, "Testing production scenarios for (anti-)(hyper-)nuclei and exotica at energies available at the cern large hadron collider", *Phys. Rev. C*, vol. 99, p. 054 905, 5 2019.

[29] A. Andronic *et al.*, "Decoding the phase structure of QCD via particle production at high energy", *Nature*, vol. 561, pp. 321–330, 2018.

[30] ALICE Collaboration, "Measurement of the lifetime and Λ separation energy of ${}^{3}_{\Lambda}\mathrm{H}$", 2022. arXiv: 2209.07360 [nucl-ex].

[31] ALICE Collaboration, "Hypertriton production in p-Pb collisions at $\sqrt{s_{NN}} = 5.02$ TeV", *Phys. Rev. Lett.*, vol. 128, p. 252 003, 25 2022.

[32] A. A. Korsheninnikov *et al.*, "Superheavy hydrogen ${}^{5}\mathrm{H}$", *Phys. Rev. Lett.*, vol. 87, p. 092 501, 9 2001.

[33] M. Meister *et al.*, "^{8}He–^{6}He: A comparative study of electromagnetic fragmentation reactions", *Nucl. Phys. A*, vol. 700, no. 1, pp. 3–16, 2002.

[34] Y. Aksyutina *et al.*, "Lithium isotopes beyond the drip line", *Phys. Lett. B*, vol. 666, no. 5, pp. 430–434, 2008.

[35] M. Agnello *et al.*, "Evidence for heavy hyperhydrogen ${}^{6}_{\Lambda}\mathrm{H}$", *Phys. Rev. Lett.*, vol. 108, p. 042 501, 4 2012.

[36] R. Wirth and R. Roth, "Light neutron-rich hypernuclei from the importance-truncated no-core shell model", *Phys. Lett. B*, vol. 779, pp. 336–341, 2018.

[37] C. Samanta, P. R. Chowdhury, and D. N. Basu, "Lambda hyperonic effect on the normal drip lines", *J. Phys. G: Nuclear and Particle Physics*, vol. 35, no. 6, p. 065 101, 2008.

[38] J. Haidenbauer *et al.*, "Hyperon–nucleon interaction at next-to-leading order in chiral effective field theory", *Nucl. Phys. A*, vol. 915, pp. 24–58, 2013.

[39] ALICE Collaboration, "$p-p, p-\Lambda$, and $\Lambda-\Lambda$ correlations studied via femtoscopy in pp reactions at $\sqrt{s} = 7\,\mathrm{TeV}$", *Phys. Rev. C*, vol. 99, p. 024 001, 2 2019.

[40] ALICE Collaboration, "Study of the Λ–Λ interaction with femtoscopy correlations in pp and p–Pb collisions at the LHC", *Phys. Lett. B*, vol. 797, p. 134 822, 2019.

[41] M. Danysz and J. Pniewski, "Delayed disintegration of a heavy nuclear fragment: I", *The London, Edinburgh, and Dublin Philosophical Magazine and Journal of Science*, vol. 44, no. 350, pp. 348–350, 1953. DOI: 10.1080/14786440308520318.

[42] S. B. Yang *et al.*, "First determination of the level structure of an sd-shell hypernucleus ${}^{19}_{\Lambda}\mathrm{F}$", *Phys. Rev. Lett.*, vol. 120, p. 132 505, 13 2018.

[43] S. N. Nakamura, "Hypernuclear Workshop", in *Jlab*, 2014.

[44] O. Hashimoto and H. Tamura, "Spectroscopy of Λ hypernuclei", *Prog. Part. Nucl. Phys*, vol. 57, no. 2, pp. 564–653, 2006.

[45] A. K. Kerman and M. S. Weiss, "Superstrange nuclei", *Phys. Rev. C*, vol. 8, pp. 408–410, 1 1973.

[46] K. J. Nield *et al.*, "Production of hypernuclei in a 2.1 GeV/nucleon oxygen beam", *Phys. Rev. C*, vol. 13, pp. 1263–1266, 3 1976.

[47] S. Avramenko *et al.*, "A study of the production and lifetime of the lightest relativistic hypernuclei", *Nucl. Phys. A*, vol. 547, no. 1, pp. 95–100, 1992.

[48] C. Rappold *et al.*, "Search for evidence of ${}^{3}_{\Lambda}n$ by observing $d+\pi^-$ and $t+\pi^-$ final states in the reaction of ^{6}Li+^{12}C at 2 AGeV", *Phys. Rev. C*, vol. 88, p. 041 001, 4 2013.

[49] Y. L. Sun *et al.*, "Production of light hypernuclei with light-ion beams and targets", *Phys. Rev. C*, vol. 98, p. 024 903, 2 2018.

[50] J. Steinheimer and M. Bleicher, "Sub-threshold Φ and Ξ^- production by high mass resonances with UrQMD", *Journal of Physics G: Nuclear and Particle Physics*, vol. 43, no. 1, p. 015 104, Dec. 2015.

[51] A. B. Larionov, T. Gaitanos, and U. Mosel, "Kaon and hyperon production in antiproton-induced reactions on nuclei", *Phys. Rev. C*, vol. 85, p. 024 614, 2 2012.

[52] T. A. Armstrong *et al.*, "Fission of heavy hypernuclei formed in antiproton annihilation", *Phys. Rev. C*, vol. 47, 5 1993.

[53] A. Sanchez Lorente *et al.*, "Hypernuclear physics studies of the PANDA experiment at FAIR", *Hyperfine Interactions*, vol. 229, no. 1, pp. 45–51, 2014.

[54] R. L. Workman *et al.*, "Review of Particle Physics", *Prog. Theo. Exp. Phys.*, vol. 2022, p. 083C01, 2022.

[55] P. A. Boyle *et al.*, "Emerging understanding of the $\Delta I{=}1/2$ rule from lattice QCD", *Phys. Rev. Lett.*, vol. 110, p. 152 001, 15 2013.

[56] W. Alberico *et al.*, "Two-nucleon induced Λ decay in nuclei", *Phys. Lett. B*, vol. 256, no. 2, pp. 134–140, 1991.

[57] I. Vidaña, "Hyperons: The strange ingredients of the nuclear equation of state", *Proc. R. Soc. A*, vol. 474, 2018.

[58] E. Hiyama *et al.*, "Three-body model study of A=6–7 hypernuclei: Halo and skin structures", *Phys. Rev. C*, vol. 53, pp. 2075–2085, 5 1996.

[59] K. Riisager, D. V. Fedorov, and A. S. Jensen, "Quantum halos", *Europhysics Letters*, vol. 49, no. 5, p. 547, 2000.

[60] A. Obertelli and H. Sagawa, "Radioactive-ion-beam physics", in *Modern Nuclear Physics: From Fundamentals to Frontiers*. Springer Singapore, 2021, pp. 371–459.

[61] K. Riisager, "Halos and related structures", *Physica Scripta*, vol. 2013, no. T152, p. 014 001, 2013.

[62] I. Tanihata *et al.*, "Measurements of interaction cross sections and nuclear radii in the light p-shell region", *Phys. Rev. Lett.*, vol. 55, pp. 2676–2679, 24 1985.

[63] P. G. Hansen and B. Jonson, "The neutron halo of extremely neutron-rich nuclei", *Europhysics Letters*, vol. 4, no. 4, p. 409, 1987.

[64] T. Kobayashi *et al.*, "Projectile fragmentation of the extremely neutron-rich nucleus ^{11}Li at 0.79 GeV/nucleon", *Phys. Rev. Lett.*, vol. 60, pp. 2599–2602, 25 1988.

[65] A. Dobrovolsky *et al.*, "Study of the nuclear matter distribution in neutron-rich Li isotopes", *Nuclear Physics A*, vol. 766, pp. 1–24, 2006.

[66] I. Tanihata, H. Savajols, and R. Kanungo, "Recent experimental progress in nuclear halo structure studies", *Prog. Part. Nucl. Phys*, vol. 68, pp. 215–313, 2013.

[67] A. Cobis, A. S. Jensen, and D. V. Fedorov, "The simplest strange three-body halo", *J. Phys. G: Nuclear and Particle Physics*, vol. 23, no. 4, p. 401, 1997.

[68] E. Hiyama *et al.*, "Three-body model study of A=6-7 hypernuclei: Halo and skin structures", *Phys. Rev. C*, vol. 53, pp. 2075–2085, 5 1996.

[69] M. Jurič *et al.*, "A new determination of the binding-energy values of the light hypernuclei (A $\leq$ 15)", *Nucl. Phys. B*, vol. 52, pp. 1–30, 1973.

[70] STAR Collaboration, "Measurement of the mass difference and the binding energy of the hypertriton and antihypertriton", *Nature Physics*, vol. 16, no. 4, pp. 409–412, 2020.

[71] P. Eckert *et al.*, *Chart of hypernuclides — Hypernuclear structure and decay data*, `https://hypernuclei.kph.uni-mainz.de`, Accessed: 2023.

[72] F. Hildenbrand and H.-W. Hammer, "Three-body hypernuclei in pionless effective field theory", *Phys. Rev. C*, vol. 100, p. 034 002, 3 2019, *Phys. Rev. C* 102:039901, 2020, (erratum).

[73] H.-W. Hammer, C. Ji, and D. R. Phillips, "Effective field theory description of halo nuclei", *J. Phys. G*, vol. 44, no. 10, p. 103 002, 2017.

[74] F. Hildenbrand and H.-W. Hammer, Private communication following Phys. Rev. C 100, 2019, Sep. 1, 2023.

[75] W. Glöckle *et al.*, "The hypertriton and its decays", *Nucl. Phys. A*, vol. 639, no. 1, pp. 297c–306c, 1998.

[76] S. Velardita *et al.*, "Method to evidence hypernuclear halos from a two-target interaction cross section measurement", *Eur. Phys. J. A*, vol. 59, no. 6, p. 139, 2023.

[77] C. Rappold and J. López-Fidalgo, "Examination of experimental conditions for the production of proton-rich and neutron-rich hypernuclei", *Phys. Rev. C*, vol. 94, p. 044 616, 4 2016.

[78] A. Ozawa *et al.*, "Measurements of interaction cross sections for light neutron-rich nuclei at relativistic energies and determination of effective matter radii", *Nuclear Physics A*, vol. 691, no. 3, pp. 599–617, 2001.

[79] W.-M. Yao *et al.*, "Review of particle physics", *J. Phys. G: Nucl. Part. Phys.*, vol. 33, pp. 1–1232, 2006.

[80] I. Sick and J. McCarthy, "Elastic electron scattering from ^{12}C and ^{16}O", *Nucl. Phys. A*, vol. 150, pp. 631–654, 1970.

[81] D. Bassano *et al.*, "Lambda-proton interactions at high energies", *Phys. Rev.*, vol. 160, pp. 1239–1244, 5 1967.

[82] S. Gjesdal *et al.*, "A measurement of the total cross-sections for Λ hyperon interactions on protons and neutrons in the momentum range from 6 GeV/c to 21 GeV/c", *Phys. Lett. B*, vol. 40, pp. 152–156, 1972.

[83] GSI, *GSI helmholtz centre for heavy ion research*, http://www.gsi.de.

[84] J. Jaros *et al.*, "Nucleus-nucleus total cross sections for light nuclei at 1.55 and 2.89 GeV/c per nucleon", *Phys. Rev. C*, vol. 18, pp. 2273–2292, 5 1978.

[85] R. L. Burden and J. D. Faires, *Numerical Analysis*, Fourth. PWS-Kent Publishing Company, 1989.

[86] S. Leray *et al.*, "Extension of the liège intra nuclear cascade model to light ion-induced collisions for medical and space applications", *J. Phys.: Conference Series*, vol. 420, p. 012 065, 2013.

[87] V. Toneev and K. Gudima, "Particle emission in light and heavy ion reactions", *Nuclear Physics A*, vol. 400, pp. 173–189, 1983.

[88] B. Gastineau *et al.*, "Progress in design and construction of the R^{3}B -GLAD large acceptance superconducting dipole spectrometer for GSI-FAIR", *IEEE Transactions on Applied Superconductivity*, vol. 20, no. 3, pp. 328–331, 2010.

[89] *The FAIR accelerator facility*, `https://www.gsi.de/en/researchaccelerators/fair/the_machine`, Accessed: 2023.

[90] P. Spiller *et al.*, "The FAIR Heavy Ion Synchrotron SIS100", *Journal of Instrumentation*, vol. 15, no. 12, T12013, 2020.

[91] T. Stöhlker *et al.*, "APPA at FAIR: From fundamental to applied research", *NIM B*, vol. 365, pp. 680–685, 2015.

[92] C. Höhne *et al.*, "The compressed baryonic matter experiment at the future accelerator facility in darmstadt", *Nuclear Physics A*, vol. 749, pp. 141–149, 2005.

[93] R. Krücken *et al.*, "The NuSTAR facilty at FAIR", *J. Phys. G: Nuclear and Particle Physics*, vol. 31, no. 10, S1807, 2005.

[94] Panda Collaboration, https://panda.gsi.de/oldwww/archive/public/panda_loi.pdf, Accessed: 2023, 2004.

[95] W. Barth *et al.*, "Upgrade program of the high current heavy ion UNILAC as an injector for FAIR", *NIM A*, vol. 577, no. 1, pp. 211–214, 2007.

[96] K. Blasche *et al.*, "The SIS Heavy Ion Synchrotron project", *IEEE Transactions on Nuclear Science*, vol. 32, no. 5, pp. 2657–2661, 1985.

[97] B. Franzke, "The heavy ion storage and cooler ring project ESR at GSI", *NIM B*, vol. 24, pp. 18–25, 1987.

[98] "GSI-FAIR Scientific Report 2018", Darmstadt, Tech. Rep. GSI Report 2019-1, 2019, 127 p. DOI: 10.15120/GSI-2019-00545.

[99] *R^3B Collaboration*, https://www.gsi.de/work/forschung/nustarenna/nustarenna_divisions/kernreaktionen/activities/r3b, Accessed: 2023.

[100] M. Xarepe *et al.*, "Resistive plate chambers for precise measurement of high-momentum protons in short range correlations at R^3B", *NIM A*, vol. 1055, p. 168 445, 2023.

[101] D. Cortina-Gil *et al.*, "CALIFA, a dedicated calorimeter for the R^3B/FAIR", *Nuclear Data Sheets*, vol. 120, pp. 99–101, 2014.

[102] K. Boretzky *et al.*, "NeuLAND: The high-resolution neutron time-of-flight spectrometer for r^3b at FAIR", *NIM A*, vol. 1014, p. 165 701, 2021.

[103] *ELJEN technologies*, https://eljentechnology.com/products/plastic-scintillators/ej-200-ej-204-ej-208-ej-212, Accessed: 2023.

[104] *Comsol multiphysics website*, https://www.comsol.com/, Accessed: 2023.

[105] H. J. Hilke, "Time projection chambers", *Reports on Progress in Physics*, vol. 73, no. 11, p. 116 201, 2010.

[106] A. Obertelli *et al.*, Hypernuclei studies at R^3B with the HYDRA TPC, LoI to the G-PAC, 2019.

[107] Y. Giomataris *et al.*, "MICROMEGAS: A high-granularity position-sensitive gaseous detector for high particle-flux environments", *NIM A*, vol. 376, no. 1, pp. 29–35, 1996.

[108] J. Giovinazzo *et al.*, "Metal-core pad-plane development for ACTAR TPC", *NIM A*, vol. 892, pp. 114–121, 2018.

[109] F. Sauli, "GEM: A new concept for electron amplification in gas detectors", *NIM A*, vol. 386, no. 2, pp. 531–534, 1997.

[110] Y.-L. Zhang *et al.*, "A hybrid structure gaseous detector for ion backflow suppression", *Chinese Physics C*, vol. 41, no. 20170521, p. 056 003, 2017.

[111] D. Pfeiffer *et al.*, “Rate-capability of the VMM3a front-end in the RD51 scalable readout system”, *NIM A*, vol. 1031, p. 166 548, 2022.

[112] F. Sauli, “Principles of operation of multiwire proportional and drift chambers”, Geneva, Tech. Rep., 1977.

[113] T. Yamashita *et al.*, “Measurements of the electron drift velocity and positive-ion mobility for gases containing CF4”, *NIM A*, vol. 283, no. 3, pp. 709–715, 1989.

[114] J. Abele *et al.*, “The laser system for the star time projection chamber”, *NIM A*, vol. 499, pp. 692–702, 2003.

[115] J. Alme *et al.*, “The ALICE TPC, a large 3-dimensional tracking device with fast readout for ultra-high multiplicity events”, *NIM A*, vol. 622, no. 1, pp. 316–367, 2010.

[116] J. Bourotte and B. Sadoulet, “Ionization of multiwire proportional chamber gas by double photon absorption”, *NIM*, vol. 173, no. 3, pp. 463–470, 1980.

[117] R. Gluckstern, “Uncertainties in track momentum and direction, due to multiple scattering and measurement errors”, *NIM*, vol. 24, pp. 381–389, 1963.

[118] W. R. Leo, *Techniques for nuclear and particle physics experiments: a how-to approach; 2nd ed.* Berlin: Springer, 1994.

[119] A. Einstein, “Über einen die Erzeugung und Verwandlung des Lichtes betreffenden heuristischen Gesichtspunkt”, *Annalen der Physik*, vol. 322, no. 6, pp. 132–148, 1905.

[120] E. Jeon *et al.*, “Magnetic field effects on the photocathode uniformity of hamamatsu R7081 photomultiplier tubes”, *NIM A*, vol. 697, pp. 46–51, 2013.

[121] R. Hawkes *et al.*, “Silicon photomultiplier performance tests in magnetic resonance pulsed fields”, in *2007 IEEE Nuclear Science Symposium Conference Record*, vol. 5, 2007, pp. 3400–3403.

[122] C. Xanthopoulou, *PUMA: Simulation of the trigger system with the geant4 extension GODDeSS*, Bachelor Thesis, TU Darmstadt, 2020.

[123] *Hamamatsu: Photon is our business*, `https://www.hamamatsu.com/content/dam/hamamatsu-photonics/sites/documents/99_SALES_LIBRARY/ssd/s13360_series_kapd1052e.pdf`, Accessed: 2023.

[124] M. Cardinali *et al.*, “Frontend electronics for high-precision single photo-electron timing using fpga-tdcs”, *NIM A*, vol. 766, pp. 231–234, 2014.

[125] C. Ugur *et al.*, “Field programmable gate array based data digitisation with commercial elements”, *Journal of Instrumentation*, vol. 8, no. 01, p. C01035, 2013.

[126] J. Adamczewski-Musch *et al.*, “Web interface for online root and daq applications”, in *2014 19th IEEE-NPSS Real Time Conference*, 2014, pp. 1–5.

[127] *ROOT: Analyzing petabytes of data, scientifically.* `https://root.cern/`, Accessed: 2023.

[128] *TRB3: FPGA TDC calibration*, `https://web-docs.gsi.de/~dabc/doc/stream/hadaq_tdc_calibr.html`, Accessed: 2023.

[129] A. Neiser *et al.*, "Trb3: A 264 channel high precision tdc platform and its applications", *Journal of Instrumentation*, vol. 8, no. 12, p. C12043, 2013.

[130] *Trb3 documentation*, https://jspc29.x-matter.uni-frankfurt.de/trbweb/?action=page&url=trb3-documents, Accessed: 2023.

[131] D. E. Groom, N. V. Mokhov, and S. I. Striganov, "Muon stopping power and range tables 10 MeV–100 TeV", *Atomic Data and Nuclear Data Tables*, vol. 78, no. 2, pp. 183–356, 2001.

[132] *R3BRoot: Simulations and data analysis for R^3B*, https://github.com/R3BRootGroup/R3BRoot, Accessed: 2023.

[133] *FAIROOT website*, https://fairroot.gsi.de/, Accessed: 2023.

[134] *GEANT4 website.* https://geant4.web.cern.ch/, Accessed: 2023.

[135] *GitHub: Svelardita/glad-tpc at dev*, https://github.com/svelardita/glad-tpc/tree/dev, Accessed: 2023.

[136] *TGenPhaseSpace class reference*, https://root.cern.ch/doc/master/classTGenPhaseSpace.html, Accessed: 2023.

[137] A. S. Botvina, K. K. Gudima, and J. Pochodzalla, "Production of hypernuclei in peripheral relativistic ion collisions", *Phys. Rev. C*, vol. 88, p. 054 605, 5 2013.

[138] A. S. Botvina, I. N. Mishustin, and J. Pochodzalla, "Production of exotic hypernuclei from excited nuclear systems", *Phys. Rev. C*, vol. 86, p. 011 601, 1 Jul. 2012.

[139] A. Kelic, M. V. Ricciardi, and K.-H. Schmidt, *ABLA07 - towards a complete description of the decay channels of a nuclear system from spontaneous fission to multifragmentation*, 2009. arXiv: 0906.4193 [nucl-th].

[140] H. Iwamoto, S. Meigo, and H. Matsuda, "A comprehensive study of spallation models for proton-induced spallation product yields utilized in transport calculation", *EPJ Web Conf.*, vol. 239, p. 06 001, 2020.

[141] The ALICE collaboration, CERN-LHCC-2013-020 / ALICE-TDR-016, 2014.

[142] H. Tamura *et al.*, "Formation of ${}^{4}_{\Lambda}$H hypernuclei from K^- absorption at rest on light nuclei", *Phys. Rev. C*, vol. 40, R479–R482, 2 1989.

[143] H. Alvarez-Pol and Y. Ayyad, Private communication, Nov. 1, 2022.

[144] R. E. Kalman, "A new approach to linear filtering and prediction problems", *Transactions of the ASME–Journal of Basic Engineering*, vol. 82, no. Series D, pp. 35–45, 1960.

[145] R. Frühwirth, "Application of kalman filtering to track and vertex fitting", *NIM A*, vol. 262, no. 2, pp. 444–450, 1987.

[146] J. Rauch and T. Schlüter, "Genfit — a generic track-fitting toolkit", *J. Phys.: Conference Series*, vol. 608, no. 1, p. 012 042, 2015.

[147] S. Anvar *et al.*, "AGET, the GET front-end ASIC, for the readout of the time projection chambers used in nuclear physic experiments", in *2011 IEEE Nuclear Science Symposium Conference Record*, 2011, pp. 745–749.

[148] A. Obertelli *et al.*, “Minos: A vertex tracker coupled to a thick liquid-hydrogen target for in-beam spectroscopy of exotic nuclei”, *EPJ A*, vol. 50, no. 1, p. 8, 2014.

[149] D. Arogancia *et al.*, “Study in a beam test of the resolution of a micromegas TPC with standard readout pads”, *NIM A*, vol. 602, no. 2, pp. 403–414, 2009.

[150] The HADES Collaboration, “Probing dense baryon-rich matter with virtual photons”, *Nature Physics*, vol. 15, no. 10, pp. 1040–1045, 2019.

[151] The HADES Collaboration, “The high-acceptance dielectron spectrometer hades”, *The European Physical Journal A*, vol. 41, no. 2, pp. 243–277, 2009.

[152] *HADES internal report.*

[153] A. Rost *et al.*, “Beam Quality Monitoring System in the HADES Experiment at GSI Using CVD Diamond Material”, in *Proc. 7th International Beam Instrumentation Conference (IBIC’18), Shanghai, China, 09-13 September 2018*, ser. International Beam Instrumentation Conference, JACoW Publishing, 2019, pp. 300–302.

[154] A. Rost *et al.*, “Performance of the CVD Diamond Based Beam Quality Monitoring System in the HADES Experiment at GSI”, in *Proc. 10th International Particle Accelerator Conference (IPAC’19), Melbourne, Australia, 19-24 May 2019*, ser. International Particle Accelerator Conference, JACoW Publishing, 2019, pp. 2507–2509.

[155] J. Pietraszko *et al.*, “Radiation damage in single crystal CVD diamond material investigated with a high current relativistic 197Au beam”, *NIM A*, vol. 763, pp. 1–5, 2014.

[156] *GSI website.* `https://www.gsi.de/en/researchaccelerators/research_an_overview/hades_experiment/configuration_of_the_hades_experiment`, Accessed: 2023.

[157] J. H. Otto, “Dielectron reconstruction in Ag+Ag at $\sqrt{s_{NN}}$=2.55 GeV with HADES”, Ph.D. dissertation, Justud-Liebig-Universitat Giessen, 2022.

[158] J. Adamczewski-Musch et al. HADES Collaboration, *Proposals for experiments at SIS18 during FAIR Phase-0-HADES 102 p.* 2017.

[159] P. Salabura, “HADES: A High Acceptance DiElectron Spectrometer”, *Acta Phys. Polon. B*, vol. 27, J. Skalski and Z. Sujkowski, Eds., pp. 421–440, 1996.

[160] C. Müntz *et al.*, “The HADES tracking system”, *NIM A*, vol. 535, no. 1, pp. 242–246, 2004.

[161] *HADES website.* `https://hades.gsi.de/node/71`, Accessed: 2023.

[162] A. Blanco *et al.*, “Performance of the HADES-TOF RPC wall in a Au-Au beam”, *PoS*, vol. RPC2012, p. 078, 2012.

[163] C. Agodi *et al.*, “The HADES time-of-flight wall”, *NIM A*, vol. 492, no. 1, pp. 14–25, 2002.

[164] D. Belver *et al.*, “The HADES RPC inner TOF wall”, *NIM A*, vol. 602, no. 3, pp. 687–690, 2009.

[165] A. Blanco *et al.*, “RPC HADES-TOF wall cosmic ray test performance”, *NIM A*, vol. 661, S114–S117, 2012.

[166] D. Belver, "The front-end electronics of the HADES timing RPCs wall: Design, development and performances analysis", Ph.D. dissertation, Universidade de Santiago de Compostela, 2009.

[167] B. Kardan, "Centrality determination at 1.23 AGeV GOLD-GOLD collision and readout- electronics for the HADES electromagnetic calorimeter", M.S. thesis, Goethe University, 2015.

[168] B. Kardan, Private communication following M.S. thesis B. Kardan Goethe University, 2019, Oct. 31, 2023.

[169] M. Sánchez, "Momentum reconstruction and pion production analysis in the HADES spectrometer at GSI", Ph.D. dissertation, University of Santiago de Compostela, 2003.

[170] J. Adamczewski-Musch *et al.*, "Centrality determination of Au + Au collisions at 1.23A GeV with HADES", *Eur. Phys. J. A*, vol. 54, no. 5, p. 85, 2018.

[171] W. Press *et al.*, *Numerical Recipes: The Art of Scientific Computing*, 3rd ed. Cambridge University Press, 2007.

[172] S. Spies, "Strange hadron production in Ag+Ag collisions at 1.58A GeV", Ph.D. dissertation, Frankfurt U., 2022.

[173] J. Podolanski and R. Armenteros, "III. Analysis of V-events", *The London, Edinburgh, and Dublin Philosophical Magazine and Journal of Science*, vol. 45, no. 360, pp. 13–30, 1954.

[174] T. Scheib, "Λ and K^0_S production in Au+Au collisions at 1.23 AGeV", Ph.D. dissertation, Geothe Universitat Frankfurt, 2017.

[175] I. Fröhlich *et al.*, "Design of the pluto event generator", *Journal of Physics: Conference Series*, vol. 219, no. 3, p. 032 039, 2010.

[176] R. Brun *et al.*, "GEANT3", 1987.

[177] A. Hoecker *et al.*, *TMVA - toolkit for multivariate data analysis*, 2009.

[178] *A NIST physical measurement laboratory service*, `https://physics.nist.gov/cgi-bin/cuu/Value?eqmdc2mev`, Accessed: 2023.

[179] L. Lyons, *Discovering the significance of 5 sigma*, 2013. arXiv: `1310.1284`.

[180] M. Bleicher *et al.*, "Relativistic hadron-hadron collisions in the ultra-relativistic quantum molecular dynamics model", *Journal of Physics G: Nuclear and Particle Physics*, vol. 25, no. 9, p. 1859, 1999.

[181] J. Weil *et al.*, "Particle production and equilibrium properties within a new hadron transport approach for heavy-ion collisions", *Phys. Rev. C*, vol. 94, p. 054 905, 5 2016.